Untersuchung der technischen Möglichkeiten zum Niedrigtemperaturfügen von LTCC-Substraten unter Verwendung nanoskaliger reaktiver Multilagensysteme

Dissertation

zur Erlangung des Grades
des Doktors der Ingenieurwissenschaften
der Naturwissenschaftlich-Technischen Fakultät
der Universität des Saarlandes

von
Erik Wiss

Saarbrücken
2025

Tag des Kolloquiums: 30.09.2025
Dekan: Prof. Dr.-Ing. Dirk Bähre
Berichterstatter: Prof. Dr.-Ing. Steffen Wiese
Prof. Dr.-Ing. Jens Müller
Vorsitz: Prof. Dr.-Ing. Chihao Xu
Akad. Mitarbeiter: Dr.-Ing. Sophie Nalbach

Kurzfassung

Das Ziel dieser Arbeit ist die experimentelle Untersuchung reaktiver Fügeprozesse auf LTCC-Substraten (**L**ow **T**emperature **C**ofired **C**eramics) sowie deren Analyse mittels Simulationen. Ein wesentlicher Vorteil dieser Verfahren liegt in der lokal begrenzten Wärmezufuhr zu den Lötstellen, wodurch thermomechanische Spannungen reduziert werden können. Diese entstehen bei konventionellen Lötverfahren durch die unterschiedlichen thermischen Ausdehnungskoeffizienten der Fügepartner und das Aufheizen der gesamten Baugruppe. Anders als bei metallischen oder siliziumbasierten Substraten, auf denen die Anwendung solcher Prozesse bereits umfassend erforscht ist, stellt die Übertragung auf die LTCC-Technologie aufgrund ihrer spezifischen Materialeigenschaften – wie hoher Oberflächenrauheit und geringer Wärmeleitfähigkeit – eine besondere Herausforderung dar.

Die vorliegende Arbeit untersucht den Einfluss der Oberflächenmorphologie auf die Abscheidung reaktiver Multilagensysteme und die Eigenschaften der exothermen Reaktion hinsichtlich Reaktionsgeschwindigkeit und Spitzentemperatur. LTCC-Proben wurden mit verschiedenen Anpressdrücken zusammengefügt und die Fügezonen durch Licht- und Rasterelektronenmikroskopie analysiert. Numerische Untersuchungen wurden durchgeführt, um Temperaturverläufe zu analysieren, Unterschiede zwischen LTCC- und Silizium-Substraten zu bewerten und die Eignung integrierter Sensoren zur Erfassung der Reaktionseigenschaften zu prüfen.

Abstract

The aim of this work is the experimental investigation of reactive joining processes on LTCC substrates (**L**ow **T**emperature **C**ofired **C**eramics) and their analysis by means of simulations. A key advantage of these processes lies in the localized heat input to the solder joints, by which thermomechanical stresses can be reduced. Such stresses typically arise in conventional soldering processes from the differing coefficients of thermal expansion between the joining partners and from heating of the entire assembly. Unlike metallic or silicon-based substrates, on which the application of such processes has already been extensively studied, the transfer to LTCC technology poses particular challenges due to its specific material properties – such as high surface roughness and low thermal conductivity.

This work investigates the influence of surface morphology on the deposition of reactive multilayer systems and on the properties of the exothermic reaction with regard to reaction velocity and peak temperature. LTCC samples were joined at various contact pressures, and the bonding zones were analyzed using light and scanning electron microscopy. Numerical studies were performed to analyze temperature profiles, compare LTCC and silicon substrates, and assess the suitability of integrated sensors for recording reaction characteristics.

Inhaltsverzeichnis

Abbildungsverzeichnis

Tabellenverzeichnis

Abkürzungsverzeichnis

AVT	*Aufbau- und Verbindungstechnik*
BSE	*Back Scattered Electron (Rückstreuelektron)*
CTE	*Coefficient of Thermal Expansion (Wärmeausdehnungskoeffizient)*
DIC	*Digital Image Correlation (digitale Bildkorrelation)*
EDX	*Energy Dispersive X-ray Spectroscopy (energiedispersive Röntgenspektroskopie)*
IMP	*Intermetallische Phase*
LM	*Lichtmikroskop*
LSM	*Laser-Scanning-Mikroskop*
LTCC	*Low Temperature Cofired Ceramics (Niedertemperatur-Einbrand-Keramiken)*
NA	*Numerische Apertur*
PVD	*Physical Vapour Deposition (physikalische Gasphasenabscheidung*
REM	*Rasterelektronenmikroskop*
RMS	*Reaktives Multilagensystem*
RoHS	*Restriction of Hazardous Substances (Beschränkung gefährlicher Stoffe)*
SAC	*SnAgCu*
SE	*Sekundärelektron*
SMD	*Surface Mount Device (Oberflächenbauelement)*
THT	*Through Hole Technology (Durchsteckmontage)*
WP	*Work Package (Arbeitspaket)*

1 Einleitung und Motivation

1.1 Einführung

Mit Ausnahme weniger Verfahren – etwa dem Ultraschall-Wedge-Wedge-Drahtbonden, dem UV-Härten leitfähiger Klebstoffe oder dem mechanischen Fügen (Crimpen, Steckverbinder) – basieren alle etablierten Methoden zur Herstellung elektrischer Verbindungen auf dem Einbringen von Wärme an die Fügestellen. Im Rahmen der industriellen Massenfertigung wird dabei nicht nur die Fügestelle selbst, sondern häufig die gesamte Baugruppe einem solchen Wärmeeintrag unterzogen. Ein typisches Beispiel hierfür ist das Reflow-Löten, das insbesondere bei oberflächenmontierten Bauelementen (SMD, **S**urface **M**ount **D**evices) zur Anwendung kommt. Dabei wird zunächst eine Lotpaste auf die Kontaktflächen des Substrats appliziert, die Bauteile anschließend positioniert und schließlich die gesamte Baugruppe in einem Reflow-Ofen auf Temperaturen oberhalb des Schmelzpunkts des Lots erhitzt.

Dabei entstehen thermomechanische Spannungen, die aus den unterschiedlichen Wärmeausdehnungskoeffizienten (CTE, **C**oefficient of **T**hermal **E**xpansion) der verwendeten Materialien resultieren – sowohl zwischen Bauteil und Substrat als auch innerhalb der Bauelemente selbst. Diese Spannungen können im Extremfall zur Entstehung von Rissen und somit zu Funktionsausfällen führen. Zudem wirken sich die hohen Prozesstemperaturen negativ auf temperaturempfindliche Komponenten aus. Diese Problematik wurde durch die Umstellung auf bleifreie Lote im Zuge der in den Jahren 2003 und 2011 erlassenen RoHS-Richtlinien (**R**estriction **o**f **H**azardous **S**ubstances) weiter verstärkt: Die Schmelztemperaturen heute üblicher bleifreier Lote (z. B. SAC-Legierungen (**S**n**A**g**C**u) bestehend aus Zinn (Sn), Silber (Ag) und Kupfer (Cu) mit 217–227 °C) liegen rund 40 °C über denen ihrer bleihaltigen Vorgänger (183–190 °C), weshalb die Prozesstemperaturen entsprechend angehoben werden mussten.

Es wäre daher insbesondere in Hinblick auf die Zuverlässigkeit wünschenswert, wenigstens einen dieser beiden Faktoren ausschließen zu können. Da eine Veränderung der Komponenten bzw. eine Änderung ihrer Materialien in der Regel mit einem erheblichem Entwicklungsaufwand verbunden ist, erscheint die Nutzung lokaler statt globaler Wärmequellen zur Reduktion des Wärmeeintrags als vielversprechender Ansatz. Eine solche Möglichkeit bieten nanoskalige reaktive Multilagensysteme (RMS) [1–14]. Diese bestehen aus alternierenden Schichten zueinander passender Materialien, die nach der Zündung – beispielsweise durch einen Laserimpuls, einen elektrischen Impuls oder das Zuführen ausreichender thermischer Energie – eine stark exotherme Reaktion eingehen [15]. Die dabei freigesetzte Wärme kann gezielt für Fügevorgänge genutzt werden [12–14, 16, 17], ohne die gesamte Baugruppe thermisch zu belasten. Ein typisches Beispiel ist das Materialsystem Aluminium/Nickel (Al/Ni).

Die bisherigen Forschungsarbeiten zum Thema des reaktiven Fügens konzentrieren sich überwiegend auf die Herstellung metallischer [9, 18–20], siliziumbasierter (Si) [2, 3, 21–26] oder hybrider Fügeverbindungen [4, 10, 27] wie beim Die-Bonding oder der Befestigung von Kühlkörpern. Der Einsatz von RMS in anderen Bereichen der Aufbau- und Verbindungstechnik (AVT) – vor allem auf Low Temperature Cofired Ceramics-Substraten (LTCC) – ist bislang nur unzureichend erforscht, obwohl die LTCC-Technologie zahlreiche Vorteile bietet. Sie zeichnet sich durch eine hohe Zuverlässigkeit, hohe thermische und mechanische Langzeitstabilität, dauerhaft hermetisch dichte Verbindungen sowie eine starke Resistenz gegenüber chemischen Einflüssen aus [28–38], weshalb sie sich ideal für High-Performance-Anwendungen im Automobil-, Militär und auch Raumfahrtbereich eignet. Weiterhin lassen sich mit LTCC-Substraten aufgrund ihrer sehr guten dielektrischen Eigenschaften auch Hochfrequenz- und Radaranwendungen realisieren [39–42]. Die direkte Integration von passiven Bauelementen wie Widerständen, Kapazitäten und Induktivitäten ist ebenso möglich wie die Strukturierung von mikrofluidischen Kanälen [31–33, 43–46], die für Kühlungszwecke oder in biomedizinischen Anwendungen genutzt werden können.

Die Übertragung reaktiver Fügeverfahren auf LTCC-Substrate würde insbesondere im Bereich der heterogenen Integration zusätzliche technologische Möglichkeiten eröffnen, stellt jedoch aufgrund der spezifischen Materialeigenschaften eine Herausforderung dar. Die Wärmeleitfähigkeit üblicher LTCC-Materialien liegt mit 2–4 W/(m·K) deutlich unter der von Metallen (z. B. Cu: ~150 W/(m·K)) oder Si (~380 W/(m·K)), und ihre Oberflächenrauheit mit 0,1–100 µm deutlich darüber (nm-Bereich) [47–49]. Die geringe Wärmeleitfähigkeit erschwert die Ableitung der bei der Reaktion freigesetzten Wärme, was zu lokaler Überhitzung und somit zu thermomechanischen Spannungen, Rissbildung, Delamination oder zur Beschädigung einzelner Schichten führen kann. Die hohe Rauheit wiederum begünstigt Inhomogenitäten in der Abscheidung eines RMS, was die Reaktionsstabilität negativ beeinflussen kann. Beide Effekte wirken sich signifikant auf den reaktiven Fügeprozess aus und unterstreichen die Notwendigkeit weiterführender Untersuchungen zur Prozessanpassung und Materialkompatibilität.

1.2 Ziele der Arbeit

Das zentrale Ziel der Arbeit ist die gezielte Weiterentwicklung reaktiver Fügeprozesse zur Anwendung in der AVT mikroelektronischer Systeme. Im Fokus steht dabei die Abscheidung von Al/Ni-RMS auf keramischen LTCC-Substraten mit hoher Oberflächenrauheit. Im Unterschied zu früheren Arbeiten, in denen RMS auf ebenen Substraten wie Metallen oder Si abgeschieden wurden, führt die Topografie der LTCC-Oberflächen zu einer ausgeprägten nicht-planaren Morphologie des RMS.

Diese Morphologie beeinflusst den Reaktionsverlauf hinsichtlich Ausbreitungsgeschwindigkeit, Temperaturentwicklung und Erstarrungsverhalten. Es soll untersucht werden, inwieweit sich diese Parameter durch eine gezielte Modifikation der Oberfläche optimieren lassen, sodass die entstehenden Verbindungen Bauteile und Substrat nicht nur kontaktieren, sondern auch eine hohe elektrische und thermische Leitfähigkeit, geringe Induktivität sowie mechanische Robustheit aufweisen.

Vor dem Hintergrund dieser Herausforderungen orientiert sich die vorliegende Dissertation an folgenden zentralen Fragestellungen [50]:

- Wie beeinflussen unterschiedliche Oberflächenmorphologien den Fügeprozess?
- Wie wirken sich die thermischen Eigenschaften verschiedener Substratmaterialien (organische und keramische Träger) auf den Reaktionsverlauf aus?
- Welche Wechselwirkungen zwischen den verschiedenen Funktionsschichten (Reaktiv- und Fügeschicht) können zur gezielten Steuerung des Fügeprozesses genutzt werden?
- Wie beeinflussen Randbedingungen wie Umgebungstemperatur und Fügedruck den Reaktionsverlauf?
- Welche mechanischen Eigenschaften ergeben sich in Abhängigkeit von Oberflächenmorphologie und Prozessierung?
- Können diese zur Reduktion mechanischer Spannungen in der Baugruppe beitragen?

Diese miteinander zusammenhängenden Fragestellungen wurden im Rahmen eines DFG-Forschungsprojekts in Zusammenarbeit mit dem Fachgebiet Elektroniktechnologie der TU Ilmenau bearbeitet. Dazu wurden die Arbeiten in sechs Arbeitspakete (WP, **W**ork **P**ackage) unterteilt, um die jeweiligen Fachkompetenzen und technischen Möglichkeiten beider Partner optimal zu kombinieren. Abb. 1 gibt einen Überblick über den Zusammenhang der einzelnen WP.

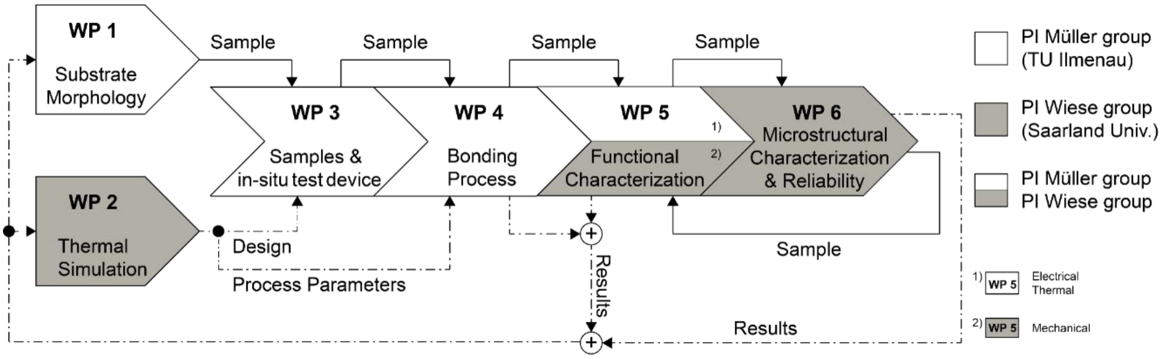

Abbildung 1: Übersicht über die einzelnen WP des Forschungsprojekts [50].

WP1 (TU Ilmenau) beschäftigt sich mit der Herstellung verschiedener Oberflächenmorphologien auf LTCC-Substraten, darunter chemisch-mechanisches Polieren (CMP, siehe Kapitel 4.1.4.1) und Laserablation (siehe Kapitel 4.1.4.2). Die Charakterisierung der Oberflächenrauheit erfolgt mit einem Laser-Scanning-Mikroskop (LSM, siehe Kapitel 4.1.8.1).

WP2 (Universität des Saarlandes) beschäftigt sich mit der thermischen Simulation des reaktiven Fügeprozesses. Untersuchte Aspekte sind unter anderem die Abhängigkeit des Wärmetransports von den thermischen Eigenschaften und der Schichtdicke der verwendeten Materialien sowie die Temperaturverläufe entlang und senkrecht zur Ausbreitungsrichtung der Reaktion. Die Simulationen liefern Schätzwerte für schwer messbare Prozessparameter wie Temperatur und Reaktionsgeschwindigkeit und unterstützen die experimentellen Arbeitspakete WP3 bis WP6.

WP3 (TU Ilmenau) beschäftigt sich mit der Entwicklung und Integration eines In-situ-Messsystems zur Erfassung von Prozessparametern wie Temperatur und mechanischer Dehnung über im Substrat eingebettete Sensoren. Die Sensorparameter werden dabei auf Basis der Simulationsergebnisse aus WP2 definiert und das Testsystem, das auch bei den Versuchen von WP4 und WP5 eingesetzt wird, entworfen.

WP4 (TU Ilmenau) beschäftigt sich mit der Entwicklung geeigneter Zündmethoden für verdeckte RMS. Im Fokus stehen dabei im Substrat eingebettete Heizelemente zur thermischen Zündung und die Nutzung von Kurzschluss-Filamenten, die in direktem elektrischem Kontakt mit dem RMS stehen und die Reaktion durch einen kurzen Stromimpuls initiieren. Die Versuche erfolgen unter definierten Umgebungsbedingungen, die mit dem Testsystem aus WP3 erfasst werden.

WP5 (TU Ilmenau, Universität des Saarlandes) beschäftigt sich mit der funktionalen Charakterisierung der reaktiv gefügten Verbindungen. Während die TU Ilmenau den

Zusammenhang zwischen Oberflächenmorphologie und den daraus resultierenden elektrischen und thermischen Eigenschaften mit dem Testsystem aus WP3 analysiert (Fragestellung D), untersucht die Universität des Saarlandes die mechanischen Eigenschaften (Fragestellungen E und F). Die dabei entwickelten Methoden werden auch in WP6 verwendet.

WP6 (Universität des Saarlandes) beschäftigt sich mit der mikrostrukturellen Charakterisierung und Langzeitzuverlässigkeit der reaktiv gefügten Verbindungen. Verschiedene Umweltprüfungen wie Temperaturauslagerungs-, Temperaturwechsel-, Temperaturschock- und Feuchtigkeitsauslagerungstests werden genutzt, um spezifische Schädigungsmechanismen in den Proben zu provozieren. Die in WP5 entwickelten Methoden zur funktionalen Charakterisierung sollen dabei vor und nach den Belastungstests genutzt werden, um die elektrischen, thermischen und mechanischen Eigenschaften zu bestimmen.

Die Arbeit orientiert sich an den erörterten Fragestellungen und ist wie folgt aufgebaut: Kapitel 2 gibt einen Überblick über die bisherigen wissenschaftlichen Veröffentlichungen des Autors zum Forschungsthema und stellt dessen Anteil an den jeweiligen Arbeiten dar. Auch Arbeiten mit indirektem Bezug zum Thema werden vorgestellt, da sie methodische Grundlagen liefern, die für zukünftige Forschungsarbeiten genutzt werden können. Kapitel 3 fasst den aktuellen Stand der Technik zusammen. Darin werden etablierte konventionelle Fügeverfahren vorgestellt und die Funktionsweise eines RMS erläutert. Kapitel 4 beschreibt die experimentelle Methodik und die Simulationsansätze, die in den Veröffentlichungen zur Anwendung kamen. Der gesamte Herstellungsprozess der Proben sowie die eingesetzten Simulationsansätze werden systematisch dargestellt. Kapitel 5 stellt eine synoptische Betrachtung der Ergebnisse bereit und ordnet die einzelnen Veröffentlichungen thematisch in das übergeordnete Forschungsthema ein. Kapitel 6 diskutiert die einzelnen Fragestellungen anhand der Resultate. Kapitel 7 schließt mit einer Zusammenfassung der Arbeit und einem Ausblick auf zukünftige Forschungsarbeiten.

2 Veröffentlichungen

Tab. 1 gibt einen Überblick über die bisherigen wissenschaftlichen Veröffentlichungen des Autors zum Forschungsthema und stellt dessen Anteil an den jeweiligen Arbeiten dar. Die letzten drei Veröffentlichungen haben keinen direkten Bezug zum Thema, beschreiben jedoch grundsätzliche Methodiken, die für zukünftige Forschungsarbeiten genutzt werden können.

Tabelle 1: Übersicht über die Veröffentlichungen zur kumulativen Promotion mit Angaben des Beitrags des Autors der Dissertation

Paper 1 [P1] **(Journal)** (veröffentlicht)	E. Wiss, A. Schulz, A. Ruh, K. Jaekel, J. Müller, S. Wiese: Morphologies of Reactive Nanolayer Stacks Sputtered on Ceramic LTCC Substrates Having a Micrometer Scale Surface Roughness, *Advanced Engineering Materials* (2025) Aufgaben des Autors der Dissertation: Konzeption und Entwicklung der Methodik; Festlegen der Vorgaben für die rasterelektronenmikroskopischen Untersuchungen; Analyse, Interpretation und grafische Aufarbeitung der Messdaten; Schreiben und Überarbeiten des Papers
Paper 2 [P2] **(Journal)** (veröffentlicht)	A. Yuile, A. Schulz, E. Wiss, J. Müller, S. Wiese: The Simulated Effect of Adding Solder Layers on Reactive Multilayer Films Used for Joining Processes, *Applied Sciences* (2022) Aufgaben des Autors der Dissertation: Analyse der Simulationsdaten; Überarbeiten eines Teils des Papers
Paper 3 [P3] **(Konferenz)** (veröffentlicht)	E. Wiss, A. Schulz, A. Yuile, J. Müller, S. Wiese: Application of Reactive Bonding Methods on LTCC Substrates, *EMPC* (2023) Aufgaben des Autors der Dissertation: Konzeption und Entwicklung der Methodik; Anfertigen der lichtmikroskopischen Aufnahmen; Analyse, Interpretation und grafische Aufarbeitung der Messdaten; Schreiben des Papers

Paper 4 [P4] **(Konferenz)** (veröffentlicht)	A. Yuile, N. Jaziri, E. Wiss, J. Müller, S. Wiese: Simulations of Thermocouple Measurements during Reactive Bonding Processes on LTCC Substrates, *ESTC* (2024) Aufgaben des Autors der Dissertation: Konzeption und Entwicklung der Methodik; Analyse, Interpretation und grafische Aufarbeitung der Messdaten; Schreiben eines Teils des Papers
Paper 5 [P5] **(Konferenz)** (veröffentlicht)	E. Wiss, A. Yuile, A. Schulz, J. Müller, S. Wiese: Reactive Die Bonding on LTCC Substrates – Analysis by CFD Simulation, *EuroSimE* (2023) Aufgaben des Autors der Dissertation: Konzeption und Entwicklung der Methodik; Festlegen der Vorgaben für die rasterelektronenmikroskopischen Untersuchungen; Analyse, Interpretation und grafische Aufarbeitung der Messdaten; Schreiben des Papers
Paper 6 [P6] **(Journal)** (veröffentlicht)	A. Yuile, A. Schulz, E. Wiss, J. Müller, S. Wiese: 2D Computational Fluid Dynamics Simulation Analysis of the Assembly of Low-Temperature Cofired Ceramics/Low-Temperature Cofired Ceramics and Si/Si Sandwiches by Reactive Bonding, *Advanced Engineering Materials* (2025) Aufgaben des Autors der Dissertation: Konzeption und Entwicklung der Methodik; Analyse der Simulationsdaten; Überarbeiten des Papers
Paper 7 [P7] **(Konferenz)** (veröffentlicht)	E. Wiss, N. Jaziri, A. Yuile, J. Müller, S. Wiese: Experimental Study on Reactive Joining Processes on LTCC Substrates, *ESTC* (2024) Aufgaben des Autors der Dissertation: Konzeption und Entwicklung der Methodik; Herstellen der Proben; Anfertigen der lichtmikroskopischen Aufnahmen; Analyse der Messdaten; Schreiben des Papers
Paper 8 [P8] **(Journal)** (veröffentlicht)	E. Wiss, N. Jaziri, J. Müller, S. Wiese: Impact of Bonding Pressure on the Reactive Bonding of LTCC Substrates, *Micromachines* (2025) Aufgaben des Autors der Dissertation: Konzeption und Entwicklung der Methodik; Herstellen der Proben; Anfertigen der lichtmikroskopischen Aufnahmen; Festlegen der Vorgaben für die rasterelektronenmikroskopischen Untersuchungen; Durchführung der Experimente; Analyse der Bildaufnahmen; Schreiben des Papers

Paper 9 [P9] **(Konferenz)** (veröffentlicht)	E. Wiss, D. Barth, S. Wiese: Concept of a Mechanical Test Setup for Packaging Materials Using Digital Image Correlation Methods, *EuroSimE* (2021) Aufgaben des Autors der Dissertation: Konzeption und Entwicklung der Methodik; Zusammenbau des Versuchsaufbaus; Programmierung der Steuerung; Probenherstellung; Analyse und grafische Aufarbeitung der Messdaten; Schreiben des Papers
Paper 10 [P10] **(Journal)** (veröffentlicht)	E. Wiss, S. Wiese: The Effect of Multiple Solder Reflows on the Formation of Cu_6Sn_5-Intermetallics and the Decomposition of SnAg3.0Cu0.5 Solder Joints in the Framework of Rework and Reuse of MLCC Components, *Metals* (2024) Aufgaben des Autors der Dissertation: Konzeption und Entwicklung der Methodik; Herstellen der Proben; Durchführung der Experimente; Anfertigen der lichtmikroskopischen Aufnahmen; Festlegen der Vorgaben für die rasterelektronenmikroskopischen Untersuchungen; Analyse, Interpretation und grafische Aufarbeitung der Messdaten; Schreiben und Überarbeiten des Papers
Paper 11 [P11] **(Konferenz)** (veröffentlicht)	E. Wiss, R. Metasch, D. Barth, V. Serea, M. Roellig, S. Wiese: Electrical diagnostics of passive components failure during reliability testing, *EuroSimE* (2022) Aufgaben des Autors der Dissertation: Konzeption und Entwicklung der Messaufbauten, die Programmierung der Software, die Probenherstellung, die Analyse und grafische Aufarbeitung der Messdaten sowie das Schreiben eines Teils des Papers.

3 Stand der Technik

3.1 Konventionelle Lötprozesse

3.1.1 Allgemeines

Im Zuge der Herstellung elektronischer Schaltungen ist es notwendig, die jeweiligen Komponenten dauerhaft mit ihren Trägermaterialien wie einer Leiterplatte zu verbinden. Eine solche Verbindung muss mehrere Anforderungen gleichzeitig erfüllen: Erstens muss sie die Verbindungspartner elektrisch möglichst niederohmig kontaktieren, um einen guten Strom- und Signalfluss zu ermöglichen. Hohe Übergangswiderstände würden zu einem Spannungsabfall und somit auch zu einer unerwünschten Wärmeentwicklung führen. Zweitens muss sie die Bauteile mechanisch befestigen, um eine ausreichende Stabilität gegenüber äußeren Einwirkungen wie Schockbelastungen, Vibrationen und thermischen Spannungen zu gewährleisten. Drittens sollte sie idealerweise auch zur Wärmeabfuhr beitragen, insbesondere bei leistungsintensiven Komponenten.

Das (Weich-)Löten stellt das am weitesten verbreitete Verfahren zur Herstellung einer solchen stoffschlüssigen Verbindungen dar. Es handelt sich hierbei um ein thermisches Fügeverfahren mit Einsatztemperaturen unterhalb von 450 °C, das sowohl manuell als auch maschinell angewendet werden kann. Während sich das manuelle Löten eher für kleinere Stückzahlen, Prototypen oder Reparaturen eignet, können mit maschinellen Verfahren auch größere Stückzahlen in kürzester Zeit hergestellt werden. Bei beiden Varianten wird ein Lotmaterial zwischen Bauteil und Substrat eingebracht und auf eine Temperatur oberhalb dessen Schmelzpunkts, aber unterhalb des Schmelzpunkts der Fügepartner erhitzt. Das geschmolzene Lot beginnt zu fließen und benetzt die metallischen Oberflächen von Komponenten und Substrat. An den jeweiligen Grenzflächen zwischen Lot und Substrat bzw. Lot und Bauteil bilden sich anschließend intermetallische Phasen (IMP) aus, die primär durch die Kombination aus Temperatur und Diffusion der verschiedenen Materialien des Lots und der Fügepartner entstehen. Diese ist zwar zwingend notwendig, um eine stabile Verbindung zu erhalten, sollte aufgrund ihrer höheren Sprödigkeit jedoch möglichst klein gehalten werden.

3.1.2 Lotmaterialien

Die Entwicklung von Lötlegierungen lässt sich bis in die Frühgeschichte zurückverfolgen und spiegelt den technologischen Fortschritt im Bereich der Metallverarbeitung wider. Bereits vor über 5000 Jahren nutzten frühe Hochkulturen wie die Ägypter lötähnliche Verfahren zur Verbindung von Edelmetallen in der Schmuckherstellung. Als Lotmaterialien kamen dabei unter anderem bronzebasierte Legierungen zum Einsatz, während Alaun (ein Aluminiumsulfat) als Flussmittel diente. Im römischen Reich wurden Sn-Pb-Legierungen (Zinn-Blei) zur Herstellung langlebiger Alltagsgegenstände wie Wasserleitungen, Kochgeschirr und Waffen verwendet. Auch im Mittelalter fand Pb breite Anwendung, etwa bei der Verbindung von Bleiglasfenstern.

Bereits vor der Erfindung der ersten massentauglichen elektrischen Glühlampe durch Thomas Alva Edison in den späten 1870er wurden die Verbindungen in elektrisch betriebenen Geräten oftmals durch Löten gesichert. Beispiele hierfür sind der elektrische Telegraf aus den 1830er Jahren, mit dem Nachrichten in kurzer Zeit über weite Entfernungen übermittelt werden konnten, oder der Elektroherd aus den 1850er Jahren, der die Art des Kochens revolutionierte. Als Lot wurde eine zu rund 60 % aus Sn und zu rund 40 % aus Pb bestehende Legierung verwendet, die aufgrund mehrerer Eigenschaften zum Standard in der Elektronikfertigung avancierte. Sie weist einen niedrigen Schmelzpunkt von unter 200 °C auf, bietet ein sehr gutes Benetzungsverhalten und ist sowohl in der Herstellung als auch in der Anwendung günstig.

Im 20. Jahrhundert wurde jedoch erkannt, dass Pb sowohl auf den menschlichen Körper als auch auf die Umwelt toxisch wirkt und zu langfristigen Schäden führen kann. Daher wurde im Jahr 2003 die EU-Richtlinie 2002/95/EG (RoHS 1) verabschiedet, die 2006 in Kraft trat und die Verwendung bestimmter gefährlicher Stoffe wie Pb, Quecksilber (Hg) und Cadmium (Cd) in elektrischen und elektronischen Geräten untersagt, mit wenigen Ausnahmen beispielsweise im medizinischen oder militärischen Bereich. Mit Verabschiedung der EU-Richtlinie 2011/65/EU (RoHS 2) im Jahr 2011, die 2013 in Kraft trat, wurden die bestehenden Beschränkungen auf eine größere Anzahl von Geräten und Stoffen ausgeweitet. Diese Verbote führten zur Entwicklung bleifreier Lotlegierungen in den späten 1990er Jahren, die ähnliche physikalische Eigenschaften wie bleihaltige Lote bieten, dafür aber weniger umwelt- und gesundheitsschädlich sind und in der Regel einen höheren Schmelzpunkt besitzen. Tab. 2 zeigt die Zusammensetzungen und Schmelztemperaturen einiger ausgewählter Lotlegierungen, sowie die Schmelztemperaturen der einzelnen Bestandteile.

Tabelle 2: Zusammensetzung und Schmelzpunkte ausgewählter, in der Elektronikfertigung häufig eingesetzter Lötlegierungen und ihrer Basismaterialien.

Bezeichnung	Zusammensetzung (Gewichts-%)	Eutektikum?	Schmelzpunkt Solidus … Liquidus
Sn	100 % Sn	-	231,9 °C
Pb	100 % Pb	-	327,5 °C
Ag	100 % Ag	-	961,8 °C
Cu	100 % Cu	-	1085 °C
Bi (Bismut)	100 % Bi	-	271,4 °C
Au (Gold)	100 % Au	-	1064 °C
Sn63Pb37	63 % Sn, 37 % Pb	Ja	183 °C
Sn60Pb40	60 % Sn, 40 % Pb	Nein	183–190 °C
Sn62Pb36Ag2	62 % Sn, 36 % Pb, 2 % Ag	Ja	179 °C
Sn96.5Ag3.5	96,5 % Sn, 3,5 % Ag	Ja	221 °C
SAC305	96,5 % Sn, 3 % Ag, 0,5 % Cu	Nein	217–219 °C
SAC0307	99 % Sn, 0,3 % Ag, 0,7 % Cu	Nein	217–227 °C
SAC3807	95,5 % Sn, 3,8 % Ag, 0,7 % Cu	Ja	217 °C
Sn42Bi58	42 % Sn, 58 % Bi	Ja	138 °C
Sn42Bi57.6Ag0.4	42 % Sn, 57,6 % Bi, 0,4 % Ag	Ja	137 °C
Sn99.3Au0.7	99,3 % Sn, 0,7 % Au	Nein	217–218 °C
Au80Sn20	20 % Sn, 80 % Au	Ja	280 °C

Die damals bereits bekannten bismut- oder goldhaltigen Lötlegierungen stellten keinen vollwertigen Ersatz für bleihaltige Lote dar. Bismuthaltige Legierungen bieten aufgrund ihres niedrigen Schmelzpunkts von unter 140 °C zwar Vorteile beim Löten von temperaturempfindlichen Bauteilen, sind jedoch aus demselben Grund nicht für Anwendungen mit hohen Betriebstemperaturen geeignet. Zudem ist die Sprödigkeit solcher Legierungen deutlich höher, was insbesondere bei mobilen Anwendungen kritisch sein kann. Die Liquidustemperaturen goldhaltiger Legierungen wie Sn99.3Au0.7 oder Au80Sn20 liegen mit 218 °C bzw. 280 °C über denen der bleihaltigen Varianten. Sie kombinieren eine hohe

Korrosionsbeständigkeit mit ausgezeichneten elektrischen Eigenschaften, sind aber aufgrund des hohen Goldanteils mit deutlich höheren Materialkosten verbunden.

Bis heute haben sich die sogenannten SAC-Lote, bestehend aus Sn mit geringen Anteilen von Ag und Cu in variabler Konzentration, als Standard im bleifreien Elektroniklöten durchgesetzt. Im Vergleich zu Pb-haltigen Loten weisen SAC-Legierungen einen deutlich höheren Sn-Anteil auf, was sich maßgeblich auf die Diffusionsprozesse während des Lötens auswirkt. Die Schmelztemperaturen liegen zwar über denen der Pb-haltigen Lotlegierungen, jedoch geringfügig unter derjenigen von reinem Sn. Zudem verbessern die Beimischungen die Benetzbarkeit, die mechanische Festigkeit sowie die thermische Zuverlässigkeit.

3.1.3 Industrielles Löten

Um die hohen Stückzahlen der industriellen Fertigung realisieren zu können, werden weitestgehend automatisierte Lötprozesse eingesetzt. Die drei am häufigsten verwendeten Verfahren sind das Reflowlöten, das Wellenlöten und das Dampfphasenlöten (auch als Kondensationslöten bezeichnet).

Beim Reflowlöten wird zunächst eine Lotpaste durch Schablonendruck oder mit einem Dispenser auf die Kontaktflächen des Substrats aufgebracht. Die Bauelemente werden anschließend mit optischen Methoden ausgerichtet und auf dem Substrat platziert. Die bestückte Baugruppe wird dann in einem Reflow-Ofen zunächst auf eine definierte Vorheiztemperatur gebracht, um eine gleichmäßige Erwärmung sicherzustellen und um das in der Lotpaste enthaltene Flussmittel zu aktivieren. Anschließend erfolgt das Aufheizen über den Schmelzpunkt des verwendeten Lots, bevor die Baugruppe kontrolliert auf Raumtemperatur abgekühlt wird. Geringfügige Fehlplatzierungen der Bauteile können dabei in der Regel vernachlässigt werden, da sie durch die Oberflächenspannung des geschmolzenen Lots automatisch ausgeglichen werden. Dieses Verfahren ist besonders gut für SMD-Bauelemente geeignet.

Beim Wellenlöten werden die Bauelemente zunächst mit einem geeigneten Klebstoff auf dem Substrat fixiert, um ein Verdrehen oder Verkippen der Bauteile während des Lötprozesses zu verhindern. Anschließend wird das Flussmittel durch Sprühen oder Schäumen aufgetragen, und die Baugruppe auf eine definierte Vorheiztemperatur aufgeheizt. Danach wird sie durch eine Lotwelle geführt, wobei das geschmolzene Lot aufgrund der Oberflächenspannung an den metallisierten Kontaktflächen des Substrats haftet. Abschließend erfolgt eine kontrollierte Abkühlung. Dieses Verfahren ist besonders gut für SMD- und THT-Bauelemente (**T**hrough **H**ole **T**echnology) geeignet.

Beim Dampfphasenlöten wird – ähnlich wie beim Reflowlöten – zunächst eine Lotpaste aufgetragen und die Bauelemente präzise platziert. In der Dampfkammer wird eine spezielle Flüssigkeit auf ihren Siedepunkt erhitzt, sodass sie verdampft. Die Baugruppe wird in diese Dampfzone eingeführt, wo der heiße Dampf gleichmäßig an ihrer Oberfläche kondensiert und dabei die zum Löten notwendige Wärme überträgt. Die Wärmeübertragung erfolgt dabei besonders gleichmäßig. Auch hier schließt der Prozess mit einer kontrollierten Abkühlung ab. Dieses Verfahren ist besonders gut für SMD-Bauelemente geeignet.

Allen Verfahren ist gemeinsam, dass die Baugruppe auf eine Temperatur oberhalb des Schmelzpunkts des verwendeten Lots erwärmt werden muss, was aufgrund der unterschiedlichen CTEs von Bauelementen und Substrat zur Entstehung thermomechanischer Spannungen führen kann. Eine vergleichende Übersicht der drei Lötverfahren ist in Tab. 3 dargestellt.

Tabelle 3: Vergleich der konventionellen Lötprozesse Reflow-, Wellen- und Dampfphasenlöten.

	Reflowlöten	**Wellenlöten**	**Dampfphasenlöten**
Wärmequelle	Konvektion, Infrarotstrahlung	Flüssiges Lot	Kondensationswärme
Typische Anwendungen	SMD-Bauteile	THT- und SMD-Bauteile	SMD-Bauteile
Vorteile	kostengünstig, schnell	geringer manueller Aufwand, schnell	keine Überhitzung möglich, gleichmäßige Wärmeverteilung
Nachteile	Überhitzungsrisiko, ungleichmäßige Wärmeverteilung möglich	Lotbrücken bei hoher Bauteildichte möglich, Vorfixierung von SMD-Komponenten erforderlich	höhere Kosten, Aufschwimmen kleiner Bauelemente möglich

3.2 Reaktive Multilagensysteme

3.2.1 Einführung

Wie bereits in der Einleitung erläutert, bieten RMS eine Möglichkeit zur lokalen Wärmefreisetzung, die sich grundlegend von konventionellen, global wirkenden Wärmequellen unterscheidet. Ein solches RMS besteht aus alternierenden Schichten von mindestens zwei Metallen, die miteinander reagieren können. Die einzelnen Schichten haben eine Dicke von 10–300 nm mit einer Gesamtdicke von bis zu 300 µm [51–54]. Die Reaktion basiert auf der Bildung von IMP, die durch Interdiffusion der Metalle an den Grenzflächen entstehen. Nach der Zündung – beispielsweise durch einen Laserimpuls, einen elektrischen Funken oder das Zuführen ausreichender thermischer Energie – diffundieren die Atome der benachbarten Metalle ineinander, wobei exotherme Reaktionen ablaufen und die im System gespeicherte chemische Energie in Form von Wärme freigesetzt wird [15, 51]. Die hohe Temperatur erhöht die kinetische Energie der Atome über die Aktivierungsenergie der Reaktion und treibt die Reaktion entlang des RMS so selbstständig weiter, was in der Literatur als selbstfortpflanzende („self-propagating“) Reaktion beschrieben wird [51, 55]. Mögliche Materialkombinationen für solche RMS sind beispielsweise Aluminium/Nickel (Al/Ni) [55], Titan/Aluminium (Ti/Al) [56, 57], Ruthenium/Aluminium (Ru/Al) [58], Palladium/Aluminium (Pd/Al) [59], Niob/Silizium (Nb/Si) [60] oder Bor/Titan (B/Ti) [61]. Abb. 2 zeigt schematisch den Aufbau eines RMS sowie die nach der Zündung fortschreitende Reaktion. Abb. 3 zeigt eine Rasterelektronenmikroskopie-Aufnahme (REM) eines auf einem LTCC-Substrat abgeschiedenen RMS.

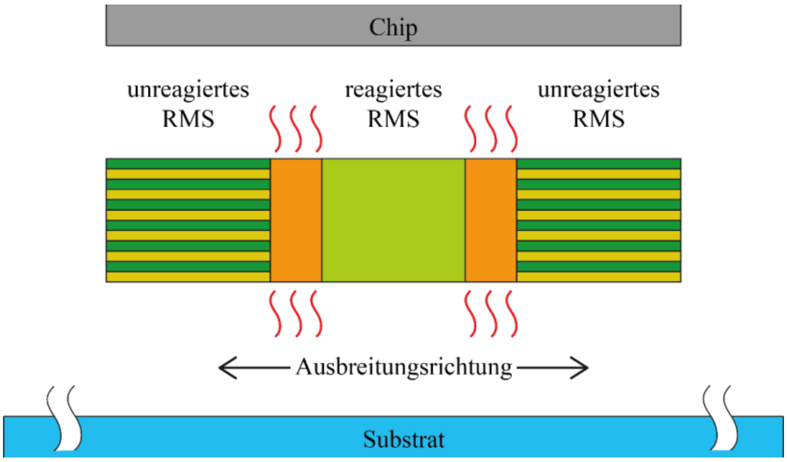

Abbildung 2: Grundlegendes Funktionsprinzip eines RMS für Fügeprozesse in der AVT. Vor der Reaktion sind die Materialien in alternierenden Nanoschichten angeordnet, die nach der Zündung (hier mittig) stark exotherm miteinander reagieren. Die Wärme dieser selbstfortpflanzenden Reaktion kann für Fügeprozesse genutzt werden.

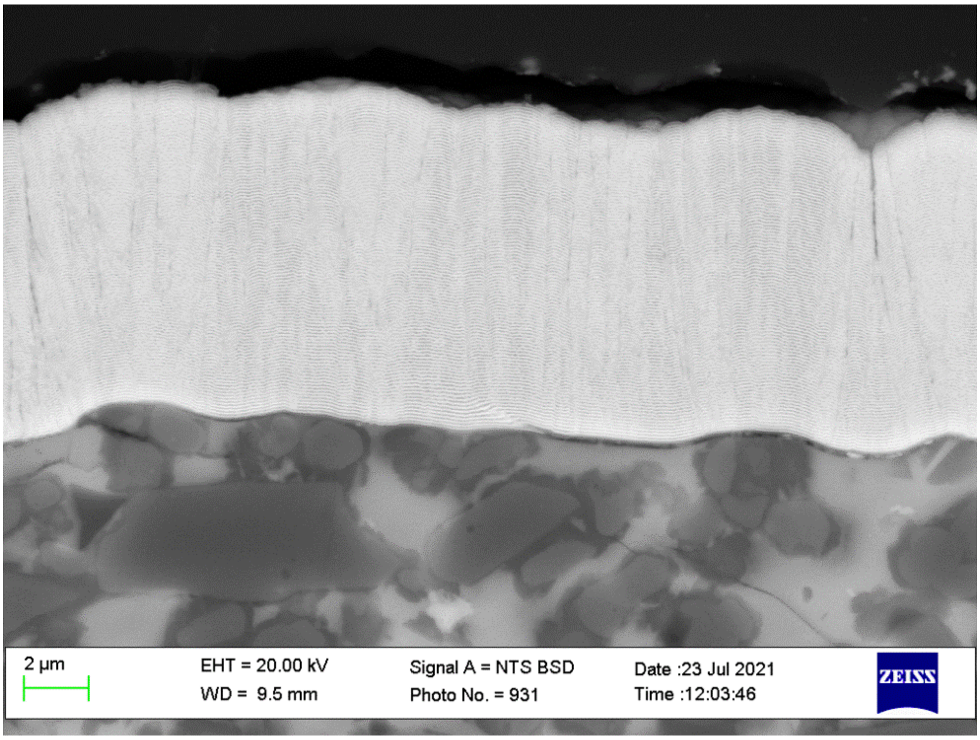

Abbildung 3: REM-Aufnahme eines RMS, das auf ein LTCC-Substrat abgeschieden wurde. Gut zu erkennen sind die einzelnen Schichten aus Al (60 nm) und Ni (40 nm). Vergrößerung: 10 000x.

4 Methodik

4.1 Experimentelle Untersuchungen

4.1.1 LTCC-Herstellung

Der Herstellungsprozess der LTCC-Substrate ist in mehrere Schritte unterteilt (siehe Abb. 4). Als Basis dient eine flexible und ungebrannte Keramikfolie Green Tape™ 951 (DuPont, Wilmington, DE, USA), die zuerst in der benötigten Anzahl – entsprechend der angestrebten Gesamtdicke des Stapels – auf ein Maß von 90 mm x 90 mm zugeschnitten und anschließend bei 80 °C für 10 Minuten getempert wurde. Dieser Schritt dient dem Abbau innerer Spannungen sowie dem Ausgasen leichtflüchtiger Lösungsmittel, wodurch das Auftreten von Verzug und Schwindung in den weiteren Prozessschritten reduziert wird. Bei Proben mit integrierten Sensorstrukturen wurden danach die notwendigen Vias gestanzt und verfüllt. Im Anschluss wurde die Pd/Ag-Paste 6146 (DuPont) im Siebdruckverfahren aufgebracht und bei 80 °C für 10 Minuten getrocknet.

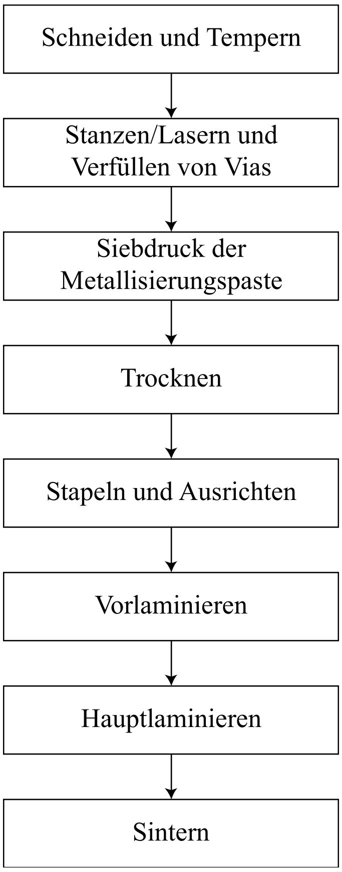

Abbildung 4: Herstellungsprozess der verwendeten LTCC-Substrate.

Die so vorbereiteten Folien wurden lagenweise gestapelt, präzise zueinander ausgerichtet und einer zweistufigen Laminierung unterzogen. Die Vorlaminierung erfolgte bei einer Temperatur von 70 °C und einem Druck von ca. 3 MPa für jeweils 2 Minuten aus zwei Richtungen, um den Lagenstapel zu fixieren und nichtideale Planparallelitäten der uniaxialen Presse auszugleichen. Vor der isostatischen Hauptlaminierung im Wasserbad wurde der Lagenstapel vakuumdicht eingeschweißt, um direkten Wasserkontakt zu vermeiden. Dieser Prozessschritt erfolgte bei einer Temperatur von 70 °C und einem Druck von 21 MPa über 10 Minuten, um eine dauerhafte und hermetisch dichte Verbindung der Lagen zu gewährleisten. Abschließend wurde der Stapel gemäß einem definierten Sinterprofil mit einer Maximaltemperatur von 875 °C gesintert. Während dieses Prozesses schrumpft das Material typischerweise um 12–15 %. Nach dem Sintern weisen die Substrate ihre charakteristischen dielektrischen, mechanischen und thermischen Eigenschaften auf.

4.1.2 Verwendete reaktive Multilagensysteme

4.1.2.1 Indium NanoFoil®

Mit der NanoFoil® (Indium Corp., Clinton, NY, USA) steht seit mehreren Jahren ein kommerziell erhältliches, vorgefertigtes RMS zur Verfügung. Die Folie besteht aus Al und Ni sowie geringen Mengen an Vanadium (V), Indium (In), Cu und Ag. Detailliertere Informationen zur Funktion dieser Zusätze wurden vom Hersteller nicht veröffentlicht. Es ist jedoch anzunehmen, dass sie zur Stabilisierung der Reaktion oder zur Anpassung der thermischen Eigenschaften beitragen. Die Folie ist in Dicken von 40 µm und 60 µm erhältlich, und ist optional mit einer Sn-Beschichtung versehen, um lötbare Metalle direkt miteinander verlöten zu können. Entgegen den Herstellerangaben, die eine Schichtdicke von 10 µm angeben, ergaben eigene Messungen eine tatsächliche Dicke von ca. 5 µm. Laut Datenblatt werden nach dem Zünden der Folie Temperaturen von 1350–1500 °C bei einer Reaktionsgeschwindigkeit von 6,5–8 m/s erreicht [62]. Für die in dieser Arbeit durchgeführten Fügeversuche unter verschiedenen Druckbedingungen wurden die 40 µm und 60 µm dicken, Sn-beschichteten Varianten verwendet. Der Zuschnitt auf die benötigten Abmessungen erfolgte manuell mit einem scharfen Skalpell.

4.1.2.2 Gesputterte Reaktivschichten

Für die in dieser Arbeit verwendeten abgeschiedenen RMS (vgl. Kapitel 4.1.3) wurden ausschließlich Al und Ni ohne weitere Zusätze eingesetzt. Das Ziel war die Freisetzung der maximal möglichen Wärmemenge während der exothermen Reaktion, die gemäß thermodynamischer Betrachtung bei Bildung der IMP mit der höchsten Reaktionsenthalpie auftritt (vgl. Kapitel 3.2.1). Tab. 4 zeigt die Bindungsenthalpien der möglichen auftretenden IMP, die sich bei der Reaktion zwischen Al und Ni ausbilden können.

Tabelle 4: Experimentell und rechnerisch ermittelte Bindungsenthalpien der verschiedenen IMP, die sich bei der Reaktion zwischen Al und Ni bilden können [63].

	$AlNi_3$	**AlNi**	**Al_3Ni_2**	**Al_3Ni**
Enthalpie in kJ/mol (experimentell)	-47,0 bis -37,6	-66,1 bis -58,0	-57,6	-37,7
Enthalpie in kJ/mol (rechnerisch)	-49,0 bis -33,0	-79,0 bis -48,0	-61,9 bis -43,0	-39,9 bis -28,0

Folglich wäre die Bildung von AlNi zu bevorzugen, da hier die Bindungsenthalpie am höchsten ist. Diese Phase entsteht bei einem Atomverhältnis von 1:1, die Stoffmengen der beiden Materialien müssen also identisch sein. Die Stoffmenge n lässt sich über die Masse m, die molare Masse M, die Dichte ρ, das Volumen V, die Dicke d, die Breite b und die Länge l wie folgt berechnen:

$$n = \frac{m}{M} = \frac{\rho \cdot V}{M} = \frac{\rho \cdot d \cdot b \cdot l}{M} \tag{1}$$

Durch Gleichsetzen der Stoffmengen und Umstellen nach dem Dickenverhältnis ergibt sich für dieses unter den Annahmen gleicher Breite und Länge:

$$\begin{aligned}
&\frac{\rho_{Al} \cdot V_{Al}}{M_{Al}} = \frac{\rho_{Ni} \cdot V_{Ni}}{M_{Ni}} \\
&\Leftrightarrow \frac{\rho_{Al} \cdot d_{Al} \cdot b_{Al} \cdot l_{Al}}{M_{Al}} = \frac{\rho_{Ni} \cdot d_{Ni} \cdot b_{Ni} \cdot l_{Ni}}{M_{Ni}} \\
&\Leftrightarrow \frac{\rho_{Al} \cdot d_{Al}}{M_{Al}} = \frac{\rho_{Ni} \cdot d_{Ni}}{M_{Ni}} \\
&\Leftrightarrow \frac{d_{Al}}{d_{Ni}} = \frac{\rho_{Ni} \cdot M_{Al}}{M_{Ni} \cdot \rho_{Al}} = \frac{8{,}9\ \frac{g}{cm^3} \cdot 26{,}98\ u}{58{,}69\ u \cdot 2{,}7\ \frac{g}{cm^3}} = 1{,}52
\end{aligned} \tag{2}$$

Aus Gleichung (2) folgt ein optimales Dickenverhältnis von 3:2 zwischen Al und Ni. Aus produktionstechnischen Gründen wurde eine Dicke von 60 nm für jede Al-, und eine Dicke von 40 nm für jede Ni-Schicht ausgewählt. Dazu wurden die einzelnen Schichten nacheinander auf das fertige LTCC-Substrat durch Magnetron-Sputtern (vgl. Kapitel 4.1.3) abgeschieden.

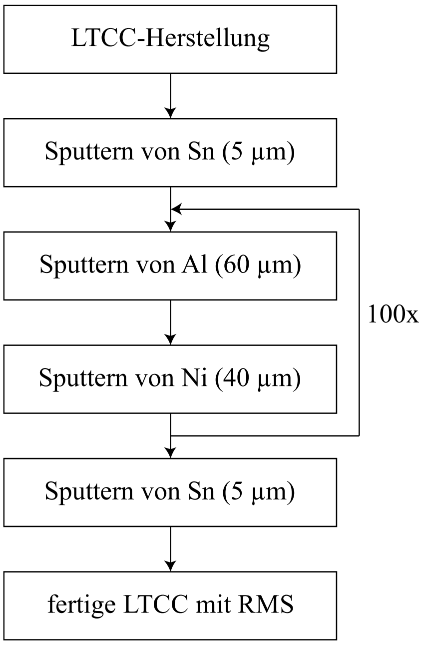

Abbildung 5: Ablauf des Abscheidungsprozesses eines RMS mit beidseitiger Lotschicht auf einem LTCC-Substrat.

4.1.3 Abscheideprozess

Die RMS wurden durch sequenzielles DC-Magnetron-Sputtern in einer PVD-Anlage (**P**hysical **V**apour **D**eposition) vom Typ CS400 (VON ARDENNE GmbH, Dresden, Deutschland) abgeschieden. Dabei handelt es sich um ein Verfahren der physikalischen Gasphasenabscheidung, bei dem Argonionen auf Targets aus hochreinem Al bzw. Ni treffen. Die aus der Targetoberfläche herausgelösten Atome werden in Richtung des Substrats transportiert und kondensieren dort zu einer dichten, zusammenhängenden Schicht.

Beim DC-Magnetron-Sputtern wird ein elektrisches Feld mit einem Magnetfeld überlagert. In der mit Argon gefüllten Vakuumkammer führt das Anlegen einer Hochspannung zwischen Target (Kathode) und Substrat (Anode) zur Ausbildung eines Plasmas. Die freien Elektronen im Plasma werden durch das elektrische Feld beschleunigt und ionisieren beim Zusammenstoß die Argonatome. Die entstehenden positiv geladenen Argonionen werden auf das negativ polarisierte Target beschleunigt und lösen beim Aufprall durch Impulsübertrag Atome aus dessen Oberfläche.

Das überlagerte Magnetfeld zwingt die Elektronen auf eine spiralförmige Bahn, wodurch sich ihre effektive Weglänge und damit die Ionisationswahrscheinlichkeit erhöht. Dies führt zu einer höheren Plasmadichte und ermöglicht ein effizientes Schichtwachstum auch bei niedrigen Prozessdrücken. Diese reduzieren die Streuung der gesputterten Atome und begünstigen damit die Ausbildung gleichmäßiger und dichter Schichten.

4.1.4 Oberflächenmodifikationen

Da die Oberflächenbeschaffenheit der Substrate einen maßgeblichen Einfluss auf die Haftfähigkeit und Homogenität der abgeschiedenen RMS hat, wurden verschiedene Oberflächenkonfigurationen systematisch analysiert. Dazu wurde das RMS auf LTCC-Substrate abgeschieden, die sich hinsichtlich ihrer Vorbehandlung unterschieden. Während Paper 3 den Einfluss von CMP und Laserablation in Hinblick auf Reaktionsgeschwindigkeit und Temperatur untersucht, konzentriert sich Paper 1 auf den Einfluss der Laserablation und des Hinzufügens einer Metallisierung und Lot-Schicht.

Die aus den jeweiligen Bearbeitungen resultierende Oberflächenform ist eine Überlagerung mehrerer Komponenten (vgl. Abb. 6): (i) generelle Formabweichung, (ii) Welligkeit und (iii) Rauheit. Während die Formabweichung keinen, und die Welligkeit aufgrund ihrer geringen Höhengradienten nur einen vernachlässigbaren Einfluss auf die Abscheidung des RMS hat, wurde im Rahmen dieser Arbeit gezielt der Einfluss der Rauheit auf Haftfähigkeit und Homogenität des RMS untersucht.

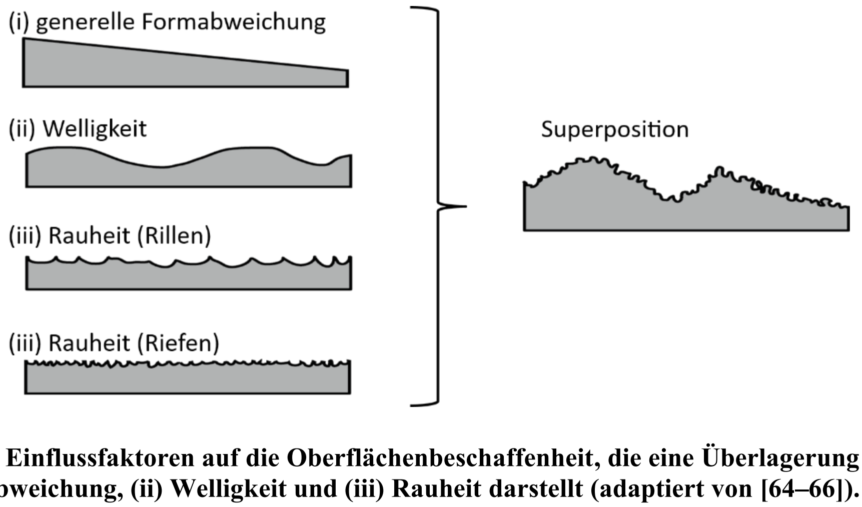

Abbildung 6: Einflussfaktoren auf die Oberflächenbeschaffenheit, die eine Überlagerung aus (i) genereller Formabweichung, (ii) Welligkeit und (iii) Rauheit darstellt (adaptiert von [64–66]).

4.1.4.1 Chemisch-mechanisches Polieren

Zur Verringerung der Rauheit wurden die Oberflächen einiger LTCC-Proben mit einer Poliermaschine PM5 (Logitech Limited, Old Kilpatrick, Schottland) chemisch-mechanisch poliert. Es erfolgte eine Optimierung der Prozessparameter, um eine minimale Rauheit der LTCC-Oberflächen zu erreichen.

4.1.4.2 Laserablation

Zur Erhöhung der Rauheit wurden die Oberflächen mit einem UV-Laser des Typs microSTRUCT C v2.0 (3D-Micromac AG, Chemnitz, Deutschland) modifiziert. Der Laser arbeitet mit einer Wellenlänge von 355 nm, einem Spotdurchmesser von 7 µm und einer Pulsenergie von bis zu 70 µJ. Die eingestellte mittlere Leistung variierte zwischen 0,5 W (für metallisierte Proben) und 0,8 W (für unbeschichtete Proben). Alle Oberflächen wurden in einem Abstand von 40 µm zweimal rasterförmig überfahren, um eine ausreichende Veränderung der Rauheit zu gewährleisten.

4.1.5 Fügeprozess

Erste Fügeversuche von LTCC-Proben mit vollflächiger Metallisierung mit einem RMS erfolgten an der TU Ilmenau. Aufgrund der großen Proben (10 mm x 10 mm) und der maximal anwendbaren Kraft des dort verfügbaren FINEPLACER® pico (Finetech, Berlin, Deutschland) von 150 N ergab sich ein geringer Fügedruck von 1,5 MPa. Während die gesputterten RMS elektrisch gezündet wurden, erfolgte die Zündung der NanoFoil® (60 µm) thermisch durch ein Aufheizen auf über 350 °C. Die beiden Konfiguration sind in Tab. 5 dargestellt.

Tabelle 5: Übersicht über die Konfigurationen der erste Fügeversuche, die an der TU Ilmenau durchgeführt wurden.

Typ des RMS	Zündung	Spitzen-temperatur in °C	Kraft in N	Fläche der Metallisie-rung in mm^2	Fügedruck in MPa
NanoFoil® (60 µm)	thermisch	350	150	10 x 10	1,5
Gesputtert (10 µm)	elektrisch	200	150	10 x 10	1,5

Um den Einfluss des Anpressdrucks auf die Qualität der entstehenden Fügezone näher zu untersuchen, wurden später an der Universität des Saarlandes LTCC-Proben unter verschiedenen Einstellungen mit NanoFoil® gefügt. Dabei wurden sowohl Proben mit vollflächiger Metallisierung von 3 mm x 3 mm als auch Proben mit vier strukturierten Pads von jeweils 0,5 mm x 0,5 mm, wie sie auch in echten elektronischen Schaltungen vorkommen, untersucht (vgl. Abb. 7). Die untersuchten Konfigurationen sind in Tab. 6 dargestellt.

Reaktives Die-Bonden

(a) **(b)** **(c)**

Reaktives Fügen von elektrischen Verbindungen

(d) **(e)** **(f)**

Abbildung 7: Verschiedene Proben für Fügeversuche unter verschiedenen Fügedrücken (nach [P8]). (a)–(c) Reaktives Die Fügen. (a) LTCC-Substrat (15 mm x 3 mm) mit vollflächiger Pd/Ag-Metallisierung. (b) NanoFoil® mit beidseitiger Sn-Beschichtung. (c) LTCC-Chip (3 mm x 3 mm) mit vollflächiger Pd/Ag-Metallisierung. (d)–(f) Reaktives Fügen von elektrischen Verbindungen. (d) LTCC-Substrat (15 mm x 3 mm) mit strukturierter Pd/Ag-Metallisierung an den Ecken (0,5 mm x 0,5 mm). (e) NanoFoil® mit beidseitiger Sn-Beschichtung. (f) LTCC-Chip (3 mm x 3 mm) mit strukturierter Pd/Ag-Metallisierung an den Ecken (0,5 mm x 0,5 mm).

Zum Fügen der Proben L1–L8 kam ein FINEPLACER® pico ma (Finetech) zum Einsatz, der eigentlich zum manuellen Die-Bonding entwickelt wurde, sich jedoch als ideales Hilfsmittel zum reaktiven Fügen erwiesen hat. Das System besteht im Wesentlichen aus einem beheizbaren Vakuumtisch zur Fixierung des Substrats (Chuck), einem ebenfalls beheizbaren Tool mit integrierter Vakuumstruktur zur Aufnahme des Chips, einer Strahlteileroptik und einer Kamera (siehe Abb. 8). Durch die Strahlteileroptik werden die Sichtfelder auf Substrat und Chip überlagert, sodass diese mit einer Platziergenauigkeit von unter 3 µm aufeinander ausgerichtet werden können. Das Tool ist an einem abschwenkbaren Arm befestigt, der während des Fügeprozesses den Chip auf das Substrat absenkt und dabei mit dem verwendeten Kraftmodul eine definierte Kraft von 4–400 N auf das System ausübt. Die integrierten Heizungen in Tool und Chuck ermöglichen eine gezielte thermische Unterstützung der exothermen Reaktion des RMS.

Tabelle 6: Übersicht über die Konfigurationen der später mit NanoFoil® (40 µm) durchgeführten Fügeversuche an der Universität des Saarlandes unter Nutzung verschiedener Fügedrücke [P8].

Konfiguration	Vorheiztemperatur in °C	Spitzentemperatur in °C	Kraft in N	Fläche der Metallisierung in mm²	Fügedruck in MPa
L1	80	200	20	3 x 3	2
L2	80	200	100	3 x 3	11
L3	80	200	200	3 x 3	22
L4	80	200	300	3 x 3	33
L5	80	200	400	3 x 3	44
L6	80	200	20	4 x 0,5 x 0,5	20
L7	80	200	100	4 x 0,5 x 0,5	100
L8	80	200	200	4 x 0,5 x 0,5	200
L9	80	200	300	4 x 0,5 x 0,5	300
L10	80	200	400	4 x 0,5 x 0,5	400

Abbildung 8: Der zum Fügen verwendete FINEPLACER® pico ma. A: Beheizbarer Vakuumtisch zur Fixierung des Substrats (Chuck). B: Beheizbares Tool mit integrierter Vakuumstruktur zur Aufnahme des Chips. C: Abschwenkbarer Arm. D: Strahlteileroptik zur Überlagerung der Sichtfelder auf Substrat und Chip. E: Kamera (auf Strahlteileroptik gerichtet).

Abb. 9 zeigt exemplarisch den zeitlichen Verlauf der Temperaturen an Tool (grün) und Chuck (blau), sowie der aufgebrachten Kraft (rot) während eines Fügeprozesses, bei dem ein LTCC-Chip auf ein paariges LTCC-Substrat mit NanoFoil® gefügt wurde (vgl. Paper 8). Ausgehend von einer Standby-Temperatur von 40 °C wurden Substrat und Chip mit der jeweils maximal möglichen Aufheizrate von 3 K/s (Chuck) bzw. 6 K/s (Tool) auf eine Vorheiztemperatur von 80 °C erwärmt. Nach einer kurzen Haltephase erfolgte ein weiterer Temperaturanstieg auf 200 °C. 60 Sekunden nach Prozessbeginn, kurz bevor beide Fügepartner die Zieltemperatur erreicht hatten, wurde der Arm des FINEPLACERS® automatisch abgeschwenkt und die zuvor definierte Anpresskraft auf den LTCC-Stapel aufgebracht. Nachdem sowohl die Zieltemperatur als auch die Anpresskraft erreicht waren, wurde die Zündung des RMS initiiert. Anschließend wurde der Arm wieder angehoben, und die Kühlung über Druckluft eingeleitet.

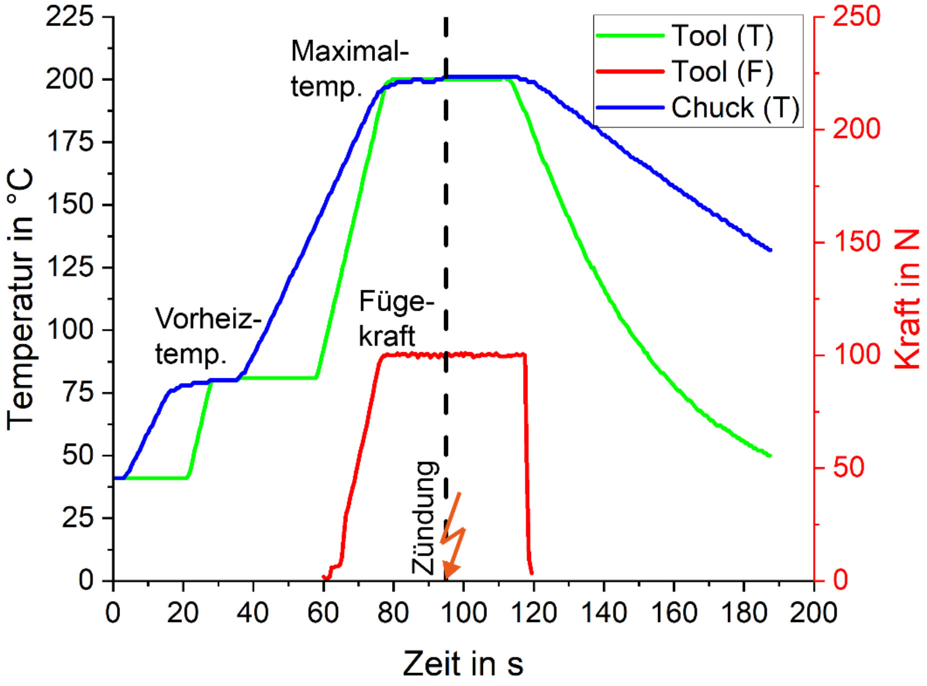

Abbildung 9: Zeitlicher Verlauf von Temperatur an Tool (grün) und Chuck (blau), und von Kraft (rot). Die vertikale, gestrichelte Linie markiert den Zeitpunkt der Zündung des RMS.

4.1.6 Temperatur- und Kraftmessungen

Der Chuck des FINEPLACER® ist 100 mm x 100 mm groß und besteht primär aus WCu (Wolfram-Kupfer), da dieses Material eine hohe Wärmeleitfähigkeit mit einem geringen CTE kombiniert. Unter dem Chuck befinden sich acht Halogenlampen (Leistung jeweils 150 W), mit denen die Platte mit einer maximalen Aufheizrate von 3 K/s auf bis zu

400 °C erwärmt werden kann. Zur Temperaturmessung ist ein Thermoelement (Typ K) an der Unterseite der Heizplatte angeschraubt, dessen Funktionsprinzip auf dem Seebeck-Effekt beruht. Dieser beschreibt die Entstehung einer elektrischen Spannung an der Kontaktstelle zweier unterschiedlicher Metalle A und B, wenn zwischen der Kontaktstelle und einem Referenzpunkt ein Temperaturunterschied besteht. Die resultierende Spannung U ergibt sich aus der temperaturabhängigen Differenz der Seebeck-Koeffizienten $S_B(T)$ und $S_A(T)$ gemäß:

$$U = \int_{T_1}^{T_2} (S_B(T) - S_A(T))\, dT \tag{3}$$

Diese Spannung wird von einer Steuerungseinheit erfasst, die auf Basis dieses Signals die Leistung der Halogenlampen regelt und so eine präzise Temperaturführung des Chucks ermöglicht.

Die Erwärmung des Tools erfolgt über einen integrierten Widerstandsheizer auf Keramik-Basis (Leistung 300 W). Die Temperatur wird über einen Pt100-Sensor, der auf die Oberseite des Heizelements geklemmt ist, gemessen und durch eine separate Steuerungseinheit geregelt. Aufgrund des deutlich geringeren Volumens kann das Tool mit einer höheren Aufheizrate von bis zu 6 K/s betrieben werden.

Die Kraftmessung erfolgt über einen im vorderen Teil des Arms integrierten Kraftsensor mit Dehnmessstreifen, deren elektrischer Widerstand sich unter mechanischer Belastung ändert. Die Widerstandsänderung wird über eine Wheatstone-Brücke detektiert und in einen entsprechenden Kraftwert umgerechnet. Der Kraftsensor liefert eine maximale Auflösung von 4 N.

4.1.7 Elektrische Zündung

Zum Zünden der RMS wurde eine Schaltung genutzt, die eine Batteriespannung von 9 V zu einer Hochspannung von 15 kV transformiert. Der Ausgang dieser Schaltung wurde an einen Zündchip mit zwei Leiterbahnen angeschlossen, die am Rand des Chips aufeinander zulaufen (siehe Abb. 10). Die Leiterbahnen sind durch eine ca. 700 µm große Lücke voneinander getrennt. Da der Quotient aus Spannung und Abstand größer ist als die Durchbruchfeldstärke von Luft unter Standardbedingungen (ca. 3 kV/mm), entsteht ein elektrischer Funke, der zur Zündung des RMS genutzt werden kann.

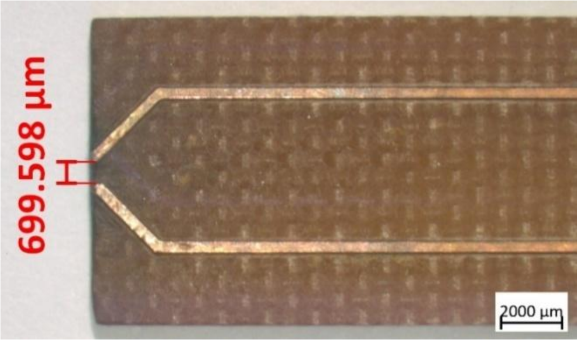

Abbildung 10: Zündchip mit zwei aufeinander zulaufenden Leiterbahnen [P8], die am Rand durch eine ca. 700 µm große Lücke voneinander getrennt sind. Aufgrund der angelegten Hochspannung von ca. 15 kV entsteht zwischen diesen ein elektrischer Funken, der zur Zündung des RMS genutzt werden kann.

4.1.8 Analyse der Topographie und Mikrostruktur

4.1.8.1 Oberflächencharakterisierung

Die Rauheitsmessungen der LTCC-Oberflächen wurden mit einem konfokalen LSM LEXT OLS4100 (Olympus Europe SE & Co. KG, Hamburg, Deutschland) mit einem 50x-Objektiv durchgeführt. Dabei wird die Oberfläche der Probe mit einem fokussierten Laserstrahl zeilenweise abgetastet und der zurückgestreute Laserstrahl detektiert. Durch die konfokale Optik wird nur das zurückgestreute Licht aus der Fokusebene detektiert, während Streulicht verworfen wird. Die gesammelten Messdaten können dann weiter ausgewertet werden, um die Oberfläche bezüglich ihrer Rauheit zu charakterisieren. Für einen ersten Vergleich der Proben wurde zunächst der arithmetische Mittenrauwert R_a bestimmt. Da dieser Wert jedoch keine Informationen über die Verteilung von Spitzen und Tälern liefert, wurden für ausgewählte Proben später weitere Rauheitsparameter aus der Abbott-Kurve bestimmt.

4.1.8.2 Methodik der Mikrostrukturanalyse

Die mikroskopische Analyse stellt ein zentrales Werkzeug zur Charakterisierung der hergestellten Proben dar. Dabei kamen sowohl lichtoptische als auch elektronenstrahlbasierte Verfahren zum Einsatz. Während ein LSM verwendet wurde, um die Rauheit der LTCC-Oberflächen nach verschiedenen Oberflächenmodifikationen vor der Abscheidung der Reaktivschichten zu bestimmen (siehe Kapitel 4.1.8.1), wurde ein Lichtmikroskop (LM) benutzt, um Aufnahmen von der Morphologie der Reaktivschicht anzufertigen (siehe Kapitel 4.1.8.4). Zur Darstellung der einzelnen Nanoschichten und zur Elementanalyse wurde ein REM (siehe Kapitel 4.1.8.5) eingesetzt.

Lichtmikroskopische Verfahren nutzen sichtbares Licht zur optischen Abbildung der Probenoberfläche und sind daher in ihrem Auflösungsvermögen durch die Wellenlänge $\lambda = 380 \ldots 780\ nm$ des sichtbaren Spektrums begrenzt. Die Abbe'sche Auflösungsgrenze beschreibt den minimalen Abstand d_{min} zweier Strukturen, bei dem diese noch als getrennte Objekte wahrgenommen werden können:

$$d_{min} = \frac{\lambda}{2 \cdot n \cdot \sin \alpha} = \frac{\lambda}{2 \cdot NA} \tag{4}$$

Dabei ist n der Brechungsindex des Mediums zwischen Objektiv und Probe, α der halbe Öffnungswinkel des Objektivs und $NA = n \cdot \sin \alpha$ die numerische Apertur. Bei einer Wellenlänge von $\lambda \approx 555\ nm$, bei dem die Empfindlichkeit des menschlichen Auges maximal ist, und der Nutzung eines Ölimmersionsobjektivs mit $NA = 1{,}4$ ergibt sich somit im Idealfall eine theoretische Auflösungsgrenze von ca. 200 nm. Bei herkömmlichen Trockenobjektiven mit geringer $NA < 1$, wie sie im Rahmen dieser Arbeit verwendet wurden, liegt die tatsächlich erreichbare Auflösung deutlich oberhalb dieser theoretischen Grenze und beträgt typischerweise mehrere hundert Nanometer. Eine lichtmikroskopische Abbildung der einzelnen Nanoschichten der abgeschiedenen Reaktivschichten mit Schichtdicken von 40–60 nm ist daher nicht realisierbar.

Für die Abbildung dieser Strukturen wurde daher ein REM eingesetzt, bei dem ein fokussierter Elektronenstrahl rasterförmig über die Probenoberfläche geführt wird. Trifft ein Primärelektron dieses Strahls auf ein Atom der Probe, kann es entweder durch elastische Streuung als Rückstreuelektron (BSE, **B**ack **S**cattered **E**lectron) reflektiert werden, oder durch inelastische Streuung – also Energieabgabe – ein Sekundärelektron (SE) aus den oberflächennahen Atomlagen herauslösen.

BSEs besitzen nahezu die Energie des Primärstrahls und können auch aus tieferliegenden Schichten stammen. Ihre Rückstreuwahrscheinlichkeit steigt mit der Ordnungszahl des Elements, sodass Bereiche mit schwereren Elementen heller erscheinen als solche mit niedriger Ordnungszahl. SEs besitzen dagegen eine deutlich niedrigere Energie und stammen aus den obersten Nanometern der Oberfläche, weshalb sie besonders kontrastreiche Informationen zur Oberflächentopografie liefern. Für die Untersuchungen dieser Arbeit wurden beide Modi verwendet.

Ein weiterer Effekt, der durch das Auftreffen des Elektronenstrahls auf die Atomkerne verursacht wird, ist die Ionisation. Dabei wird durch inelastische Streuung des

Elektronenstrahls ein Elektron aus einer der inneren Elektronenschalen entfernt. Aufgrund des Prinzips der Energieminimierung wird diese Fehlstelle durch ein Elektron aus einer äußeren Schale aufgefüllt, wobei die Energiedifferenz in Form eines Röntgenquants emittiert wird. Diese Röntgenstrahlung ist charakteristisch für das jeweilige Element und kann mittels energiedispersiver Röntgenspektroskopie (EDX) detektiert werden. Die EDX-Analyse diente in dieser Arbeit zur Bestimmung der Elementverteilung nach Abschluss der jeweiligen Lötprozesse.

4.1.8.3 Metallographie

Um die Proben im LM und REM analysieren und damit die Struktur der abgeschiedenen Reaktivschichten sowie die Struktur der Fügezone beurteilen zu können, wurden die Proben in mehreren aufeinanderfolgenden Schritten präpariert. Diese Präparation erfolgte unter Berücksichtigung der Anforderungen der lichtmikroskopischen und REM-Analyse (siehe Kapitel 4.1.8.4 und 4.1.8.5).

Zunächst wurden die Proben in geeignete Einbettformen eingelegt und eine ausreichende Menge transparenten Epoxidharzes angerührt. Dazu wurden Harz und Härter des EpoFix-Kits (Struers, Champigny-sur-Marne, Frankreich) im Verhältnis 2:1 von Hand miteinander vermischt und vorsichtig in die Probenformen gegossen. Die Aushärtung erfolgte über einen Zeitraum von 24 Stunden in einem Topf bei leichtem Unterdruck, um eingeschlossene Luftblasen aus dem Harz zu entfernen.

Nach ihrer vollständigen Aushärtung wurden die Proben aus den Formen herausgenommen und auf einer Schleifmaschine des Typs LaboPol-25 (Struers) plan geschliffen. Zunächst erfolgte ein Grobschliff mit SiC-Nassschleifpapier (Siliziumcarbid) mit Körnung P500, anschließend ein Feinschliff mit Körnung P1200. Das Schleifen erfolgte jeweils über einen Zeitraum von 1–3 Minuten bei einem Anpressdruck von 20–25 N pro Probe. Zwischen den einzelnen Schleifstufen wurden die Proben mit Wasser gespült und gereinigt.

Zur weiteren Glättung der Oberfläche wurden die Proben auf einer Poliermaschine des Typs Tegramin-25 (Struers) mit Diamantsuspensionen unterschiedlicher Partikelgrößen (9 µm, 3 µm und 1 µm) poliert. Die Politur erfolgte jeweils über einen Zeitraum von ebenfalls 1–3 Minuten bei einem Anpressdruck von 15–20 N pro Probe. Zwischen den einzelnen Politurstufen wurden die Proben mit Wasser gespült und gereinigt.

Für die Endpolitur wurde eine kolloidale SiO_2-Suspension (Siliziumdioxid) mit einer Partikelgröße von 0,25 µm auf einer Vibrationspoliermaschine des Typs Saphir Vibro

(ATM Qness, Mammelzen, Deutschland) verwendet. Mit diesen Schritten konnte eine möglichst glatte Oberfläche mit minimaler Rauheit erzielt werden.

Zur Vermeidung von Aufladungseffekten im REM und um eine Elementanalyse per EDX zu ermöglichen, wurden die Proben mit einer ca. 20 nm dicken, leitfähigen Kohlenstoffschicht bedampft. Die Bedampfung erfolgte per Fadenverdampfung auf einem Q150T Coater (Quorum Technologies Ltd., über Quantum Design, Pfungstadt, Deutschland). Die lichtmikroskopische Analyse wurde vor dem Aufbringen der Kohlenstoffschicht durchgeführt, da diese die Bildqualität leicht beeinträchtigt.

4.1.8.4 Lichtmikroskopie

Die lichtmikroskopischen Untersuchungen wurden mit einem Axio Imager.M2m (Carl Zeiss, Oberkochen, Deutschland) unter Verwendung eines 20x-Objektivs durchgeführt. Das Ziel dieser Untersuchungen war die qualitative Beurteilung der Mikrostruktur der Fügezone, insbesondere hinsichtlich der Homogenität der Lotverteilung, Rissbildung sowie der Ausbildung von Poren oder Delaminationen der Reaktiv- bzw. Lotschicht von der Metallisierung.

Das verwendete Mikroskop verfügt über einen motorisierten Objekttisch, der die automatisierte Aufnahme sogenannter Mosaikbilder ermöglicht. Dabei werden leicht überlappende Einzelaufnahmen entlang der gesamten Probenoberfläche erstellt und softwaregestützt zu einem hochauflösenden Gesamtbild zusammengesetzt. Diese Technik erlaubt eine systematische und vergleichende Analyse der verschiedenen Proben im Hinblick auf ihre mikrostrukturellen Merkmale. Zudem erleichtert sie die Auswahl repräsentativer Bereiche für detailliertere Einzelaufnahmen und die EDX-Analyse im REM.

4.1.8.5 Elektronenstrahlanalyse

Für eine tiefergehende Analyse stand ein REM des Typs EVO MA15 (Carl Zeiss) zur Verfügung. Mit diesem konnte eine deutlich höhere Vergrößerung als mit dem LM erzielt werden, sodass auch die Darstellung der einzelnen Al- und Ni-Schichten möglich war. Dies erwies sich als besonders hilfreich bei der Analyse der Morphologie des abgeschiedenen RMS nach verschiedenen Oberflächenmodifikationen (vgl. Paper 1).

Das REM wurde mit einer LaB_6-Kathode bei einer Beschleunigungsspannung von 20 kV und einem Strahlstrom von 40 μA betrieben. Die EDX-Analyse erfolgte mit einem XFlash-Detektor (Bruker, Billerica, MA, USA) mit einer Energieauflösung von 123 eV.

4.2 Simulationen

Die Simulationen wurden von Dr. Adam Yuile (Universität des Saarlandes) mit der Software ANSYS Fluent durchgeführt. Der Autor dieser Arbeit war in die Konzeption und Entwicklung der Methodik sowie in die Analyse und Interpretation der Simulationsdaten eingebunden. Da die exotherme Reaktion eines RMS mit hoher Reaktionsgeschwindigkeit abläuft und die Kontaktstellen in der Mikroelektronik – etwa bei flächigen Bauelementen – häufig verdeckt und zudem relativ klein sind, ist eine direkte experimentelle Beobachtung dieses Prozesses nur eingeschränkt möglich. Die Simulationen stellen daher ein wichtiges Werkzeug dar, um die zugrunde liegenden physikalischen Prozesse zu analysieren.

Die Simulationen basieren auf Methoden der Computational Fluid Dynamics (CFD), die sich besonders gut zur Abbildung der exothermen Reaktion eines RMS eignen. Mit diesen Methoden lassen sich die einzelnen Schichten des RMS mit ihren unterschiedlichen thermischen Eigenschaften sowie die zeitabhängige Wärmefreisetzung der Reaktion und auch Phasenübergänge modellieren. Dadurch kann die entstehende Temperaturverteilung sowohl zeitlich als auch räumlich aufgelöst simuliert werden.

Im Zentrum aller Modelle befindet sich der Schichtstapel, der in eine größere Luftdomäne eingebettet ist, um Randeffekte durch fehlende Wärmeabfuhr an die Umgebung zu vermeiden. Abb. 11 zeigt exemplarisch ein solches „Shoebox"-Modell mit den verschiedenen Schichten (LTCC, RMS, Lot und Si-Chip).

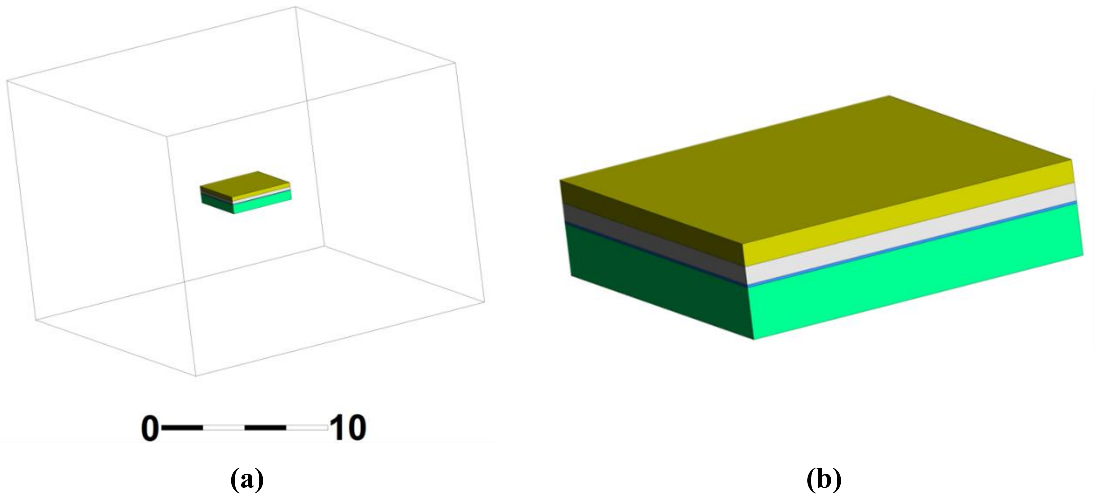

(a) (b)

Abbildung 11: Exemplarische 3D-Ansicht des (a) kompletten CFD-Modells inklusive umgebender Luft und (b) detaillierten Schichtstapels [P2], bestehend aus LTCC-Substrat (grün), RMS (blau), Lotschicht (grau) und Si-Chip (gelb).

Auf eine explizite Modellierung der Oberflächenrauheit wurde aus Gründen der Komplexität verzichtet. Während in den ersten Modellen noch vergleichsweise dicke RMS- und Lotschichten verwendet wurden ([67]: RMS 40 µm, Lot 200 µm; Paper 2 und 3: RMS 30 µm, Lot 200 µm), kamen in späteren Modellen realistischere Schichtdicken zum Einsatz, die auf den experimentellen Ergebnissen basieren (Paper 4, 5 und 6: RMS 10 µm, Lot 2 bzw. 5 µm).

In den ersten Simulationen wurde die Reaktion des RMS aus Stabilitätsgründen mit einer Wahrscheinlichkeitsdichtefunktion (PDF, **P**robability **D**ensity **F**unction) der folgenden Form modelliert:

$$A \cdot D \cdot exp\{-B \cdot (x + C - D \cdot t)^2\} \tag{5}$$

Dabei bezeichnen A die Amplitude der Reaktion, B die Breite der PDF, C einen räumlichen Offset und D die Reaktionsgeschwindigkeit.

In Paper 6 wurde hierfür ein alternativer Ansatz in Form einer rechteckförmigen Funktion gewählt, um einen präziseren und besser kontrollierbaren Energieeintrag zu gewährleisten. Die zugrundeliegende volumetrische Leistungsdichte wird durch folgende Funktion beschrieben:

$$P = \frac{C}{u \cdot w_r \cdot \Delta t} \tag{6}$$

Dabei bezeichnen C eine Konstante, u die Reaktionsgeschwindigkeit, w_r die Breite der Reaktionszone und Δt die Dauer eines jeden Zeitschritts.

5 Ergebnisse

Dieses Kapitel enthält ausgewählte wissenschaftliche Veröffentlichungen, die im Rahmen des übergeordneten Forschungsthemas entstanden sind und die Grundlage der vorliegenden Dissertation bilden. Insgesamt wurden elf Beiträge veröffentlicht – davon fünf in begutachteten Fachzeitschriften und sechs in Konferenzbänden.

Die ersten acht Arbeiten adressieren unterschiedliche Aspekte des reaktiven Löt- und Fügeprozesses. Dazu zählen die Kompatibilität des Abscheideprozesses auf LTCC-Substraten, die theoretische Modellierung des Fügeprozesses über Simulationen, experimentelle Fügeversuche sowie die Analyse der entstandenen Fügestellen.

Die letzten drei Beiträge bilden die Grundlage für zukünftige Arbeiten. Sie befassen sich mit einem Prüfstand zur mechanischen Charakterisierung von Fügestellen, der Durchführung von In-situ-Messungen während Umweltprüfversuchen sowie der Entwicklung einer Methodik zur analytischen Untersuchung von Schadstellen.

Jede Veröffentlichung wird in einem eigenen Unterkapitel vorgestellt, beginnend mit formalen Angaben zur jeweiligen Veröffentlichung. Anschließend folgen eine Synopse und die thematische Einordnung in das Gesamtprojekt sowie der vollständige Artikel. Eine übergreifende Diskussion der zentralen Forschungsfragen erfolgt abschließend in Kapitel 6.

5.1 Paper 1: Morphologies of Reactive Nanolayer Stacks Sputtered on Ceramic LTCC Substrates Having a Micrometer Scale Surface Roughness

5.1.1 Veröffentlichungshinweise

Erik Wiss[1], Alexander Schulz[2], Andreas Ruh[1], Konrad Jaekel[2], Jens Müller[2], Steffen Wiese[1]

[1]Chair of Microintegration and Reliability, Faculty of Natural Sciences and Technology, Saarland University, Saarbrücken, Germany

[2]Electronics Technology Group, Faculty of Electrical Engineering and Information Technology, TU Ilmenau, Ilmenau, Germany

Advanced Engineering Materials (2025), 27.3, 2302284

Die Originalveröffentlichung ist abrufbar unter:
https://doi.org/10.1002/adem.202302284

5.1.2 Synopse

Diese Veröffentlichung untersucht den Einfluss der Oberflächenmorphologie keramischer LTCC-Substrate auf die Abscheidung und Funktionsfähigkeit eines RMS. Die Motivation ergibt sich aus der im Vergleich zu Metallen und Si deutlich höheren Rauheit von LTCC-Substraten, auf denen reaktive Fügeprozesse bislang weniger etabliert sind. Ziel der Arbeit war es, die Morphologie der abgeschiedenen Schichten zu analysieren, deren Zündfähigkeit zu prüfen sowie Temperatur und Geschwindigkeit der Reaktion zu messen.

Hierzu wurden RMS auf verschiedene LTCC-Substrate mit unterschiedlicher Oberflächenstruktur abgeschieden. Dazu zählten eine unbearbeitete LTCC ohne Metallisierung, eine laserbearbeitete LTCC ohne und mit Metallisierung sowie eine laserbearbeitete LTCC mit Metallisierung und zusätzlicher Sn-Beschichtung. Vor der Abscheidung wurde die Rauheit der jeweiligen Oberflächen mit einem LSM gemessen, und nach der Abscheidung die Morphologie der darauf abgeschiedenen Schichten mit einem REM analysiert. Die maximale Temperatur der Reaktion wurde mit einem Pyrometer, und die mittlere Geschwindigkeit der Reaktion mit einer Hochgeschwindigkeitskamera erfasst.

Die Ergebnisse zeigen, dass auf unbearbeiteten LTCC-Substraten durchgängige, geschlossene Schichten abgeschieden werden können, die die Morphologie des Substrats nahezu vollständig abbilden können. Eine durch Lasermodifikation erhöhte Rauheit führt zu lokalem Materialabtrag und damit zur Ausbildung von Gräben, wodurch das RMS in einzelne säulenartige Bereiche aufgeteilt wird, deren Wände nicht vollständig miteinander verbunden sind. Dieser Effekt wird durch das Hinzufügen einer Metallisierung und einer zusätzlichen Sn-Beschichtung weiter verstärkt.

Alle untersuchten Konfigurationen konnten erfolgreich elektrisch gezündet werden. Die höchste Reaktionstemperatur (ca. 1100 °C) und -geschwindigkeit (ca. 5 m/s) wurden auf der unbehandelten LTCC erzielt. Bei den anderen Konfigurationen lagen die Werte deutlich niedriger (739-838 °C bzw. 2,2-2,9 m/s). Die Ursachen hierfür liegen in der Segmentation des RMS, die an den Kontaktflächen zu einer kurzen Unterbrechung der Reaktion und somit zu einer verzögerten Wärmefreisetzung über längere Zeit führt, sowie in der besseren Wärmeleitfähigkeit der Metallisierung.

Im Kontext des Gesamtprojekts leistet diese Veröffentlichung einen Beitrag zur Beantwortung der Frage der Abscheidungs- und Zündfähigkeit eines RMS auf keramischen LTCC-Substraten mit hoher Rauheit.

5.1.3 Vollständiger Artikel

RESEARCH ARTICLE

ADVANCED ENGINEERING MATERIALS
www.aem-journal.com

Morphologies of Reactive Nanolayer Stacks Sputtered on Ceramic Low-Temperature Cofired Ceramic Substrates Having a Micrometer-Scale Surface Roughness

Erik Wiss, Alexander Schulz, Andreas Ruh, Konrad Jaekel, Jens Müller, and Steffen Wiese*

The deposition of reactive multilayer systems (RMSs) is investigated on low-temperature cofired ceramic (LTCC) substrates having different surface morphologies. In this study, the morphologies of RMS layers that are deposited on glass-ceramic LTCC substrates are analyzed. Different surface morphologies are prepared through pretreatments of the LTCC surface. The considered surfaces encompass an untreated natural LTCC surface, a modified sintered LTCC surface by laser ablation, a surface with a deposited metallization layer, and finally, a surface with an additional solder layer put on the deposited metallization layer. The different pretreatments lead to significant differences in the roughness of the LTCC substrates, resulting in different reaction velocities and peak temperatures on the various surface morphologies after the RMS's reaction. As a result, different grades of structural integrity (liftoff, crack formation) between the reacted RMS layer and the LTCC are observed.

1. Introduction

All established interconnection technologies in microelectronics (except ultrasonic wedge–wedge bonding and UV curing) are based on the transfer of heat into the joining zone. When heat is put in from the external sources, severe thermomechanical stresses can be induced into the assembly because of significant differences in the coefficients of thermal expansion (CTEs) between the component and the substrate materials. Heat might also be critical for sensitive components. To reduce the peak temperature and the total thermal budget for the global interconnection process, various approaches attempt to use localized heat sources from an exothermic reaction of a reactive compound deposit.[1–11]

These reactive compounds or reactive multilayer systems (RMSs) consist of two or more reactant partners, which are arranged in alternating nanolayers in the range of 10–300 nm with a total stack thickness of up to 300 μm.[12,13] A new intermetallic phase is built through intermixing on atomic level, if a sufficient amount of energy is applied (e.g., by a laser pulse, an electrical spark, or high temperature). During this exothermic process, a large amount of heat is released while the reaction front moves through the materials in the lateral direction.[14] If the amount of heat that was generated this way is higher than that removed by thermal diffusion, the exothermic reaction is termed self-propagating and keeps moving along the area of the RMS.[15] Properties like generated heat, peak temperature, and reaction speed can be modified by changing the material combination, the ratio of the layer thicknesses, and the total thickness of the RMS stack. In addition to the Al–Ni system, which was used in this work, there are many other possible material combinations that can be used for RMS like Ti–Al, Nb–Si, or Pd–Al for example.[16–18]

Whereas most of the RMS-related research focuses on silicon/silicon, metal/metal, or metal/silicon assemblies like die bonding or heat spreader mounting, there is a very limited amount of studies in other areas, which includes low-temperature cofired ceramics (LTCC).[1–11] The use of RMS in the world of LTCC substrates would open another promising technological pathway, especially for heterogeneous assembly, but the properties of the ceramics affect the exothermic reaction. Compared to other materials like metal and silicon, the LTCC shows a higher surface roughness and a significantly lower thermal conductivity, which makes it very challenging to adapt the current knowledge to this technology.[19,20] Therefore, further investigation is necessary to accomplish optimal circumstances for the deposition process of the RMS and hence the reaction itself.

The higher roughness of the LTCC substrate has a particular importance for any reactive joining technology. One aspect is the

---

E. Wiss, A. Ruh, S. Wiese
Chair of Microintegration and Reliability
Saarland University
66123 Saarbruecken, Germany
E-mail: erik.wiss@uni-saarland.de

A. Schulz, K. Jaekel, J. Müller
Department of Electronics Technology
Faculty of Electrical Engineering and Information Technology
TU Ilmenau
98693 Ilmenau, Germany

The ORCID identification number(s) for the author(s) of this article can be found under https://doi.org/10.1002/adem.202302284.

DOI: 10.1002/adem.202302284

compatibility with the deposition processes which are used to create a reactive multilayer on top of the surface. Some of these deposition processes, such as electrochemical deposition, demand a very even and smooth surface to deposit a stack of alternating thin layers with well-controlled thicknesses.[6]

Another aspect is the mechanical strength of the bonded or soldered joints, which benefits from a high surface area (e.g., roughness or surface modification of the bonding partners), resulting in high mechanical interlocking between the component surface and the bonding agent.[21–23]

Considering aspects of the joining process itself, the morphology of the component surface has a strong influence on the wetting behavior. In addition, the roughness of a ceramic substrate has an impact on the adhesion strength of applied thick films by influencing the mechanical interlocking. Thin films coated on a surface with a specific roughness show a similar surface morphology as the original surface.

To be able to address the question how the surface roughness or morphology alters the reaction of the RMS, the aim of the study was to manufacture-specified surface morphologies on glass-ceramic substrates. Therefore, different technologies which could provide surface morphologies in different scales had to be investigated. While an untreated LTCC substrate was used as a reference material, the surface of the other samples was modified using laser ablation to increase their roughness. In addition to this first surface treatment, a metallization layer using AgPd paste was screen-printed on the LTCC substrate before the RMS was deposited. Another variation consists of the deposition of a solder layer (Sn) on top of the screen-printed metallization before and after the deposition of the RMS.

2. Experimental Section

2.1. LTCC Substrates

To investigate the effects of different surface modifications of LTCC substrates on the deposition of reactive multilayers, various samples were produced and prepared in four different configurations. **Table 1** shows an overview in terms of the use of laser ablation and which type of metallization and solder coating was used, if any.

A commercially available DuPont GreenTape 951 was used for manufacturing the LTCC substrates under standard LTCC processing conditions, resulting in a total thickness of 840 μm after sintering. One of the substrates was used as reference material (configuration 1) without further processing, whereas the surface of the sample of configuration 2 was laser ablated to achieve higher roughness. For configuration 3, an AgPd metallization with a thickness of 5 μm was screen-printed on the LTCC substrate using a DuPont 6146 paste before laser ablation. Configuration 4 was prepared in the same way, but an additional Sn-based solder coating of 2 μm was applied before and after the RMS was deposited to promote bonding adhesion to metal surfaces. After finishing all preparation steps, the samples were cut in smaller pieces of 15 mm × 7 mm out of larger sheets by wafer sawing.

Table 1. Overview about the investigated samples.

Configuration	Laser ablation	Metallization	Solder coating
1	No	No	No
2	Yes	No	No
3	Yes	AgPd	No
4	Yes	AgPd	Yes

2.2. Laser Ablation

The AgPd-based metallization, which was screen-printed on the surface of the samples, was modified using laser ablation to achieve higher roughness on the metallization compared to the reference sample. The objective of this modification was the enhancement of the adhesion of the sputtered RMS layer. Modifying the surface in this way proved to be a good possibility due to its high precision and repeatability.[24] Therefore, a 355 nm picosecond UV laser system microSTRUCT C v2.0 (3D-Micromac AG) was used. It provided a small laser spot diameter of 7 μm, very short laser pulses in a time range less than 10 ps, and a high laser pulse energy of up to 70 μJ, so that the heat- affected zone around the target was as small as possible. In this work, the laser power varied between 0.5 W (with metallization) and 0.8 W (without metallization), and the distance between two laser cutting lines was 40 μm with two repetitions.

2.3. Surface Characterization

Before the RMS was deposited, the surface of both the modified and the unmodified LTCC surfaces was measured using a laser scanning microscope (LSM) Olympus LEXT OLS4100 (Olympus Europa SE & Co. KG) with a 50× objective and a numerical aperture of 0.95. Therefore, the surface was scanned in smaller areas of 250 μm × 250 μm. The values used in this work are the core height S_k, the reduced peak height S_{pk}, the reduced dale height S_{vk}, and the material ratios S_{mr1} and S_{mr2}, which are presented in Abbott–Firestone curves.

2.4. Deposition of RMS and Solder Layer

The deposition of the RMS on all the differently prepared LTCC substrates as well as the deposition of the solder layer for configuration 4 were realized by a sputter process using a PVD system CS400 (VON ARDENNE GmbH) whose working principle is predicated on magnetron deposition. In case of configuration 4, a thin layer of 2 μm tin was sputtered first on the metallization. After that — and in every other case — the RMS itself was deposited, consisting of alternating layers of aluminum and nickel. To achieve the maximum heat release during the exothermic reaction layer, thicknesses of 60 nm for aluminum and 40 nm for nickel, corresponding to a stoichiometry ratio of 3:2, were chosen with 100 bilayers leading to a total thickness of 10 μm for the RMS. Again, only the samples of configuration 4 were covered with 2 μm tin.

2.5. Scanning Electron Microscopy Analysis

The cross sections of the samples were prepared for scanning electron microscopy (SEM) using a ZEISS EVO MA15 (Carl

Zeiss Microscopy). The targeted magnification was in the range between 2000× and 80 000×. Therefore, samples were prepared in a specific manner using the following sequence of five preparation steps. Step 1: after embedding with Struers EpoFix kit, the samples were cut using an IsoMet 4000 precision saw (Buehler). Step 2: grinding of metallographic samples was carried out on SiC foils with grits of 500 and 1200 on a LabPol-25 (Struers). Step 3: the first polishing steps were carried out on a Tegramin-25 (Struers) by using various diamond suspensions having 9, 3, and 1 µm particle sizes. Step 4: the final polishing was performed on an ATM Saphir Vibro vibratory polishing machine using a colloidal silicon oxide. This resulted in an extremely even surface with ultralow roughness which enables to resolve the RMS nanolayers in the later SEM. Step 5: the sample coating was carried out on a Q150T Coater (Quantum Design). A very thin carbon film was sputtered on the sample to retain the even surface of the final polishing step. The target thickness of the carbon film was 20 nm. The ZEISS EVO was configured with a LaB_6 cathode, 20 kV accelerating voltage, and a beam current of 40 µA to carry out the respective microscopy.

2.6. Determination of Reaction Front Velocity and Peak Temperature

To achieve information about the speed and temperature of the reaction, corresponding measurements were performed. Therefore, a high-speed pyrometer KGA Series 840 (KLEIBER Infrared GmbH) with a measurement time of 10 µs and a high-speed camera Fastcam SA-X2 type 480 K (Photron Deutschland GmbH) with a Navitar 12x zoom lens were used. The RMSs were ignited electrically by connecting two test probes to a power supply (25 V, 4 A), that were shorted by a section of the RMS.

3. Results

3.1. Raw Unmachined LTCC

The cross section of a sample without further processing is shown in **Figure 1** (remark: the gap between the RMS and the LTCC in Figure 1a is supposed to be caused by the mechanical preparation of the sample). The reactive Al–Ni multilayer (narrow light gray stripe on top) was directly deposited on the raw unmachined LTCC substrate (mixed gray area). Due to the higher roughness of the ceramic compared to silicon or metal substrates, the deposited RMS follows the surface and looks wavy, but still continuous without any interruptions. In the 15 000-times magnified Figure 1b of the RMS, the single nanolayers can be seen.

3.2. Laser-Ablated LTCC

The cross section of a sample, which was laser ablated before the RMS was deposited, can be seen in **Figure 2**. The RMS changed from a wavy look with continuous layers to a stack consisting of many separated columns, whose sidewalls are not fully connected. The locations, which were engraved by the laser, experienced a material deposition leading to a height difference in the surface. Due to this difference, it is not possible to form a continuous layer anymore, although the deposition still reaches the bottom of the LTCC substrate.

3.3. Laser-Ablated LTCC with Metallization Layer

The laser-ablated samples with the AgPd metallization show the same behavior as the laser-ablated samples without metallization regarding the formation of separated columns. Adding this layer results in a surface, which is more rugged than in the other cases (see **Figure 3**). This effect is even more visible when solder layers are used (see **Figure 4**; remark: the round whitish particles with a diameter of ≈100 nm in Figure 3b and 4b are only a side effect of the sputter-coating preparation).

3.4. LSM Measurements

The LSM measurements of all configurations are depicted as Abbott–Firestone curves that are aligned to the average height. The used parameters are the core height S_k, the reduced peak height S_{pk}, the reduced dale height S_{vk}, and the material ratios S_{mr1} and S_{mr2}, which can be found in **Table 2**.

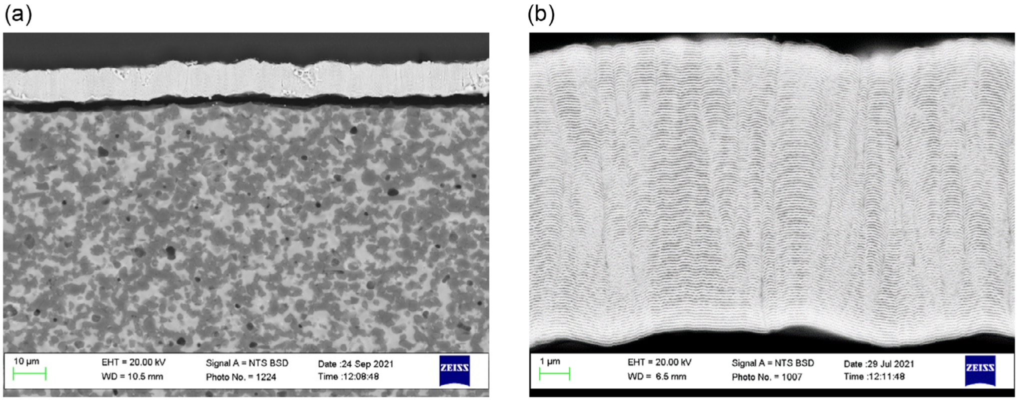

Figure 1. SEM images of the sputtered RMS (light gray) on an unmachined LTCC substrate (mixed gray). The RMS seems to be very smooth with nearly no interruptions. Magnification: a) 2000× and b) 15 000×.

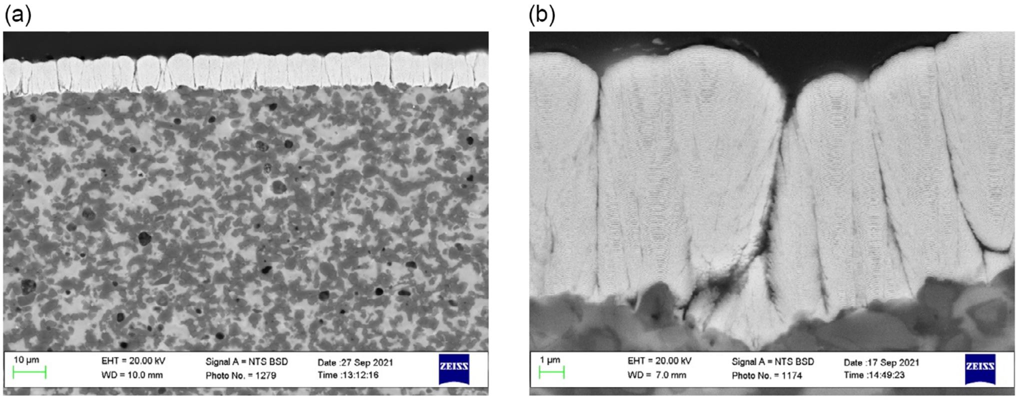

Figure 2. SEM images of the sputtered RMS (light gray) on a laser-ablated LTCC substrate (mixed gray). The RMS seems to be rugged with a lot of interruptions and separated columns whose sidewalls are not fully connected. Magnification: a) 2000× and b) 15 000×.

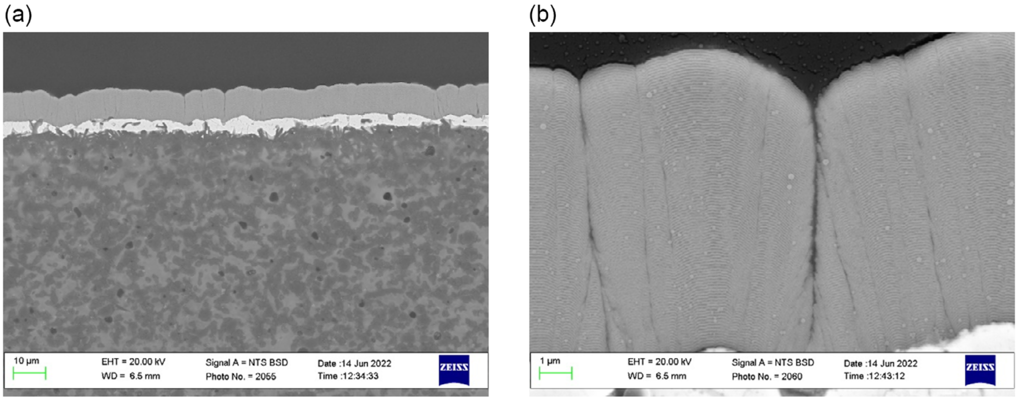

Figure 3. SEM images of the sputtered RMS (dark gray) on a laser-ablated LTCC substrate (mixed gray) with AgPd metallization (light gray). The metallization transmits the rugged surface of the LTCC to the RMS, which forms separated columns. Magnification: a) 2000× and b) 20 000×.

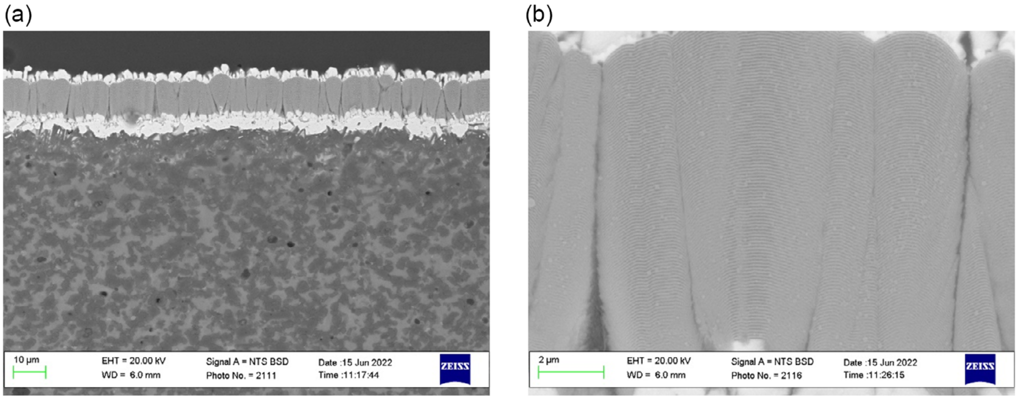

Figure 4. SEM images of the sputtered RMS (dark gray) on a laser-ablated LTCC substrate (mixed gray) with AgPd metallization and solder layers (light gray). Both the metallization and the solder layer transmit the rugged surface of the LTCC to the RMS. Magnification: a) 2000× and b) 20 000×.

Table 2. Results of the LSM measurements: core height S_k, reduced peak height S_{pk}, reduced dale height S_{vk}, and material ratios S_{mr1} and S_{mr2}.

Configuration	Core height S_k [µm]	Reduced peak height S_{pk} [µm]	Reduced dale height S_{vk} [µm]	Material ratio S_{mr1} [%]	Material ratio S_{mr2} [%]
1	1.4097	0.6138	0.5187	9.69	89.85
2	1.9667	0.8175	0.6621	10.82	91.67
3	2.8483	1.1915	1.0783	9.02	89.75
4	2.9521	1.5055	1.0375	10.09	90.61

The calculated values are in good agreement with the SEM images of the cross sections: the core height of the unmachined LTCC sample has the lowest value of 1.41 µm, followed by 1.97 µm for the laser-ablated samples, and 2.85 µm and 2.95 µm for the samples with metallization, both with and without solder layers, respectively.

Figure 5 shows the effect of the laser ablation on the morphology. Whereas the distribution of the core height is relatively small in case of the unmachined LTCC sample, there is a small widening after modifying the surface. The core height increases by ≈0.56 µm, and the reduced peak and dale height increase by ≈0.14–0.2 µm.

Adding an AgPd metallization layer results in a greater widening of the height distribution as before (see **Figure 6**) and in an increase of the measured values (core height of 2.85 µm, reduced peak height of 1.19 µm, and reduced dale height of 1.1 µm), what indicates a more rugged surface. The effect is even more visible when the metallization layer is combined with additional solder layers (core height of 2.95 µm, reduced peak height of 1.51 µm, and reduced dale height of 1.04 µm).

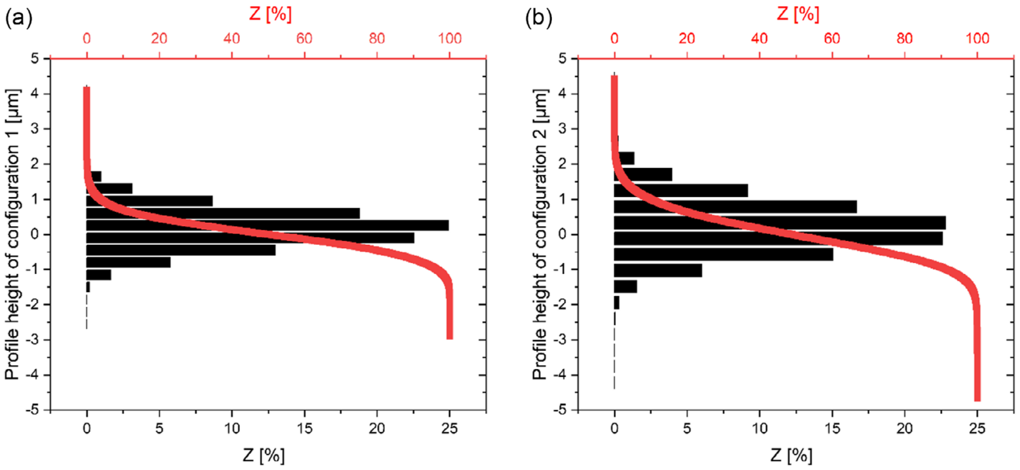

Figure 5. Abbott–Firestone curves of a) configuration 1 (raw unmachined reference material) and b) configuration 2 (laser-ablated LTCC). The laser ablation of the LTCC surface results in a small widening of the height distribution.

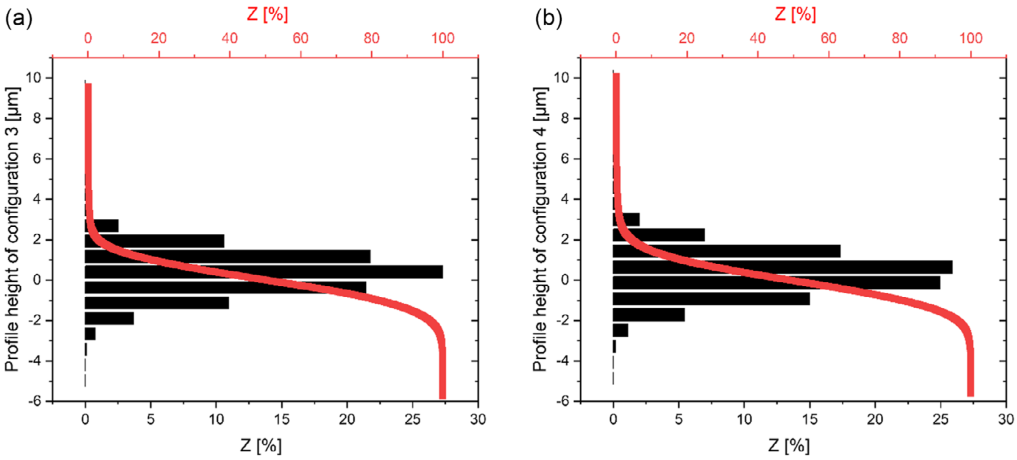

Figure 6. Abbott–Firestone curves of a) configuration 3 (laser-ablated LTCC with AgPd metallization) and b) configuration 4 (laser-ablated LTCC with AgPd metallization and additional solder layers). Compared to the previous curves, the metallization seems to cause a greater widening of the height distribution.

3.5. Reaction Front Velocity and Peak Temperature

The velocity and temperature measurements of the reactive multilayers exothermic reaction are shown in **Table 3** and have been described in detail earlier.[25,26] The unmodified LTCC substrate shows the highest peak temperature with almost 1100 °C and the highest reaction front velocity with 5.0 m s^{-1}. Modifying the surface by laser ablation and the use of a metallization layer decrease these values, e.g., configuration 3 reached the lowest values with a peak temperature of only 739 °C and a reaction front velocity of 2.2 m s^{-1}. Adding the solder layers in configuration 3 results in a small increase in the measured values. The results of configurations 2–4 do not differ significantly, given the fact that the depositions of the respective RMS layers were not carried out in the same process. Therefore, it is very difficult to read a trend from the three latter results in Table 3.

Table 3. Results of the mean speed and maximum temperature measurements for the different configurations.[25,26]

Configuration	Peak temperature [°C]	Reaction front velocity [m s^{-1}]
1	1092	5.0
2	803	2.9
3	739	2.2
4	838	2.4

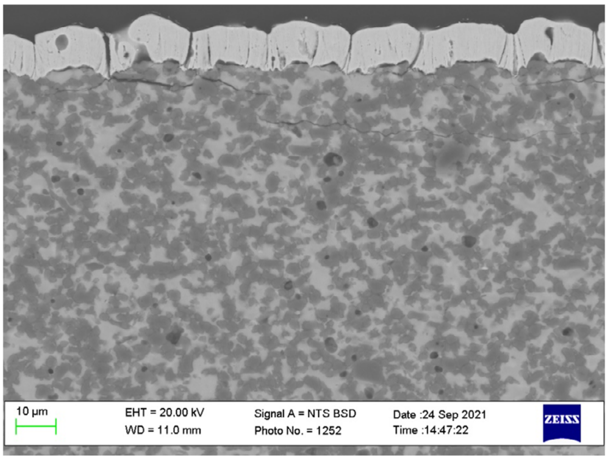

Figure 7. SEM image of a detached RMS (dark gray) from a laser-ablated LTCC substrate (mixed gray) with cracks in the ceramic after ignition. Magnification: 2000×.

Figure 7 shows the SEM image of a reacted RMS on a laser-ablated LTCC substrate. The RMS is detached from the surface over large areas and there are some cracks within the ceramic substrate due to the high temperature of the reaction, caused by the difference in the CTEs of the deposited RMS and the ceramic substrate. Local adhesion is reached where the laser engraved the surface.

A top view of a deposited RMS can be seen in **Figure 8**a while a reacted RMS is shown in Figure 8b. Several pores and microcracks have formed on the surface of the multilayer. Such pores could not be observed in reacted multilayers that were deposited and ignited on raw unmachined LTCC surfaces. The pores seem to support the adhesion between the multilayer and the LTCC substrate, and their formation seems to prevent major cracks within the layer due to a shrinkage in its volume during the exothermic reaction. In literature, a decrease in the volume of up to 12% is reported.[27]

4. Discussion

The comparison of the four studied configurations with different surface modifications reveals significant differences in the appearance of the RMS, which can have several consequences for following joining processes.

In the case of the unmodified reference LTCC substrate, its morphology is transmitted to the deposited RMS, leading to a wavy surface and continuous layers without any interruptions although the roughness of the surface in the range of several hundred micrometers is much higher than that of silicon with less than 1 nm. From the ignition experiments, it can be deducted that this continuity lets the reaction progress at the highest speed of the four configurations, reaching the highest

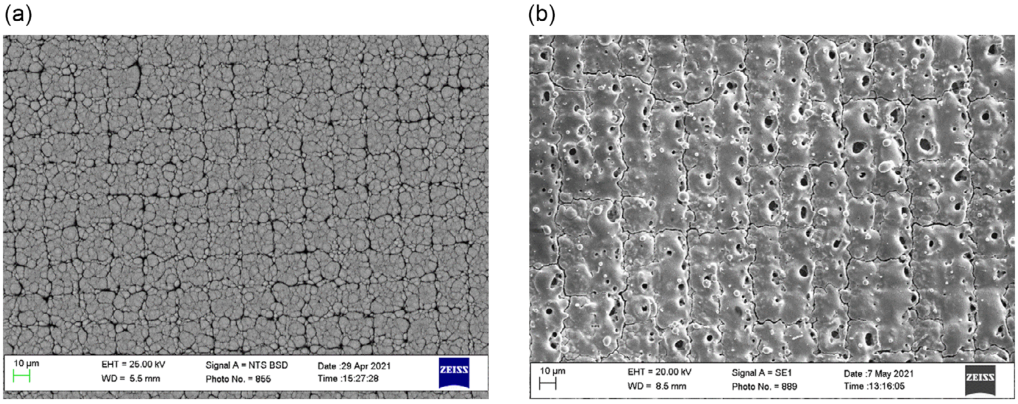

Figure 8. a) Top view of an RMS that was deposited on a laser-ablated LTCC surface. It can be seen where the laser engraved the ceramic. Magnification: 1000×. b) Top view of a reacted RMS with microcracks and pores within the surface of the RMS. Magnification: 1000×.

peak temperature of almost 1100 °C. One reason for this high temperature is the much lower thermal conductivity of the LTCC ($3.3\,\mathrm{W\,m^{-1}\,K^{-1}}$) compared to silicon ($152\,\mathrm{W\,m^{-1}\,K^{-1}}$) or silver ($429\,\mathrm{W\,m^{-1}\,K^{-1}}$), fortified by the observed liftoff of the RMS that removes the direct contact between the RMS and the substrate. It can be assumed that this liftoff is caused by the formation of huge thermomechanical stress within the material due to the very high temperature rise in a very short time period of a few milliseconds. Additionally, the volume of the RMS decreases during the exothermic reaction, which lowers the adhesion in combination with the mismatch in the CTEs of the different materials.

The adhesion can be increased by laser ablating the surface of the substrate. The local material removal at the processed areas results in the formation of trenches across the entire surface. If the RMS is deposited on a surface treated in this way, no continuous layers can be created due to the abrupt changes in height. The morphology of the nanolayers changes from a wavy look to a more rugged one, with a lot of interruptions resulting in the formation of separated columns that are not fully connected between their sidewalls. This has several consequences: first, at every interruption, the intermixing of the materials and, hence, the reaction front is stopped until the generated heat reactivates the process in the next section, which can be assumed to be the main factor for the observed decrease in the reaction speed. Furthermore, the same amount of heat as before is released in less time, resulting in a decrease in absolute temperature and thus, lowers thermomechanical stress. Second, the adhesion is improved due to the anchoring effect of the deposited RMS in the substrate. Third, the mechanical anchoring of the RMS in combination with the mismatch in the CTEs and the volume reductions leads to microcracks in the structure. Furthermore, less peeling effects could be observed.

As before, the usage of a laser-ablated metallization layer and, if applied, an additional solder layer leads to a rugged appearance in the RMS and the formation of unconnected columns. The velocity of the reaction and the temperature are reduced due to the same reasons as in the last configuration. The drop in temperature is higher because a part of the thermal energy is absorbed in the metallization. It is supposable that the solder layer can also be used to fill potential microcracks within the RMS, if enough pressure is used during the joining process.

5. Conclusions

The deposition of RMSs has been investigated on glass-ceramic LTCC substrates, having different surface morphologies. The results show that the deposition of an RMS on unmachined LTCC substrates results in uninterrupted layers with a very smooth and wavy appearance. This morphology of layers shows the highest peak temperature and highest velocity of the exothermic reaction and leads to a liftoff of the resulting intermetallic layer after the reaction. It is assumed that the high temperature gradients, which cause high thermomechanical stress, and the different CTEs are responsible for the liftoff. The usage of an additional metallization layer underneath RMS partly prevents the liftoff but creates cracks in the LTCC surface.

When the roughness of the ceramic substrate is increased by laser ablation, an improved local adhesion of the reacted multilayer can be observed. The deposited RMS appears as an interrupted layer with a column-like structure. Despite its noncontinuous appearance, the reaction still propagates along the surface, but shows both a lower peak temperature and reaction velocity. Although a liftoff is prevented, cracks in the LTCC surface are observed after the reaction. The addition of a solder layer leads to a similar appearance of the deposited multilayer. However, no cracks are observed after the reaction.

It is believed that the low thermal conductance of the glass-ceramic LTCC substrate leads to higher temperature gradients compared to other substrate materials like Si or metal. Thus, higher thermomechanical stresses during the reaction may cause a liftoff of the reacted RMS layer. Increasing the LTCC surface roughness by laser ablation or deposition of metallization layers helps to increase the layer adhesion. The introduction of an intermediate solder layer seems to effectively reduce the thermomechanical stresses and prevents crack formation within the LTCC substrate.

Acknowledgements

This work was funded by the Deutsche Forschungsgemeinschaft (DFG, German Research Foundation) — Project ID 426204742 and funding codes BA 6161/1-1 and BA 6161/1-2.

Support in sample preparation (LTCC manufacturing, sputter processing) was received from Ms. Ina Koch and Mr. Joachim Döll from the Center of Micro- and Nanotechnologies (ZMN) (DFG resources reference: RI_00009), which runs DFG-funded core facilities (grant nos. MU 3171/2-1 + 6-1, SCHA 632/19-1 + 27-1, HO 2284/4-1 + 12-1) at TU Ilmenau.

Open Access funding enabled and organized by Projekt DEAL.

Conflict of Interest

The authors declare no conflict of interest.

Data Availability Statement

Research data are not shared.

Keywords

Al–Ni, joining, low-temperature cofired ceramics, reactive multilayers, reactive multilayer system

Received: December 31, 2023
Revised: May 1, 2024
Published online: May 29, 2024

---

[1] J. Braeuer, T. Gessner, *J. Micromech. Microeng.* **2014**, *24*, 115002.
[2] B. Boettge, J. Braeuer, M. Wiemer, M. Petzold, J. Bagdahn, T. Gessner, *J. Micromech. Microeng.* **2010**, *20*, 064018.
[3] J. Braeuer, J. Besser, M. Wiemer, T. Gessner, *Sens. Actuator, A* **2012**, *188*, 212.
[4] S. Kanetsuki, S. Miyake, K. Kuwahara, T. Namazu, *Jpn. J. Appl. Phys.* **2016**, *55*, 06GP17.

[5] S. Kanetsuki, K. Kuwahara, S. Egawa, S. Miyake, T. Namazu, *Jpn. J. Appl. Phys.* **2017**, *55*, 06GN16.

[6] S. Hertel, W. Schulte, M. Weiser, M. Becker, M. Wiemer, T. Otto, in *Micro-Nano-Integration; 7th GMM-Workshop (VDE)* **2018**, p. 1.

[7] X. Qiu, *Master Thesis*, *Louisiana State University*, August **2007**.

[8] J. Wang, E. Besnoin, A. Duckham, S. J. Spey, M. E. Reiss, O. M. Knio, M. Powers, M. Whitener, T. P. Weihs, *Appl. Pys. Lett.* **2003**, *83*, 3987.

[9] J. Matteau, in *Proc. Int. Symp. Microelectron*, Long Beach, CA, October **2011**, Vol. *1*, p. 000521.

[10] J. S. Subramanian, P. Rodgers, J. Newson, T. Rude, Z. He, E. Besnoin, T. P. Weihs, V. Eveloy, M. Pecht, in *EuroSimE*, Berlin, Germany, April **2005**, p. 681.

[11] A. P. McClure, *Master Thesis*, *University of Maryland*, October **2008**.

[12] S. Sen, M. Lake, N. Kroppen, P. Farber, J. Wilden, P. Schaaf, *Appl. Surf. Sci.* **2017**, *396*, 1490.

[13] D. P. Adams, *Thin Solid Films* **2015**, *576*, 98.

[14] K. Raić, R. Rudolf, P. Ternik, Z. Žunič, V. Lazić, D. Stamenković, T. Tanasković, I. Anžel, *Mater. Tehnol.* **2011**, *45*, 335.

[15] A. J. Gavens, D. Van Heerden, A. B. Mann, M. E. Reiss, T. P. Weihs, *J. Appl. Phys.* **2000**, *87*, 1255.

[16] A. S. Rogachev, A. É. Grigoryan, E. V. Illarionova, I. G. Kanel', A. G. Merzhanov, A. N. Nosyrev, N. V. Sachkova, V. I. Khvesyuk, P. A. Tsygankov, *Combust., Explos. Shock Waves* **2004**, *40*, 166.

[17] M. E. Reiss, C. M. Esber, D. Van Heerden, A. J. Gavens, M. E. Williams, T. P. Weihs, *Mater. Sci. Eng. A* **1999**, *261*, 217.

[18] A. S. Ramos, M. T. Vieria, *Intermetallics* **2012**, *25*, 70.

[19] H. Jantunen, T. Kangasvieri, J. Vähäkangas, S. Leppävuori, *J. Eur. Ceram. Soc.* **2003**, *23*, 2541.

[20] M. Matters-Kammerer, U. Mackens, K. Reimann, R. Pietig, D. Hennings, B. Schreinemacher, R. Mauczok, S. Gruhlke, C. Martiny, *Microelectron. Reliab.* **2006**, *46*, 134.

[21] Satyanarayan, K. N. Prabhu, *J. Mater. Sci. Technol.* **2013**, *29*, 1430.

[22] J. K. Shang, D. Yao, *J. Electron. Packag.* **1996**, *118*, 170.

[23] B. Feng, J. Cao, Y. Wang, J. Feng, *ECS J. Solid State Sci. Technol.* **2015**, *5*, P41.

[24] N. Gutzeit, T. Welker, K. H. Drüe, J. Müller, in *Additional Papers and Presentations (CICMT)*, Denver, CO, April **2016**, Vol. *2016*, p. 000103.

[25] A. Schulz, H. Bartsch, N. Gutzeit, S. Matthes, M. Glaser, A. Ruh, J. Müller, P. Schaaf, J. P. Bergmann, S. Wiese, in *MikroSystemTechnik Congress (VDE)*, Ludwigsburg, Germany, November **2021**.

[26] A. Schulz, A. Ruh, S. Wiese, J. Müller, in *Ceramic Interconnect and Ceramic Microsystems Technologies (CICMT)*, Vienna, Austria, July **2022**.

[27] T. Namazu, K. Ohtani, K. Yoshiki, S. Inoue, in *16th Inter. Solid-State Sensors, Actuators and Microsystems Conf. (IEEE)*, IEEE, Beijing, China **2011**, p. 1368.

5.2 Paper 2: The Simulated Effect of Adding Solder Layers on Reactive Multilayer Films Used for Joining

5.2.1 Veröffentlichungshinweise

Adam Yuile[1], Alexander Schulz[2], Erik Wiss[1], Jens Müller[2], Steffen Wiese[1]

[1]Chair of Microintegration and Reliability, Faculty of Natural Sciences and Technology, Saarland University, Saarbrücken, Germany

[2]Electronics Technology Group, Faculty of Electrical Engineering and Information Technology, TU Ilmenau, Ilmenau, Germany

Applied Sciences (2022), 12, 2397

Die Originalveröffentlichung ist abrufbar unter:
https://doi.org/10.3390/app12052397

5.2.2 Synopse

Diese Veröffentlichung untersucht den Einfluss zusätzlicher Lotschichten auf den reaktiven Fügeprozess sowie die Möglichkeit der Temperaturmessung über in das LTCC-Substrat eingebettete Pt-Sensoren. Die Motivation ergibt sich aus der Notwendigkeit, Lotmaterialien zur Herstellung elektrischer Verbindungen in reaktive Fügeverfahren zu integrieren, sowie aus der Tatsache, dass in der Realität keine direkte Temperaturmessung in den einzelnen Schichten möglich ist. Ziel der Arbeit war es, die Auswirkungen des Lots auf die Temperaturentwicklung während der exothermen Reaktion zu analysieren und die Machbarkeit der Temperaturmessung über eingebettete Sensoren zu überprüfen.

Hierzu wurde ein dreidimensionales CFD-Modell mit einer Gesamtgröße von 20 mm x 20 mm x 15 mm entwickelt, in dessen Zentrum sich ein 1235 µm hoher Schichtstapel befindet. Das Referenzmodell besteht aus einem LTCC-Substrat (570 µm) mit drei eingebetteten Pt-Sensoren im Abstand von jeweils 1 mm sowie einer Isolationsschicht (35 µm) zur elektrischen Trennung der Sensoren vom RMS (30 µm). Im erweiterten Modell wurden zusätzlich eine Lotschicht (200 µm) und ein Si-Chip (400 µm) hinzugefügt. Die exotherme Reaktion wurde durch eine sich mit 1 m/s vom linken zum rechten Rand ausbreitende Wahrscheinlichkeitsdichtefunktion modelliert.

Die Ergebnisse zeigen, dass im Referenzmodell Temperaturen von bis zu 800 °C im RMS erreicht werden, während die Pt-Sensoren lediglich ca. 250 °C messen. Im erweiterten Modell sinken die Temperaturen auf ca. 275 °C im RMS bzw. 100 °C an den Sensoren. Die Lotschichten beeinflussen die Temperaturverteilung also signifikant und können somit gezielt zur Modifikation des Reaktionsverhaltens eingesetzt werden. Aufgrund der großen Isolationsschicht zwischen RMS und Sensoren ist eine exakte Temperaturmessung zwar nicht möglich, jedoch lassen sich durch eine entsprechende Sensoranordnung Rückschlüsse auf die Reaktionsgeschwindigkeit ziehen.

Im Kontext des Gesamtprojekts leistet diese Veröffentlichung einen Beitrag zur Beantwortung der Frage, wie sich die thermische Charakteristik von RMS durch zusätzliche Schichten beeinflussen lässt. Zudem wird eine Methodik zur indirekten Abschätzung der Reaktionsgeschwindigkeit vorgestellt.

5.2.3 Vollständiger Artikel

applied sciences

IMPACT FACTOR 2.5

CITESCORE 5.3

Article

The Simulated Effect of Adding Solder Layers on Reactive Multilayer Films Used for Joining Processes

Adam Yuile, Alexander Schulz, Erik Wiss, Jens Müller and Steffen Wiese

Special Issue
Fundamentals and Applications of Reactive Materials
Edited by
Dr. Christoph Pauly and Dr. Karsten Woll

MDPI

https://doi.org/10.3390/app12052397

applied sciences

MDPI

Article

The Simulated Effect of Adding Solder Layers on Reactive Multilayer Films Used for Joining Processes

Adam Yuile [1,*], Alexander Schulz [2], Erik Wiss [1], Jens Müller [2] and Steffen Wiese [1]

[1] Chair of Microintegration and Reliability, Saarland University, 66123 Saarbrucken, Germany; erik.wiss@uni-saarland.de (E.W.); s.wiese@mx.uni-saarland.de (S.W.)
[2] Faculty of Electrical and Computer Engineering, Department of Electronics Technology, TU Ilmenau, 98693 Ilmenau, Germany; Alexander.Schulz@tu-ilmenau.de (A.S.); jens.mueller@tu-ilmenau.de (J.M.)
* Correspondence: adam.yuile@uni-saarland.de; Tel.: +49-681-302-71827

Abstract: In order to introduce new bonding methods in the area of electronic packaging a theoretical analysis was conducted, which should give substantial information about the potential of reactive multilayer systems (rms) to create sufficient local heat for joining processes between silicon chips and ceramic substrates. For this purpose, thermal CFD (computational fluid dynamics) simulations have been carried out to simulate the temperature profile of the bonding zone during and after the reaction of the rms. This thermal analysis considers two different configurations. The first configuration consists of a silicon chip that is bonded to an LTCC-substrate (Low Temperature Co-fired Ceramics) using a bonding layer that contains an rms and a solder preform. The reaction propagation speed of the reactive multilayer was set to a value of 1 m/s, in order to partially melt a solder preform underneath a silicon chip. The second configuration, which consists only of the LTCC-substrate and the rms, was chosen to study the differences between the thermal outputs of the two arrangements. The analysis of the CFD simulations was particularly focused on interpretations of the temperature and liquid fraction contours. The CFD thermal simulation analysis conducted contains a melting/solidification model which can track the molten/solid state of the solder in addition to modelling the influence of latent heat. To provide information for the design of a test-substrate for experimental investigations, the real behaviour of Pt-100 temperature probes on the LTCC-substrate was simulated, in order to monitor an actual bonding in the experiment. All simulations were carried out using the ANSYS Fluent software.

Keywords: CFD; thermal simulation analysis; reactive multilayer systems; joining

check for updates

Citation: Yuile, A.; Schulz, A.; Wiss, E.; Müller, J.; Wiese, S. The Simulated Effect of Adding Solder Layers on Reactive Multilayer Films Used for Joining Processes. *Appl. Sci.* **2022**, *12*, 2397. https://doi.org/10.3390/app12052397

Academic Editors: David García Fresnadillo, Christoph Pauly and Karsten Woll

Received: 19 November 2021
Accepted: 27 January 2022
Published: 25 February 2022

1. Introduction

Thermal mechanical stresses are one of the most crucial issues in joining processes in microelectronics. These stresses are usually caused by two factors. Factor one is the differences in thermal expansion of the materials to be joined. Factor two is the high process temperatures that are needed for most joining processes. Eliminating one of the two factors helps to significantly reduce the thermal-mechanical stress after bonding. One idea to achieve this goal is the usage of localised heat in the joining zone without a global heating of the entire assembly. There are different approaches for low-temperature localised bonding techniques. One such method of realising this is to use nanoscale reactive multilayer technologies to deploy a heat source on a targeted area. Established reactive multilayer systems consist of an alternating stack of layers of different metals, such as Fe and Ni, which can create a self-propagating exothermal reaction. One targeted area for the application of these reactive multilayers in microelectronics are additive bonding processes in LTCC technology, in order to prevent critical thermal-mechanical stresses in sensitive structures within the LTCC multilayer.

LTCC provides special 3D-structuring abilities, which enables liquid cooling system integration [1], special biomedical sensors [2–4] and fluidic structures [2,5]. Such LTCC architectures are sensitive to thermo-mechanical stresses. Another strength is its specific dielectric properties, that make LTCC a very beneficial substrate for specific areas, such as high frequency or millimetre wave circuits [6–8] or RF-antennas (radio-frequency antennas) and radars [7,9]. Other applications of LTCC substrates are power LED (light-emitting diode) packaging [10] and fibre optical applications [11].

In addition to this multifaceted functionality, LTCC packages are capable of offering a high reliability [8,12], with respect to superior thermal mechanical integrity, a high level of hermiticity [8,13] and excellent chemical resistance [13–15]. The requirements for such characteristics make the LTCC technology an excellent candidate for automotive applications [9,12]. However, due to high costs, LTCC applications are presently best suited to specific high-performance applications, such as military, space, biomedical and millimetre wave communication [12].

While the deposition of reactive multilayers on silicon substrates is well-established [16], it is somewhat more challenging to achieve deposition on LTCC substrates. The main hindrance is the intrinsic roughness of the LTCC substrate, the roughness of which ranges from 0.4 to 1 µm [17–19]. The reactive multilayer thin films are constructed from well-defined energetic materials that are heterogenous in their structure and contain stored chemical energy [20]. These multilayers have thin layers of reactants which alternate between layers of different metastable solids, each of which have a thickness in the range of 10–300 nm [21]. These alternating layers are typically combined up to a total thicknesses in the range of ~0.1–300 µm [20]. The layers are chosen based on their ability to make a reaction and to release heat, and the most straight-forward method for obtaining such a multilayer system is by using layer-by-layer magnetron-assisted deposition [22], however alternative approaches such as vacuum deposition and more cost-effective mechanical methods can also be used [23].

Should the reactants by sufficiently perturbed, e.g., through heat, then they begin to spontaneously intermix on the atomic level, as per Figure 1, where the reaction propagates from left to right, releasing heat in the process [24], and once the reaction is initiated, the subsequent heat release is sufficient such that the reaction continues to self-propagate [20]. Alternate methods for initiating the reaction include the means of using an electric spark or laser pulse [22], whereafter the reaction can also continue to self-propagate.

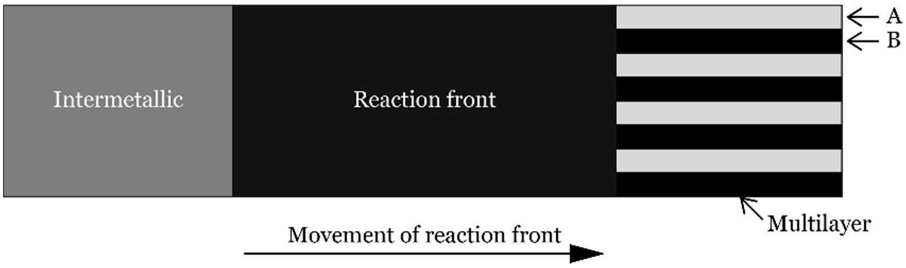

Figure 1. Schematic showing the progression of the reactive multilayer system (RMS).

A successful deposition of reactive multilayers on LTCC substrates has been reported [25]. Here, the LTCC substrates were covered by a brazeable silver system, whereafter an additional 5 µm SAC (Tin–Silver–Copper) solder was deposited to further adapt the rough LTCC substrate to the reactive nanolayer pile.

The intention is to deposit the reactive multilayer on a surface that is well-isolated electrically. In order to adapt the nanolayer pile to the rough surface of the LTCC substrate, a dielectric layer is printed on top, as per Figure 2, with a cross section of the reactive multilayer on an LTCC substrate being shown in Figure 3 complete with a GreenTape^{TM} DuPont (DP) 951 isolation layer. Figure 2 shows the formation required for a so-called tape-on-substrate (TOS) process [26], and furthermore, screen-printed dielectric paste is added to the fired substrate, which then requires a brief drying step and an additional 2 h sintering process.

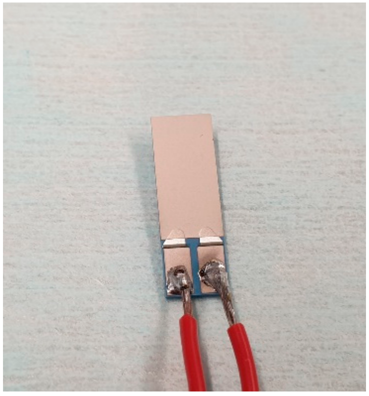

Figure 2. Deposition of dielectric layer on LTCC.

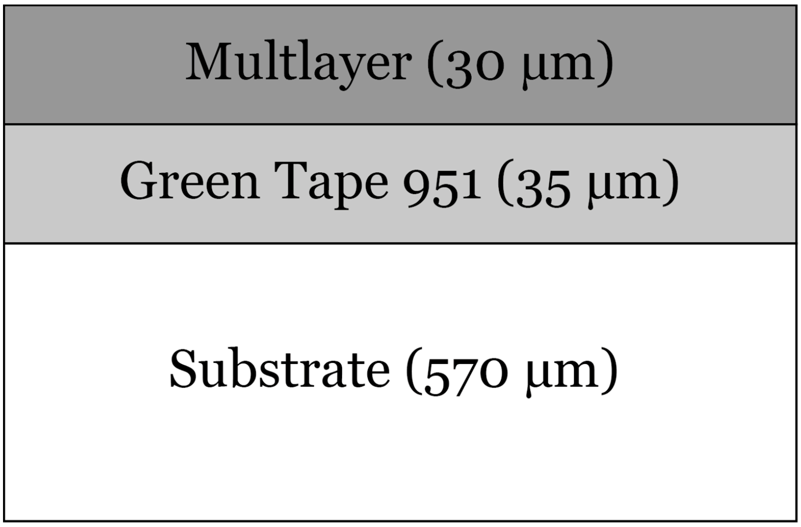

Figure 3. Schematic of reactive multilayer on LTCC substrate with DP 591 isolation layer.

Figure 4 shows a cross-section performed on one of these LTCC substrates with similar embedded temperature probe structures using light microscopy. Here, the reactive multilayer (RMS), the probe and the isolation layer (IL) between the probe and the reactive layer is clearly visible. One can observe from this cross section that each of these structures contains significant roughness, which is not captured in the model where each of the edges are taken to be orthogonal to their respective neighbours and completely straight.

In this work, CFD models are utilised which model and simulate the heat release of such a reactive foil for the purposes of bonding a chip to an LTCC substrate. The localised heat release causes the solder to melt, and thereafter, once the reaction has expired, the structures cool down. The purpose of the simulations is to determine the effect of adding solder layers upon reactive multilayer films and to offer guidelines as to how these would potentially be interpreted by temperature instrumentation in a similar laboratory environment. Comparisons are made between simulations with and without the presence of the solder above the reactive multilayer systems. The CFD models are based on a macroscopic approach and do not take things like surface roughness or pre-treatments to smooth out the layers into account. The simulations are designed towards a generic, hypothetical system as a proof of concept, with the goal of adapting them to experimental configurations for the purpose of comparison when they have been successfully manufactured.

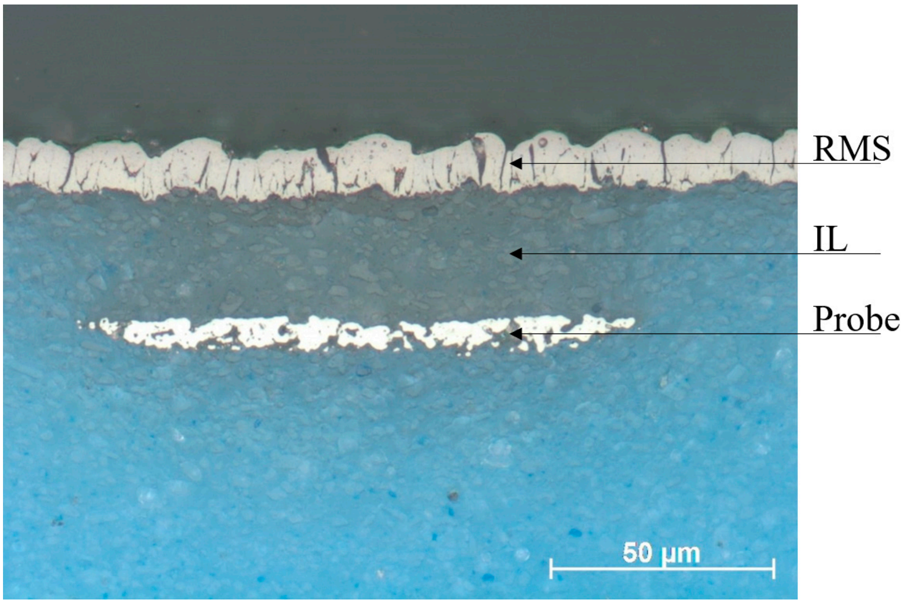

Figure 4. Cross section performed with light microscope.

2. Materials and Methods

There have been various methods used to model reactive multilayer foils that have been studied to enhance the understanding of the limits of their usability and functionality, but these are mainly concentrated on their operating states [27–29] as opposed to their respective performance during manufacture. Therefore, simulations targeting reactive bonding processes in microsystems and microelectronics packaging (such as [30–34]) are generally at an elementary stage compared to the average simulation methodology in the field. The approach used here is the CFD method, as similarly simulated in [35], where a 3-D shoebox model was created comprising various layers, namely a chip, solder, reactive multilayer, substrate and the surrounding air environment.

The extent of the boundaries surrounding the model, where the domain is 20 mm × 20 mm × 15 mm in size, a volume which was chosen to provide sufficient displacement of the external boundaries from the main region of interest whilst maintaining a reasonably sized mesh. The respective thicknesses of the layers were 400 µm for the Si chip, solder thickness of 200 µm, a total reactive foil thickness of 30 µm and an LTCC thickness of 570 µm.

The mesh was subdivided in a manner such that consistent mesh sizing with edge length of 10 µm could be prescribed in the y direction, with a mesh edge length of 100 µm in the x and z directions, as shown in Figure 5. The mesh comprised approximately 5,000,000 cells, representing a mesh significantly larger than that used in similar previous work [35]. The fixed mesh lengths of 100 and 10 µm ensured that the aspect ratio of the cells was within a reasonable range (10:1, for x and z:y), albeit the aspect ratios were slightly larger in the isolation layer, for example, where 4 cells span the 35 µm gap.

Three temperature probes, P1–P3, approximating Pt-100 temperature sensors with silver vias, were integrated into the model inside the LTCC substrate. In Figure 6, the main dimensions of each probe in the x–z plane and the layer thicknesses are shown.

Figure 5. Close-up of mesh of solid structures towards leading edge of reactive foil (Yellow = Si, Brown = Solder, Blue = reactive foil, Green = Green tape ceramics, Turquoise = Temperature probe).

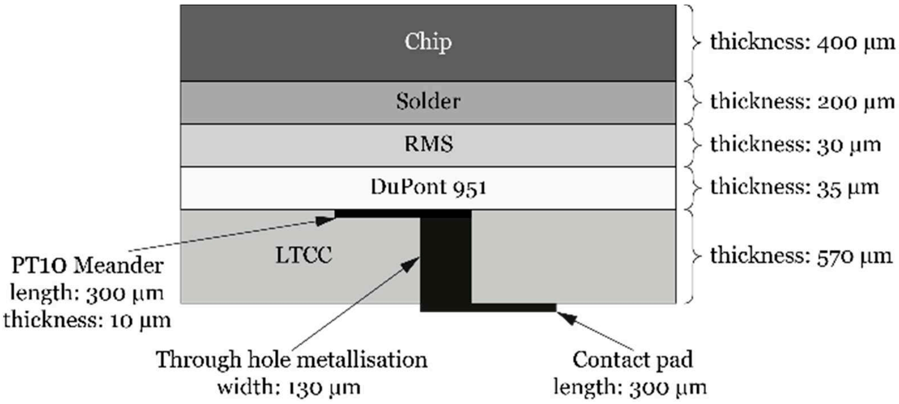

Figure 6. Dimensions of probes and layer thicknesses in x–z plane.

Similarly, in Figure 7, the main dimensions in the x–y plane are illustrated for the model and the 3 temperature probes, P1–P3, are also highlighted.

The sensing volume, i.e., the part for which volume-averaged temperatures were calculated, was 430 µm × 210 µm × 10 µm, corresponding to a sensing volume of 0.0009 mm^3. These probes are displaced from the next probe by 1 mm in the x direction, with the front edge of P1 displaced by 0.3 mm from the leading edge of the reactive multilayer. The top surface is 35 µm displaced below the reactive foil, meaning they are separated by the full thickness of the isolation layer.

Note that there was only one element through the thickness of the Pt probes, which is not ideal, but increasing the number of cells through the thickness of the probes would have a highly detrimental effect on the aspect ratio of the cells, and therefore the stability of the model. These probes were included to help in developing the understanding of the requirements for manufacturing similar prototypes, and furthermore, to understand the interference caused by the presence of the probes themselves.

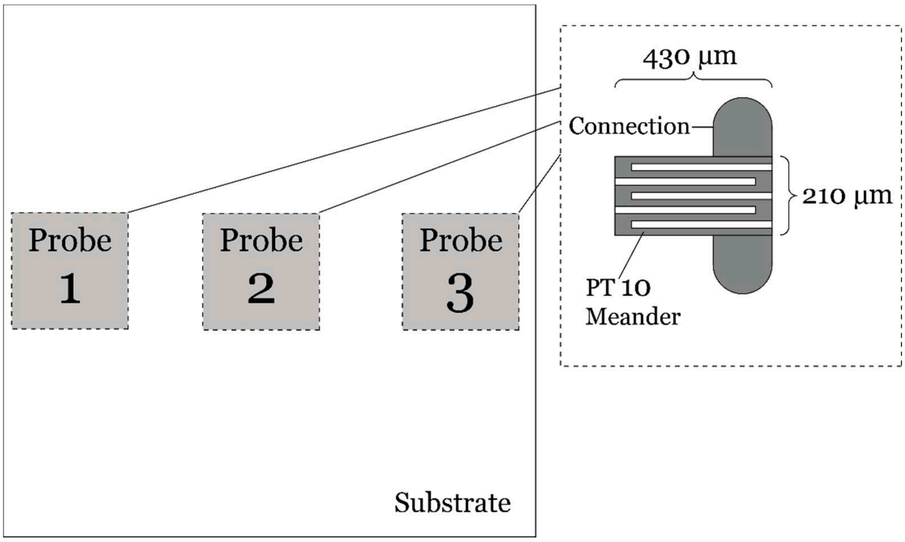

Figure 7. Detailed dimensions in x–y plane.

It is considered to be relatively straight-forward to measure the propagation velocity of reactive foils, due to the intense luminescence of the wave front. However, temperature measurements are more complicated owing to the interference caused by the presence of the thermocouples. The thermocouples are known to typically provide underestimated values of temperature due to their susceptibility to remove heat and interfere with the combustion process [22]. These simulations can offer some insight into the removal of heat, but the heat released will be unaffected by their presence.

The domain comprises both fluid and solid mesh structures, with the respective thermal properties shown in Table 1. These properties are drawn from the ANSYS Fluent material databases and the GreenTape$^{\text{TM}}$ DuPont DP 951 material data sheet. The silicon, reactive foil, ceramic, platinum and silver structures have solid states assigned, whereas the air and solder have fluid status and utilise fluid models in the ANSYS Fluent solver. The melting/solidification model is activated in ANSYS Fluent for the solder, in order that the transitions between the molten and solid behaviour, and the associated latent heat transfer throughout, are modelled. The pure solvent melting heat for the solder is 58.5 kJ/kg. A liquidus temperature of 217 °C and solidus temperature of 220 °C were used for the solder. These values correspond closely to typical thermal properties of a SAC solder.

The heat released by the reactive multilayer system was modelled in ANSYS Fluent through a heat source profile in the form of Equation (1). This heat source profile is a probability density function (PDF) propagating in the positive x direction, starting at the leading edge of the reactive multilayer. The reaction is assumed to initiate at time = 0 s and continually propagates as a function of time.

$$Ae^{B(x+C-Dt)^2} \tag{1}$$

The coefficient A corresponds to the amplitude of the reaction wave, 6×10^{12}, B the width of the PDF, -8×10^6, C is an offset to align with the leading edge, 2 mm in the x direction, and D is the velocity of the reaction. For the results presented here, a reaction speed, D, of 1 m/s has been modelled. The reaction speed is known to vary with respect to several factors, for example the ignition potential [21]. In [20], the general range of these multilayer reactions was quoted as being between 0.1 and 100 m/s, therefore a reaction speed of 1 m/s is comfortably within this range. The entire domain was initialised to a temperature of 300 K, in other words no preheating was used.

Table 1. Material properties for solid domains.

	Silicon	LTCC	Solder	Platinum	Silver
ρ kg/m^3	2500	3100	7000	21,460	10,490
Cp J/kg.K	710	600	230	132.04	234.28
K W/m.K	100	3.3	63.2	71.538	419.97

In ANSYS Fluent, the pressure-coupled transient solver is used in combination with the implicitly formulated Volume-of-Fluid (VOF) model complete with 2 Eulerian phases, namely air and solder. The 2-equation k-Ω SST model is used for turbulence modelling with the energy equation also solved numerically. The melting/solidification model, which makes use of the enthalpy–porosity approach [36], was used with a mushy zone parameter of 100,000. This method does not track the melt front explicitly but rather computes a liquid fraction, which indicates the fraction of the cell volume that is in the molten state, i.e., a liquid fraction of 1 corresponds to molten solder, whereas 0 is solder in the solid state.

An inlet boundary condition was specified on the y-max boundary with a velocity of 0.1 m/s, with a corresponding outlet pressure boundary condition at 0 Pa (gauge pressure) on the opposing y min extremity. The turbulence intensity and viscosity ratios were specified to be the same, 0.1% and 10, on each boundary. These boundaries enabled the domain to have incoming and outgoing air, and this was found to be beneficial from a stability standpoint. Given that this crossflow inlet velocity was low, it was considered that artificial crossflow cooling effects would be negligible.

The PISO pressure–velocity coupling method was used with 2nd-order upwind schemes for spatial discretisation. Likewise, for the transient formulation, 2nd-order schemes were used, only this time they were bounded implicit schemes. Furthermore, in order to capture the effects of buoyancy caused by temperature gradients in the air, the Boussinesq approximation was used with a constant thermal expansion coefficient of 0.0034/K.

The time-step size used was 10^{-6} s for 10,000 time steps. Convergence for each conservation equation was achieved for every time step, typically within 100 iterations for the initial time steps, with convergence occurring after just one time step later in the solution process. The temperatures at various probe locations were written out for every time step, with the larger solution files containing field data for the entire domain written out every 100 time steps.

3. Results

The results are presented in two subsections, one for simulations conducted with the presence of a thick layer of solder and a chip above the deposited multilayer on the LTCC, corresponding to Section 3.1, and simulations without the presence of the solder and chip above the reactive multilayer, Section 3.2. These results are first presented individually and then compared more directly in the Section 4.

3.1. Thermal Simulation Results with Solder and Silicon Included

In Figure 8, the temperature contours, for the case with solder and silicon included in the model, are shown 1 ms after the initiation of the reactive foil at the leading edge. The crest of the reaction wave was seen to have propagated approximately 1 mm from the leading edge from time = 0 s, hence corresponding to the prescribed reaction velocity of 1 m/s.

In Figure 9, the temperature contours are shown after 3 ms. The reaction is continuing its propagation from left to right, and approximately half of the silicon has a temperature over 100 °C. The heat release is seen to penetrate relatively well in the positive z-direction, in other words in the direction of the solder from the reactive multilayer, and much less so in the negative z direction. This is due to the relative disparities in the thermal conductivities and the solder acting as a much better heat sink.

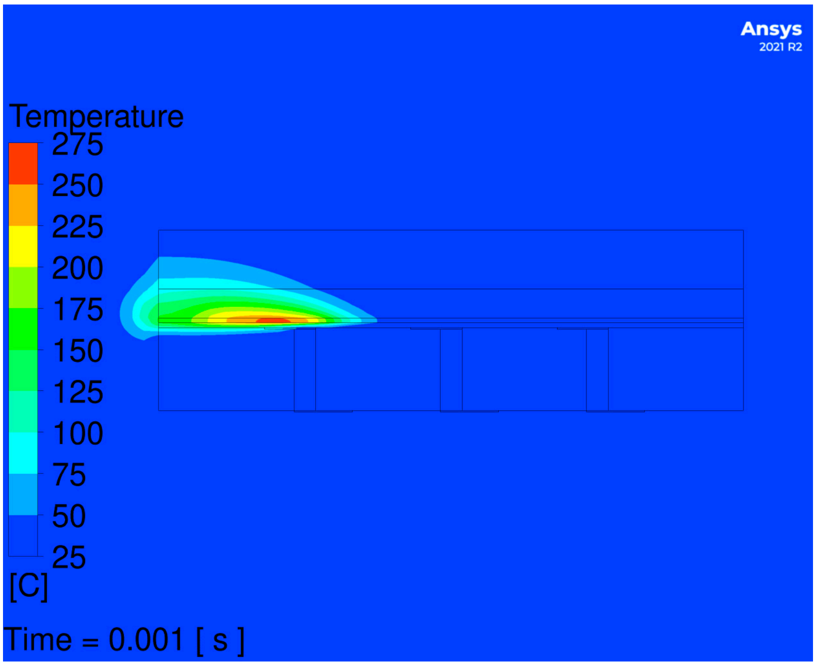

Figure 8. Temperature contours after 1 ms.

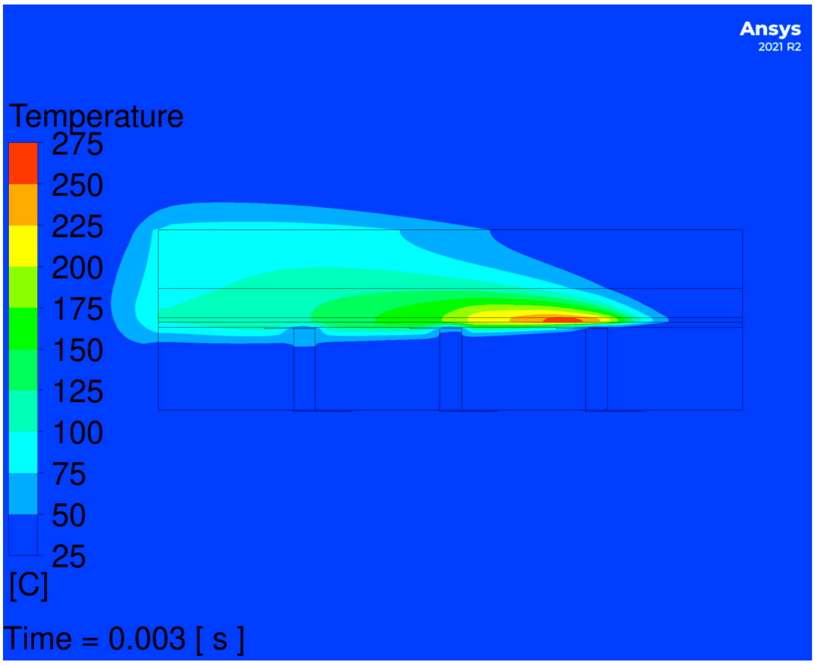

Figure 9. Temperature contours after 3 ms.

Figure 10 shows the liquid fraction contours in the solder region after 3 ms. Here, one can see that there is a small bubble of molten solder adjacent to where, with reference back to Figure 9, the main reaction wave crest is present. Upstream of this bubble of molten solder, one can observe that the solder resolidifies as the wave passes and the structures begin to cool down again. Only a small percentage of the solder is melted in this case as the solder used in this model is very thick.

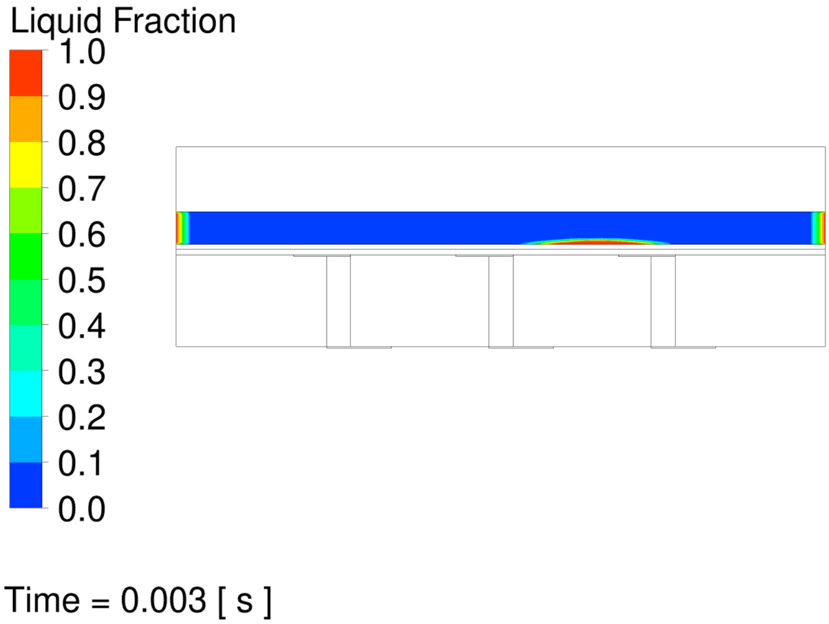

Figure 10. Contours of liquid fraction after 3 ms.

Figure 11 shows the temperature contours at 4 ms, corresponding approximately to the time of reaction exhaustion. By this stage, almost all of the silicon has reached over 100 °C, but the LTCC still has a large percentage of its structure holding on to its initial temperature of 27 °C (300 K).

In Figure 12, the temperature contours are shown 10 ms after reaction initiation, which corresponds to the final time step solved for in the model, time step 10,000. By this point, the reaction wave has long since passed and the backside of the LTCC is still largely unaffected. There is by this point a significant amount of heat which is conducted down through the silver vias, and by this point it is clear that there is some disturbance around the sensing volumes of the probes caused by the presence of these structures. It seems as though the vias act somewhat as a heat sink for the probes, but interpreting results through the thickness of the probes should be exercised with caution here, given that there is only one element through the probe thickness.

In Figure 13 the time–temperature histories of the three probe locations, P1–P3, are shown. Three clear peaks are observed in each of the temperature probes, and by measuring the time offset between these three peaks one would be able to 'sense' the propagation of the reaction at this isolation depth of 35 µm within the LTCC substrate. Based on these simulations, temperature probes manufactured to this specification should be capable of measuring a reaction, at least in the 1 m/s range, assuming that the sampling frequency and frequency response of the temperature measuring equipment was of sufficient specification.

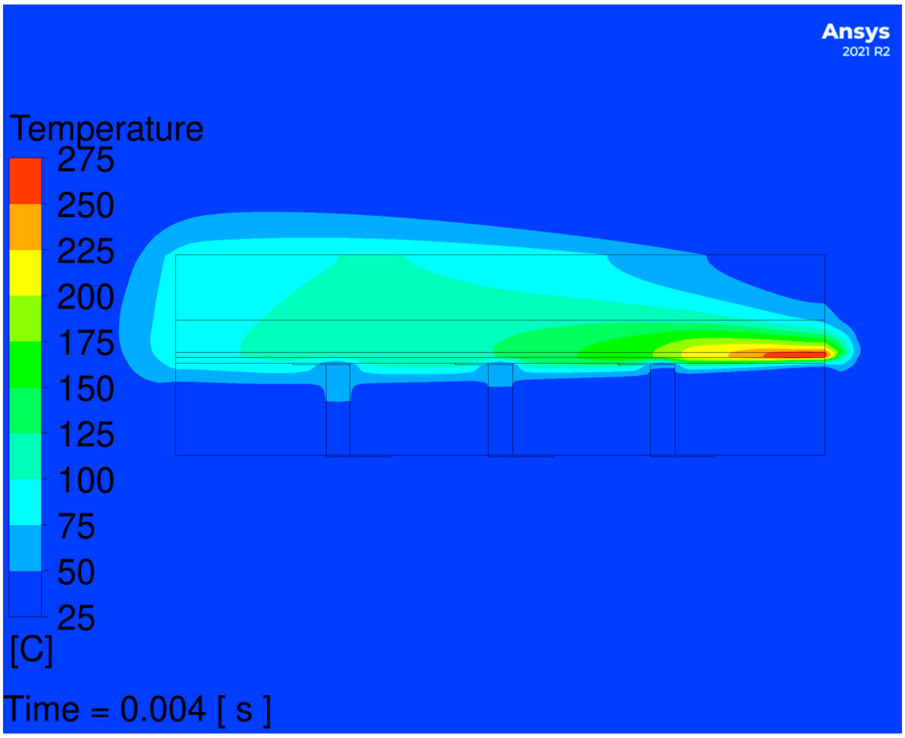

Figure 11. Temperature contours after 4 ms.

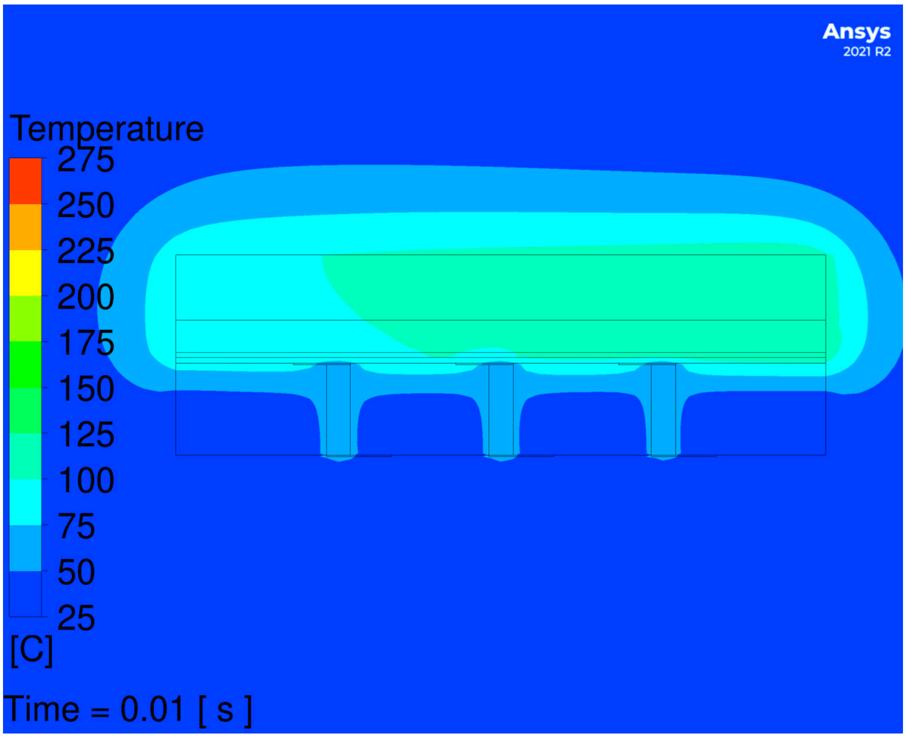

Figure 12. Temperature contours after 10 ms.

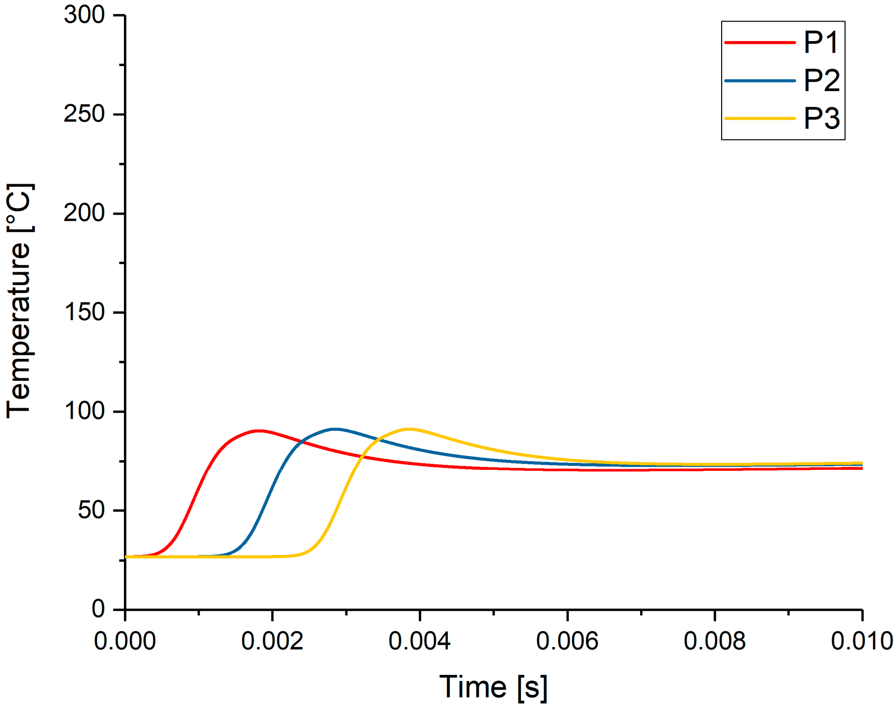

Figure 13. Time–temperature history for the three temperature probes, P1–P3, with solder and silicon included in the model.

3.2. Thermal Simulation Results without Solder and Silicon

Simulations were also performed on an almost identical model as those in Section 3.1, only the solder and silicon were removed and replaced directly with air. No solder was therefore included in these simulations and therefore the melting/solidification model parameters were not required to be solved for numerically.

Figure 14 shows the temperature contours for a reactive foil with the exact same heat release UDF equation as in Section 3.1 after 3 ms. The results are qualitatively very similar to that of Figure 9 but the temperatures are significantly higher, owing to the absence of the solder acting as a heat sink for the exothermic heat release. The peak temperatures for this particular heat-release profile reach a temperature of approximately 800 °C.

Figure 15 again shows the temperature contours post exhaustion, for 10 ms after the initiation of the reaction. Here, again the contours are qualitatively similar to the counterpart including solder and silicon of Figure 12, but the temperatures are quantitatively much higher.

Figure 16 shows the time–temperature history of the three temperature probes embedded in the LTCC, P1–P3. The peaks are similar to those in Figure 13, but the first peak is slightly lower in magnitude than the peaks for the P2 and P3 probes because there is more thermal inertia and less spreading of the heat without the heat sink of the solder.

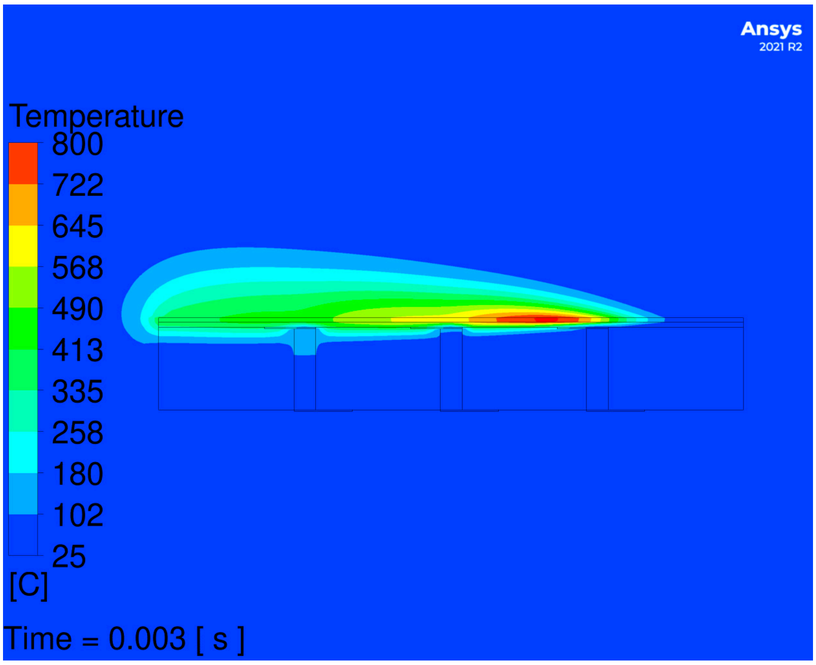

Figure 14. Temperature contours after 3 ms, without solder and silicon.

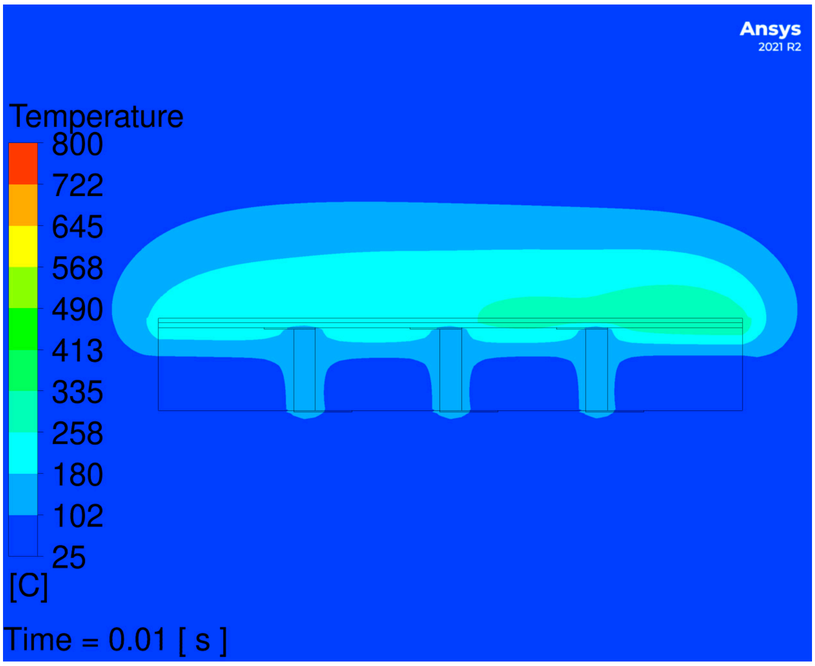

Figure 15. Temperature contours after 10 ms, without solder and silicon.

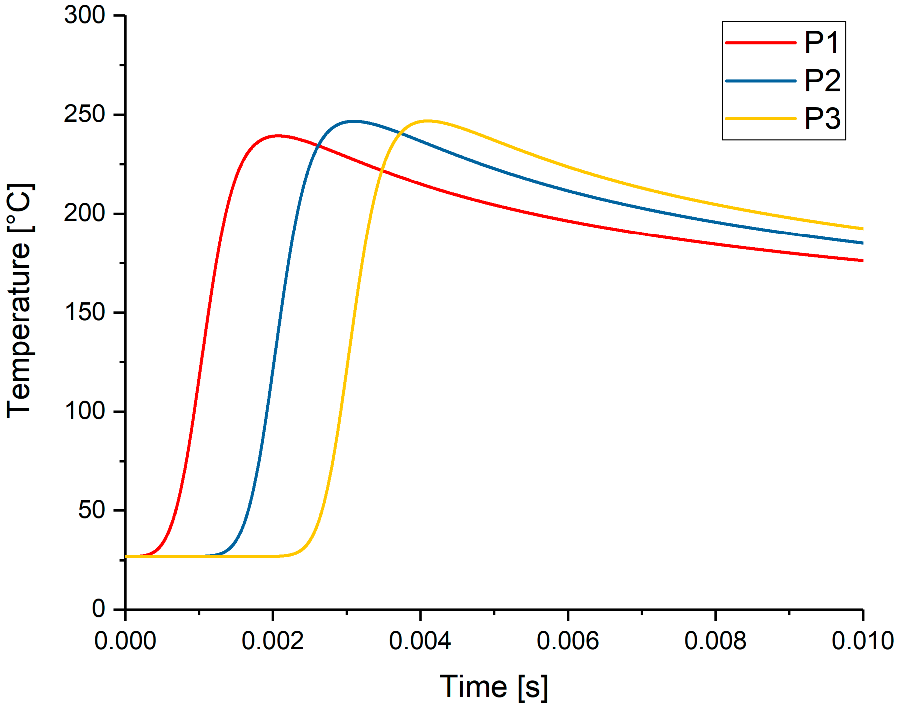

Figure 16. Time–temperature history for the three temperature probes, P1–P3, without solder and silicon.

4. Discussion

In order to make some more detailed comparisons between the two cases discussed, more temperature probes were realised from the models directly above the P2 probes, in the centre of the reactive multilayer system (rms) and the solder, where it exists.

Figure 17 shows the time–temperature progression at each of these locations with the solder and silicon included in the model, whereas Figure 18 shows the time–temperature traces without the solder and silicon. In ANSYS Fluent, vertex-averaged temperatures were used for T_{rms} and T_{solder} and comparing the two figures it is clear that the peak temperatures were much higher without the solder and silicon.

From Figure 17 it is also fair to assume that the heat released from the reactive multilayer propagates far easier in the +z -direction than in the -z direction, in other words, the solder acts to spread the heat much more effectively than the LTCC does.

It is important to note that in a real-world environment the temperature probes would not merely be present in a passive mode but rather they would have current passing through them, resulting in a preheating due to their electrical resistivity, resulting in localised heating, and potentially, further interfering in the reaction process.

In both cases, p_2 is significantly lower than T_{rms}, which is particularly attributable to the presence of the isolation layer between the probe and the reactive multilayer. Nevertheless, probes built to these specifications have been shown to be feasible at this depth.

One thing of particular note in Figure 17 is that during cooldown, kinks in the p_2 and T_{rms} curves are witnessed, due to the latent heat of the solder between the liquidus and solidus temperatures of 220 and 217 °C, but this information is not sensed by the P2 temperature probe. This could be significant in a real-world scenario because the reaction speed may be affected clearly by the presence of the surrounding solder, but also by the effect of the latent heat.

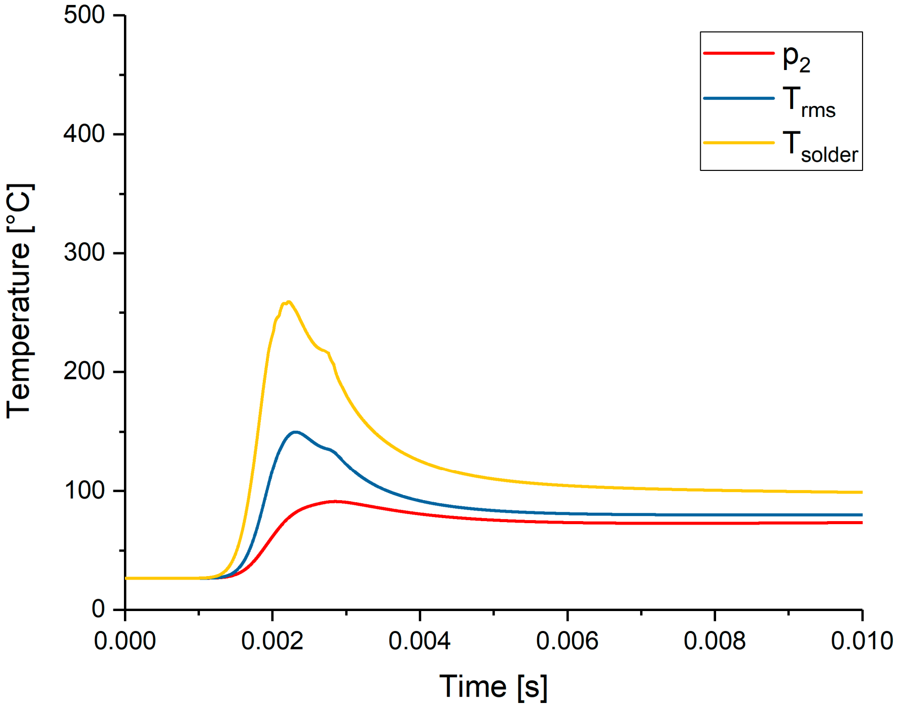

Figure 17. Time–temperature history for three locations, the probe p_2, T_{rms} and T_{solder}.

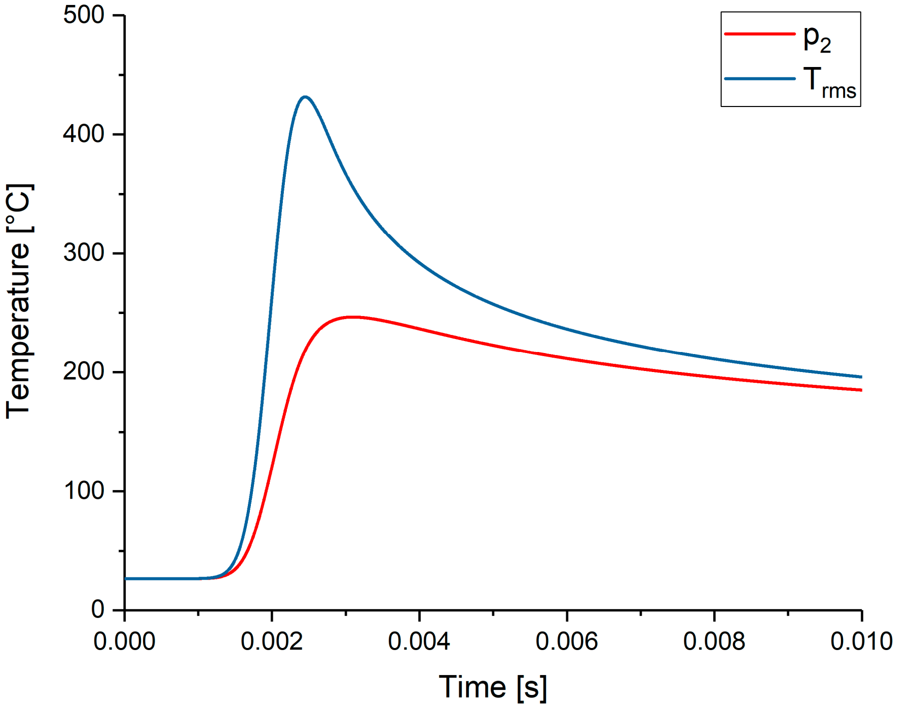

Figure 18. Time–temperature history for p_2 and T_{rms}, without solder and silicon.

5. Conclusions

Thermal CFD simulations have been conducted to simulate the temperature profile of the bonding zone during and after the reaction of the rms. The goal was to estimate theoretically the potential of reactive multilayer systems to create sufficient local heat for joining processes between silicon chips and ceramic substrates. Two different configurations have been considered. The first configuration consists of a silicon chip that is bonded to an LTCC-substrate using a bonding layer that contains a rms and a solder preform, while the second configuration consisted only of the LTCC-substrate and the rms. The simulations are capable of resolving a reaction wave propagating at 1 m/s.

Significant temperature differences were found between the two cases studied here in that the temperatures in the reactive multilayer were much higher for the system without the solder and silicon. The presence of the solder would likely have a significant influence on the real propagation of the reaction through causing greater suppression of the reaction wave. The solder dimensions chosen were extremely thick in order to possess high mesh resolution throughout its thickness and to exaggerate its influence, so the difference between the two configurations may be somewhat exaggerated here.

The enthalpy–porosity method used by the melting/solidification model in ANSYS Fluent allows for incorporation of the effects of latent heat when solving the energy equation, and the encapsulation of this behaviour is something that is not readily available using alternative simulation approaches for an analysis of the solder behaviour during bonding. This means that CFD and these models could offer a leading simulation approach when it comes to assessing the thermal behaviour of reactive foils during bonding. For example, the heat release could potentially be used to determine the total number of layers required to form a functioning solder joint between components. This would effectively offer a crucial insight into manufacturing requirements. Furthermore, a whole new world of multiphysics simulations could be opened by using the temperature fields as inputs to achieve reasonable estimations of stresses induced during a bonding process, and to ultimately determine probable reliability characteristics from these assessments.

Author Contributions: Conceptualization, A.Y., J.M. and S.W.; methodology, A.Y. and A.S.; investigation, A.Y., A.S. and E.W.; supervision, J.M. and S.W.; writing, A.Y.; review and editing, S.W.; funding acquisition, J.M. and S.W. All authors have read and agreed to the published version of the manuscript.

Funding: This research work was supported by funding from the Deutsche Forschungsgemeinschaft (DFG, German Research Foundation)—Project-ID 426204742. The DFG is the German Research Foundation and is a funding institution which promotes science and research in the Federal Republic of Germany.

Acknowledgments: The authors would like to offer particular thanks to Andreas Ruh for his help in preparing cross-sections and for his support in editing the drawings.

Conflicts of Interest: The authors declare no conflict of interest.

References

1. Seok, S.; Kim, J.; Lahti, M. A Study on the Effect of Wire Bonding Interconnects of BCB Capped CPW to CPW on LTCC Substrate. *Microw. Opt. Technol. Lett.* **2014**, *56*, 1378–1381. [CrossRef]
2. Uhlig, P. LTCC Technology for Planar Microwave Antenna Systems. Ph.D. Thesis, Universität Duisburg-Essen and Dresden, Dresden, Germany, 2018.
3. Wilde, J. B4. 1-Trends in Assembly and Packaging of Sensors. *Proc. Sens.* **2009**, *I*, 205–210.
4. Lee, C.K.; Ahn, J.K.; Lee, C.R.; Kim, D.; Baek, B.J. Thermal Analysis of LED Lamp with LTCC-COB Package. *Microelectron. Int.* **2013**, *30*, 3–9.
5. Welker, T. *Methoden Und Technologien Zur Optimierung Der Entwärmung Aktiver Und Passiver Komponenten Auf Keramischen Mehrlagensubstraten*; TU Ilmenau Universitätsbibliothek: Ilmenau, Germany, 2018.
6. Uhlig, P.; Günner, C.; Holzwarth, S.; Kassner, J.; Kulke, R.; Lauer, A.; Rittweger, M. LTCC Short Range Radar Sensor for Automotive Applications at 24 GHz. In Proceedings of the IMAPS 2004—37th Annual Symposium on Microelectronics, Long Beach, CA, USA, 14–18 November 2004; pp. 1–5.

7. Wörhoff, K.; Prak, A.; Postma, F.; Leinse, A.; Wu, K.; Peters, T.J.; Tichem, M.; Amaning-Appiah, B.; Renukappa, V.; Vollrath, G. Photonic Hybrid Assembly through Flexible Waveguides. In Proceedings of the Silicon Photonics and Photonic Integrated Circuits V, International Society for Optics and Photonics, Brussels, Belgium, 3–7 April 2016; Volume 9891, p. 98911P.
8. De Torres, H.B.; Rensch, C.; Fischer, M.; Schober, A.; Hoffmann, M.; Müller, J. Thick Film Flow Sensor for Biological Microsystems. *Sens. Actuators Phys.* **2010**, *160*, 109–115. [CrossRef]
9. Fournier, Y.; Maeder, T.; Boutinard-Rouelle, G.; Barras, A.; Craquelin, N.; Ryser, P. Integrated LTCC Pressure/Flow/Temperature Multisensor for Compressed Air Diagnostics. *Sensors* **2010**, *10*, 11156–11173. [CrossRef] [PubMed]
10. Johannessen, E.; Krushinitskaya, O.; Sokolov, A.; Häfliger, P.; Hoogerwerf, A.; Hinderling, C.; Kautio, K.; Lenkkeri, J.; Strömmer, E.; Kondratyev, V. Toward an Injectable Continuous Osmotic Glucose Sensor. *J. Diabetes Sci. Technol.* **2010**, *4*, 882–892. [CrossRef] [PubMed]
11. Ciosek, P.; Zawadzki, K.; Lopacińska, J.; Skolimowski, M.; Bembnowicz, P.; Golonka, L.J.; Brzózka, Z.; Wróblewski, W. Monitoring of Cell Cultures with LTCC Microelectrode Array. *Anal. Bioanal. Chem.* **2009**, *393*, 2029–2038. [CrossRef]
12. Golonka, L.; Bembnowicz, P.; Jurkow, D.; Malecha, K.; Roguszczak, H.; Tadaszak, R. Low Temperature Co-Fired Ceramics (LTCC) Microsystems. *Opt. Appl.* **2011**, *41*, 383–388.
13. Fournier, Y. *3D Structuration Techniques of LTCC for Microsystems Applications*; EPFL: Lausanne, Switzerland, 2010.
14. Bittner, A.; Schmid, U. The Porosification of Fired LTCC Substrates by Applying a Wet Chemical Etching Procedure. *J. Eur. Ceram. Soc.* **2009**, *29*, 99–104. [CrossRef]
15. Thelemann, T.; Fischer, M.; Groß, A.; Müller, J. LTCC-Based Fluidic Components for Chemical Applications. *J. Microelectron. Electron. Packag.* **2007**, *4*, 167–172. [CrossRef]
16. Adams, D.P. Reactive Multilayers Fabricated by Vapor Deposition: A Critical Review. *Thin Solid Films* **2015**, *576*, 98–128. [CrossRef]
17. Sen, S.; Lake, M.; Kroppen, N.; Farber, P.; Wilden, J.; Schaaf, P. Self-Propagating Exothermic Reaction Analysis in Ti/Al Reactive Films Using Experiments and Computational Fluid Dynamics Simulation. *Appl. Surf. Sci.* **2017**, *396*, 1490–1498. [CrossRef]
18. Rogachev, A.S.; Mukasyan, A.S. Combustion of Heterogeneous Nanostructural Systems. *Combust. Explos. Shock Waves* **2010**, *46*, 243–266. [CrossRef]
19. Rogachev, A.S. Exothermic Reaction Waves in Multilayer Nanofilms. *Russ. Chem. Rev.* **2008**, *77*, 21. [CrossRef]
20. Raić, K.; Rudolf, R.; Ternik, P.; Žunič, Z.; Lazić, V.; Stamenković, D.; Tanasković, T.; Anžel, I. CFD Analysis of Exothermic Reactions in Al-Au Nano Multi-Layered Foils. *Mater. Tehnol.* **2011**, *45*, 335–338.
21. Braeuer, J.; Besser, J.; Wiemer, M.; Gessner, T. A Novel Technique for MEMS Packaging: Reactive Bonding with Integrated Material Systems. *Sens. Actuators Phys.* **2012**, *188*, 212–219. [CrossRef]
22. Bittner, A.; Ababneh, A.; Seidel, H.; Schmid, U. Influence of the Crystal Orientation on the Electrical Properties of AlN Thin Films on LTCC Substrates. *Appl. Surf. Sci.* **2010**, *257*, 1088–1091. [CrossRef]
23. Jantunen, H.; Kangasvieri, T.; Vähäkangas, J.; Leppävuori, S. Design Aspects of Microwave Components with LTCC Technique. *J. Eur. Ceram. Soc.* **2003**, *23*, 2541–2548. [CrossRef]
24. Matters-Kammerer, M.; Mackens, U.; Reimann, K.; Pietig, R.; Hennings, D.; Schreinemacher, B.; Mauczok, R.; Gruhlke, S.; Martiny, C. Material Properties and RF Applications of High k and Ferrite LTCC Ceramics. *Microelectron. Reliab.* **2006**, *46*, 134–143. [CrossRef]
25. Grieseler, R.; Welker, T.; Müller, J.; Schaaf, P. Bonding of Low Temperature Co-Fired Ceramics to Copper and to Ceramic Blocks by Reactive Aluminum/Nickel Multilayers. *Phys. Status Solidi A* **2012**, *209*, 512–518. [CrossRef]
26. Patterson, F.K.; Gantzhorn, J.E.; Daly, T.P.; Rellick, J.R.; Iwabuchi, M.; Kawasaki, S. Tape on Substrate, a New Systems Approach for Manufacturing Multilayer Hybrid Circuits. In Proceedings of the Japan IEMT Symposium, Sixth IEEE/CHMT International Electronic Manufacturing Technology Symposium, Nara, Japan, 26–28 April 1989; pp. 147–151.
27. Liu, S.; Liu, Y. *Modeling and Simulation for Microelectronic Packaging Assembly: Manufacturing, Reliability and Testing*; John Wiley & Sons: Hoboken, NJ, USA, 2011.
28. Madenci, E.; Guven, I. *The Finite Element Method and Applications in Engineering Using ANSYS®*; Springer: Berlin/Heidelberg, Germany, 2015.
29. Rzepka, S. FEM Für Die Mikroelektronik: Erfordernis, Theorie Und Anwendung Der Finiten Element-Methode Bei Der Belastungs-, Schwachstellen-Und Ausfallanalyse Mikroelektronischer Aufbauten Sven Rzepka. Ph.D. Thesis, Universität Duisburg-Essen and Dresden, Dresden, Germany, 2003.
30. Qiu, X. Reactive Multilayer Foils and Their Applications in Joining. Master's Thesis, Louisiana State University, Baton Rouge, LA, USA, 2007.
31. Subramanian, J.S.; Rodgers, P.; Newson, J.; Rude, T.; He, Z.; Besnoin, E.; Weihs, T.P.; Eveloy, V.; Pecht, M. Room Temperature Soldering of Microelectronic Components for Enhanced Thermal Performance. In Proceedings of the Thermal, Mechanical and Multi-Physics Simulation and Experiments in Micro-Electronics and Micro-Systems, Berlin, Germany, 18–20 April 2005; pp. 681–686.
32. Masser, R.; Braeuer, J.; Gessner, T. Modelling the Reaction Behavior in Reactive Multilayer Systems on Substrates Used for Wafer Bonding. *J. Appl. Phys.* **2014**, *115*, 244311. [CrossRef]
33. Wang, J.; Besnoin, E.; Duckham, A.; Spey, S.J.; Reiss, M.E.; Knio, O.M.; Powers, M.; Whitener, M.; Weihs, T.P. Room-Temperature Soldering with Nanostructured Foils. *Appl. Phys. Lett.* **2003**, *83*, 3987–3989. [CrossRef]

34. Amini-Manesh, N.; Basu, S.; Kumar, R. Modeling of a Reacting Nanofilm on a Composite Substrate. *Energy* **2011**, *36*, 1688–1697. [CrossRef]
35. Yuile, A.; Wiese, S. CFD Simulations of Reactive Multi-Layer Usage in Joining Processes. In Proceedings of the 2020 21st International Conference on Thermal, Mechanical and Multi-Physics Simulation and Experiments in Microelectronics and Microsystems (EuroSimE), Cracow, Poland, 5–8 July 2020; pp. 1–5.
36. Voller, V.R.; Brent, A.D.; Prakash, C. The Modelling of Heat, Mass and Solute Transport in Solidification Systems. *Int. J. Heat Mass Transf.* **1989**, *32*, 1719–1731. [CrossRef]

5.3 Paper 3: Application of Reactive Bonding Methods on LTCC Substrates

5.3.1 Veröffentlichungshinweise

Erik Wiss[1], Alexander Schulz[2], Adam Yuile[1], Jens Müller[2], Steffen Wiese[1]

[1]Chair of Microintegration and Reliability, Faculty of Natural Sciences and Technology, Saarland University, Saarbrücken, Germany

[2]Electronics Technology Group, Faculty of Electrical Engineering and Information Technology, TU Ilmenau, Ilmenau, Germany

2023 24th European Microelectronics and Packaging Conference & Exhibition (EMPC)

Die Originalveröffentlichung ist abrufbar unter:
https://doi.org/10.23919/EMPC55870.2023.10418406

5.3.2 Synopse

Diese Veröffentlichung untersucht erste Zündversuche von abgeschiedenen RMS auf LTCC-Substraten mit unterschiedlichen Oberflächenbehandlungen sowie die resultierende Temperaturverteilung verschiedener Konfigurationen innerhalb der einzelnen Schichten über CFD-Simulationen. Die Motivation ergibt sich aus der Notwendigkeit, die Zündfähigkeit der abgeschiedenen Schichten zu überprüfen und ein detailliertes Verständnis der thermischen Ausbreitung während der Reaktion er erlangen. Ziel der Arbeit war es, die grundsätzliche Eignung des reaktiven Fügens auf LTCC-Substraten zu evaluieren.

Hierzu wurden RMS auf LTCC-Substrate mit verschiedenen Oberflächenbehandlungen abgeschieden und elektrisch gezündet. Als Referenz diente ein unbehandeltes LTCC-Substrat, weitere Varianten umfassten Proben nach chemisch-mechanischer Politur sowie nach Laserbearbeitung mit und ohne zusätzliche Pd/Ag-Metallisierung. Die maximale Temperatur der Reaktion wurde mit einem Pyrometer, und die mittlere Geschwindigkeit der Reaktion mit einer Hochgeschwindigkeitskamera erfasst. Ergänzend wurden Simulationen durchgeführt, um die Temperaturverteilung sowohl entlang der Reaktionsausbreitungsrichtung als auch senkrecht durch den Schichtstapel zu analysieren. Das verwendete dreidimensionale CFD-Modell mit einer Gesamtgröße von 10 mm x 10 mm x 5 mm enthält einen Stapel der Größe 4 mm x 4 mm x 1,490 mm aus LTCC-Substrat (825 µm), Isolationsschicht (35 µm), RMS (30 µm), Lot (200 µm) und Si-Chip (400 µm). Die Wärmefreisetzung wurde durch eine sich mit 1 m/s ausbreitende Wahrscheinlichkeitsdichtefunktion mit verschiedenen Parametern modelliert.

Die Ergebnisse zeigen, dass es bei unbehandelten und chemisch-mechanisch polierten Substraten zu Ablösungen des RMS kommt, während es bei laserbearbeiteten Proben zu einer punktuellen Haftung kommt. Das chemisch-mechanische Polieren hatte kaum Einfluss auf Temperatur und Reaktionsgeschwindigkeit, wohingegen die Laserbearbeitung zu einer signifikanten Reduktion beider Größen führte. Die Simulationen zeigen eine in der Höhe nahezu identische, zeitlich versetzte Reaktion der horizontal angeordneten Temperatursensoren, während die Temperatur in vertikaler Richtung schnell stark abfällt.

Im Kontext des Gesamtprojekts leistet diese Veröffentlichung einen Beitrag zur Beantwortung der Frage nach dem Verhalten eines RMS auf keramischen Substraten sowie zur Charakterisierung der entstehenden Temperaturverteilung während des Fügevorgangs.

5.3.3 Vollständiger Artikel

Application of Reactive Bonding Methods on LTCC Substrates

Erik Wiss
Chair of Microintegration and Reliability
Saarland University
Saarbruecken, Germany
erik.wiss@uni-saarland.de

Alexander Schulz
Electronics Technology Group
TU Ilmenau
Ilmenau, Germany
alexander.schulz@tu-ilmenau.de

Adam Yuile
Chair of Microintegration and Reliability
Saarland University
Saarbruecken, Germany
adam.yuile@uni-saarland.de

Jens Müller
Electronics Technology Group
TU Ilmenau
Ilmenau, Germany
jens.mueller@tu-ilmenau.de

Steffen Wiese
Chair of Microintegration and Reliability
Saarland University
Saarbruecken, Germany
s.wiese@mx.uni-saarland.de

***Abstract* – This paper discusses the application of reactive bonding for the area of Low Temperature Cofired Ceramics (LTCC) assemblies. The goal is to reduce the thermal-mechanical stresses during soldering by transferring heat only locally to the solder joints without heating the entire component. Such a reactive multilayer system (RMS) consists of alternating nanolayers (10 - 300 nm) of at least two metal components which produce an exothermal reaction after ignition. Although the deposition of an RMS is established on silicon substrates for the use in micro-electromechanical systems (MEMS), it is very challenging to create them on LTCC substrates. One of the main obstacles is to overcome all issues connected with the significant roughness, because it is not an optimum territory to deposit nanolayers. In this paper, different methods like chemical mechanical polishing (CMP) and laser ablation, to modify the surface morphology, are presented. A direct relation between the morphology and the exothermal reaction can be observed. In addition, 3-D Computational Fluid Dynamics (CFD) simulations were conducted to analyze the process in more detail. These simulations make use of a shoebox model with different layers and an adjustable user-defined function for the heat release of the RMS to adapt the reaction front velocity and the combustion temperature to the experimental values.**

Keywords – LTCC, RMS, reactive multilayer systems, Al-Ni, joining.

I. INTRODUCTION

The chemical reaction of nitrogen monoxide (NO) with ozone leads not only to the formation of nitrogen dioxide and oxygen, but also to the emission of radiation in the wavelength range between 600 to 2600 nm with a maximum in the infrared area at 1200 nm [1]. Measuring this radiation can be used to determine low concentrations of NO in gas flows. Therefore, a measurement device was developed and presented in [2]-[4] using LTCC (Low Temperature Cofired Ceramics) technology (see Fig. 1). It consists of three different modules: first, there is an ozone generator with a high voltage source, that is applied to a gas flow using embedded electrodes. Then, the ozone is transported via microfluidic channels to a chemiluminescence detection reaction chamber where it is mixed with the gas that contains an unknown amount of NO. An infrared transparent window is bonded onto the LTCC substrate, and a photo diode that measures the emitted radiation is placed on it. The last module is an exhaust gas treatment to decompose the ozone into nonhazardous oxide. Therefore, a heating structure was embedded in the LTCC substrate and a platinum paste, that can be applied to the substrate, was used as a catalysator.

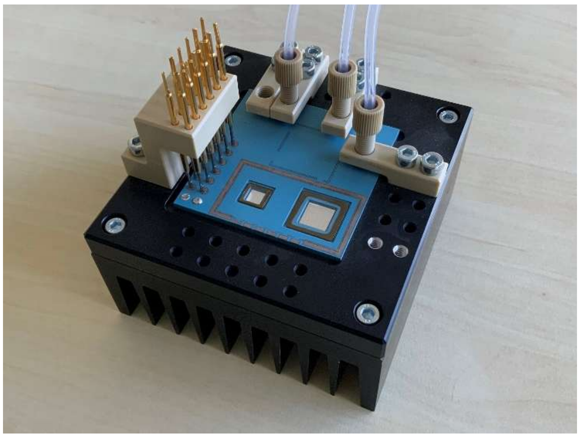

Fig. 1. Measurement device for low concentrations of nitrogen monoxide in gas flows, realized using LTCC technology.

The LTCC technology is an excellent candidate for such devices because it enables the possibility of three-dimensional structuring [5]-[7] and shows very good hermetic sealing properties [8], [9]. Additionally, it provides not only excellent robustness under harsh environmental and mechanical conditions [10], [11], but also chemical resistance [9]-[13]. Due to this properties, LTCC technology can even be used in automotive and aerospace. It is also possible to add passive elements using conventional surface mounting technology like reflow soldering. Therefore, both the component and the substrate need to be heated up to a temperature above the melting point of the used solder, which can be critical for heat sensitive components. Adding heat locally to the solder joints can be an option to avoid damages during this process e.g., through using a reactive multilayer system (RMS). While the use of an RMS is well established on silicon substrates [14], it is very challenging to deposit such a system on LTCC substrates due to their high roughness in the range of 0.4 to 1 µm [15]-[17].

An RMS consists of at least two different materials that are applied on a substrate in an alternating way e.g., through magnetron sputtering [10]. The thickness of every single layer is in the range of 10 to 300 nm [19] and the total stack thickness varies in the range of 0.1 to 300 µm [20]. After the system is ignited (e.g., by providing sufficient heat, by using an electrical spark or by using a laser pulse) the materials begin to intermix on atomic level building a new intermetallic phase. This leads to a self-propagating reaction [21] that is profoundly exothermal [22]. The released heat of this process can be used for joining processes by melting an additional solder layer, among other things. The propagation speed will depend on the materials used, the bilayer thicknesses, the ratio of the materials, the total stack thickness and the amount of heat released. However, the mechanical pre-processing of the substrates also has an influence on the speed of the reaction, what should be discussed here.

II. SAMPLE PREPARATION

A. Reference sample and laser ablation

As described in [23] the samples were prepared in different ways. For the reference samples, and the samples that were modified by laser ablation, a standard LTCC technology was processed using 6-layer DuPont 951 P2 resulting in a thickness of 817 nm ± 2.5 nm. Without further processing a roughness of 390 nm ± 16.6 nm was reached for the reference samples.

To achieve other roughnesses the surface of the LTCC substrate was laser ablated in a grid-like way using a 355 nm picosecond UV laser system. Different cutting distances between 5 and 30 µm and a laser power between 0.5 W and 1 W were used, which resulted in a roughness between 572 nm ± 14.4 nm and 874 nm ± 20.5 nm. Finally, the samples were cut into pieces of 15 mm x 7 mm. After that a 20 nm thick layer of titanium was sputtered onto the samples as an adhesion layer, followed by the subsequentially deposition of the RMS. With a total thickness of 10 µm, 100 bilayers were chosen with a thickness of 60 nm for the aluminum and 40 nm for the nickel. After processing the samples, they were ignited by an electrical spark using two electrodes and a power supply limited to 25 V and 4 A.

B. Chemical/mechanical lapping and polishing (CMP)

The other possibility for the sample preparation persists in using a CMP machine to achieve lower roughness. An 8-layer DuPont 951 P2 was processed in a standard LTCC technology resulting in a thickness of 1080 µm. The substrates were lapped down chemically/mechanical on both sides to achieve a plane surface with a thickness of 810 µm ± 5,5 µm. Further polishing led to a roughness in the range between 105 nm ± 19.5 nm and 258 nm ± 16.5 nm. As before the samples were cut into smaller pieces and both the adhesion layer and the RMS were deposited.

C. Laser ablation with additional metallization

Some samples obtained an additional AgPd metallization between the LTCC substrate and the RMS [24]. Therefore, a standard LTCC technology was processed using 4-layer DuPont 951 PX resulting in a thickness of 839 µm ± 2.6 µm. The surface morphology was modified using the laser system in the same way as before. The reference sample (without further processing) reached a roughness of 525 nm ± 30 nm, whereas the other ones reached a roughness of 537 nm ± 12 nm (LS 3) and 773 nm ± 29 nm (LS 5). Finally, the samples were cut into pieces of 15 mm x 7 mm and the RMS was deposited.

D. Roughness characterization

The roughness of the surface was characterized by using a laser scanning microscope [23], [24]. An area of 250 µm x 250 µm was chosen for the measurements. The lowest roughness of about 100 nm was found for the CMP samples without metallization whereas the laser ablated samples show the highest roughness with a maximum of about 870 nm. Without processing the roughness is about 400 nm (see Fig. 2). For the samples with metallization, a roughness of 525 nm (reference) respectively 537 nm and 773 nm were reached (laser ablated samples).

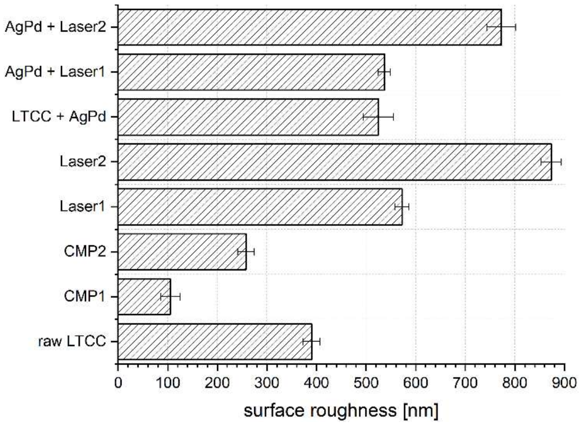

Fig. 2. Resulting surface roughness for some samples with different preparation methods, measured by LSM [23], [24].

III. CFD MODEL

A. CFD model description

To achieve more information about the reactive joining process a suitable CFD model was already developed and presented in [25]-[27] (see Fig. 3). It consists of the aluminum-nickel bilayer (blue), the LTCC substrate (green) and the isolation layer (green) between, some simulations also contain a solder layer. The base of the model has a primary surface of 4 mm x 4 mm with a surrounding air environment of the dimensions 10 mm x 10 mm x 5 mm to avoid interactions between the region of interest and the boundary conditions. Due to stability and convergence reasons no titanium layer was considered in the simulation model.

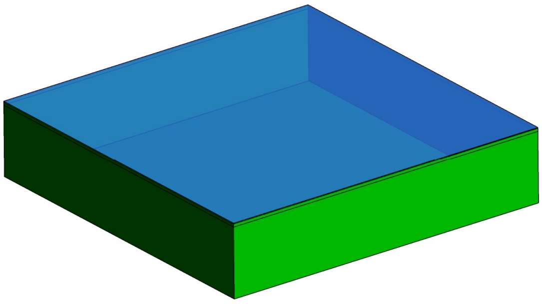

Fig. 3. The CFD simulation model mainly consists of the reactive multilayer system (blue) and the LTCC substrate with an isolation layer (green) [25].

The material properties and the dimensions of the individual layers are shown in Table I. The properties of the LTCC substrate and the isolation layer were assumed to be identical (GreenTape^{TM} DuPont DP951), which is why the effective thickness of the LTCC substrate is 860 µm. The properties of the RMS match with an unreacted multilayer [28], and the properties for the solder and the silicon chip were taken from the ANSYS Fluent material databases.

Table I. Dimensions and properties of the layers used in the CFD simulation model [26], [28].

layer	thickness [µm]	ρ [kg/m^3]	k [W/m•K]	C_p [J/kg•K]
LTCC	825	3100	3.3	600
Isolation	35	3100	3.3	600
RMS	30	5500	152	830
Solder	200	7000	63.2	230
Chip	400	2500	100	710

A 3x3 matrix of temperature probes was used to measure the temperatures during the movement of the reaction front. The probes in the same vertical position (e.g., P1, P2, P3) give information about the reaction velocity (through the time delay in the recorded values), and the probes in the same horizontal direction (e.g., P1, P4, P7) can be used to determine the peak temperature. For additional information the temperatures were also measured in the middle of the RMS, at the interface between the RMS and the solder, and at distances of 10 and 20 µm in the solder starting from the interface.

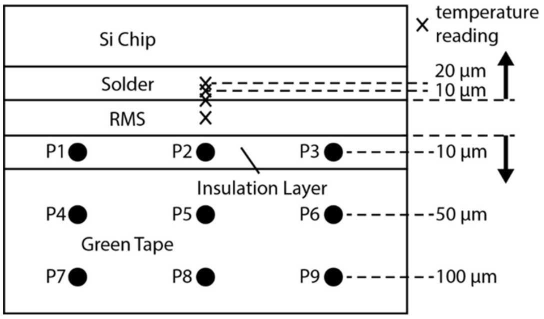

Fig. 4. Locations of the platinum temperature probes (P1 to P9) and the measurement points in the solder and the RMS.

All the structures were meshed in ANSYS Workbench 2023R1 with a length of 100 µm for the mesh edges in x- and y-direction, and with a length of 10 µm in the z-direction leading to a total number of 5,001,000 cells. The time-step size was fixed to 10^{-6} s for 10,000 time-steps which results in a simulation time of 10 ms. For a more detailed view see [25], [26]. To simulate the propagation of the reaction front, a probability density function in the form of (1) was used.

$$A \bullet D \bullet exp\{B^{(x+C-D\bullet t)^2}\} \qquad (1)$$

The four parameters A, B, C and D are used to control the heat release function, where A and B approximately correspond to the amplitude and width, C is an offset for the alignment with the leading edge of the reactive multilayer system and D corresponds to the velocity.

IV. RESULTS

A. *Experimental analysis*

As described in [23], all the samples showed a good adhesion behavior before ignition (see Fig. 5). After ignition, a peel-off effect could be observed at both the unmachined reference sample and the CMP prepared samples with low roughness (105 … 390 nm). In contrast the samples that were laser ablated with a roughness between 572 nm and 874 nm still show a good adhesion even after ignition, but SEM images show the occurrence of micro cracks within the RMS. Both the micro cracks and the peel-off effect are mainly caused by the different coefficients of thermal expansion of the materials. As an additional factor, there is a shrinkage in volume of approximately 12 % in the RMS due to lattice-spacing reduction [29] which may also affect the adhesion.

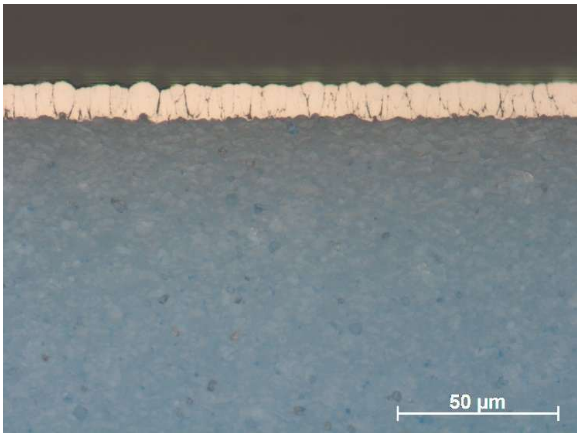

Fig. 5. Reflected light microscopy image reveals a good adhesion of the reactive multilayer on the LTCC substrate (blue) before ignition.

To determine the peak temperatures and the reaction speed, high velocity pyrometer measurements and high-speed camera measurements were done simultaneously [23], [24]. The pyrometer measurements show that the unmachined LTCC substrate reaches the highest peak temperature (1092 °C), followed by the samples that were prepared by CMP with nearly the same temperature (1067 and 1062 °C). The samples that were prepared by laser ablation reach the lowest temperatures (811 and 803 °C). It is remarkable that there is nearly no difference within the laser ablated samples although they differ in their roughness (572 nm to 873 nm). It can be assumed that the higher temperatures occur due to the peel-off of the RMS: the heat cannot be dissipated through the air as fast as if the RMS was still in contact with the substrate.

In case of the laser ablated samples with AgPd metallization, the lift-off effect was not as pronounced as in the other samples without the metallization. There is a punctual adhesion of the reactive multilayer, whereas some areas are separated from the metallization (see Fig. 6). The reference sample reaches a peak temperature of 854 °C whereas the laser ablated samples reach 847 and 739 °C. This temperature drop (compared to the first samples) may be caused by the additional metallization layer that absorbs some of the released heat.

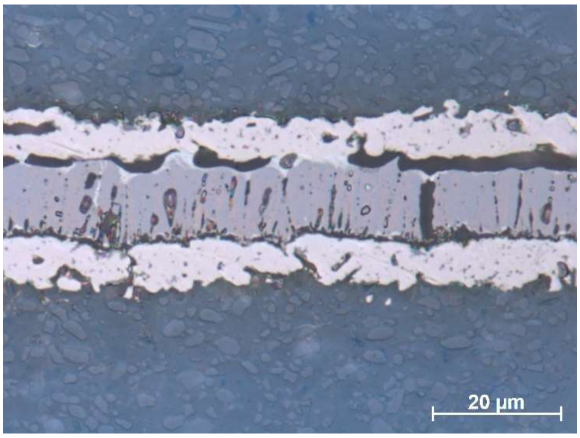

Fig. 6. Reflected light microscopy image of a reactive multilayer system between two LTCC substrates (blue) with AgPd metallization (bright areas) after ignition. There is only punctual adhesion of the RMS, whereas most areas of the RMS separated from the metallization.

The high-speed measurements show a velocity of around 5 m/s for the reaction front of both the reference sample and the CMP prepared samples. In contrast, the laser ablated samples show a reduction in velocity down to 3.7 m/s (roughness 572 nm) and 2.9 m/s (roughness 873 nm). The same effect can be observed on the samples with AgPd metallization: the velocity reduces from 3.7 m/s (roughness 525 nm) to 2.8 m/s (roughness 537 nm) and 2.2 m/s (roughness 773 nm). The measured values are clearly represented in Table II.

Table II. Overview of the reached peak temperatures and reaction front velocities depending on different substrate preparation methods and resulting surface roughness [23], [24].

	substrate preparation	surface roughness [nm]	peak temp. [°C]	reaction front velocity [m/s]
LTCC without metallization	CMP 1	105	1067	5.1
	CMP 2	257	1062	4.7
	Ref.	390	1092	5.1
	LS 1	572	811	3.7
	LS 2	873	803	2.9
LTCC with metallization	AgPd + Ref.	525	854	3.7
	AgPd + LS 3	537	847	2.8
	AgPd + LS 5	773	739	2.2

B. CFD comparisons

Simulations were performed for a model with solder (Fig. 7) and for a model without solder (Fig. 8). A velocity for the reaction front of 1 m/s and a time-step size of 10^{-6} s was chosen for the temperature recordings.

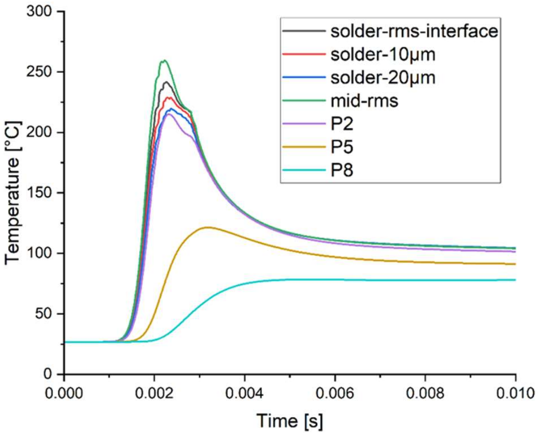

Fig. 7. Temperature contour plot of the interface between the solder and RMS, within the solder and the RMS, and at the temperature probes P2, P5 and P8 for a velocity of 1 m/s.

As depicted in Fig. 7 the maximum temperature of about 260 °C was reached within the RMS which is only slightly above the required temperature of 240 °C [26]. At the interface between the RMS and the solder it reaches around 240 °C and the lowest value with around 220 °C is reached at a distance of 20 µm within the solder.

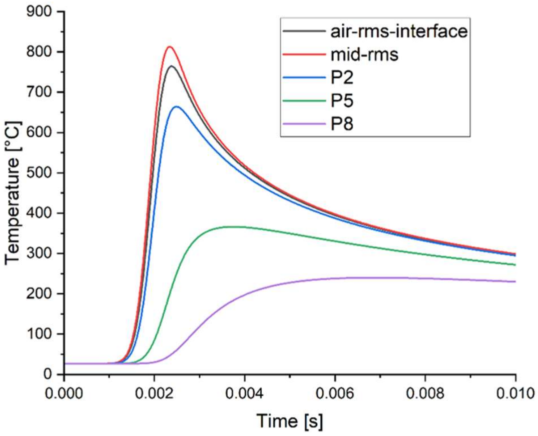

Fig. 8. Temperature contour plot for the model without solder of the interface between the air and RMS, within the RMS and at the temperature probes P2, P5 and P8 for a velocity of 1 m/s.

Fig. 8 shows the temperature plot for the model without a solder layer. The reached temperature within the RMS is raised by more than 200 % up to 820 °C while the temperature at the interface between the surrounding air and the RMS is above 750 °C. By comparison to the previous model, it can be assumed that the melting and solidification of the solder is responsible for this significant drop of the RMS peak temperature, so the amount of solder deposited on the RMS should be a good parameter to control the peak temperature during reactive bonding. A similar relation was already considered by Wang [30].

V. CONCLUSIONS

This paper discusses the application of reactive bonding methods on LTCC substrates. Therefore, a reactive multilayer system (RMS) consisting of alternating nanolayers of aluminum and nickel with a total thickness of 100 µm was deposited after two different surface modifications were applied. Then, the samples were electrically ignited which was recorded by a high velocity pyrometer and a high-speed camera for temperature and velocity measurements. The first preparation method is chemical mechanical polishing (CMP) of a LTCC substrate, without metallization, which lowers the surface roughness down to around 100 nm. Compared to the reference sample (roughness 390 nm), the CMP does not seem to influence the peak temperature or the reaction front velocity. In addition, there is a peel-off of the RMS structure. The second method uses a picosecond laser to modify the LTCC substrate morphology, whereby the roughness can be increased up to 873 nm. This leads to a decrease in the peak temperature by nearly 300 °C and a decrease in the reaction front velocity by around 27 - 43 %. In case of the laser ablated surfaces no peel-off effects could be observed but some micro cracks in the RMS could be found. Both the peel-off effects and the micro cracks occur due to different coefficients of thermal expansion and the volume shrinkage during the exothermal reaction. An additional reason for the problems in adhesion is the lower thermal conductance of the LTCC substrate compared to silicon substrates.

Laser ablation was also done for samples with an additional AgPd metallization between the LTCC substrate and the deposited RMS. After ignition, less peel-off effects could be observed. The drop in the RMS peak temperature is not as high as in the other version, but the velocity of reaction front was slowed down by around 24 - 41 %. The experimental data show that the adhesion still has to be improved.

CFD simulations were conducted to analyze the process in more detail. A shoebox model with the different layers (LTCC, RMS and solder) was presented and compared to another model without a solder layer. An adjustable user-defined function for the heat release of the RMS during the reaction was used to adopt the reaction front velocity and the combustion temperature to the experimental values. The temperature during the exothermal reaction was recorded at different positions with a time-step size of 10^{-6} s. The measurements suggest that the solder layer can be used to control the peak temperature during the reactive bonding process.

Acknowledgment

This research work was supported by funding from the Deutsche Forschungsgemeinschaft (DFG, German Research Foundation) – Project ID 426204742.

The authors would like to offer many thanks to Andreas Ruh for preparing and performing the cross-sections.

References

[1] P. N. Clough and B. A. Thrush, “Mechanism of Chemiluminescent Reaction between Nitric Oxide and Ozone,” Transactions of the Faraday Society, 1967, vol. 63, pp. 915-925.

[2] T. Geiling, T. Welker, H. Bartsch and J. Müller, “Design and Fabrication of a Nitrogen Monoxide Measurement Device Based on Low Temperature Co-Fired Ceramics,” International Journal of Applied Ceramic Technology, 2012, vol. 9, no. 1, pp. 37-44.

[3] T. Welker, T. Geiling, H. Bartsch and J. Müller, “Design and Fabrication of Transparent and Gas-Tight Optical Windows in Low-Temperature Co-Fired Ceramics,” International Journal of Applied Ceramic Technology, 2013, vol. 10, no. 3, pp. 405-412.

[4] T. Geiling, T. Welker, C. Ehrling and J. Müller, “Design, Fabrication, and Operation of a Nitrogen Monoxide Measurement Device Based on LTCC,” Journal of microelectronics and electronic packaging, 2012, vol. 9, no. 4, pp. 171-177.

[5] K. Malecha and L. J. Golonka, “Microchannel Fabrication Process in LTCC Ceramics,” Microelectronics Reliability, 2008, vol. 48, no. 6, pp. 866-871.

[6] H. Bartsch de Torres, C. Rensch, M. Fischer, A. Schober and M. Hoffmann, “Thick Film Flow Sensor for Biological Microsystems,” Sensors and Actuators A: Physical, 2010, vol. 160, no. 1-2, pp. 109-115.

[7] P. Ciosek et al., “Monitoring of Cell Cultures with LTCC Microelectrode Array,” Analytical and bioanalytical chemistry, 2009, vol. 393, pp. 2029-2038.

[8] J. Wilde, “B4. 1-Trends in Assembly and Packaging of Sensors,” Proceedings SENSOR 2009, vol. 1, 2009, pp. 205-210.

[9] Y. Fournier, “3D Structuration Techniques of LTCC for Microsystems Applications,”, EPFL, 2010.

[10] P. Uhlig et al., “LTCC Short Range Radar Sensor for Automotive Applications at 24 GHz,” Proceedings of the IMAPS, 2004.

[11] L. Golonka, P. Bembnowicz, D. Jurków, K. Malecha, H. Roguszczak and R. Tadaszak, “Low temperature co-fired ceramics (LTCC) microsystems,” Optica Applicata, 2001, vol. 41, no. 2, pp. 383-388.

[12] A. Bittner and U. Schmid, “The Porosification of Fired LTCC Substrates by Applying a Wet Chemical Etching Procedure,” Journal of the European Ceramic Society, 2009, vol. 29, no. 1, pp. 99-104.

[13] T. Thelemann, M. Fischer, A. Groß and J. Müller, “LTCC-based Fluidic Components for Chemical Applications,” Journal of microelectronics and electronic packaging, 2007, vol. 4, no. 4, pp. 167-172.

[14] J. Braeuer, J. Besser, M. Wiemer and T. Gessner, “A novel technique for MEMS packaging: Reactive bonding with integrated material systems,” Sensors and Actuators A: Physical, 2012, vol. 188, pp. 212-219.

[15] H. Jantunen, T. Kangasvieri, J. Vähäkangas and S. Leppävuori, “Design aspects of microwave components with LTCC technique,” Journal of the European Ceramic Society, 2003, vol. 23, no. 14, pp. 2541-2548.

[16] M. Matters-Kammerer et al., “Material properties and RF applications of high k and ferrite LTCC ceramics,” Microelectronics Reliability, 2006, vol. 46, no. 1, pp. 134-143.

[17] A. Bittner, A. Ababneh, H. Seidel and U. Schmid, “Influence of the crystal orientation on the electrical properties of AlN thin films on LTCC substrates,” Applied surface science, 2010, vol. 257, no. 3, pp. 1088-1091.

[18] A. S. Rogachev and A. S. Mukasyan, “Combustion of Heterogeneous Nanostructural Systems (Review),” Combustion, Explosion and Shock Waves, 2010, vol. 46, pp. 243-266.

[19] S. Sen, M. Lake, N. Kroppen, P. Farber, J. Wilden and P. Schaaf, “Self-propagating exothermic reaction analysis in Ti/Al reactive films using experiments and computational fluid dynamics simulation,” Applied Surface Science, 2017, vol. 396, pp. 1490-1498.

[20] D. P. Adams, “Reactive Multilayers Fabricated by Vapor Deposition (Review),” Thin Solid Films, 2015, vol. 576, pp. 98-128.

[21] A. J. Gavens, D. Van Heerden, A. B. Mann, M. E. Reiss and T. P. Weihs, “Effect of intermixing on self-propagating exothermic reactions in Al/Ni nanolaminate foils,” Journal of Applied Physics, 2000, vol. 87, no. 3, pp. 1255-1263.

[22] K. T. Raić et al., “CFD analysis of exothermic reactions in Al-Au nano multi-layers foils,” Materiali in tehnologije, 2011, vol. 45, no. 4, pp. 335-338.

[23] A. Schulz et al., “Characterization of Reactive Multilayer Systems deposited on LTCC featuring different surface morphologies,” MikroSystemTechnik Congress 2021; Congress. VDE, 2021, pp. 1-5.

[24] A. Schulz, A. Ruh, S. Wiese and J. Müller, “Characterization of Reactive Multilayer Systems deposited on LTCC screen printing pastes featuring different surface morphologies suitable for reactive joining applications,” Ceramic Interconnect and Ceramic Microsystems Technologies (CICMT) 2022; Congress, 2022.

[25] E. Wiss, A. Yuile, A. Schulz, J. Müller and S. Wiese, “Reactive Die Bonding on LTCC Substrates – Analysis by CFD Simulation,” 24th International Conference on Thermal, Mechanical and Multi-Physics Simulation and Experiments in Microelectronics and Microsystems (EuroSimE). IEEE, 2023, pp. 1-5.

[26] A. Yuile, A. Schulz, E. Wiss, J. Müller and S. Wiese, “The Simulated Effect of Adding Solder Layers on Reactive Multilayer Films Used for Joining Processes,” Applied Sciences, 2022, vol. 12, no. 5, p. 2397.

[27] A. Yuile, A. Schulz, J. Müller and S. Wiese, “Analysis of selective bonding processes using reactive multi-layers for system integration on LTCC based SiPs,” Microsystem Technologies, 2022, vol. 28, no. 9, pp. 1995-2009.

[28] S. Liang, Y. Zhong, S. Robertson, A. Lio, Z. Zhou and C. Liu, “Investigation of Thermo-mechanical and Phase-change Behavior in the Sn/Cu Interconnects during Self-Propagating Exothermic Reaction Bonding,” 2020 IEEE 70th Electronic Components and Technology Conference (ECTC). IEEE, 2020, pp. 269-275.

[29] T. Namazu, K. Ohtani, K. Yoshiki, S. Inoue, “Crack propagation direction control for crack-less solder bonding using Ni/Al flash heating technique,” 2011 16th International Solid-State Sensors, Actuators and Microsystems Conference. IEEE, 2011, pp. 1368-1371.

[30] J. Wang et al., “Joining of stainless-steel specimens with nanostructured Al/Ni foils,” Journal of applied physics, 2004, vol. 95, no. 1, pp. 248-256.

5.4 Paper 4: Simulations of Thermocouple Measurements during Reactive Bonding Processes on LTCC

5.4.1 Veröffentlichungshinweise

Adam Yuile[1], Nesrine Jaziri[2], Erik Wiss[1], Jens Müller[2], Steffen Wiese[1]

[1]Chair of Microintegration and Reliability, Faculty of Natural Sciences and Technology, Saarland University, Saarbrücken, Germany

[2]Electronics Technology Group, Faculty of Electrical Engineering and Information Technology, TU Ilmenau, Ilmenau, Germany

2024 IEEE 10th Electronics System-Integration Technology Conference (ESTC)

Die Originalveröffentlichung ist abrufbar unter:
https://doi.org/10.1109/ESTC60143.2024.10712001

5.4.2 Synopse

Diese Veröffentlichung untersucht die Eignung von in die LTCC eingebetteten Thermopaaren zur Temperaturmessung während des reaktiven Fügeprozesses. Die Motivation ergibt sich aus der nur eingeschränkten Eignung herkömmlicher Temperatursensoren auf Pt-Basis (siehe Paper 2), die aufgrund ihrer Größe und der notwendigen großen Isolationsschicht keine realitätsnahe Messung erlauben. Ziel der Arbeit war es, durch Simulationen zu analysieren, ob Ag/AgPd-Thermopaare eine präzisere Erfassung der Temperaturverläufe ermöglichen.

Hierzu wurde ein Schichtstapel mit einer Gesamtgröße von 3 mm x 3 mm x 1 mm entwickelt, in dessen Zentrum sich das eigentliche Modell befindet. Es besteht aus einem LTCC-Substrat (840 µm) mit integrierten Ag- und AgPd-Säulen gleicher Höhe (Durchmesser 300 µm), die über ein Ag-Pad (7 µm) innerhalb der Isolationsschicht (9 µm) elektrisch miteinander verbunden sind, gefolgt von einer Ag-Metallisierung (2 µm), einer Lotschicht (2 µm) und dem RMS (10 µm). Die exotherme Reaktion wurde durch eine sich mit 5 m/s vom linken zum rechten Rand ausbreitende Wahrscheinlichkeitsdichtefunktion modelliert. Aufgrund des Seebeck-Effekts (siehe Kapitel 4.1.6) entsteht durch die Temperatur an der Kontaktstelle der unterschiedlichen Materialien ein Potentialunterschied, der durch thermoelektrische Simulationen nachgebildet werden kann.

Die Ergebnisse zeigen, dass die Temperatur an der Kontaktstelle des Thermopaares mit ca. 700 °C aufgrund der dünnen Isolationsschicht lediglich rund 100 °C unterhalb der maximalen Temperatur im RMS (ca. 800 °C) liegt. Die maximale Potentialdifferenz beträgt dabei 3,5 mV. Damit zeigt sich, dass Thermopaare eine geeignete Alternative zu den zuvor verwendeten Pt-Sensoren darstellen können.

Im Kontext des Gesamtprojekts leistet diese Veröffentlichung einen Beitrag zur Beantwortung der Frage, wie hoch die während der exothermen Reaktion tatsächlich entstehenden Temperaturen sind.

5.4.3 Vollständiger Artikel

Simulations of Thermocouple Measurements during Reactive Bonding Processes on LTCC Substrates

Adam Yuile
Chair of Microintegration and Reliability
Saarland University
66123 Saarbruecken, Germany
adam.yuile@uni-saarland.de

Nesrine Jaziri
Electronics Technology Group
TU Ilmenau
98693 Ilmenau, Germany
nesrine.jaziri@tu-ilmenau.de

Erik Wiss
Chair of Microintegration and Reliability
Saarland University
66123 Saarbruecken, Germany
erik.wiss@uni-saarland.de

Jens Müller
Electronics Technology Group
TU Ilmenau
98693 Ilmenau, Germany
jens.mueller@tu-ilmenau.de

Steffen Wiese
Chair of Microintegration and Reliability
Saarland University
66123 Saarbruecken
s.wiese@mx.uni-saarland.de

Abstract – The usage of room-temperature bonding processes offers several advantages, e.g., the thermo-mechanical stress can be reduced through a localized heat transfer that is especially beneficial for heat-sensitive components. One of the ways to do this is through the use of a reactive multilayer system (RMS) which consists of at least two suitable reactant partners that release a large amount of heat after the system is ignited. This process is already well-established on silicon and metal substrates, but the specific characteristics of low-temperature cofired ceramics (LTCC) like higher roughness and lower thermal conductivity make it difficult to transfer the process into this field. To achieve a better understanding of this process, it is important to have an accurate knowledge of the emerging temperatures, but because it takes place at the interface between the two bonding partners, no direct measurement via pyrometer (or similar) is possible. Previous work introduced embedded platinum sensors for indirect temperature measurement, but it was confronted with several problems, e.g., the necessary electrical isolation of the RMS and the sensor results in a signal distortion due to the larger distance between both layers. As a new approach, an integrated thermocouple system using different thick-film pastes (Ag and AgPd) was proposed generating a thermoelectric voltage that can be measured externally. A suitable CFD simulation model was developed to analyze the feasibility of this approach, and the results are presented in this work.

Keywords – LTCC, RMS, reactive multilayer system, Al/Ni, temperature/voltage assessment.

I. INTRODUCTION

With the advent of modern electronics, the demand for efficient and reliable soldering techniques has increased significantly. Traditional methods such as reflow soldering require the entire printed circuit board (PCB) to be heated to temperatures above 200 °C. This uniform heating is important to melt the solder paste and ensure stable electrical connections. However, thermal expansion variation between different components due to their different thermal expansion coefficients leads to thermo-mechanical stress, which can result in component failure and reduced device reliability.

In response to these challenges, localized soldering techniques have attracted attention due to their potential to reduce such thermo-mechanical stress by concentrating heat only on the solder joints rather than the entire assembly. One promising approach involves the use of reactive multilayer systems (RMS), which consist of alternating layers of nanoscale reactive materials. These multilayer systems, typically ranging in thicknesses from 10 to 300 nm per layer and up to 300 µm for the entire structure, can be ignited by heat, electrical sparks, or laser pulses [1]. Initiation triggers an exothermic reaction as the materials mix at the atomic level, sustaining a self-propagating reaction that localizes heat generation [2,3].

Despite established deposition techniques for reactive multilayer systems (RMS) on silicon substrates, extending this technology to low temperature co-fired ceramic (LTCC) substrates presents significant challenges [4-7]. LTCC technology, known for its high reliability, hermeticity, and chemical resistance, is predominantly used in high-performance applications due to its cost [8-13]. Furthermore, LTCC technology is also noted excellent compatibility with built-in passive devices and for being able to operate at high temperatures, namely up to 500 °C [14]. Having an accurate temperature measurement during the reactive bonding process is critical to understand and optimize these reactions. However, direct temperature measurement is impractical because the reaction occurs at the interface between solid opaque structures.

Previous work introduced a test device with embedded platinum (Pt) sensors to measure temperature indirectly [15,16]. However, this method has limitations, such as the need for electrical isolation of the sensor from the RMS, resulting in a significant distance between them and subsequent signal distortion. As an innovative alternative, the integration of a thermocouple system made of silver (Ag) and silver-palladium (AgPd) paste into the LTCC multilayer structure was proposed. These pastes are partly chosen due to their compatibility with LTCC technology, owing to their high glass frit percentages which enable them to adhere to the LTCC substrate and endure the processing conditions [14].

This system generates a thermoelectric voltage at the contact point of the two materials, owing to the different Seebeck coefficients of Ag and AgPd, which can then be measured externally to infer the temperature. Simulation models were developed to validate the functionality of the sensor and estimate the cooling effect created by the metal structures of the thermocouple, potentially lowering the measured temperature compared to pure LTCC regions. The impact of this heat flow on the temperature values is analyzed through these simulations to improve the accuracy of temperature measurement during reactive bonding processes.

II. SIMULATION DETAILS

A. *CFD Simulation*

The simulations were broken down into two parts, firstly the CFD simulations and, secondly the thermoelectric simulations, both of which simulations refer to the same global geometry. CFD simulations have proven as an adequate tool for the simulation of reactive processes [15-17] and are further being employed in this field to make predictions about the reactive multilayer performance.

The geometry is shown schematically in Figure 1, where the RMS has a thickness of 10 µm, Sn 2 µm, an insulation layer 9 µm and an LTCC total thickness of 840 µm. Inside the LTCC, two full-length cylindrical vias were embedded, one made from Ag, the other AgPd, and these were each 300 µm diameter. The interconnection on the top and the contact pads on the bottom were all 7 µm thick and made from Ag. This geometry was akin to the thermoelectric generators (TEGs) used in [14], albeit in a more simplified form without heat spreaders and limited to one thermocouple module only.

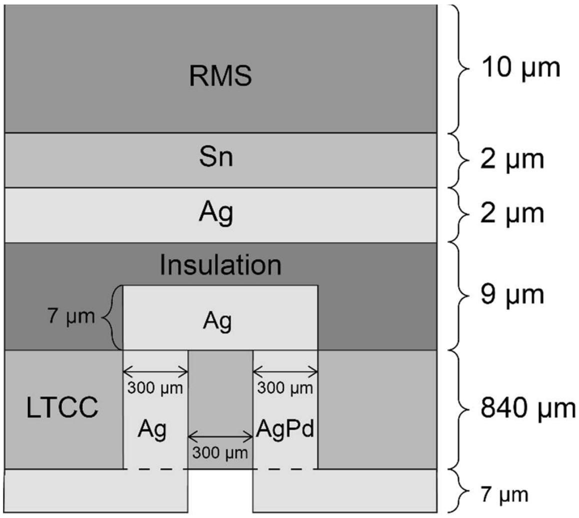

Figure 1: Schematic of the model including all the layers that were used in the model with their thicknesses. The thermocouple is embedded in the LTCC layer, consisting of two different materials (Ag and AgPd) to make use of the Seebeck effect.

The model geometry is shown in Figure 2 with the LTCC substrate made to be semi-transparent, such that the internal structures are also visible. The vias of the thermocouple (yellow: Ag, dark green: AgPd) are embedded within the LTCC (light green) with the RMS on top (red). Underneath the RMS, there is a thin solder layer of 2 µm Sn (pink) and a metallization layer of 7 µm Ag. The contact pads (dark green) on the bottom side allow the measurement of the generated thermoelectric voltage, that is generated due to the temperature evoked by the heat release of the RMS. The pad on the left is denoted A and, likewise, the pad on the right is denoted pad B – where ultimately the respective voltages are V_a and V_b.

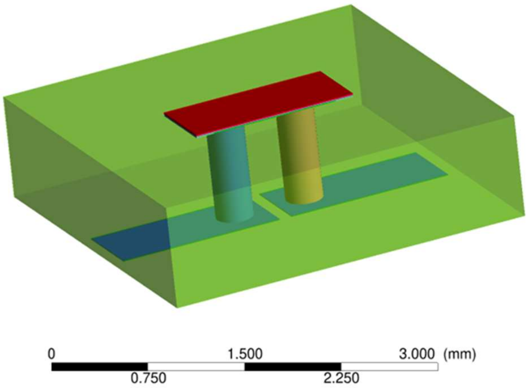

Figure 2: Three-dimensional view of the CFD simulation model with its different layers. The legs of the thermocouple (yellow: Ag, dark green: AgPd) are embedded within the LTCC (light green) with the RMS on top (red). Underneath the RMS, there is a thin solder layer of 2 µm Sn (pink - barely visible) and a metallization layer of 2 µm Ag. The contact pads (dark green) on the bottom side allow the measurement of the generated thermoelectric voltage, that is generated due to the temperature evoked by the heat release of the RMS.

The material properties for both the CFD and thermoelectric simulations are shown in table 1 below.

Table 1: Material properties for RMS, Sn, LTCC, Ag and AgPd that are used in the CFD and thermoelectric simulations in terms of thermal conductivity, Seebeck coefficient, resistivity, density and specific heat capacity.

	RMS	**Sn**	**LTCC**	**Ag**	**AgPd**
k [W/m·K]	152	492.9	3.3	271.7	146.4
S [µV/K]	-19.5	-1	30	1.5	-6
Resistivity [Ω·m]	7E-8	1.5E-7	1E+12	2.7E-8	5E-8
Density [kg/m³]	5500	7295	3100	10490	10490
C_p [J/kg·K]	830	221.89	600	234.28	234.28

The CFD simulations solve the energy equation for each of the components in the domain where convection boundaries with a heat transfer coefficient of 20 W/m²·K and a freestream temperature of 300 K were used on all the external boundaries.

A user-defined function, as per [17], was used as a volumetric power density heat source in the RMS, such that a wave of exothermic energy release, propagating in the positive x-direction, was represented in a realistic manner. This simulated a reaction velocity of 5 m/s and a reaction width of 100 µm of an Al/Ni RMS.

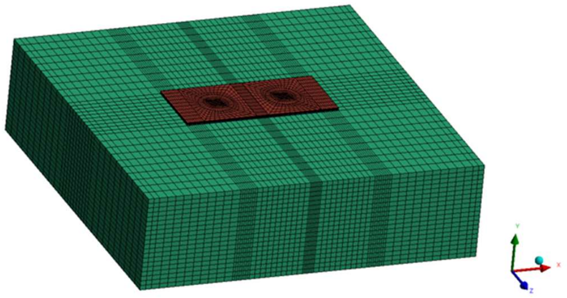

Figure 3: Mesh of the CFD simulation model. While a coarser mesh is sufficient at the side parts of the model, a finer mesh was chosen in the area of the legs of the thermocouple.

In Figure 3 the multi-block structured hexagonal mesh is shown for the CFD model where some larger elements are used on the external boundaries of the LTCC (where the temperature gradients are negligible), and a finer mesh is used around the cylindrical via structures.

Note, an outwardly identical mesh to that of Figure 3 was used for the thermoelectric simulations in that the number of elements and the element spacings were equal – albeit different element types are used with respect to the type of physics that is being evaluated.

In ANSYS Fluent 1000 time-steps were solved, for a convergence criterion of 10^{-6} for the energy equation, with a time-step of 10^{-6} s, thus leading to solution data from 0 to 1 ms. In Figure 4 the temperature contours are shown on the external surfaces 0.05 ms after RMS ignition, where it can be observed that the heat is concentrated exclusively to the leading edge where reaction initiation has taken place.

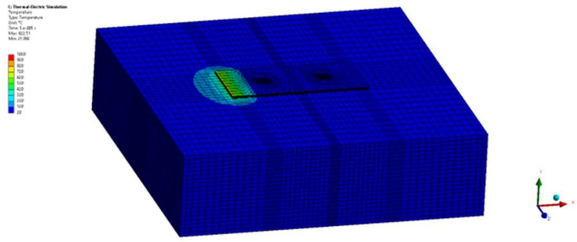

Figure 4: Surface temperature contour plot of the model with an Sn layer of 2 µm thickness, shown 0.05 ms after the ignition of the RMS. The temperatures around the starting point of the reaction reach almost 800 °C.

The peak temperatures seen at this juncture are in the order of 800 °C, which is a typical temperature that could be observed through pyrometer measurements on configurations with an Al/Ni RMS on single LTCC substrates [18,19].

B. Thermoelectric simulation

Upon establishing these temperature fields for the RMS in CFD, the surface temperatures on the RMS were used as inputs for the thermoelectric simulations in ANSYS Workbench, together with room temperature boundaries on the pads and the external perimeter of the LTCC substrate. Furthermore, a voltage boundary of 0 V was prescribed on the top surface of the RMS.

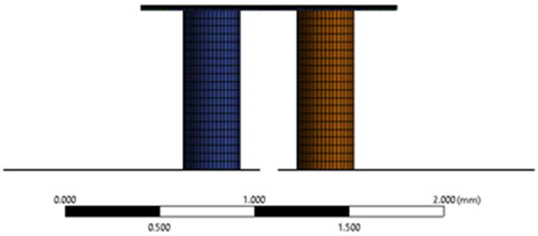

Figure 5: Side view of the embedded legs of the thermocouple. The thermoelectric voltage is generated at the contact area between both columns (orange: Ag, blue: AgPd) and can be measured between the pads at the bottom side.

In Figure 5, a side view of the vias of the electrically active components of the thermocouple is shown and this is where thermoelectric simulation focuses given that with reference to Table 1 the resistivity of the LTCC/isolation layer is many orders of magnitude greater than the other structures.

The surface temperatures of the RMS obtained from the CFD were used as inputs for the thermoelectric simulation at 23 load steps with respect to the other given boundary conditions. This resulted in load steps every 10 µs between 0 and 100 µs, every 20 µs between 100 and 200 µs and every 100 µs between 200 and 1000 µs.

III. RESULTS

In Figure 6 the electric potential contours are shown after 1 ms. Here, it can be observed that the voltage on the RMS is maintained at 0 V, as per the specified boundary condition, and the left pad pertains to a higher voltage than the right pad, where V_a = 0.5 mV and V_b = -0.9 mV. This results in an overall potential difference V_{ab} of 1.4 mV for a Sn thickness of 2 µm.

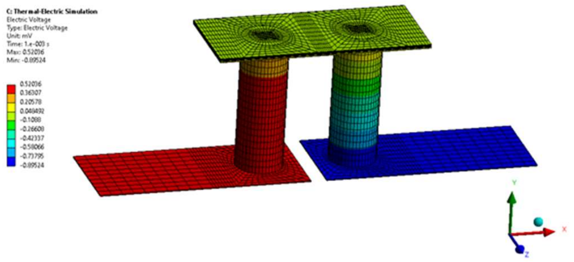

Figure 6: Electrical potential within both the pads and the columns of the thermocouple, shown 1 ms after the ignition of the RMS. While the potential on the left-hand side is around 0.52 mV, it is around -0.90 mV on the right-hand side, resulting in a measured voltage of approximately 1.42 mV between both pads.

Additionally, in both Figure 7 and Figure 8, the surface temperature contours are shown after 0.15 and 1 ms. In Figure 7 it can be observed that the peak temperatures occur on the RMS outwith the confines of the Ag via, which acts as a large heat sink. This effect is further demonstrated in Figure 8 where the entirety of the RMS is visibly at a lower temperature contour above the Ag via and predominantly so above the AgPd via.

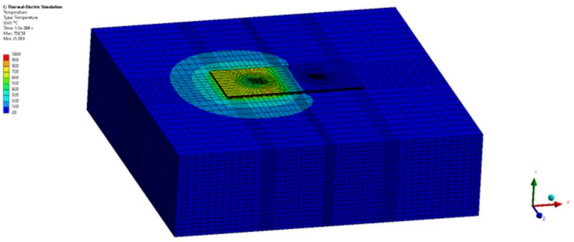

Figure 7: Surface temperature contour plot of the model with an Sn layer of 2 µm thickness, shown 0.15 ms after the ignition of the RMS. Almost half of the area of the reactive layer reaches a temperature of almost 800 °C. In the area of the left column of the thermocouple, the temperature is slightly decreased due to its high thermal mass.

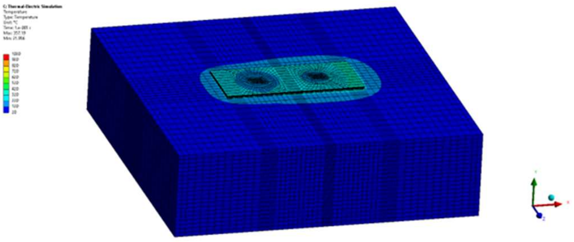

Figure 8: Surface temperature contour plot of the model with an Sn layer of 2 µm thickness, shown 1 ms after the ignition of the RMS. Approximately 0.3 ms after the ignition, the exothermic reaction of the RMS has finished, and the surface cools down. After a further 0.7 ms, most areas dropped to a temperature of almost 350 °C.

In Figure 9 the maximum temperatures (evoked by the simulation of the exothermic reaction) within the different layers are shown with respect to their progression throughout time. This graphic shows that there is a particular region (approximately between 0.1 and 0.3 ms) where the vias act very effectively to sink the heat released from the RMS. The temperatures of the RMS and Sn are almost identical with an offset of approximately 100 °C to the Ag metallization.

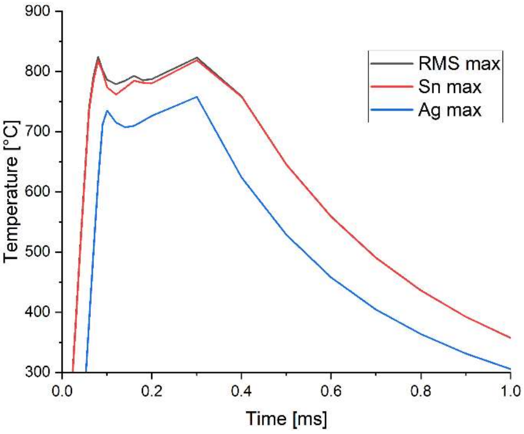

Figure 9: Time-temperature plot for the first millisecond of the simulation for the different layers RMS, the solder layer, and the metallization layer. The maximum temperature that was reached was nearly 825 °C for the RMS and the solder, and around 750 °C for the metallization. The temperature between the RMS and the Sn layer are mostly the same except for a few degrees Celsius. Approximately 0.3 ms after the ignition of the RMS, the exothermic reaction has finished, and the surface can start to cool down again.

In Figure 10 the time-voltage plot is shown for V_{ab} up to 1 ms. This graph shows the time-voltage history for the first millisecond after reaction initiation and that the peak voltage almost reaches 3.5 mV after just under 0.3 ms and tails off to just over 1.4 mV after 1 ms, as already displayed in Figure 6.

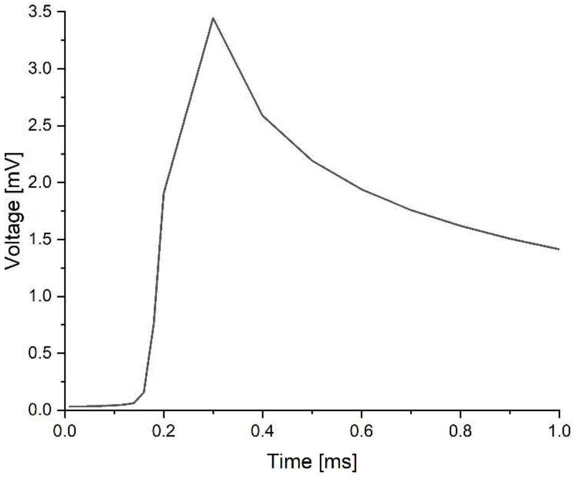

Figure 10: Time-voltage plot within the Sn layer for 2 µm thick Sn layer. The peak voltage of just under 3.5 mV is attained after approximately 0.3 ms.

IV. CONCLUSIONS

The simulations show that an Ag/AgPd thermocouple could be a possibility to measure the temperature during reactive joining processes. For a 10 µm thick Al/Ni RMS ignited on a 2 µm thick Sn layer, a peak output voltage of approximately 3.5 mV would be obtained. This voltage would be expected to occur approximately 0.3 ms after the initiation of the reaction propagating at a speed of 5 m/s.

For future work other thermocouple configurations will be studied, namely ones with additional vias that provide direct contact to the metallization, and it will be interesting to observe what will be seen both in the simulations and experimentally. It would also be conceivable to connect several such thermocouples in series in order to increase the resulting voltage and thus simplify the measurement.

ACKNOWLEDGMENTS

This research work was supported by the Deutsche Forschungsgemeinschaft (DFG, German Research Foundation) – Project-ID 426204742.

REFERENCES

[1] D. P. Adams, "Reactive multilayers fabricated by vapor deposition: A critical review," Thin Solid Films, 2015, vol. 576, pp. 98-128.

[2] K. T. Raić, R. Rudolf, P. Ternik, Z. Žunič, V. Lazić, D. Stamenković, T. Tanasković, I. Anžel, "CFD analysis of exothermic reactions in Al-Au nano multi-layered foils," Mater. Tehnol., 2011, vol. 45, no. 4, pp. 335-338.

[3] A. J. Gavens, D. Van Heerden, A. B. Mann, M. E. Reiss, T. P. Weihs, "Effect of intermixing on self-propagating exothermic reactions in Al/Ni nanolaminate foils," J. Appl. Phys., 2000, vol. 87, no. 3, pp. 1255-1263.

[4] J. Braeuer, T. Gessner, "A hermetic and room-temperature wafer bonding technique based on integrated reactive multilayer systems," J. Micromech. Microeng., 2014, vol. 24, no. 11, p. 115002.

[5] J. Braeuer, J. Besser, M. Wiemer, T. Gessner, “A novel technique for MEMS packaging: reactive bonding with integrated material systems,” Sens. Actuat. A Phys., 2012, vol. 188, pp. 212-219.

[6] B. Boettge, J. Braeuer, M. Wiemer, M. Petzold, J. Bagdahn, T. Gessner, “Fabrication and characterization of reactive nanoscale multilayer systems for low-temperature bonding in microsystem technology,” J. Micromech. Microeng., 2010, vol. 20, no. 6, p. 064018.

[7] J. Wang, E. Besnoin, A. Duckham, D. J. Spey, M. E. Reiss, O. M. Knio, M. Powers, M. Whitener, T. P. Weihs, “Room-temperature soldering with nanostructured foils,” Appl. Phys. Lett., 2003, vol. 83, no. 19, pp. 3987-3989.

[8] C. Jacq, T. Maeder, P. Ryser, “Sensors and packages based on LTCC and thick-film technology for severe conditions,” Sadhana, 2009, vol. 34, pp. 677-687.

[9] L. Golonka, P. Bembnowicz, D. Jurków, K. Malecha, H. Roguszczak, R. Tadaszak, “Low temperature co-fired ceramics (LTCC) microsystems,” Opt. Appl., 2011, vol. 41, no. 2, pp. 383-388.

[10] J. Wilde, “B4.1 – Trends in assembly and packaging of sensors,” Proceedings SENSOR, 2009, vol. I, pp. 205-210.

[11] T. Thelemann, M. Fischer, A. Groß, J. Müller, “LTCC-based fluidic components for chemical applications,” J. Microelectron. Electron. Packag., 2007, vol. 4, no. 4, pp. 167-172.

[12] D. Nowak, A. Dziedzic, “LTCC package for high temperature applications,” Microelectron. Reliab., 2011, vol. 51, no. 7, pp. 1241-1244.

[13] M. Santo Zarnik, D. Belavic, “Study of LTCC-based pressure sensors in water,” Sens. Actuat. A Phys., 2014, vol. 220, pp. 45-52.

[14] N. Jaziri, N. Gutzeit, H. Bartsch, A. Boughamoura, J. Müller, F. Tounsi, “LTCC-based Y-type thermoelectric generator with an improved heat flow guide for automotive waste heat recovery,” Sustain. Energy Fuels, 2022, vol. 6, no. 9, pp. 2330–2342.

[15] A. Yuile, A. Schulz, E. Wiss, J. Müller, S. Wiese, “The simulated effect of adding solder layers on reactive multilayer films used for joining processes,” Appl. Sci., 2022, vol. 12, no. 5, p. 2397.

[16] A. Yuile, A. Schulz, J. Müller, S. Wiese, “Analysis of selective bonding processes using reactive multi-layers for system integration on LTCC based SiPs,” Microsyst. Technol., 2022, vol. 28, no. 9, pp. 1995-2009.

[17] E. Wiss, A. Yuile, A. Schulz, J. Müller, S. Wiese, “Reactive die bonding on LTCC substrates–analysis by CFD simulation,” EuroSimE (IEEE), 2023, pp. 1–5.

[18] A. Schulz, H. Bartsch, N. Gutzeit, S. Matthes, M. Glaser, A. Ruh, J. Müller, J. P. Bergmann, S. Wiese, “Characterization of reactive multilayer systems deposited on LTCC featuring different surface morphologies,” MikroSystemTechnik Congress (VDE), 2021, pp. 1-5.

[19] A. Schulz, A. Ruh, S. Wiese, J. Müller, “Characterization of reactive multilayer systems deposited on LTCC screen printing pastes featuring different surface morphologies suitable for reactive joining applications,” CICMT, 2022, pp. 1-5.

5.5 Paper 5: Reactive Die Bonding on LTCC Substrates – Analysis by CFD Simulation

5.5.1 Veröffentlichungshinweise

Erik Wiss[1], Adam Yuile[1], Alexander Schulz[2], Jens Müller[2], Steffen Wiese[1]

[1]Chair of Microintegration and Reliability, Faculty of Natural Sciences and Technology, Saarland University, Saarbrücken, Germany

[2]Electronics Technology Group, Faculty of Electrical Engineering and Information Technology, TU Ilmenau, Ilmenau, Germany

2023 24th International Conference on Thermal, Mechanical and Multi-Physics Simulation and Experiments in Microelectronics and Microsystems (EuroSimE)

Die Originalveröffentlichung ist abrufbar unter:
https://doi.org/10.1109/EuroSimE56861.2023.10100772

5.5.2 Synopse

Diese Veröffentlichung analysiert die exotherme Reaktion eines RMS auf LTCC-Substraten mittels CFD-Simulationen. Die Motivation ergibt sich aus der Notwendigkeit, experimentelle Beobachtungen und theoretische Modellierungen systematisch miteinander zu verknüpfen, um die physikalischen Mechanismen der Wärmeausbreitung während des Fügevorgangs besser zu verstehen. Ziel der Arbeit war es, die mit einer Wahrscheinlichkeitsdichtefunktion modellierte Wärmefreisetzung des RMS mit experimentellen Temperaturmessungen zu vergleichen und die Eignung dieses Ansatzes zu bewerten.

Hierzu wurde ein dreidimensionales CFD-Modell mit einer Gesamtgröße von 10 mm x 10 mm x 5 mm entwickelt, das einen Stapel der Größe 4 mm x 4 mm x 0,870 mm aus LTCC-Substrat (825 µm), Isolationsschicht (35 µm) und RMS (10 µm) enthält. Die Wärmefreisetzung wurde durch eine sich mit 5 m/s ausbreitende Wahrscheinlichkeitsdichtefunktion mit verschiedenen Parametern modelliert. Die Temperaturverläufe verschiedener Konfigurationen (unbearbeitete LTCC, LTCC mit laserbearbeiteter Ti-Zwischenschicht und LTCC mit laserbearbeiteter Pd/Ag-Metallisierung) wurden mit einem Pyrometer erfasst.

Die Ergebnisse zeigen, dass die beste Übereinstimmung mit den experimentell aufgenommen Temperaturverläufen bei der laserbearbeiteten Pd/Ag-Metallisierung erzielt wird. Bei der Variante mit Ti-Zwischenschicht konnte lediglich eine eingeschränkte Korrelation festgestellt werden, was auf die in der Simulation aus Stabilitätsgründen nicht berücksichtigte, lediglich 20 nm dünne Ti-Schicht zurückzuführen ist. Aufgrund der Ablösung des RMS von der unbearbeiteten LTCC und der damit verbundenen deutlich verschlechterten Wärmeabfuhr wurde auf einen quantitativen Vergleich mit der Referenzkonfiguration verzichtet.

Im Kontext des Gesamtprojekts leistet diese Veröffentlichung einen Beitrag zur Beantwortung der Frage, ob sich die exotherme Reaktion eines RMS realitätsnah simulieren lässt.

5.5.3 Vollständiger Artikel

Reactive Die Bonding on LTCC Substrates – Analysis by CFD Simulation

Erik Wiss[1], Adam Yuile[1], Alexander Schulz[2], Jens Müller[2], Steffen Wiese[1]
[1] Saarland University, Chair of Microintegration and Reliability, Germany
[2] TU Ilmenau, Electronics Technology Group, Germany
erik.wiss@uni-saarland.de

Abstract

To improve the understanding of reactive multilayer systems as a joining process computational fluid dynamics (CFD) simulations have been performed and compared with experimental measurements made using a pyrometer. These CFD simulations consist of a shoebox model which contains different layers. The layers in the model are an Ni/Al reactive multilayer, low temperature co-fired ceramic (LTCC) substrate and the surrounding air environment. To simulate the heat released by the multilayer system, a user defined function of probability density function (PDF) form was written for the heat source. The peak energy intensity, reaction width and reaction speed can be controlled via the PDF to adapt the simulation to the real model.

1. Introduction

Reactive multilayer systems used for bonding interconnects are composed of alternating heterogeneous layers of nanoscale film materials, such as Ni/Al, with stored chemical energy [1]. Upon ignition these layers intermix and release high amounts of energy as heat and are additionally capable of maintaining self-propagation [2]. This exothermic heat release can be used to bond interconnects by, for example, melting solder paste, which upon solidification could then help form a permanent bond.

In recent times interest in reactive multilayer systems has increased in many fields of application, for example in die bonding [3], [4]. This increased interest is primarily driven by the desire to integrate thermally disparate components (e.g. those with high divergent coefficients of thermal expansion) onto specialised components, whilst minimising thermally induced stresses and maintaining reliability.

The deposition of reactive multilayers on silicon based substrates has been well established [5], but the intrinsic roughness of LTCC substrates (ranging from 0.4 to 1 µm [6]–[8]) makes the deposition on LTCC substrates more challenging.

Traditional soldering techniques, such as reflow soldering, require all structures to endure a heat cycle, whereas with reactive multilayer systems, the heat sources can be directed to very specific localised regions.

Owing to the high speed nature of these reactive multilayers, and the fact that during operation for actual bonding they can be hidden from sight, there is significant scope for simulation technologies to be used to enhance the understanding of the thermal performance of the reactive multilayer systems, but given the various approximations and assumptions that need to be made to these macroscopic models it is vital that calibrations, of sorts, are made to experimental data.

2. CFD model and pyrometer measurements

2.1 CFD model description

To make comparisons with experimental results, contribute towards the enhancement of simulation tools and their application in reactive multilayer systems, CFD simulations have been developed for this work. These models represent an adaptation of previous CFD shoebox models, see [9]–[11], and encompass an Al-Ni reactive multilayer, isolation layer and LTCC substrate. These various layers are shown in the 3-D view of Figure 1, where the base of the shoebox is 4 mm in both length and breadth.

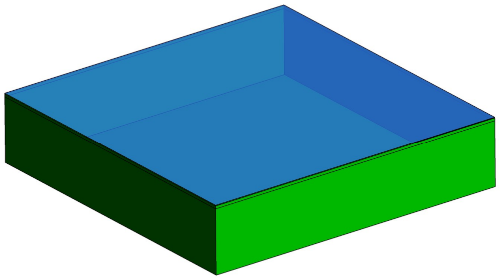

Figure 1: 3-D view of shoebox model layers from top to bottom (Blue = reactive foil, Green = LTCC substrate)

A side view and detailed drawing (for detail A) are shown in Figure 2, where the dimensions of the LTCC have a total thickness of 825 µm, on top of which an isolation layer thickness of 35 µm and a reactive multilayer thickness of 10 µm are placed.

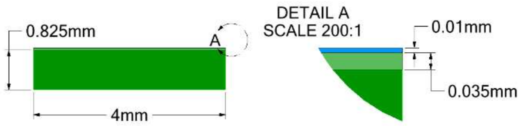

Figure 2: Side view and detailed drawing showing model dimensions

The material properties used in the model are shown in Table 1. Note that the material properties for the

LTCC substrate and 'isolation layer' are identical and correspond to that of GreenTape^{TM} DuPont DP951 material. Therefore, the LTCC substrate has 860 µm thickness, in effect. The material properties for the Al-Ni reactive multilayer are the same as in [12] for a non-reacted layer.

Table 1: Solid material properties for CFD model

	ρ [kg/m3]	k [W/m·K]	C_p [J/kg·K]
LTCC	3100	3.3	600
RMS	5500	152	830

The CFD model comprised solid structures with the aforementioned material properties and air of density 1.225 kg/m^3, specific heat capacity of 1006.43 J/kg·K and thermal conductivity of 0.0242 W/m·K which surrounded them.

The air enveloping the solid structures was itself contained within a 10 mm x 10 mm x 5 mm structure, a volume that was chosen to allow for the region of interest to be significantly displaced from the external boundary conditions. The Boussinesq approximation with a coefficient of expansion of 0.0034/K is used for air to approximate air buoyancy effects caused by temperature gradients in the air with respect to a gravitational acceleration of 9.81 m/s^2.

All of these structures were meshed in ANSYS Workbench 2023R1 using a similar meshing approach as in [10], where the mesh edges were 100 µm in length in the x- and y- directions and 10 µm in the z-direction, hence corresponding to a mesh aspect ratio of 10:1 (x,y:z).

The heat transfer inside the domain, including between the solid structures and air, is accommodated for via the implementation of coupled boundaries and by the energy equation which is solved for numerically in ANSYS Fluent. In addition to the energy equation the continuity, x-, y- and z-momentum equations are also solved numerically for 10,000 time-steps, with a fixed time-step size of 10^{-6} s.

Velocity inlet and pressure outlet boundaries were used on the maximum and minimum y-extents of the domain, where a cross flow of 0.1 m/s, with a turbulence intensity of 5 % and turbulent viscosity ratio of 10 were used, both for the inlet and outlet boundaries respectively.

To provide the model with a thermal input, such as to approximate the behaviour of the reactive foils exothermic heat release, a user defined function (UDF) in the form of equation 1 is implemented in ANSYS Fluent. This heat source is a probability density function (PDF) controllable through parameters, called here A, B, C and D, where C is merely an offset to align with the leading edge of the reactive foil, D corresponds to the velocity and A and B approximately correspond to the amplitude and PDF width. D, the reaction velocity, was given as 5 m/s for the LTCC substrate, as per the high speed camera measurements calculated in [13].

$$A.D \times e^{B(x+C-Dt)^2} \qquad (1)$$

The mesh comprised 5,001,000 cells and took approximately 24 hours to solve using 32 cores with convergence for all governing equations for all 10,000 time steps.

2.2 Pyrometer temperature measurements and sample preparation

Various configurations of reactive multilayer systems on LTCC substrates were studied using micrograph analysis in cross sections, both before and after reactive foil ignition, and by making temperature measurements using a KGA 840 pyrometer.

The KGA 840 pyrometer measured the temperature of each substrate and reactive foil combination at a sampling frequency of 10 kHz and did so in a non-intrusive manner.

3. Results

3.1 Cross-sections and pyrometer measurements

Here the results for various pyrometer measurements and simulation results are discussed and compared with cross-sections presented, where available, to aid with the discussion and interpretation of the results.

4 combinations of 10 µm Ni/Al reactive multilayer and LTCC substrate sample preparation presented (details regarding their preparation discussed in significantly more detail in [13]) are as follows as configuration 1 through 4:

Configuration 1 = Ni/Al on LTCC without surface pre-treatment ("LTCC")
Configuration 2 = Ni/Al on LTCC with 20 nm Ti seed layer ("Ti")
Configuration 3 = Ni/Al on LTCC with 20 nm Ti seed layer and laser surface ablation ("Ti + Laser")
Configuration 4 = Ni/Al on LTCC with AgPd layer and laser ablation of LTCC (AgPd)

Note that the extremely thin structures, e.g. the 20 nm Ti treatment for configuration 2 and surface roughness, are not incorporated into the CFD models as the 3-D CFD models represent a macroscopic approach and such thin structures are beyond the scope of what is realistically feasible to simulate, and mesh, in three dimensions.

Configuration 1 was Ni/Al deposited on LTCC without any surface pre-treatments or enhancements to improve adhesion. The time-temperature histories of this Ni/Al deposited on LTCC and the 3 other configurations (2-4) are shown in Figure 3.

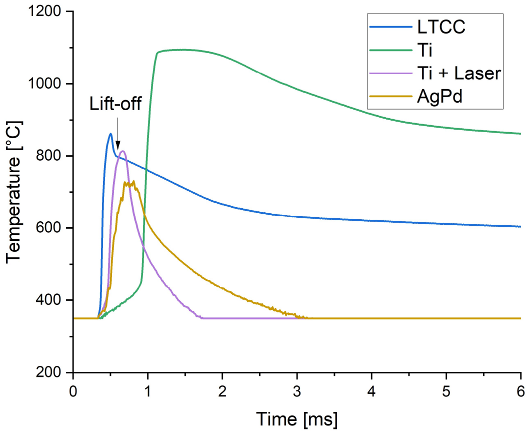

Figure 3: Pyrometer measurements for Ni/Al on LTCC and 3 additional treatment alternatives

In each curve a rapid temperature increase is observed, whereafter a peak temperature value is reached and then a decay in temperature follows. The rate at which this decay occurs is a particularly interesting part, where lift-off of the RMS from the LTCC substrate is suspected at the indicated point in the graph for configuration 1.

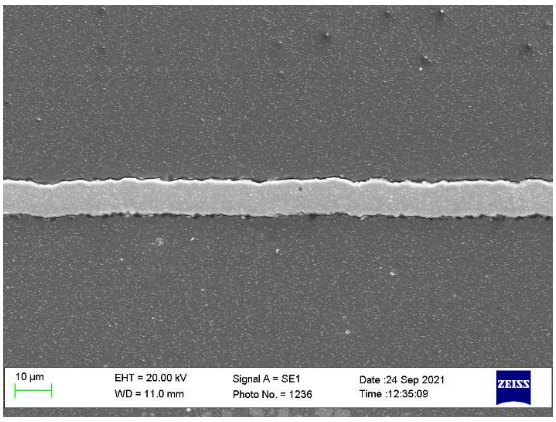

Figure 4: SEM image of deposited and ignited RMS on raw unmachined LTCC morphology (configuration 2)

Figure 4 shows the cross section of an ignited sample where the RMS + 20 nm Ti seed layer was directly deposited on the raw unmachined LTCC substrate with a total thickness of 10 µm – configuration 2. The general shape of the multilayer still looks mostly uniform without any pores, but there is a complete lift-off of the RMS from the substrate. Through the reduced contact between the RMS and the substrate, the heat generated during the exothermic reaction with a peak temperature of about 1100 °C cannot be transported away so that the cooldown takes a lot of time (see Figure 3). Owing to this fact it was not possible to simulate this situation with the current model that does not allow for lift-off, or an air gap of any sort between the substrate and the RMS.

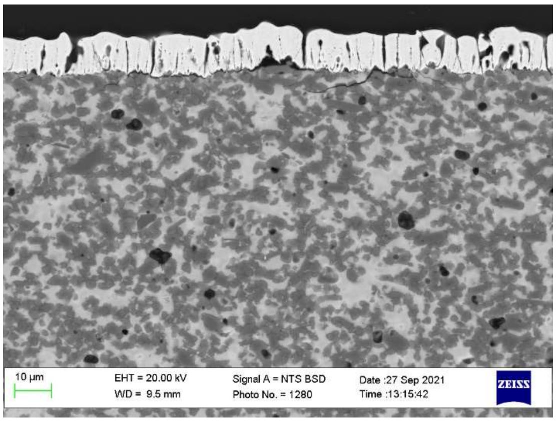

Figure 5: SEM image of deposited and ignited RMS on laser ablated LTCC morphology (configuration 3)

To achieve better adhesion, the LTCC substrate of another sample was laser ablated before the RMS was deposited – configuration 3. The laser ablation of the substrate leads to a good punctual adhesion of the multilayer (see Figure 5). Additionally, the creation of some pores within the multilayer indicates a constraint between the multilayer and the substrate. Some columns within the multilayer were formed, which split the multilayer into some smaller areas whose size depends on the pattern in which the laser is moved across the surface. It can be assumed that a smaller grid of the laser movement results in smaller gaps between the multilayer and the RMS.

Figure 3 shows a peak temperature of more than 800 °C for configuration 3. Due to the enhanced adhesion offered by this pre-treatment the cooldown takes place more effectively.

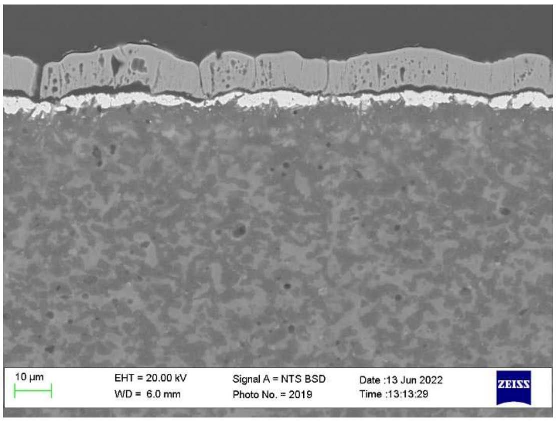

Figure 6: SEM image of deposited and ignited RMS on laser ablated AgPd metallisation (configuration 4)

To improve the adhesion even more for configuration 4 an additional layer of an AgPd metallisation was deposited on the LTCC substrate of another sample (see Figure 6) and laser ablated before the multilayer was deposited. As before, some columns that separate the multilayer were created, and the number of pores increased. Figure 3 shows a peak temperature of more than 700 °C for this configuration.

3.2 CFD comparisons

Given that lift-off could be presumed for at least two of the configurations from the pyrometer measurements – configurations 1 and 2, comparisons were made with the other two configurations (3 and 4) where adhesion was enhanced. Namely, in the case of the Ti seed layer + laser ablation treatment and in the AgPd case, too.

The CFD temperature recordings were written at the central point of the reactive multilayer, on the top surface thereof on the RMS-air interface, for every 10^{-6}s time-step. The pyrometer values are synchronised in time to the CFD data by matching where both curves intersect at 350 °C. Note that there are many pyrometer measurements which saturate at 350 °C, both before and after ignition, owing to the chosen temperature measurement range of the KGA 840 pyrometer.

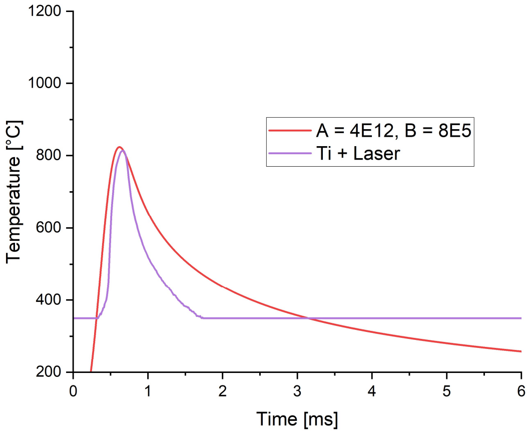

Figure 7: Comparison between CFD model with A = 4E12, B = 8E5 and pyrometer measurement on 20nm Ti + laser ablation configuration (configuration 3)

For configuration 3, the simulation results in Figure 7 show a very close correlation in terms of their peak temperatures, but the warming and cooling rates are under-represented. This discrepancy could potentially be due to the enhanced thermal performance caused by the presence of the Ti that is not included in the CFD model, or perhaps due to imprecise calibration of the heat source parameters in terms of this simulation.

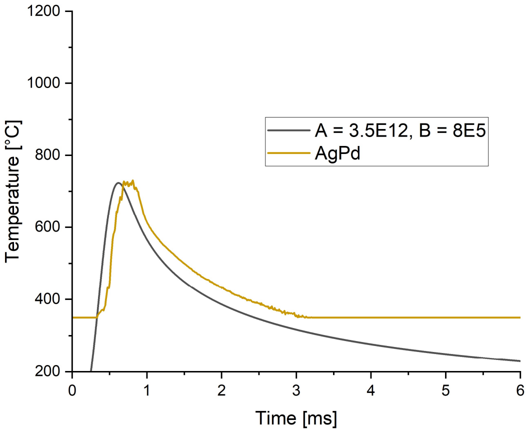

Figure 8: Comparison between CFD model with A = 3.5E12, B = 8E5 and pyrometer measurement on AgPd + laser ablation configuration (configuration 4)

In the configuration 4 sample of Figure 8 there is a good match in the time-temperature histories of the experimental and simulation profiles. The peak temperature, as well as the decay rate appear to be in excellent agreement. It was previously asserted that agreement between the measurements and simulations is heavily compromised due to lift-off. Yet in this instance there is both a good agreement and lift-off. This could indicate that lift-off occurred at some time later under 350 °C.

The experimental trace of Figure 8 is replotted in Figure 9 by shifting -0.112 ms, to match the respective peak values. By evaluating the regions of decay between 0.75 and 2 ms the following expressions for exponential decay were converged on with R^2 values > 0.99 for the experimental (configuration 4) and simulation results as equation (2) and (3), respectively.

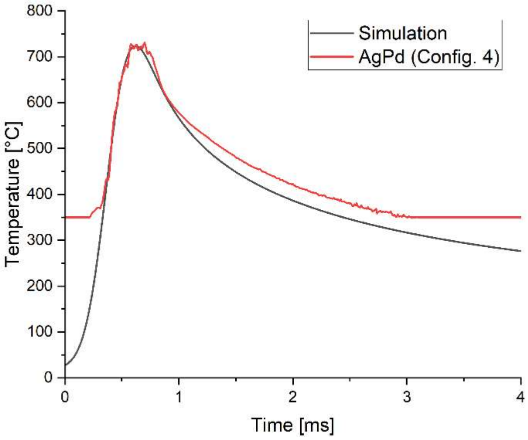

Figure 9: Configuration 4 pyrometer measurements re-adjusted to match peak values

$$T(experiment) = 391.86 + 312.5exp\left(-\frac{(t-0.714)}{0.603}\right) \quad (2)$$

$$T(simulation) = 343.76 + 343.17exp\left(-\frac{(t-0.732)}{0.6366}\right) \quad (3)$$

The magnitudes of the various parameters in these respective exponential decay curve fits are another indicator of the strong agreement for configuration 4 in terms of the post-peak thermal decay behaviour.

4. Conclusions

CFD and experimental measurements can achieve excellent temperature-time history agreement in cases where lift-off of the reactive multilayers does not occur. Should adhesion be insufficient to maintain a bond between substrate and reactive multilayer then subsequent air gaps overturn this agreement.

The use of a PDF as a heat source input function is appropriate in terms of matching the exponential decay of the system post peak temperature and the retrofitting exponentially decaying curves a short period after the peaks have occurred provides close similarities in the temperature decay relationship between the CFD simulations and the experiments.

Acknowledgments

This research work was supported by the Deutsche Forschungsgemeinschaft (DFG, German Research Foundation) – Project-ID 426204742. The authors would like to place on record many thanks to Andreas Ruh for preparing and performing the micro-sections for this paper.

References

[1] D. P. Adams, ‘Reactive multilayers fabricated by vapor deposition: a critical review’, *Thin Solid Films*, vol. 576, pp. 98–128, 2015.

[2] K. Raić *et al.*, ‘CFD analysis of exothermic reactions in Al-Au nano multi-layered foils’, *Materiali in tehnologije*, vol. 45, no. 4, 2011.

[3] A. Syed-Khaja, C. Kaestle, M. Mueller, and J. Franke, ‘A Comprehensive Study on the Automation Potentials and Complexities of Advanced and Alternative Die-Attach Technologies for Power Electronic Applications’, in *Applied Mechanics and Materials*, Trans Tech Publ, 2015, pp. 320–327.

[4] H. Ji, M. Li, S. Ma, and M. Li, ‘Ni3Sn4-composed die bonded interface rapidly formed by ultrasonic-assisted soldering of Sn/Ni solder paste for high-temperature power device packaging’, *Materials & Design*, vol. 108, pp. 590–596, 2016.

[5] J. Braeuer, J. Besser, M. Wiemer, and T. Gessner, ‘A novel technique for MEMS packaging: Reactive bonding with integrated material systems’, *Sensors and Actuators A: Physical*, vol. 188, pp. 212–219, 2012.

[6] H. Jantunen, T. Kangasvieri, J. Vähäkangas, and S. Leppävuori, ‘Design aspects of microwave components with LTCC technique’, *Journal of the European Ceramic Society*, vol. 23, no. 14, pp. 2541–2548, 2003.

[7] M. Matters-Kammerer *et al.*, ‘Material properties and RF applications of high k and ferrite LTCC ceramics’, *Microelectronics Reliability*, vol. 46, no. 1, pp. 134–143, 2006.

[8] A. Bittner, A. Ababneh, H. Seidel, and U. Schmid, ‘Influence of the crystal orientation on the electrical properties of AlN thin films on LTCC substrates’, *Applied surface science*, vol. 257, no. 3, pp. 1088–1091, 2010.

[9] A. Yuile and S. Wiese, ‘CFD Simulations of Reactive Multi-Layer Usage in Joining Processes’, in *21st International Conference on Thermal, Mechanical and Multi-Physics Simulation and Experiments in Microelectronics and Microsystems (EuroSimE)*, IEEE, 2020, pp. 1–5.

[10] A. Yuile, A. Schulz, E. Wiss, J. Müller, and S. Wiese, ‘The Simulated Effect of Adding Solder Layers on Reactive Multilayer Films Used for Joining Processes’, *Applied Sciences*, vol. 12, no. 5, p. 2397, 2022.

[11] A. Yuile, A. Schulz, J. Müller, and S. Wiese, ‘Analysis of selective bonding processes using reactive multi-layers for system integration on LTCC based SiPs’, *Microsystem Technologies*, pp. 1–15, 2022.

[12] S. Liang, Y. Zhong, S. Robertson, A. Liu, Z. Zhou, and C. Liu, ‘Investigation of thermo-mechanical and phase-change behavior in the Sn/Cu interconnects during self-propagating exothermic reaction bonding’, in *2020 IEEE 70th Electronic Components and Technology Conference (ECTC)*, IEEE, 2020, pp. 269–275.

[13] A. Schulz *et al.*, ‘Characterization of Reactive Multilayer Systems deposited on LTCC featuring different surface morphologies’, in *MikroSystemTechnik Congress 2021; Congress*, VDE, 2021, pp. 1–5.

5.6 Paper 6: 2D Computational Fluid Dynamics Simulation Analysis of the Assembly of Low-Temperature Cofired Ceramics/Low-Temperature Cofired Ceramics and Si/Si Sandwiches by Reactive Bonding

5.6.1 Veröffentlichungshinweise

Adam Yuile[1], Alexander Schulz[2], Erik Wiss[1], Jens Müller[2], Steffen Wiese[1]

[1]Chair of Microintegration and Reliability, Faculty of Natural Sciences and Technology, Saarland University, Saarbrücken, Germany

[2]Electronics Technology Group, Faculty of Electrical Engineering and Information Technology, TU Ilmenau, Ilmenau, Germany

Advanced Engineering Materials (2025), 27.3, 2302283

Die Originalveröffentlichung ist abrufbar unter:
https://doi.org/10.1002/adem.202302283

5.6.2 Synopse

Diese Veröffentlichung untersucht den Einfluss des Substratmaterials auf den reaktiven Fügeprozess anhand eines Vergleichs zwischen LTCC/LTCC- und Si/Si-Stapeln. Die Motivation ergibt sich aus der deutlich geringeren Wärmeleitfähigkeit der LTCC im Vergleich zu Si, was sich maßgeblich auf die Temperaturentwicklung im Lot auswirkt. Ziel der Arbeit war es, den Schmelz- und Erstarrungsprozess des Lots zu analysieren, mit besonderem Fokus auf den Temperaturverläufen und dem zeitlichen Verlauf des Anteils an flüssigem Lot.

Hierzu wurde ein zweidimensionales CFD-Modell mit einer Gesamtgröße von 10 mm x 5 mm entwickelt, in dessen Zentrum sich der 4 mm lange und 1,63 mm hohe Stapel befindet. Die LTCC- bzw. Si-Schichten besitzen jeweils eine Dicke von 0,8 mm und sind mit einer 5 µm dicken Ag-Metallisierung versehen, auf die eine ebenso dicke Lotschicht aufgebracht ist (Schmelztemperatur 220 °C, Erstarrungstemperatur 217 °C). Die Dicke des RMS beträgt 10 µm. Die exotherme Reaktion wurde durch eine sich mit 5 m/s vom linken zum rechten Rand ausbreitende Rechteckfunktion modelliert.

Die Ergebnisse zeigen, dass in beiden Systemen die Zeit bis zum Erreichen des Temperaturmaximums im Lot vergleichbar ist. Allerdings liegt dieses im LTCC-Stapel mit ca. 500 °C deutlich über dem des Si-Stapels mit 250 °C. Während sich beim Si-Stapel das flüssige Lotvolumen stets auf einen schmalen Bereich beschränkt, erreicht das Lot im LTCC-Stapel zeitweise einen vollständig flüssigen Zustand. Die Abkühlzeit zwischen Schmelz- und Erstarrungstemperatur ($\Delta T = 3\ °C$) beträgt beim Si-Stapel lediglich 5 µs, während sie beim LTCC-Stapel bei 357 µs liegt, was der latenten Wärme eine erheblich wichtigere Rolle zukommen lässt.

Im Kontext des Gesamtprojekts leistet diese Veröffentlichung einen Beitrag zur Beantwortung der Frage, wie sich die thermophysikalischen Eigenschaften der Substratmaterialien auf Temperaturentwicklung und Schmelzverlauf während des reaktiven Fügeprozesses auswirken.

5.6.3 Vollständiger Artikel

RESEARCH ARTICLE

ADVANCED ENGINEERING MATERIALS
www.aem-journal.com

2D Computational Fluid Dynamics Simulation Analysis of the Assembly of Low-Temperature Cofired Ceramics/Low-Temperature Cofired Ceramics and Si/Si Sandwiches by Reactive Bonding

Adam Yuile, Alexander Schulz, Erik Wiss, Jens Müller, and Steffen Wiese*

Numerical computational fluid dynamics simulations have been performed on 2D sandwich models to compare the performance of low-temperature cofired ceramics (LTCC)/LTCC and Si/Si sandwiches used in reactive bonding. In the sandwich model layers of solder, silver and a reactive multilayer used to bond the substrates are modeled. Additional to this, the surrounding air environment is also modeled. For simulating the heat released by the multilayer system, a user-defined function in the form of a square wave is written for the heat source with a defined width, corresponding to the reaction width, and this propagates at a fixed speed. Two sandwiches, one with LTCC/LTCC, and the other with Si/Si, are simulated and their response analyzed in terms of the solidification/melting of the solder and their respective time–temperature histories.

1. Introduction

Reactive multilayer systems (RMSs), used for bonding interconnects, prove highly effective for nanoscale film materials, such as Ni/Al, which contain stored chemical energy.[1] Subsequent to ignition, for example, via a spark, these layers bond, releasing substantial energy as heat which allows the system to self-propagate.[2] This exothermic heat release can then be used for melting solder paste to achieve localized soldering of heat-sensitive components,[1] as an example, which downstream from the melting phase could then help form a permanent bond, upon solidification.[3]

In recent times, there has been a growing interest in RMSs across various applications, notably in die bonding.[4,5] This surge in interest stems from the essential need to integrate thermally diverse components[6] (e.g., those with significantly different coefficients of thermal expansion) into specialized components while concurrently minimizing thermally induced stresses to uphold reliability.

On silicon-based substrates, the deposition of reactive multilayers has already been successfully implemented,[7] but the intrinsic roughness of low-temperature cofired ceramics (LTCC) substrate technologies (in the range of 0.4–1 μm[8–10]) makes this deposition more difficult to achieve on LTCC technologies, despite the need and demand to diversify manufacturing technologies.[11]

Conventional soldering techniques, like reflow soldering, mandate that all structures on a PCB must endure a heat cycle, a process which inflicts undesired stresses on the components.[3] In contrast, RMSs allow the directed focus of heat sources onto specific localized areas.

Owing to the high-speed attributes of these RMSs and the innate nature of their propagation, during bonding, it becomes an ideal ground for simulation technology to be applied.[1] This technology represents one of the most advanced simulation methodologies.

While simulation methods in electronic packaging have primarily focused on electrical, thermal, and thermomechanical issues during the operation of assemblies, the simulation of joining processes, particularly reactive bonding, is still developing. Simulations of reactive bonding processes often use finite-element/volume methods to model heat flow in multilayer substrates.

For instance in ref. [12], a cylindrically symmetrical grid has been used to approximate temperature distributions and reaction front velocities, assuming the propagation direction of the reaction front. Other simulation approaches, such as ref. [13], make use of 2D finite-element models that simulate the temperature and solder melting/solidification progression, albeit for different types of substrates, namely copper.

Further to this, in this article, the emphasis is very much placed on LTCC/LTCC and Si/Si bonding and comparing the performance of the two different substrate types/combinations. The vast majority of previous investigations in the RMS bonding

---

A. Yuile, E. Wiss, S. Wiese
Chair of Microintegration and Reliability
Saarland University
Saarbruecken 66123, Germany
E-mail: adam.yuile@uni-saarland.de

A. Schulz, J. Müller
Faculty of Electrical and Computer Engineering
Department of Electronics Technology
TU Ilmenau
Ilmenau 98693, Germany

The ORCID identification number(s) for the author(s) of this article can be found under https://doi.org/10.1002/adem.202302283.

DOI: 10.1002/adem.202302283

field have almost always been related to the joining exclusively of silicon to silicon,[7,14–16] metal to metal[17,18] and silicon to metal.[19] With respect to the reactive bonding process, there are two major differences, first the thermal conductivity and, second, the surface roughness. The thermal conductivity of an LTCC substrate is orders of magnitude lower than those of silicon and copper. Owing to the high aforementioned intrinsic LTCC roughness, the deposition of reactive nanolayers leads to a very different structure of the RMS compared to the smooth surfaces of silicon and metal substrates; hence, the behavioral differences are likely to be important and warrant significant investigative effort.

2. Computational Fluid Dynamics Model

To study the performance differences between Si/Si, case (i), and LTCC/LTCC, case (ii), sandwiches, a new 2D model was made using the ANSYS Workbench 2023R2 software, in contrast to the 3D models that were previously studied.[20] This meant that the models are principally similar to other 2D analyses, e.g.,[13] only that the air surrounding the solid bodies is also modeled and therefore no convection boundaries are prescribed on the solid boundaries.

In this new 2D model, a domain with extents of 10 × 5 mm was modeled, in which a centrally located sandwich model, 4 mm in length, of either Si/Ag/solder/RMS/solder/Ag/Si, case (i), or LTCC/Ag/solder/RMS/solder/Ag/LTCC, case (ii), was housed.

In LTCC technology, the intrinsic surface roughness, and the scatter thereof, are known to affect the RMS behavior in ways that are not similarly suffered for by Si substrates. However, for simplicity of direct comparison, all layers are present in both cases and even the same substrate thicknesses are used, despite Si substrates tending to be thinner.

Table 1. Model layer thicknesses, for case (i) and (ii).

	Layer thickness [μm]
LTCC/Si	800
Ag	5
Solder	5
RMS	10

The computational fluid dynamics (CFD) model extent of 10 × 5 mm was considered large enough to mitigate any significant influence of the external boundaries on the progression of the reaction. The respective model thicknesses being as per **Table 1**.

These same model thicknesses are also shown in **Figure 1**, with a detailed view of the thin layers (DETAIL A) also presented on the right.

The RMS, approximating an Ni/Al-based system, was effectively ignited from the left of the sandwich and the exothermic heat release propagated in the positive x direction, based on a square wave function, as per Equation (1). The propagation velocity is $5\ \mathrm{m\,s^{-1}}$, a typical value for RMS propagation on LTCC, without pretreatment.[21] C is a constant, of magnitude 1.44×10^5, u is the velocity, w_r the reaction width, and Δt the time step

$$P = \frac{C}{u w_\mathrm{r}\,\Delta_\mathrm{t}} \qquad (1)$$

This volumetric power density, P, was only nonzero out with the bounds of the reaction, which started at the leading edge and moved, consistent with the reaction width and reaction velocity, in the positive x direction. The output of these functions would supply the 2D model with a volumetric power density, effectively as a heat input function, which was assumed to be equivalent to the exothermic heat released by the RMS, differing from the previous probability density-function-based approach.[22]

Table 2 shows the solid material properties that were used for the LTCC—GreenTape DuPont DP951, Si, Ag, and RMS—corresponding to a non-reacted layer,[13] where the Si and Ag material properties are sourced from ANSYS Fluent material databases. These parameters were assumed to be constant values, which could be improved upon in future work, given that the temperature variations are large and significant disparities in material properties could be present.

The air in the CFD model, which envelopes the solid structures, has density of $1.225\ \mathrm{kg\,m^{-3}}$, thermal conductivity of $0.0242\ \mathrm{W\,m^{-1}\,K^{-1}}$, and a specific heat capacity of $1006.43\ \mathrm{J\,kg^{-1}\,K^{-1}}$. A coefficient of expansion of $0.0034\ \mathrm{K^{-1}}$ is used for air, through the Bousinessq approximation, to estimate air buoyancy effects caused by temperature gradients, with

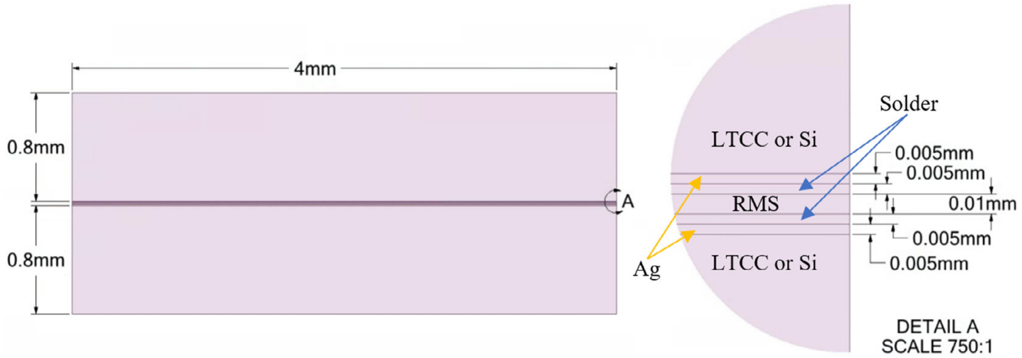

Figure 1. 2D CFD sandwich model dimensions, case (i) and (ii), with detail A highlighting 750:1 view of thin layers, and Ag, with Ni/Al RMS and solder layers highlighted.

Table 2. Solid material properties for CFD model, based on ANSYS fluent material database, GreenTape DuPont DP951 data sheet, and non-reacted nanofoil.[13]

	ρ [kg m^{-3}]	k [W m^{-1} K^{-1}]	C_p [J kg^{-1} K^{-1}]
LTCC	3100	3.3	600
Si	2500	710	100
Ag	10 490	234.28	419.97
Ni/Al RMS[13]	5500	152	830

respect to a gravitational acceleration of 9.81 m s^{-2} enacting body forces on the air.

To model solder transitions between the liquid/molten and solid state, and the accompanying latent heat, the melting/solidification model was turned on in ANSYS Fluent. The melting/solidification model in ANSYS Fluent makes use of an enthalpy–porosity approach which provides an indication of the fraction of a cell volume that is in the molten state, where a liquid fraction of 0 corresponds to the solid state and, likewise, a liquid fraction of 1 the molten state. The pure solvent melting heat for the solder is 58.5 kJ kg^{-1}. And, 217 and 220 °C were given as the liquidus and solidus temperatures of the solder, thermal properties that closely resemble a typical SAC (tin–silver–copper) solder. The solder was specified to have density of 7000 kg m^{-3}, specific heat capacity of 230 J kg^{-1} K^{-1}, thermal conductivity of 63.2 W m^{-1} K^{-1}, and dynamic viscosity of 0.1 Pa s^{-1}.

All of the aforementioned solid and fluid structures were meshed using ANSYS Workbench 2023R2, by applying a similar approach to that previously utilized.[22] The mesh was 1 800 000 cells in size with edge lengths of 1.6667 and 16.667 μm in the vertical and horizontal directions. These mesh specifications corresponded to a minimum of three elements throughout the thickness of the thinnest structures—i.e., that of the Ag metallization, leading to a standard cell aspect ratio of 10:1.

On the left boundary, a velocity inlet of 0.1 m s^{-1}, with 5% turbulence intensity and turbulence viscosity ratio of 10, was used with a pressure outlet boundary on the opposite side having identical turbulence properties and a gauge pressure of 0 Pa.

Heat transfer within the domain, including between solid structures and air, is accounted for through the implementation of coupled boundaries in combination with the energy equation. The energy equation is solved numerically in ANSYS Fluent, together with the continuity, and x- and y-momentum equations for 10 000 individual time steps, with a fixed time step increment of 10^{-6} s.

Using 32 cores to solve numerically, convergence was attained for all 10 000 time steps, using default convergence criteria and under-relaxation factors. The initial time steps required on the order of 50 iteration cycles to converge, thereafter convergence was achieved in a handful of iterations, for each time step.

3. Results

Here, the results are presented and compared for the two aforementioned cases, namely case (i) with Si/Si sandwich and case (ii) with LTCC/LTCC sandwich. First, to use an appropriate amount of heat as input, comparisons between experimental measurements presented in ref. [20] made on 10 μm Ni/Al RMS deposited on pure LTCC (Experiment 1) and titanium metallization + laser structuring (Experiment 2) and an additional CFD model were made for different reaction widths—100, 300, and 900 μm, where the temperature contour results are shown in **Figure 2** and the time–temperature progression at a measuring point on the symmetry line inside the RMS (2 mm downstream from reaction initiation location) in **Figure 3**.

The temperature contours, shown here 0.4 ms after reaction initiation in Figure 2, demonstrate the reaction moving in the positive x direction with wider temperature contours being left in the wake of the reaction and a tight temperature peak in the reaction zone. Note due to the thin, high aspect ratio nature of the RMS, and other structures that only the first 2 mm of the sandwich is displayed, concentrated toward the leading edge of the domain. This holds true for subsequent plots of temperature and liquid fraction contours.

In **Figure 4**, a zoomed-in view of that of Figure 2 shows the temperature contour levels in more detail, together with a scale which shows that the highest temperature band (880–975 °C) after 0.4 ms covers an area wider than 100 μm (approximately half of the reaction width—150 μm) and is limited to the

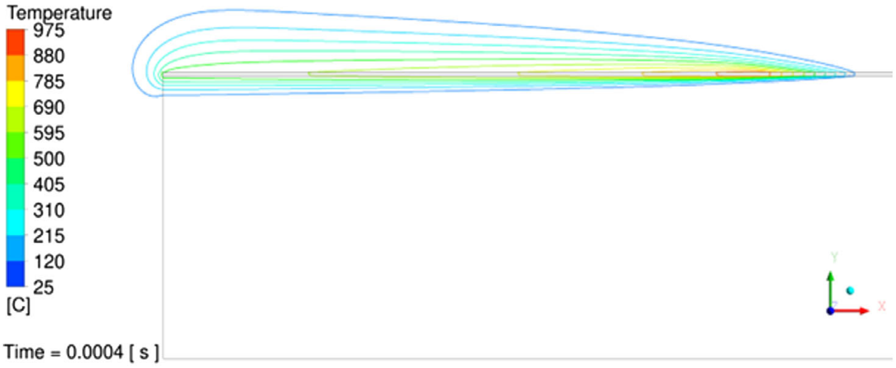

Figure 2. Temperature contours 0.4 ms after reaction initiation for 10 μm Ni/Al RMS deposited on 800 μm LTCC substrate with 300 μm RMS reaction width.

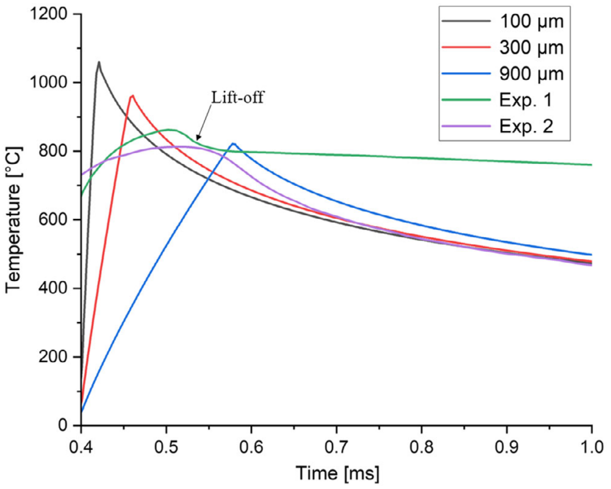

Figure 3. Square wave function reaction width variation (100, 300 and 900 µm) versus experimental pyrometer measurements for 10 µm Ni/Al RMS on pure LTCC substrate. Exp. 1 = 10 µm Ni/Al RMS deposited on pure LTCC, Exp. 2 = titanium metallization + laser–structure treatment.

thickness of the RMS, less a slight incursion into the air above the RMS. Even with a zoomed-in view focused on the reaction area, it is observed that the contour bands are very tight inside the LTCC, and thus the temperature gradients are very strong.

It was hypothesized in the experimental measurements of Figure 3 that liftoff, as highlighted on the figure, occurred during the pyrometer measurements[20] of experiment 1—owing to the inadequate adhesion of RMS deposited on pure LTCC, so the temperature data there should be interpreted with some caution. That said, a reaction width of around 300 µm was found to offer a sensible match, both in terms of peak temperature attained and temperature decay rate, post-peak. The influence of this suspected liftoff of the 10 µm Ni/Al RMS deposited on LTCC is further demonstrated with experimental configuration 2, for an LTCC with titanium metallization and laser-structured treatment to improve adhesion,[20] where a closer match between the simulated and experimental results is obtained, albeit for a slightly different configuration.

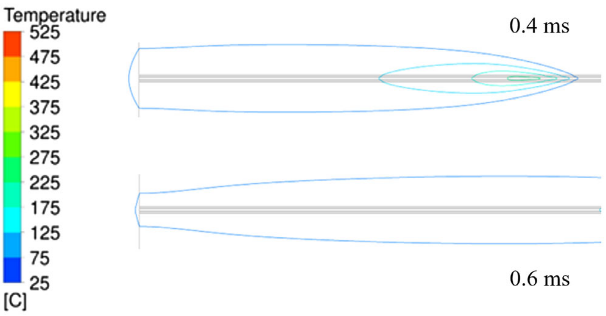

Figure 5. Temperature contours after 0.4 ms, case (i). Model assumptions: bottom substrate = Si, thickness = 800 µm, top substrate = Si, thickness 800 µm, joining zone: bottom and top surface layer = Ag, thickness 5 µm, Ni–Al RMS layer, thickness = 10 µm placed centrally between solder layers of 5 µm thickness.

Moving forward with a reaction width value for the square wave function of 300 µm, comparisons were then made between the performance of Si/Si, case (i), and LTCC/LTCC sandwiches, case (ii), in ANSYS Fluent, using the CFD modeling approach that has previously been described.

The temperature contours for the Si/Si sandwich are shown for 0.4 and 0.6 ms as shown in **Figure 5**. The peak temperatures are relatively modest and the spreading of the heat away from the bonding zone is observed to be quite effective, with all areas in the first 2 mm of the sandwich under 125 °C by 0.6 ms.

In **Figure 6**, the liquid fraction contour plots are shown, also for 0.4 and 0.6 ms after reaction initiation. After 0.4 ms, a small region of molten solder, narrower even than the reaction width, is observed and this small bubble of molten solder has already been observed to have completely resolidified by 0.6 ms.

In **Figure 7**, the temperature contours at 0.4, 0.6, and 1.2 ms after reaction initiation are shown for case (ii). Comparing back to case (i), in Figure 5, for 0.4 and 0.6 ms, one can observe that the temperatures are significantly higher for the LTCC/LTCC sandwich, despite the same amount of energy being provided through the volumetric power density/heat source input function.

Furthermore, the temperature contour bands are much narrower, and this is because the heat is spread less effectively,

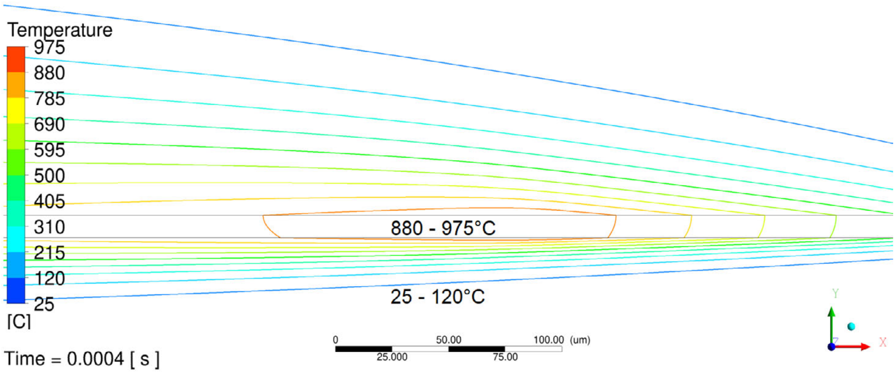

Figure 4. Zoomed-in temperature contour levels for 10 µm Ni/Al RMS on pure LTCC substrate, with highest and lowest contour levels highlighted.

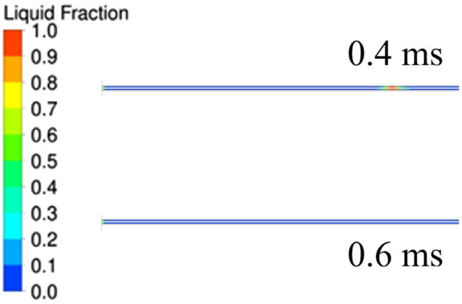

Figure 6. Liquid fraction contours for Si/Si sandwich after 0.4 ms (upper) and 0.6 ms (lower), case (i). Model assumptions: bottom substrate = Si, thickness = 800 µm, top substrate = Si, thickness 800 µm, joining zone: bottom and top surface layer = Ag, thickness 5 µm, Ni–Al RMS layer, thickness = 10 µm placed centrally between solder layers of 5 µm thickness.

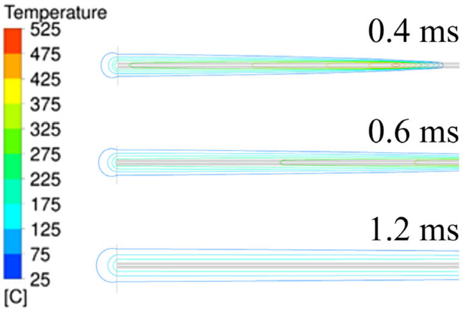

Figure 7. Temperature contours for LTCC/LTCC sandwich after 0.4 ms (upper), 0.6 ms (center), and 1.2 ms (lower) case (ii). Model assumptions: bottom substrate = LTCC, thickness = 800 µm, top substrate = LTCC, thickness 800 µm, joining zone: bottom and top surface layer = Ag, thickness 5 µm, Ni–Al RMS layer, thickness = 10 µm placed centrally between solder layers of 5 µm thickness.

owing to the low thermal conductivity of the LTCC material. This is particularly true for 1.2 ms where there is still much more significant elevated temperature inside the LTCC, long after this heat had already dissipated for the Si/Si case—case (ii).

These prolonged elevations in the local temperature in the bonding zone leave a pronounced influence on the liquid fraction contours. In **Figure 8**, the molten solder volume is orders of magnitude larger than in the Si/Si case of Figure 6 at 0.4 ms post-ignition, to the extent that by 0.6 ms the entire solder in the region of interest is still in the molten state.

At 1.2 ms after reaction initiation, the solder in the LTCC/LTCC sandwich has started to resolidify and a bond can be successfully formed. In some cases, it may prove advantageous to have such a large percentage of the solder being molten concurrently, but from another perspective, it could highlight a lack of controlled precision with the method, in practice.

In **Figure 9**, direct graphical comparisons are made between the LTCC/LTCC and Si/Si sandwiches at several points in the models, all 2 mm downstream from leading edge at the center of the RMS, solder and at 5 µm depth into the substrate (Si or LTCC). The temperatures are clearly elevated by an additional 250 °C for the LTCC and the amount of time to achieve cooldown is also significantly longer. This is perhaps not ideal for bonding precision, and neither for the solder performance, but can help to reduce thermal shock.

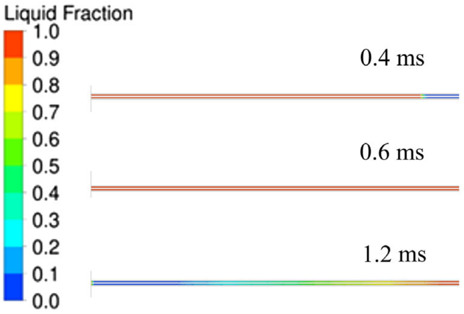

Figure 8. Liquid fraction contours for LTCC/LTCC sandwich after 0.4 ms (upper), 0.6 ms (center), 1.2 ms (lower), case (ii). Model assumptions: bottom substrate = LTCC, thickness = 800 µm, top substrate = LTCC, thickness 800 µm, joining zone: bottom and top surface layer = Ag, thickness 5 µm, Ni–Al RMS layer, thickness = 10 µm placed centrally between solder layers of 5 µm thickness.

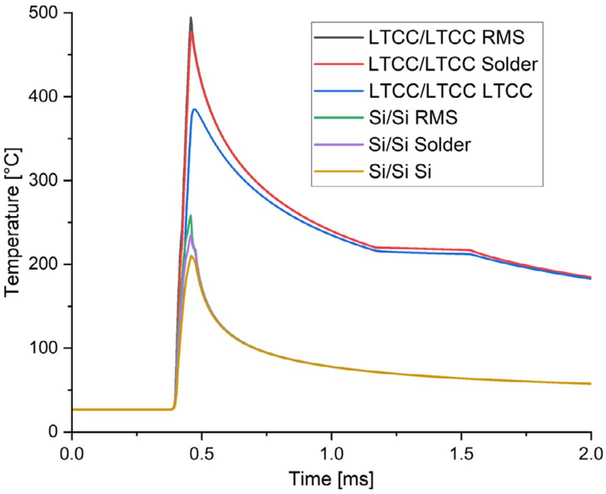

Figure 9. Comparisons between observed temperatures in the LTCC/LTCC versus Si/Si sandwiches in the RMS, solder and within the sandwiches themselves—at 5 µm depth into the substrates.

Table 3. Time for solder to reach peak temperature, solder liquidus, and solidus temperature.

Substrate combination	t_{peak}	t_{liquidus}	t_{solidus}
LTCC/LTCC	0.461	1.174	1.531
Si/Si	0.458	0.468	0.473

These significant deviations, in not just thermal performance but also temporal differences, are highlighted in **Table 3**. In Table 3, it is clear to see that although the time from ignition to reach peak temperature does not differ significantly between

LTCC and Si, the time for the solder to cool back down to solder liquidus and solidus temperatures is significantly longer. Furthermore, while the time to cool down the 3 °C between the solder solidus and liquidus temperatures takes only 10 µs for Si/Si, this takes 357 µs for LTCC/LTCC, which is significantly longer and shows that the latent heat of the solder plays a much more noteworthy role for LTCC substrates.

4. Conclusion

While using LTCC substrates can bring many advantages, e.g., significant reductions in manufacturing cost relative to Si counterparts, the CFD simulation results show that the temperatures seen in LTCC/LTCC sandwiches are much higher than those in Si/Si. This is due to the lower thermal conductivity of the LTCC substrates and their relative inability to transport heat away from the bonding zone. Before this work, the temperature fields and solder progression were not studied in such detail for LTCC/LTCC.

Based on this CFD analysis, it was also highlighted that the latent heat of the solder plays a much more substantial role during the cooldown for the LTCC than the Si substrates, and that the time taken for the cooldown to transition between the solder liquidus and solidus temperatures was 35x greater for the LTCC substrates.

This extra heat could contribute to a longer than necessary melting phase of the solder, at much higher temperatures, which contribute to detrimental effects on the bonding performance as well as the increased impact, in terms of the stresses inflicted during the bonding necessitating the use of thicker solder layers to sustain these extra loads.

The question as to how to solve this remains uncertain, but perhaps using thicker solder pastes and more precisely calculated RMS deposition thicknesses could be an option based on these CFD simulation results. This analysis quantifies the severity of the issue to show the magnitude of the temperatures experienced in the bonding zone, which are extremely difficult to determine through experimental means.

Acknowledgements

This research work was supported by the Deutsche Forschungsgemeinschaft (DFG, German Research Foundation)—project ID 426204742.

Open Access funding enabled and organized by Projekt DEAL.

Conflict of Interest

The authors declare no conflict of interest.

Author Contributions

Adam Yuile: Formal analysis (lead); Investigation (lead); Writing—original draft (lead); Writing—review & editing (lead). **Alexander Schulz**: Data curation (equal). **Erik Wiss**: Formal analysis (equal); Funding acquisition (equal); Supervision (lead). **Jens Müller**: Funding acquisition (equal); Supervision (supporting). **Steffen Wiese**: Formal analysis (supporting); Writing—review & editing (supporting).

Data Availability Statement

Research data are not shared.

Keywords

computational fluid dynamics, low-temperature cofired ceramics, reactive multilayers, Si/Si

Received: December 31, 2023
Revised: July 12, 2024

[1] D. P. Adams, *Thin Solid Films* **2015**, *576*, 98.
[2] K. Raić, R. Rudolf, P. Ternik, Z. Žunič, V. Lazić, D. Stamenković, T. Tanasković, I. Anžel, *Mater. Tehnol.* **2011**, *45*, 335.
[3] M. Mueller, J. Franke, in *2014 IEEE 16th Electronics Packaging Technology Conf. (EPTC)*, IEEE, Singapore **2014**.
[4] H. Ji, M. Li, S. Ma, M. Li, *Mater. Des.* **2016**, *108*, 590.
[5] A. Syed-Khaja, C. Kaestle, M. Mueller, J. Franke, *Appl. Mech. Mater.* **2015**, *794*, 320.
[6] J. Braeuer, J. Besser, M. Wiemer, T. Gessner, in *2011 16th Int. Solid-State Sensors, Actuators and Microsystems Conf.*, IEEE, Beijing, China **2011**.
[7] J. Braeuer, J. Besser, M. Wiemer, T. Gessner, *Sens., Actuators A* **2012**, *188*, 212.
[8] M. Matters-Kammerer, U. Mackens, K. Reimann, R. Pietig, D. Hennings, B. Schreinemacher, R. Mauczok, S. Gruhlke, C. Martiny, *Microelectron. Reliab.* **2006**, *46*, 134.
[9] H. Jantunen, T. Kangasvieri, J. Vähäkangas, S. Leppävuori, *J. Eur. Ceram. Soc.* **2003**, *23*, 2541.
[10] A. Bittner, A. Ababneh, H. Seidel, U. Schmid, *Appl. Surf. Sci.* **2010**, *257*, 1088.
[11] M. Glaser, S. Matthes, S. S. Riegler, J. Hildebrand, J. P. Bergmann, P. Schaaf, I. Gallino, in *Engineering for a Changing World: Proc.; 60th ISC, Ilmenau Scientific Colloquium*, Technische Universität Ilmenau, Ilmenau, Germany **2023**.
[12] R. Masser, J. Braeuer, T. Gessner, *J. Appl. Phys.* **2014**, *115*, 244311.
[13] S. Liang, Y. Zhong, S. Robertson, A. Liu, Z. Zhou, C. Liu, in *2020 IEEE 70th Electronic Components and Technology Conf. (ECTC)*, IEEE, Orlando, FL **2020**.
[14] K. Maekawa, K. Kodama, S. Miyake, T. Namazu, *Jpn. J. Appl. Phys.* **2021**, *60*, SCCL15.
[15] B. Boettge, J. Braeuer, M. Wiemer, M. Petzold, J. Bagdahn, T. Gessner, *J. Micromech. Microeng.* **2010**, *20*, 064018.
[16] K. Maekawa, S. Ito, T. Namazu, *Jpn. J. Appl. Phys.* **2020**, *59*, SIIL01.
[17] J. Wang, E. Besnoin, A. Duckham, S. J. Spey, M. E. Reiss, O. M. Knio, T. P. Weihs, *J. Appl. Phys.* **2004**, *95*, 248.
[18] J. Matteau, in *Int. Symp. on Microelectronics, Int. Microelectronics Assembly and Packaging Society*, Andover, Hampshire **2011**.
[19] H. Ji, Y. Qiao, M. Li, *Scr. Mater.* **2016**, *110*, 19.
[20] E. Wiss, A. Yuile, A. Schulz, J. Müller, S. Wiese, in *2023 24th Int. Conf. on Thermal, Mechanical and Multi-Physics Simulation and Experiments in Microelectronics and Microsystems (EuroSimE)*, IEEE, Graz, Austria **2023**.
[21] A. Schulz, H. Bartsch, N. Gutzeit, S. Matthes, M. Glaser, A. Ruh, J. Mueller, P. Schaaf, J. P. Bergmann, S. Wiese, in *MikroSystem Technik Congress 2021*, VDE, Ludwigsburg, Germany **2021**.
[22] A. Yuile, A. Schulz, E. Wiss, J. Müller, S. Wiese, *Appl. Sci.* **2022**, *12*, 2397.

5.7 Paper 7: Experimental Study on Reactive Joining Processes on LTCC Substrates

5.7.1 Veröffentlichungshinweise

Erik Wiss[1], Nesrine Jaziri[2], Adam Yuile[1], Jens Müller[2], Steffen Wiese[1]

[1]Chair of Microintegration and Reliability, Faculty of Natural Sciences and Technology, Saarland University, Saarbrücken, Germany

[2]Electronics Technology Group, Faculty of Electrical Engineering and Information Technology, TU Ilmenau, Ilmenau, Germany

2024 IEEE 10th Electronics System-Integration Technology Conference (ESTC)

Die Originalveröffentlichung ist abrufbar unter:
https://doi.org/10.1109/ESTC60143.2024.10712029

5.7.2 Synopse

Diese Veröffentlichung untersucht den Fügeprozess eines LTCC-Chips auf einem LTCC-Substrat mit einer elektrisch gezündeten NanoFoil®. Die Motivation ergibt sich aus der Notwendigkeit, zuverlässige Fügeverbindungen zu erzeugen, die den thermischen, mechanischen und elektrischen Anforderungen mikroelektronischer Anwendungen genügen. Ziel der Arbeit war es, erste Fügeversuche unter verschiedenen Anpressdrücken durchzuführen und die Fügezonen mit einem LM zu bewerten.

Hierzu wurden LTCC-Chips (3 mm x 3 mm) mit vollflächiger Metallisierung auf passende Substrate (15 mm x 3 mm) gefügt. Nach der exakten Ausrichtung des Chips zum Substrat mit dem FINEPLACER® wurde die in 4 mm x 4 mm große Stücke geschnittene Reaktivfolie auf dem Substrat platziert und der Fügeprozess gestartet. Nach Erreichen von Zieltemperatur und Anpressdruck (ca. 2, 22 und 44 MPa) wurde die Folie elektrisch gezündet. Anschließend wurden Querschliffe der Proben angefertigt und im LM untersucht.

Die Ergebnisse zeigen, dass das reaktive Fügen zweier LTCC-Komponenten mit vollflächiger Metallisierung mit einem RMS grundsätzlich realisierbar ist. Der Anpressdruck beeinflusst die Qualität der Fügezone signifikant: Bei zu geringem Druck bildeten sich großflächige Lücken zwischen Metallisierung und RMS bzw. Lot, bei zu hohem Druck lösten sich Metallisierung und Lot vollständig ineinander auf. Die Ergebnisse liefern erste Erkenntnisse zur Druckabhängigkeit des Prozesses und bilden die Grundlage für die vertiefte Analyse in Paper 8.

Im Kontext des Gesamtprojekts leistet diese Veröffentlichung einen Beitrag zur Beantwortung der Frage, wie sich der Anpressdruck auf den reaktiven Fügeprozess auswirkt.

5.7.3 Vollständiger Artikel

Experimental Study on Reactive Joining Processes on LTCC Substrates

Erik Wiss
Chair of Microintegration and Reliability
Saarland University
66123 Saarbruecken, Germany
erik.wiss@uni-saarland.de

Nesrine Jaziri
Electronics Technology Group
TU Ilmenau
98693 Ilmenau, Germany
nesrine.jaziri@tu-ilmenau.de

Adam Yuile
Chair of Microintegration and Reliability
Saarland University
66123 Saarbruecken, Germany
adam.yuile@uni-saarland.de

Jens Müller
Electronics Technology Group
TU Ilmenau
98693 Ilmenau, Germany
jens.mueller@tu-ilmenau.de

Steffen Wiese
Chair of Microintegration and Reliability
Saarland University
66123 Saarbruecken
s.wiese@mx.uni-saarland.de

Abstract – Reducing the thermo-mechanical stress during manufacturing respectively during soldering processes is very important to avoid high failure rates. As an example, a reactive multilayer system (RMS) can be used to transfer the heat only locally to the solder joints instead of heating the entire system, what is already a well-established process on silicon and metal substrates. The adaptation of this high-temperature process to the field of low-temperature cofired ceramic (LTCC) substrates would offer new technological possibilities but is very challenging due to their specific properties like higher roughness and lower thermal conductivity compared to silicon. Among other things, one parameter that influences the quality of the joining process using an RMS is the joining pressure. For an analysis of this aspect, LTCC chips with a full-surface metallization consisting of AgPd and their corresponding counter pieces were manufactured and bonded together with a commercially available reactive multilayer foil using different settings. Cross-sections of the samples were then prepared and analyzed by light microscopy, revealing the differences in respect to different joining pressures.

Keywords – LTCC, RMS, reactive multilayer system, Al-Ni, joining.

I. INTRODUCTION

In a conventional soldering process like reflow soldering, every component and the PCB are heated up to temperatures above 200 °C. These high temperatures are necessary to melt the solder paste and therefore to create a stable connection, but it also creates thermo-mechanical stress due to the different coefficients in thermal expansion, resulting in failures of the system. Reducing this stress by transferring the heat locally to the solder joints can lower the risk of damages, especially to heat-sensitive components. One possibility for such a room-temperature joining process is the use of a reactive multilayer system (RMS), what is already a well-established process on silicon and metal substrates [1-4].

Although the low-temperature cofired ceramics (LTCC) technology offers similar features, the use of RMS in this area is very limited so far. With this technology, three-dimensional structuring as needed in biomedical applications or for cooling purposes can be realized [5-7]. Additionally, it provides an excellent robustness under harsh environmental and mechanical conditions [8,9]. The use of an RMS in this context would open additional promising technological pathways, but the adaptation of this process is very challenging due to the higher surface roughness and lower thermal conductivity compared to silicon or metals [10,11].

II. EXPERIMENTAL DETAILS

A. RMS Theory

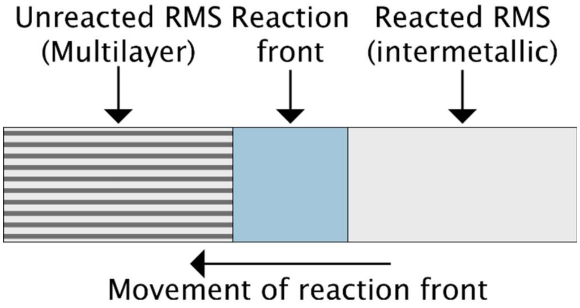

Figure 1: Basic principle of an RMS. After ignition (e.g., with an electrical spark), the atoms of the different materials intermix on an atomic level. During this process, a lot of heat is released which can be used for joining processes.

An RMS consists of at least two reactant partners (see Figure 1), that are arranged in a large number of alternating nanolayers with a total stack thickness of up to 300 µm [12]. The materials begin to intermix on atomic level, if a sufficient amount of energy is applied to the system (e.g., by a laser pulse or an electrical spark). During this profoundly exothermic process, the stored chemical energy is converted into heat that can be used for joining processes [13]. Among other things, the released heat and the propagation speed depend on properties like the material combination, the material ratio, and the nanolayer and the total stack thickness. Some possible material combinations for an RMS are Al-Ni (which was used in this work), Pd-Al and Nb-Si [14-16].

B. LTCC Samples

In order to carry out the experiments of this work, appropriate samples were manufactured using a DuPont 951 green tape under standard LTCC processing conditions, resulting in a thickness of 840 µm after sintering. For the substrate, a dimension of 15 mm x 3 mm was chosen, whereas a dimension of 3 mm x 3 mm was chosen for the chip counter-piece (see Figure 2). An AgPd metallization paste was screen-printed on the entire surface of the samples to enable the wetting of the solder. For the joining process, a commercially available reactive foil NanoFoil® NF40 (Indium Corp.) was used. The RMS of this reactive foil consists of aluminum and nickel layers with a total thickness of 40 µm, and additional tin layers of 5 µm on each side. It can be cut into smaller pieces using a sharp scalpel for example.

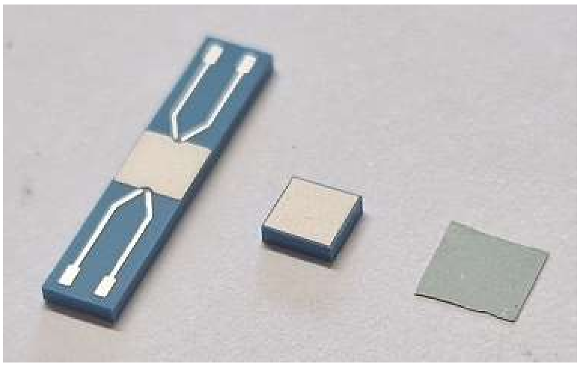

Figure 2: LTCC substrate (left) of dimension 15 mm x 3 mm and LTCC chip (middle) of dimension 3 mm x 3 mm, with a thickness of 840 µm after sintering. An AgPd metallization paste was screen-printed on both parts to enable the wetting of the solder, enhancing the height by 5 µm. The reactive foil (right) has a thickness of 40 µm and is covered with additional tin layers of 5 µm on each side. It was cut with a scalpel to a size of approximately 4 mm x 4 mm.

C. *Joining Process*

A rework machine FINEPLACER pico (Finetech) was used for the joining process of the samples. Figure 3 shows a sketched side view of the machine. The LTCC substrate is placed next to the ignition chip on a vacuum chuck which keeps it on place. The LTCC chip is picked up and held by a tool that is mounted on a movable arm using a vacuum structure. An additional force module can be used to exert a force and therefore a specific pressure on the joining partners. The live images of two cameras (one is aimed at the substrate, and the other one is aimed at the chip) are overlayed to allow precise alignment. After placing the reactive foil on the substrate, the joining process can be started.

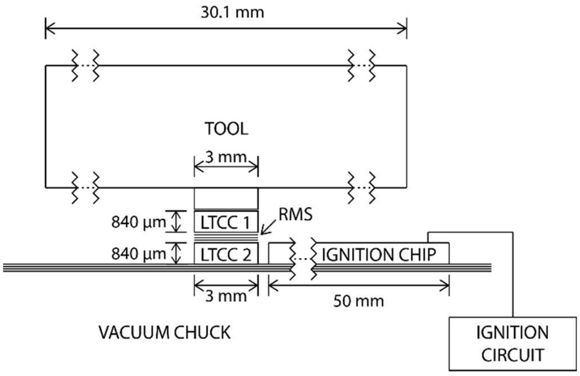

Figure 3: Sketched side view of the joining setup. The main components are a heatable vacuum chuck and a movable arm to which the tool with an integrated heating element is attached. After the LTCC chip ('LTCC 1') is picked up and held on the tool by vacuum, it can be precisely aligned with the LTCC substrate ('LTCC 2') on which the reactive foil is placed. Then, the heating process of both the tool and the vacuum chuck is started. At a specific temperature point, the arm moves downwards and pushes the chip on the substrate with the desired force. The ignition circuit and ignition chip are used to ignite the RMS with an electrical spark.

Both the vacuum chuck and the tool contain an integrated heating element to preheat the parts that should be joined. A maximum temperature of 160 °C was chosen for both parts, with an intermediate stage of 80 °C. Due to the much bigger mass of the vacuum chuck compared to the tool, it needs more time for the heating process. A temperature change of 3 K/s was chosen for the chuck, and a temperature change of 6 K/s was chosen for the tool (see Figure 4). After a preheating time of 50 seconds, the arm was moved downwards placing the chip on the substrate, and the force module of the machine applied a force on the stack. Approximately 80 seconds after the start of the process, the ignition process was initiated, and the joining is completed. For the experiments in this study, three different forces (20 N, 200 N and 400 N) were used, resulting in a pressure of 2.22 MPa, 22.2 MPa and 44.4 MPa for the given size of the LTCC of 9 mm².

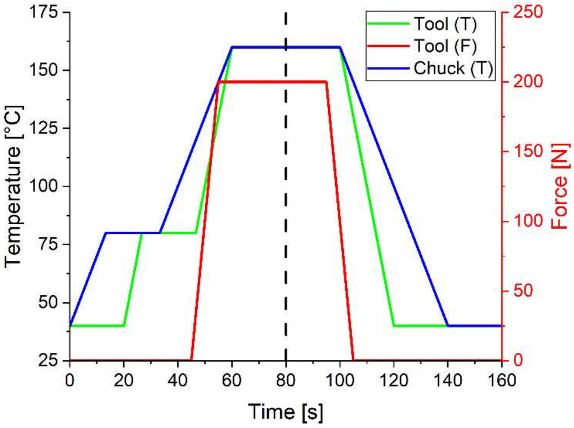

Figure 4: Idealized time-temperature (green: tool; blue: vacuum chuck) and time-force (red) profile of the rework machine. Due to the different heating speeds of the tool and the vacuum chuck, there is a shift in the starting times of the heating processes. Similar to a conventional reflow process, there is an intermediate stage for the temperature. Before the maximum temperature is reached, the tool is moved downwards and exerts the set force and therefore the pressure on the stack. After 80 seconds from the beginning, the ignition circuit initiates an electrical spark to ignite the RMS.

Figure 5 shows the ignition circuit that was used to ignite the RMS. Two capacitors need to be loaded with electrical energy from a usual 9 V battery by pushing a button for at least 2 seconds. When the button is released, the stored energy is released and transformed into a high voltage of 15.000 V, that is lead into the ignition chip (see Figure 6) via two wires. The two copper traces of the ignition chip are brought together at the end with a small gap of approximately 600 µm, resulting in an electrical spark, as the quotient of the voltage and the gap is greater than the breakdown field strength of air (3 kV/mm for dry air and standard pressure). This spark can be used to ignite the RMS.

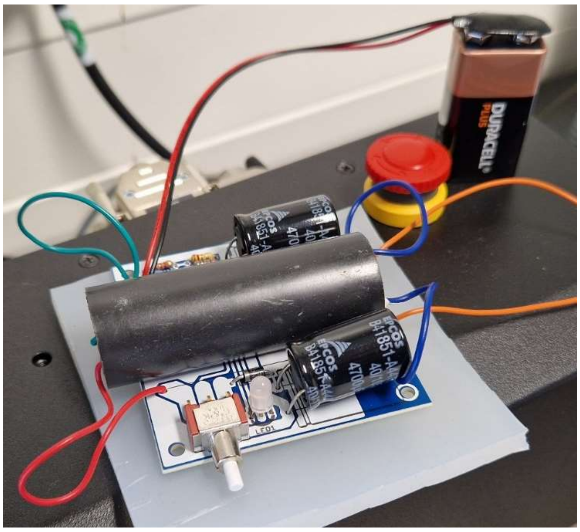

Figure 5: Ignition circuit to ignite the RMS, powered by a usual 9 V battery. The white button is used to load the two capacitors, what takes approximately 2 seconds. When the button is released, the stored energy is released into a transformer (black roll) that creates an output voltage of approximately 15.000 V.

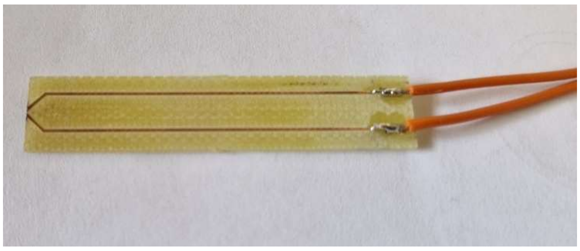

Figure 6: Ignition chip that is placed next to the LTCC stack and the RMS. On the right-hand side, the copper pads are connected to the ignition circuit via two orange wires. On the left-handed side, the copper traces are interrupted to create an electrical spark between them, which can be used to ignite the RMS.

III. RESULTS

The ignited samples were analyzed by light microscopy, why they had to be prepared in a specific way. After they were embedded in epoxy using EpoFix kit (Struers), the hardened samples were grinded on a LabPol-25 (Struers) by using SiC foils with grits of 500 and 1200 and polished on a Tegramin-25 (Struers) using different diamond suspensions with particle sizes of 9, 3 and 1 µm.

The results show that the RMS always broke at several points, regardless of the pressure that was used. The main differences are visible in the behavior of the solder and the metallization layer (remark: the solder appears just slightly brighter than the metallization).

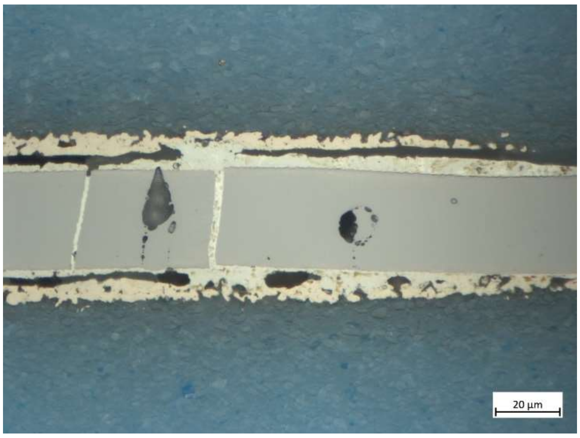

Figure 7: Light microscopy image of a reacted multilayer (gray) between the LTCC substrate and the chip (blue) with a joining pressure of 2.22 MPa. The RMS broke at several points, and the solder (white-yellow) and the metallization (red-yellow) did not form a good bond. A lot of gaps are visible between the layers, indicating a bad adhesion.

Figure 7 shows the LTCC and the reacted multilayer with the lowest joining pressure of 2.22 MPa. The distribution of the solder layer indicates that the enough heat was released to melt the solder, but the gaps indicate a bad adhesion between the layers.

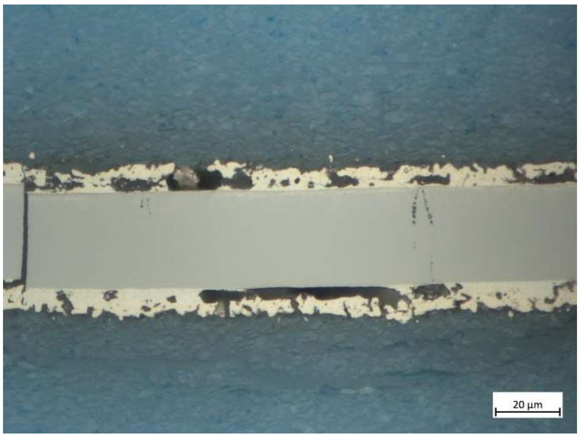

Figure 8: Light microscopy image of a reacted multilayer (gray) between the LTCC substrate and the chip (blue) with a joining pressure of 22.2 MPa. The RMS broke at several points, and the solder (white-yellow) is connected to the metallization (red-yellow) on more areas than before.

Figure 8 shows the LTCC and the reacted multilayer with a joining pressure of 22.2 MPa. The solder layer and the metallization layer are still separated, forming a proper intermetallic phase at the contact areas. The higher pressure helps to avoid larger gaps, even if they are still present.

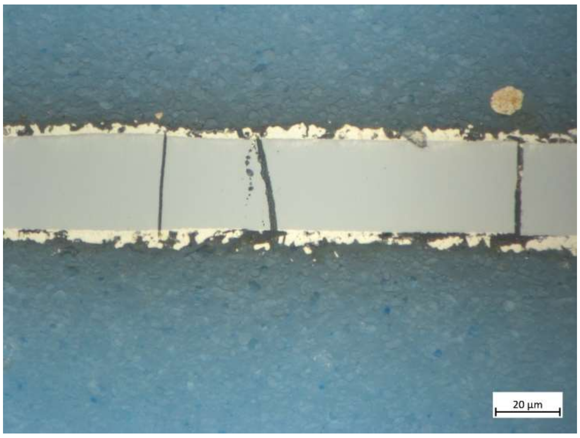

Figure 9: Light microscopy image of a reacted multilayer (gray) between the LTCC substrate and the chip (blue) with a joining pressure of 44.4 MPa. The RMS broke at several points, and the solder (white-yellow) and the metallization (red-yellow) appear to be fully mixed together.

Figure 9 shows the LTCC and the reacted multilayer with the highest joining pressure of 44.4 MPa. The high pressure ensures that the solder layer and the metallization layer fully intermix, and no separation between them is visible anymore.

IV. DISCUSSION

In general, the results show that an RMS can be used to join two ceramic substrates with an AgPd metallization. Among other things, the quality of the joints is highly dependent of the pressure that is applied to the joining partners. Low joining pressures result in a poor adhesion between the solder and the metallization, most probably caused by a decrease in the volume of up to 12% during the high-temperature exothermic reaction [17]. Although the solder melts, the shrinkage of the RMS ensures that not all of the resulting gaps can be filled with the solder. It can be assumed that the reliability of the connection is not as good as it should be for a use in real electronic devices. A higher pressure can help to avoid the forming of larger gaps because it counteracts the volume reduction. At medium pressures, the solder and the metallization seem to form proper intermetallic layers. If the pressure is too high, the borders between the solder layer and the metallization layer disappear. Regardless of the pressure used for the joining process, cracks could be observed along the entire layer of the RMS, most probably caused by the high temperature and the low thermal conductivity of the LTCC.

V. CONCLUSIONS

This work presents some joining experiments of LTCC substrates with RMS in respect to different joining forces (between 20 N and 400 N) respectively joining pressures (between 2.22 MPa and 44.4 MPa). Therefore, an AgPd metallization was screen-printed on several LTCC substrates and their corresponding counter pieces. A commercially available reactive foil consisting of aluminum and nickel nanolayers was placed between them and ignited to start the exothermic process. After the joining process was completed, the samples were embedded in epoxy and analyzed by light microscopy. The results show that a low joining pressure results in the formation of large gaps between the solder layer and the metallization, and a very high joining pressure results in the intermixing of the solder and the metallization layer. A medium pressure seems to be the most promising option for further experiments, forming proper intermetallic layers.

ACKNOWLEDGMENTS

This research work was supported by the Deutsche Forschungsgemeinschaft (DFG, German Research Foundation) – Project-ID 426204742. The authors would like to thank Andreas Ruh for preparing and performing the cross-sections.

REFERENCES

[1] J. Wang, E. Besnoin, A. Duckham, D. J. Spey, M. E. Reiss, O. M. Knio, M. Powers, M. Whitener, T. P. Weihs, “Room-temperature soldering with nanostructured foils,” Appl. Phys. Lett., 2003, vol. 83, no. 19, pp. 3987-3989.

[2] J. Braeuer, J. Besser, M. Wiemer, T. Gessner, “A novel technique for MEMS packaging: reactive joining with integrated material systems,” Sens. Actuat. A Phys., 2012, vol. 188, pp. 212-219.

[3] B. Boettge, J. Braeuer, M. Wiemer, M. Petzold, J. Bagdahn, T. Gessner, “Fabrication and characterization of reactive nanoscale multilayer systems for low-temperature joining in microsystem technology,” J. Micromech. Microeng., 2010, vol. 20, no. 6, p. 064018.

[4] J. Braeuer, T. Gessner, “A hermetic and room-temperature wafer joining technique based on integrated reactive multilayer systems,” J. Micromech. Microeng., 2014, vol. 24, no. 11, p. 115002.

[5] Y. Fournier, “3D structuration techniques of LTCC for microsystems applications,” Ph.D. dissertation, École polytechn. Féd. de Lausanne (EPFL), Lausanne, Vaud, Switzerland, 2010.

[6] T. Welker, J. Müller, “Design, simulation and fabrication of liquid cooled LTCC devices utilizing integrated channels,” ITherm (IEEE), 2016, pp. 830-835.

[7] A. L. Chlebowski, E. Y. Chow, C. Ellison, P. P. Irazoqui, “Integrated LTCC packaging for use in biomedical devices,” Biomed. Mater. Eng., 2012, vol. 22, no. 6, pp. 361-372.

[8] L. Golonka, P. Bembnowicz, D. Jurków, K. Malecha, H. Roguszczak, R. Tadaszak, “Low temperature co-fired ceramics (LTCC) microsystems,” Opt. Appl., 2011, vol. 41, no. 2, pp. 383-388.

[9] C. Jacq, T. Maeder, P. Ryser, “Sensors and packages based on LTCC and thick-film technology for severe conditions,” Sadhana, 2009, vol. 34, pp. 677-687.

[10] H. Jantunen, T. Kangasvieri, J. Vähäkangas, S. Leppävuori, “Design aspects of microwave components with LTCC technique,” J. Eur. Ceram. Soc., 2003, vol. 23, no. 14, pp. 2541-2548.

[11] M. Matters-Kammerer, U. Mackens, K. Reimann, R. Pietig, D. Hennings, B. Schreinemacher, R. Mauczok, S. Gruhlke, C. Martiny, “Material properties and RF applications of high k and ferrite LTCC ceramics,” Microelectron. Reliab., 2006, vol. 26, no. 1, pp. 134-143.

[12] D. P. Adams, “Reactive multilayers fabricated by vapor deposition: A critical review,” Thin Solid Films, 2015, vol. 576, pp. 98-128.

[13] K. T. Raić, R. Rudolf, P. Ternik, Z. Žunič, V. Lazić, D. Stamenković, T. Tanasković, I. Anžel, “CFD analysis of exothermic reactions in Al-Au nano multi-layered foils,” Mater. Tehnol., 2011, vol. 45, no. 4, pp. 335-338.

[14] A. J. Gavens, D. Van Heerden, A. B. Mann, M. E. Reiss, T. P. Weihs, “Effect of intermixing on self-propagating exothermic reactions in Al/Ni nanolaminate foils,” J. Appl. Phys., 2000, vol. 87, no. 3, pp. 1255-1263.

[15] A. S. Ramos, M. T. Vieria, “Intermetallic compound formation in Pd/Al multilayer thin films,” Intermetallics, 2012, vol. 25, pp. 70-74.

[16] M. E. Reiss, C. M. Esber, D. Van Heerden, A. J. Gavens, M. E. Williams, T. P. Weihs, “Self-propagating formation reactions in Nb/Si multilayers,” Mater. Sci. Eng. A, 1999, vol. 264, no. 1-2, pp. 217-222.

[17] T. Namazu, K. Ohtani, K. Yoshiki, S. Inoue, “Crack propagation direction control for crack-less solder joining using Al/Ni flash heating technique,” 16th Int. Conf. Solid-State Sens. Actuators Microsyst. (IEEE), pp. 1368-1371.

5.8 Paper 8: Impact of Bonding Pressure on the Reactive Bonding of LTCC Substrates

5.8.1 Veröffentlichungshinweise

Erik Wiss[1], Nesrine Jaziri[2], Jens Müller[2], Steffen Wiese[1]

[1]Chair of Microintegration and Reliability, Faculty of Natural Sciences and Technology, Saarland University, Saarbrücken, Germany

[2]Electronics Technology Group, Faculty of Electrical Engineering and Information Technology, TU Ilmenau, Ilmenau, Germany

Micromachines (2025), 16.3, 321

Die Originalveröffentlichung ist abrufbar unter:
https://doi.org/10.3390/mi16030321

5.8.2 Synopse

Diese Veröffentlichung untersucht den Einfluss des Anpressdrucks während des reaktiven Fügeprozesses auf die Ausbildung der Fügestelle bei LTCC-Substraten. Die Motivation hierzu ergab sich aus den Arbeiten zu Paper 3 und 7, die bereits eine signifikante Druckabhängigkeit der Fügequalität aufzeigten. Ziel der Arbeit war es, diese sowie die resultierenden mikrostrukturellen Veränderungen innerhalb der Fügezone zu analysieren.

Hierzu wurden LTCC-Chips mit NanoFoil® und dem FINEPLACER® auf passende Gegenstücke unter Verwendung verschiedener Anpressdrücke gefügt. Diese variierten zwischen 2 und 44 MPa bei vollflächig metallisierten Proben, und zwischen 20 und 400 MPa bei Proben mit strukturierter Metallisierung (vier Pads mit jeweils 0,5 mm x 0,5 mm). Die Zündung der Folien erfolgte elektrisch, sobald der eingestellte Anpressdruck erreicht war. Nach dem Fügen wurden Querschliffe von den Proben angefertigt, die im LM und REM auf Integrität der Metallisierung und Elementverteilung untersucht wurden.

Die Ergebnisse zeigen, dass ein niedriger Anpressdruck von 2 MPa während des Fügens vollflächig metallisierter Proben zu unvollständigen Verbindungen mit vielen Lücken zwischen RMS und Metallisierung sowie zwischen RMS und Lot führte. Diese reduzieren die effektive Kontaktfläche zwischen Chip und Substrat, erhöhen den elektrischen Kontaktwiderstand und verschlechtern sowohl die thermische Leitfähigkeit als auch die mechanische Stabilität. Das Lot kumuliert aufgrund der Oberflächenspannung an einigen wenigen Stellen, was lokal die Diffusion der Metallisierung ins Lot fördert. Im Gegensatz dazu verbessern hohe Anpressdrücke von 33 und 44 MPa zwar die Haftung zwischen RMS und Metallisierung, führten jedoch zu einer Delamination der Metallisierung von der LTCC sowie zu starker Rissbildung innerhalb des RMS. Bei 44 MPa konnten sogar Brüche in der Keramik beobachtet werden. Bei mittleren Anpressdrücken von 11 und 22 MPa lösten sich große Mengen der Metallisierung ins Lot, eine vollständige Auflösung der Metallisierung konnte jedoch nicht beobachtet werden. Stattdessen blieb ein schmaler Streifen mit hoher Konzentration der Elemente der Metallisierung intakt, und es ergab sich ein vollflächiger Kontakt entlang der gesamten Fügezone.

Ein vergleichbares Verhalten wurde bei den strukturierten Proben beobachtet. Bei einem Druck von 20 MPa waren nur wenige Lücken im Bereich der Pads sichtbar, und auch Lot und Metallisierung waren noch klar voneinander abgrenzbar. Bei Drücken von 100 und 200 MPa stieg die Rissanzahl deutlich an, und die Dicken von Lot und Metallisierung sind reduziert. Diese Effekte traten bei 300 und 400 MPa noch stärker hervor und verursachten klar erkennbare Beschädigungen an der Metallisierung. Auffällig ist, dass trotz der hohen Anpressdrücke weder eine Separierung des RMS noch Brüche in der Keramik beobachtet werden konnten.

Im Kontext des Gesamtprojekts leistet diese Veröffentlichung einen Beitrag zur Beantwortung der Frage, wie sich der Anpressdruck auf den reaktiven Fügeprozess auswirkt.

5.8.3 Vollständiger Artikel

micromachines

IMPACT FACTOR 3.0
Indexed in: PubMed
CITESCORE 5.2

Article

Impact of Bonding Pressure on the Reactive Bonding of LTCC Substrates

Erik Wiss, Nesrine Jaziri, Jens Müller and Steffen Wiese

Special Issue
Microelectronics Assembly and Packaging: Materials and Technologies, 2nd Edition

Edited by
Dr. Liangxing Hu, Dr. Youngwoo Kim and Dr. Peng Zhao

MDPI

https://doi.org/10.3390/mi16030321

micromachines

Article

Impact of Bonding Pressure on the Reactive Bonding of LTCC Substrates

Erik Wiss [1], Nesrine Jaziri [2], Jens Müller [2] and Steffen Wiese [1,*]

[1] Chair of Microintegration and Reliability, Faculty of Natural Sciences and Technology, Saarland University, 66123 Saarbrücken, Germany; erik.wiss@uni-saarland.de
[2] Electronics Technology Group, Faculty of Electrical Engineering and Information Technology, TU Ilmenau, 98693 Ilmenau, Germany; nesrine.jaziri@tu-ilmenau.de (N.J.); jens.mueller@tu-ilmenau.de (J.M.)
* Correspondence: s.wiese@mx.uni-saarland.de; Tel.: +49-681-302-71820

Abstract: Reactive bonding can overcome the issues associated with conventional soldering processes, such as potential damage to heat-sensitive components and the creation of thermomechanical stress due to differing coefficients of thermal expansion. The risk of such damage can be reduced by using localized heat sources like reactive multilayer systems (RMS), which is already a well-established option in the field of silicon or metal bonding. Adapting this process to other materials, such as low temperature co-fired ceramics (LTCC), is difficult due to their differing properties, but it would open new technological possibilities. One aspect that significantly affects the quality of the bonding joints is the pressure applied during the bonding process. To investigate its influence more closely, various LTCC samples were manufactured, and cross-sections were prepared. The microscopical analysis reveals that there is an optimum range for the bonding pressure. While too little pressure results in the formation of lots of voids and gaps, most likely in poor mechanical and electrical properties, too high pressure seems to cause a detachment of the metallization from the base material.

Keywords: LTCC; reactive multilayers; RMS; Al/Ni; bonding

Academic Editors: Youngwoo Kim, Liangxing Hu and Peng Zhao

Received: 15 February 2025
Revised: 4 March 2025
Accepted: 5 March 2025
Published: 11 March 2025

Citation: Wiss, E.; Jaziri, N.; Müller, J.; Wiese, S. Impact of Bonding Pressure on the Reactive Bonding of LTCC Substrates. *Micromachines* **2025**, *16*, 321. https://doi.org/10.3390/mi16030321

1. Introduction

Reflow soldering is the standard process in the manufacturing of electronic assemblies, particularly for surface-mount technology (SMT) applications. This process begins with the application of solder paste, composed of powdered solder and flux, to the contact pads of a printed circuit board (PCB). In the next step, components are placed onto these pads on the PCB using automated pick-and-place machines, ensuring accurate positioning. The assembled PCB is then passed through a reflow oven, where it is subjected to a specified heating profile, typically involving two temperature zones: a preheating zone below the melting point of the solder paste, and a reflow zone above the melting point of the solder paste. The preheating zone ensures uniform heating of the PCB and all components, while the reflow zone melts the solder paste, creating a proper mechanical and electrical connection by forming an intermetallic compound (IMC). Although reflow soldering is a relatively simple and quick process, it has some disadvantages primarily attributed to global heat exposure. These include the risk of damage to heat-sensitive components and the development of thermomechanical stress due to differing coefficients of thermal expansion (CTE) between the components and the base material, potentially leading to failures. A new approach to preventing or minimizing such damage involves using localized heat sources instead of global ones, such as the exothermic reaction of reactive multilayer systems (RMS) [1–3].

An RMS consists of numerous nanoscale bilayer stacks of at least two different reactant partners, with a total stack thickness of up to 300 µm [4,5]. Some possible material combinations are Ni and Al, Ti and Al, Nb and Si, or B and Ti [6–9]. When supplied with sufficient energy, for example through a laser pulse or an electric spark, the materials react with each other to form an IMC. Since the enthalpy of this reaction is negative, it is exothermic [10], meaning that energy is released in the form of heat, which can be used to locally melt the solder material. The released heat is so substantial that the reaction is self-sustaining and continues until all the available material has been converted. Further, the reaction occurs within fractions of a second; depending on the material system and layer thicknesses, velocities of more than 10 m/s can be achieved. Other potential future applications of RMS could include self-repairing solder joints or the large-scale removal of components for recycling purposes. The basic principle of the heat release of an RMS is shown in Figure 1.

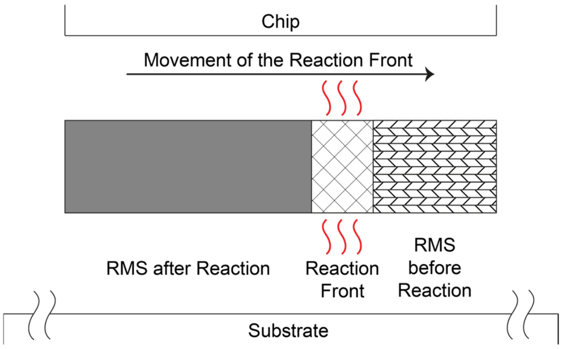

Figure 1. The fundamental principle of the usage of a reactive multilayer system (RMS) for bonding processes in electronics packaging. In the initial state, the materials are arranged in alternating nanolayers. Ignition, for example, by a laser pulse or an electric spark, causes intermixing of the materials. The heat released from this exothermic reaction can be used for a localized soldering process.

The application of RMS is already a well-established process in the field of silicon or metal bonding [11–13]. However, adapting this process to other base materials, such as conventional PCB material or low-temperature co-fired ceramics (LTCC), is technologically challenging due to their much higher roughness and significantly lower thermal conductivity [14,15]. Nevertheless, this adaptation would open new possibilities, particularly in the area of heterogeneous integration. Therefore, a better understanding of the reaction in combination with these materials is necessary. Previous studies have already addressed the deposition process of RMS on various pre-treated LTCC surfaces [16–18], the influence of additional solder layers on the evolving temperatures [19], and the influence of bonding pressure on both the reactive joining of metals [20] and the thermal resistance of Si chips [21]. In this study, the influence of bonding pressure on the quality of the bonding joints will be investigated and compared.

2. Materials and Methods

2.1. Sample Preparation

In order to investigate the influence of the bonding pressure on the quality of the bonding zones, different bonding pressures were used to manufacture the samples. All samples were manufactured of a widely used LTCC material, GreenTape 951 (DuPont, Wilmington, DE, USA), in combination with a suitable Pd/Ag thick-film paste 6146 (DuPont) for metallization. A size of 3 mm × 3 mm, matching the tool size of the bonding machine (see Section 2.2), was chosen for the chips. The Pd/Ag metallization was applied to the entire surface of Samples L1–L5, and only to four small pads measuring 0.5 mm × 0.5 mm in the corners of samples L6–L10 (see Table 1). This reduction in the effective bonding area allowed much higher bonding pressures to be achieved. The substrates had a size of 15 mm × 3 mm to allow easier embedding by matching the size of the embedding forms. Here, the Pd/Ag metallization was applied centrally, either as a single area or as individual pads, depending on the respective variant. After sintering under standard LTCC processing conditions, thicknesses of approximately 840 µm for the substrate and 10 µm for the metallization were achieved.

Table 1. Overview of the sample types that were used for the experiments.

Configuration	**Base Material**	**Substrate Size [mm^2]**	**Chip Size [mm^2]**	**Type of Metallization**	**Effective Bonding Area [mm^2]**
L1–L5	LTCC	15 × 3	3 × 3	Pd/Ag	3 × 3
L6–L10	LTCC	15 × 3	3 × 3	Pd/Ag	4 × 0.5 × 0.5

A commercially available reactive foil NanoFoil® NF40 (Indium Corp., Clinton, NY, USA) was used for the bonding process. As described in the introduction, it consists of numerous bilayers of aluminum and nickel with a total stack thickness of approximately 40 µm. The individual layers also contain small amounts of vanadium, indium, silver, and copper to enhance the reaction properties, such as mechanical stability and electrical and thermal conductivity. Both sides of the foil are pre-coated with an approximately 5 µm thick layer of tin, eliminating the need for additional solder paste. The foil was cut into small pieces with a sharp scalpel. Their size was chosen to be slightly larger than the Pd/Ag areas to simplify the manual placement process and to be able to reach them easily with the ignition module. Figure 2 shows the LTCC samples and the reactive foils.

Reactive Die Bonding

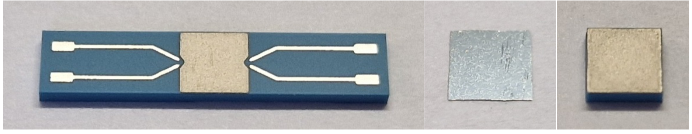

(**a**) (**b**) (**c**)

Reactive Bonding of Interconnects

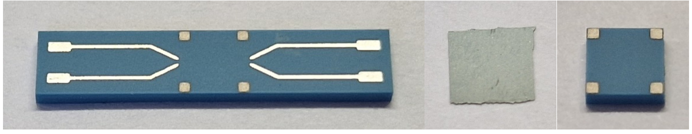

(**d**) (**e**) (**f**)

Figure 2. (**a**–**c**) Reactive die bonding. (**a**) LTCC substrate (15 mm × 3 mm) with full-area Pd/Ag metallization. (**b**) Reactive foil with Sn coating on both sides. (**c**) LTCC chip (3 mm × 3 mm) with full-area Pd/Ag metallization. (**d**–**f**) Reactive bonding of interconnects. (**d**) LTCC substrate (15 mm × 3 mm) with Pd/Ag metallization on four corner pads (0.5 mm × 0.5 mm). (**e**) Reactive foil with Sn coating on both sides. (**f**) LTCC chip (3 mm × 3 mm) with Pd/Ag metallization on four corner pads (0.5 mm × 0.5 mm).

2.2. Bonding Process

The bonding process was carried out on a die bonder FINEPLACER pico (Finetech, Berlin, Germany), which has already proven its suitability for bonding processes using RMS several times [22,23]. The main components are a vacuum chuck with an integrated heater, a tool with an integrated vacuum holder and heater mounted on a movable arm, a force module to exert a specific force of up to 400 N on the bonding partners, and a visual alignment system consisting of two cameras. Figure 3a shows the schematic side view of the bonding setup.

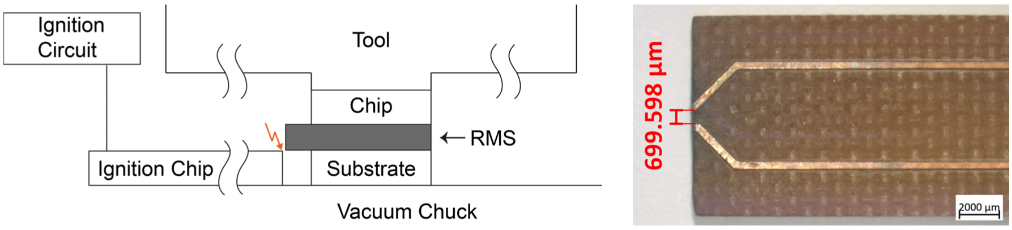

(**a**) (**b**)

Figure 3. (**a**) Schematic side view of the bonding setup. The tool head uses a vacuum mechanism to pick up the chip. After aligning with the substrate, the RMS foil is positioned on the substrate with a slight protrusion towards the ignition chip. Then, the bonding process is initiated, during which the tool presses the chip onto the substrate with a defined force. After reaching the set parameters, the ignition chip is manually brought close to the foil, and the ignition is triggered. (**b**) Ignition chip with two converging tracks at the edge, separated by a gap of approximately 700 µm. The electric spark generated between the tracks upon triggering the ignition circuit can be used to ignite the RMS.

The ignition circuit transforms a low voltage of 9 V from a battery to approximately 15 kV, and is connected to an ignition chip with two tracks that converge at its edge with a small gap of approximately 700 µm between them (see Figure 3b). As the quotient of the voltage and the gap is greater than the breakdown field strength of air (3 kV/mm for dry air and standard pressure), an electrical spark is generated when the ignition circuit is triggered. This spark has a sufficient amount of energy to initiate the start of the reaction of the RMS.

The substrate was placed on the vacuum chuck, and the chip was picked up by the tool using a vacuum. The videos from both cameras, one pointing at the substrate and one at the chip, were overlapped to allow very precise alignment of the bonding partners. The cut RMS foil was then placed on the substrate with a slight protrusion towards the ignition chip, and the actual bonding process was initiated. For the temperature profile, a preheat temperature of 80 °C and a peak temperature of 200 °C were chosen. The target temperature on the tool corresponds to that of the chuck, but it requires more time to heat up due to its much greater thermal mass. After the preheating phase was completed, the arm was automatically moved downwards, placing the chip on the substrate, and the force module started to apply the force, and thus a pressure, on the bonding partners. Table 2 summarizes the different sample configurations regarding the bonding profiles and the resulting bonding pressures, and Figure 4 exemplarily shows the course of the bonding profile with a bonding force of 100 N.

Once the set force was reached, the ignition chip was manually moved to the side of the foil and the ignition process was initiated. The foil is ignited approximately in the center, causing the reaction to propagate outward (see Figure 5).

Table 2. Bonding profiles and resulting bonding pressures for the LTCC samples. The preheat and peak temperatures were set identically on both the chuck and the tool. Due to the much smaller bonding area in the case of samples with four corner pads, the pressure is many times higher.

Configuration	Preheat Temperature [°C]	Peak Temperature [°C]	Force [N]	Metallization Area [mm^2]	Bonding Pressure [MPa]
L1	80	200	20	3 × 3	2
L2	80	200	100	3 × 3	11
L3	80	200	200	3 × 3	22
L4	80	200	300	3 × 3	33
L5	80	200	400	3 × 3	44
L6	80	200	20	4 × 0.5 × 0.5	20
L7	80	200	100	4 × 0.5 × 0.5	100
L8	80	200	200	4 × 0.5 × 0.5	200
L9	80	200	300	4 × 0.5 × 0.5	300
L10	80	200	400	4 × 0.5 × 0.5	400

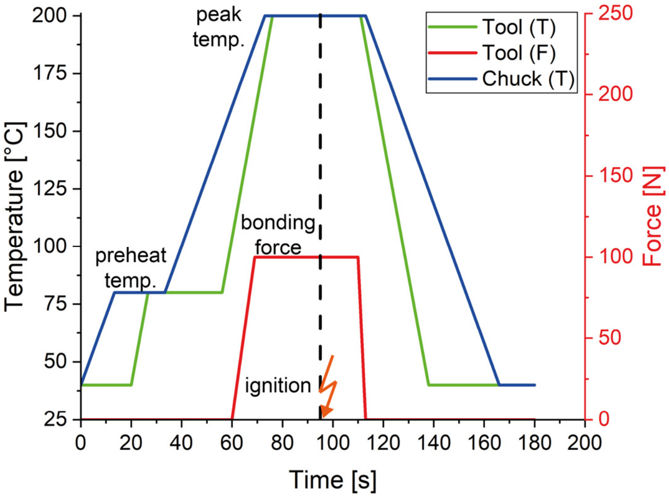

Figure 4. Idealized time–temperature (green: tool, blue: vacuum chuck) and time–force (red) profiles of the die bonder for the LTCC samples. While the force was set to 100 N, the preheat and maximum temperature were set to 80 °C and 200 °C, respectively. The vertical dashed line marks the timestamp of the ignition of the reactive foil.

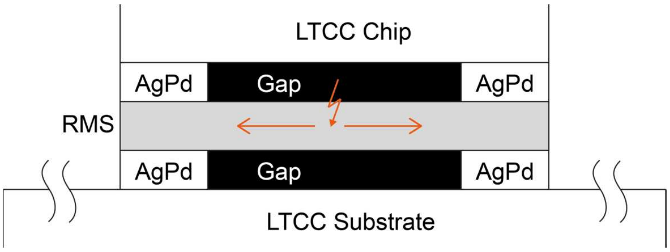

Figure 5. The ignition of the foil is initiated approximately in its center, causing the reaction to propagate outward.

2.3. Microscopical Analysis

Cross-sections of the samples were prepared in several steps to facilitate light microscopy, scanning electron microscopy (SEM), and energy dispersive X-ray spectroscopy (EDX) analyses. These techniques were used to evaluate the quality of the bonding zones and to estimate their mechanical and electrical properties. Initially, the samples were embedded in epoxy resin using an EpoFix kit (Struers, Ballerup, Denmark), and cured for 24 h under slight negative pressure to remove air bubbles. Next, plane and fine grinding were performed on a LabPol-25 (Struers) using SiC foils with grits of 500 and 1200. Diamond polishing followed on a Tegramin-25 (Struers) using suspensions with particle sizes of 9 µm, 3 µm, and 1 µm. The samples were then subjected to final polishing with a 0.25 µm silicon oxide suspension on a Saphir Vibro (ATM Qness, Mammelzen, Germany) vibratory polishing machine to obtain an extremely flat surface with ultra-low roughness. Lastly, a thin carbon layer of approximately 20 nm thickness was applied using a Q150T Coater (Quantum Design, Pfungstadt, Germany) to prevent charging effects during SEM analysis caused by electron accumulation or the formation of space–charge regions. Light microscopy analysis using an Axio Imager.M2m (Zeiss, Oberkochen, Germany), equipped with a 20× objective was performed to obtain stitched images of the samples. The SEM analysis was carried out on an EVO MA15 (Zeiss) equipped with a LaB_6 cathode, operating at an accelerating voltage of 20 kV and a beam current of 40 µA. EDX analysis utilized an XFlash detector (Bruker, Billerica, MA, USA) with an energy resolution of 123 eV.

3. Results

3.1. Light Microscopy

The image stitching method was used first to obtain an overall view of the bonding zones of every sample. Multiple individual images were combined into a single composite image, allowing the entire bonding zone to be displayed in high resolution. This approach simplifies the direct comparison of the samples with respect to properties such as gap or crack formation, solder contribution, and integrity of the metallization.

Figure 6 shows the stitched images of samples L1–L5 with full-area Pd/Ag metallization, bonded under pressures of approximately 2 MPa (L1), 11 MPa (L2), 22 MPa (L3), 33 MPa (L4), and 44 MPa (L5). Figure 7 presents more detailed images at 50× magnification, representative of the respective samples. Figure 6a shows that using a very low bonding pressure of 2 MPa results in a very uneven joint. While the left-hand side and the center appear relatively decent, the right-hand side exhibits significantly poorer connection, characterized by large gaps between the metallization and the RMS, as well as the solder. Additionally, some cracks have formed in the reactive layer, which, in a few cases, have been filled with solder. Figure 7a shows a location with poor wetting behavior of the solder, which appears to accumulate in a few spots, except for a very thin layer on the RMS. The metallization and the solder are clearly distinguishable as separate layers throughout the entire area.

Increasing the bonding pressure to 11 MPa results in a much better appearance than before (Figures 6b and 7b). Although many gaps are still visible, they have become smaller and less extensive. The number of cracks in the RMS, most of which remain unfilled, has increased. The more detailed image reveals that the bonding zone is narrower than before, offering the possibility of improved formation of an IMC between the solder and the metallization. A further increase in bonding pressure to 22 MPa leads to similar results (Figures 6c and 7c). Compared to the bonding pressure of 2 MPa, the gaps become smaller, and the number of cracks has increased. Overall, the bonding zone looks the best here.

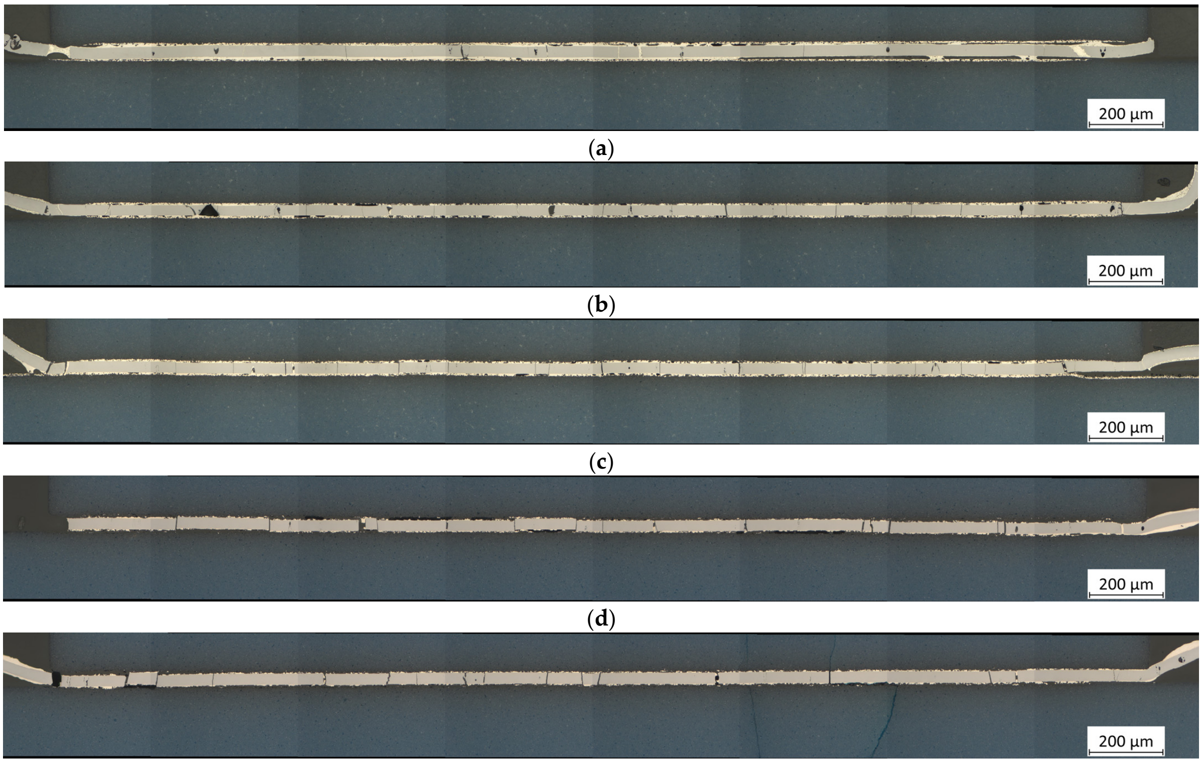

(**a**)

(**b**)

(**c**)

(**d**)

(**e**)

Figure 6. Stitched images of LTCC samples L1–L5 with full-area Pd/Ag metallization (blue: LTCC material; gray: RMS after the reaction; white-yellow: solder; red-yellow: metallization). The samples were bonded under pressures of approximately (**a**) 2 MPa, (**b**) 11 MPa, (**c**) 22 MPa, (**d**) 33 MPa, and (**e**) 44 MPa. Bonding at low pressures results in the formation of numerous gaps and poor adhesion between the Pd/Ag metallization and the solder. Medium pressures reduce the number of gaps and voids, thereby improving the overall performance. However, if the pressure is too high, the RMS experiences significant thermo-mechanical stress, leading to multiple fractures that remain predominantly unfilled. At the highest pressure, fractures are even generated within the LTCC material. Magnification: 20×.

Significant differences become visible when the pressure is increased to 33 MPa (Figures 6d and 7d) or even 44 MPa (Figures 6e and 7e). The high pressure, in combination with the high temperatures of the reaction, causes the RMS to break at several points, forming separate blocks. In the case of the highest pressure, cracks were also found in the LTCC material. As before, most of the cracks in the RMS remain unfilled. Judging by the more detailed images, the metallization layers were also damaged here.

Figure 8 shows the stitched images of samples L6–L10 with Pd/Ag metallization on four corner pads of size 0.5 mm × 0.5 mm, bonded under significantly higher pressures of approximately 20 MPa (L6), 100 MPa (L7), 200 MPa (L8), 300 MPa (L9), and 400 MPa (L10) due to the much smaller metallization area. Figure 9 presents more detailed images at 50× magnification, representative of the respective samples. Fundamentally, similar observations can be made here as with the samples with full-area metallization. According to previous results, a bonding pressure of 20 MPa already seems to lead to good results (Figures 8a and 9a). Thus, there are few gaps in the pad area, and the separation between solder and metallization is still clearly visible. While cracks in the RMS in the pad area mostly remain unfilled, the solder is almost always drawn into the crack at the unmetallized areas.

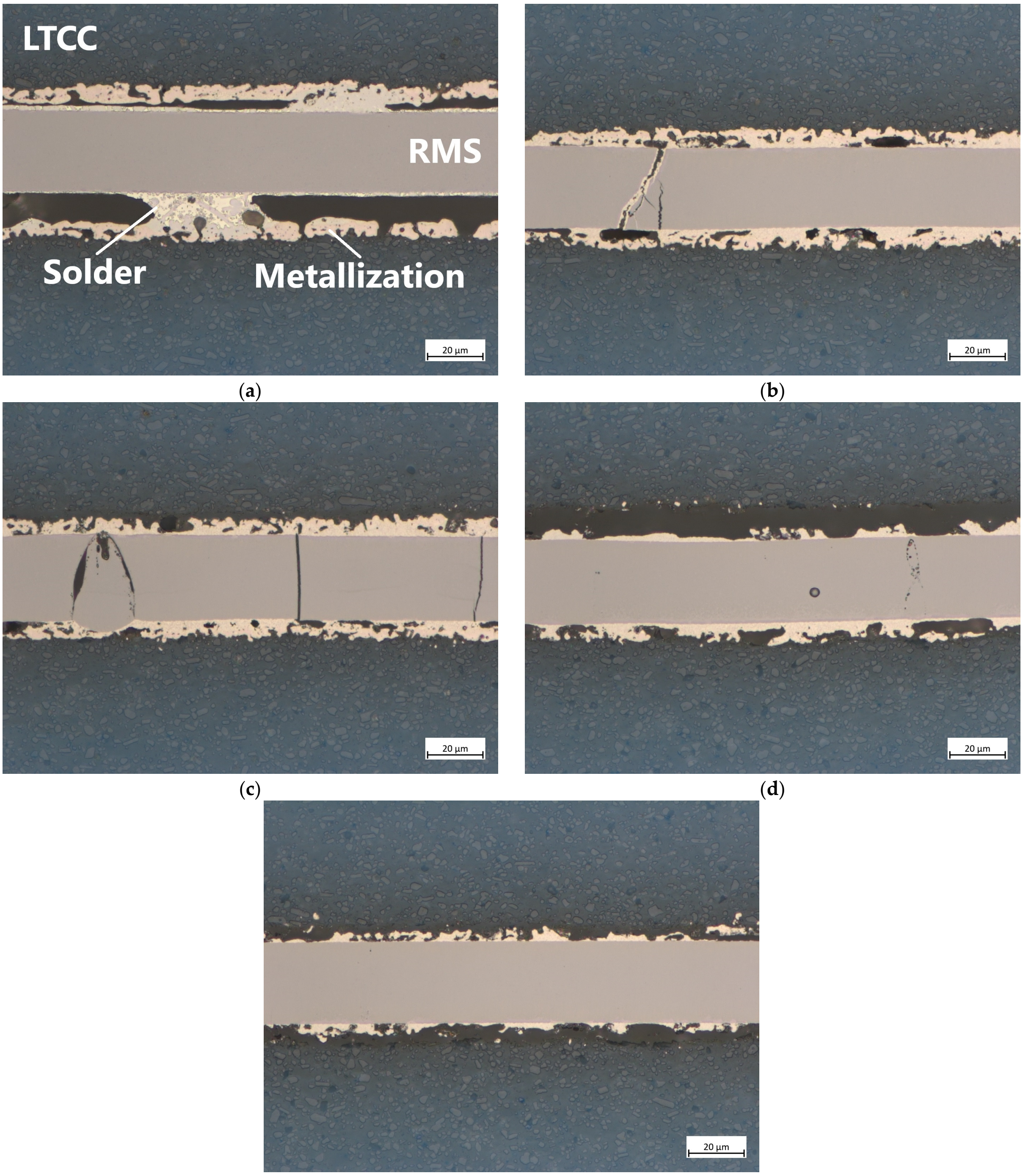

Figure 7. Detailed pictures of LTCC samples L1–L5 with full-area Pd/Ag metallization (blue: LTCC material; gray: RMS after reaction; white-yellow: solder; red-yellow: metallization). The samples were bonded under pressures of approximately (**a**) 2 MPa, (**b**) 11 MPa, (**c**) 22 MPa, (**d**) 33 MPa, and (**e**) 44 MPa. Magnification: 50×.

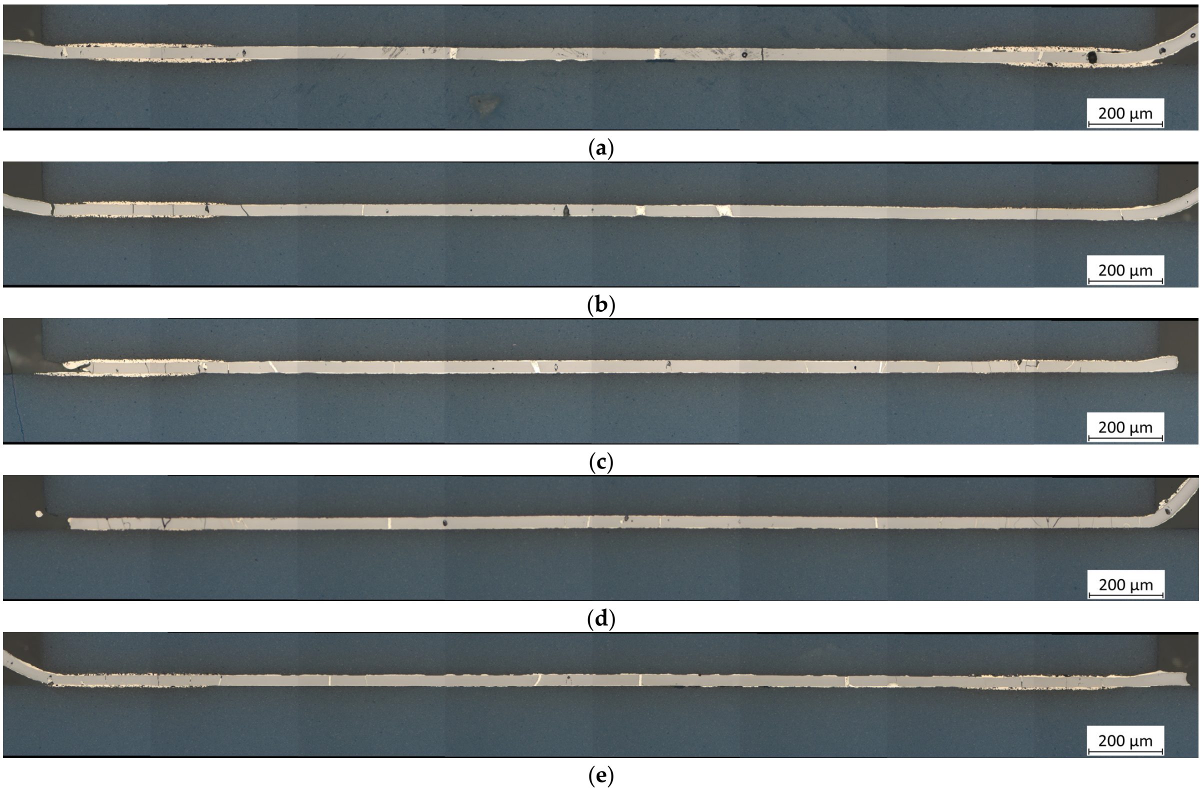

Figure 8. Stitched images of LTCC samples L6–L10 with Pd/Ag metallization on four corner pads of size 0.5 mm × 0.5 mm (blue: LTCC material; gray: RMS after reaction; white-yellow: solder; red-yellow: metallization). Compared to the previous samples, the applied pressures of (**a**) 20 MPa, (**b**) 100 MPa, (**c**) 200 MPa, (**d**) 300 MPa, and (**e**) 400 MPa are significantly higher due to the considerably reduced metallization area. As expected, a pressure of 20 MPa seems to form an acceptable bonding joint. Compared to the samples with full-area metallization, the fractures occurring in the RMS are almost always filled with solder, most likely because they cannot form cohesive bonds with the ceramic material in the unmetallized areas. It is noteworthy that, despite the high pressures, no fractures were found in the ceramic. Magnification: 20×.

In the medium pressure range of 100 MPa (Figures 8b and 9b) and 200 MPa (Figures 8c and 9c), the number of cracks increases significantly, especially in the pad area, while the thicknesses of the solder and metallization shrink. With a further increase in pressure to 300 MPa (Figures 8c and 9c) or 400 MPa (Figures 8d and 9d), these effects are further intensified. Additionally, in these cases, the metallization is also damaged, but neither separation of the RMS nor cracks in the LTCC could be observed.

3.2. EDX Analysis

The distribution of some of the occurring elements in the upper interface between the RMS and the metallization was analyzed by EDX for bonding pressures of 2 MPa, 11 MPa, and 22 MPa. Figures 10–12 provide detailed images of this zone, presented as SEM images in secondary electron contrast (SE) mode, along with EDX maps for the elements Sn (from RMS coating), Pd (from metallization), Ag (predominantly from metallization), Al (from RMS), and Ni (from RMS). Note that the LTCC material contains Al_2O_3 in comparatively high concentrations, making the very low concentration of Al in the Sn layer barely detectable.

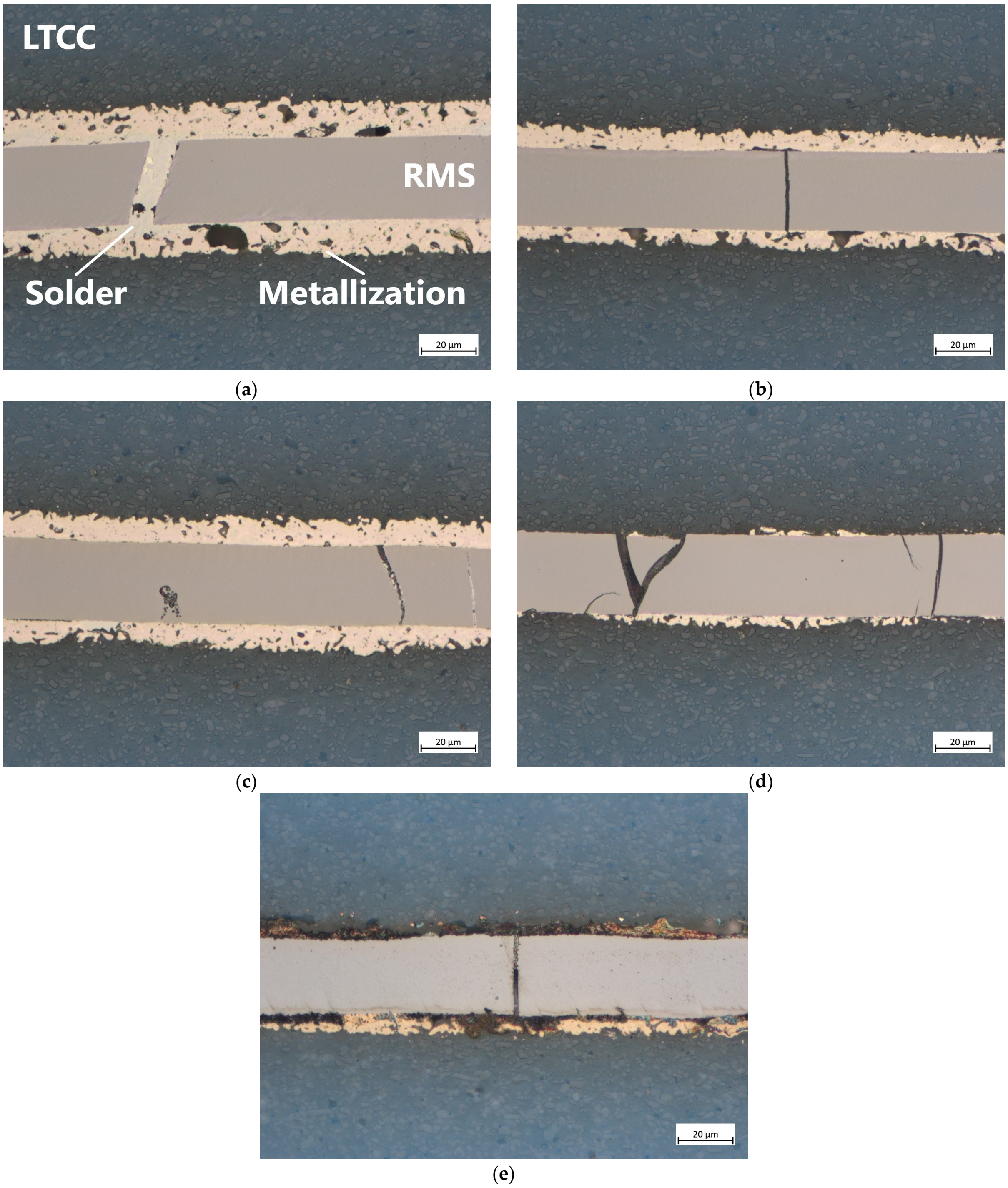

(**a**) (**b**) (**c**) (**d**) (**e**)

Figure 9. Detailed pictures of LTCC samples L6–L10 with Pd/Ag metallization on four corner pads of size 0.5 mm × 0.5 mm (blue: LTCC material; gray: RMS after reaction; white-yellow: solder; red-yellow: metallization). Compared to the previous samples, the applied pressures of (**a**) 20 MPa, (**b**) 100 MPa, (**c**) 200 MPa, (**d**) 300 MPa, and (**e**) 400 MPa are significantly higher due to the considerably reduced metallization area. Magnification: 50×.

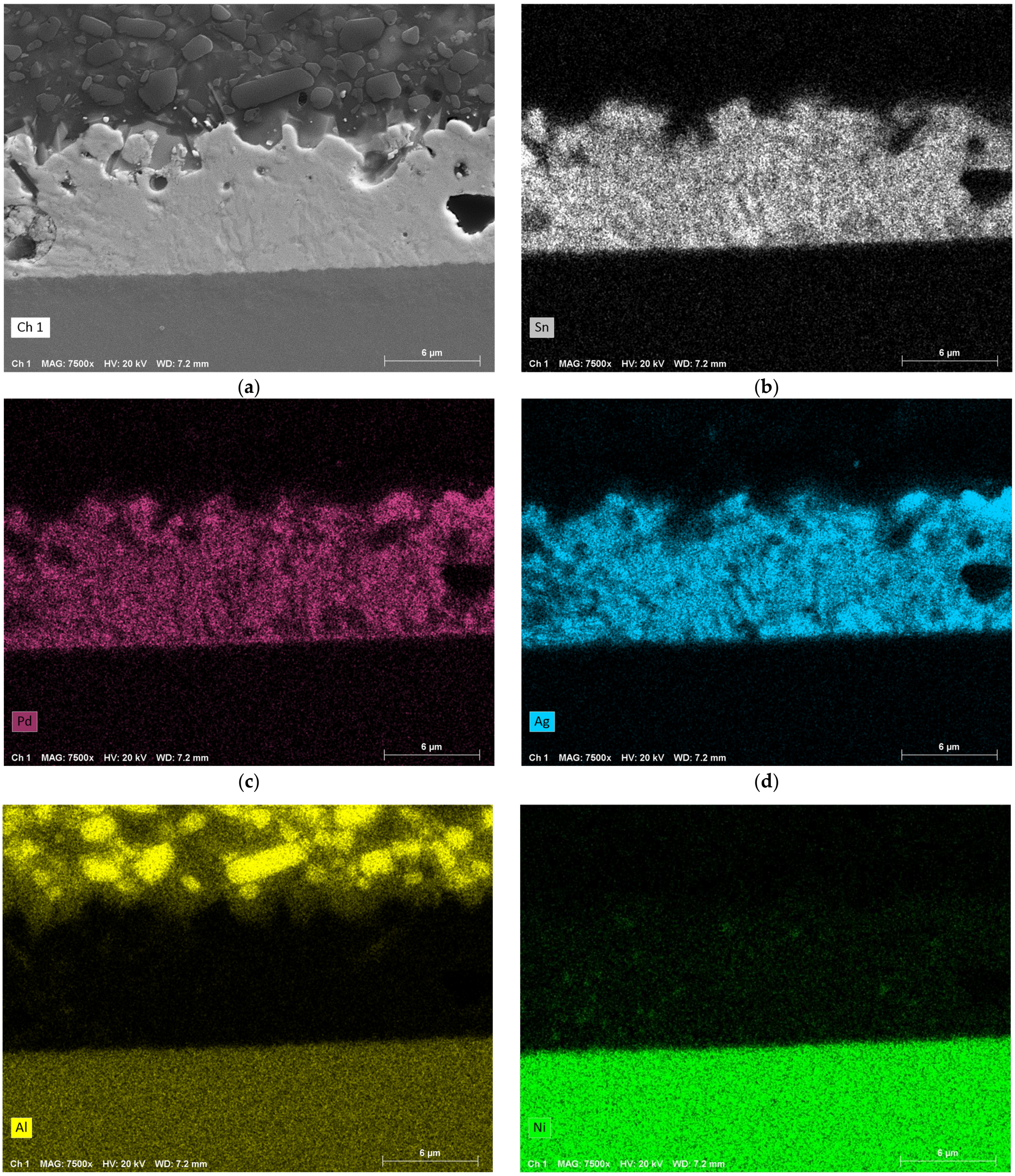

(**a**) (**b**) (**c**) (**d**) (**e**) (**f**)

Figure 10. EDX analysis of a sample that was bonded under a pressure of approximately 2 MPa (bottom: RMS; top: LTCC; center: intermixing zone). (**a**) SEM image in SE mode. (**b**) EDX map of Sn. (**c**) EDX map of Pd. (**d**) EDX map of Ag. (**e**) EDX map of Al. (**f**) EDX map of Ni. Magnification: 7500×.

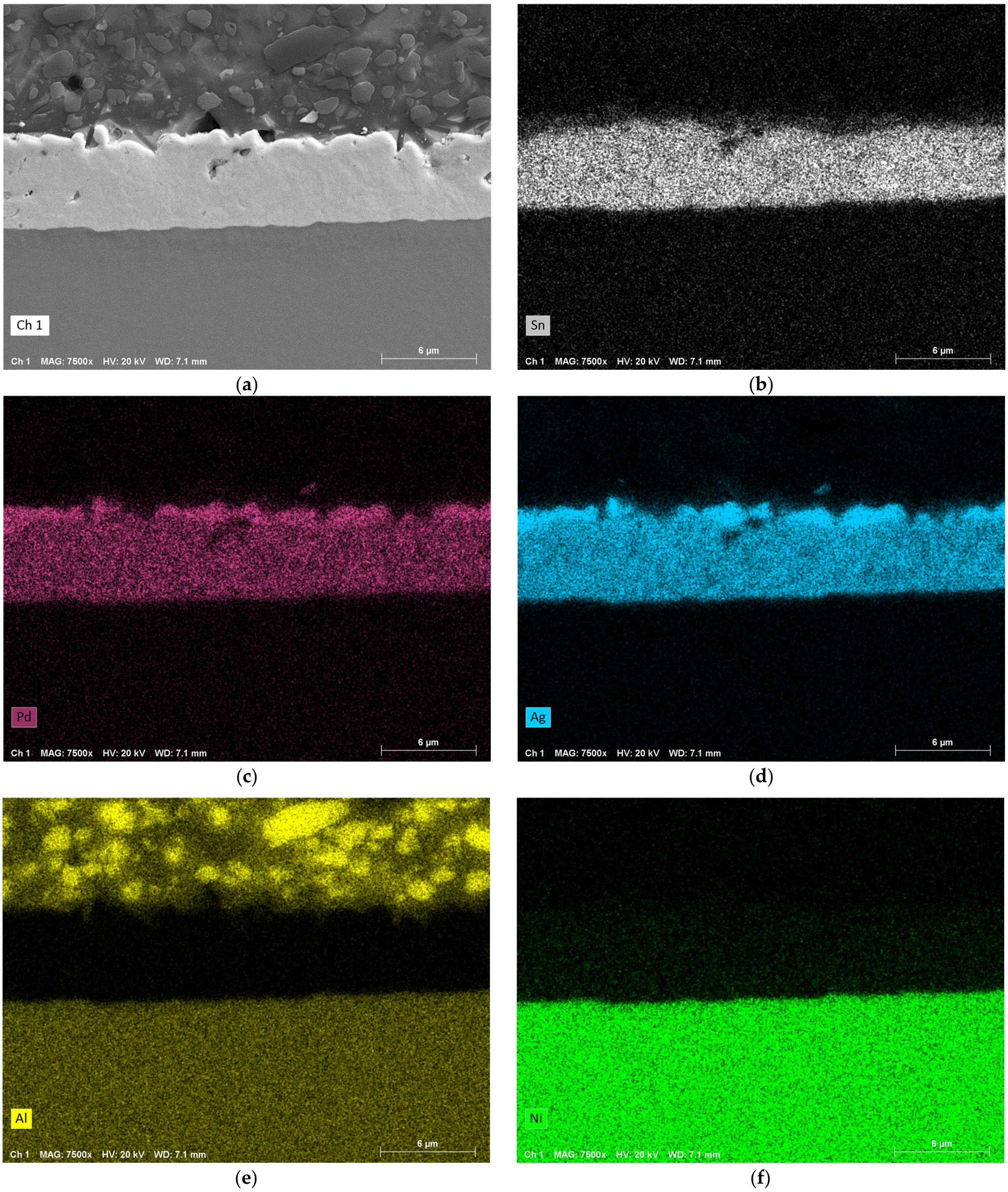

(**a**) (**b**) (**c**) (**d**) (**e**) (**f**)

Figure 11. EDX analysis of a sample that was bonded under a pressure of approximately 11 MPa (bottom: RMS; top: LTCC; center: intermixing zone). (**a**) SEM image in SE mode. (**b**) EDX map of Sn. (**c**) EDX map of Pd. (**d**) EDX map of Ag. (**e**) EDX map of Al. (**f**) EDX map of Ni. Magnification: 7500×.

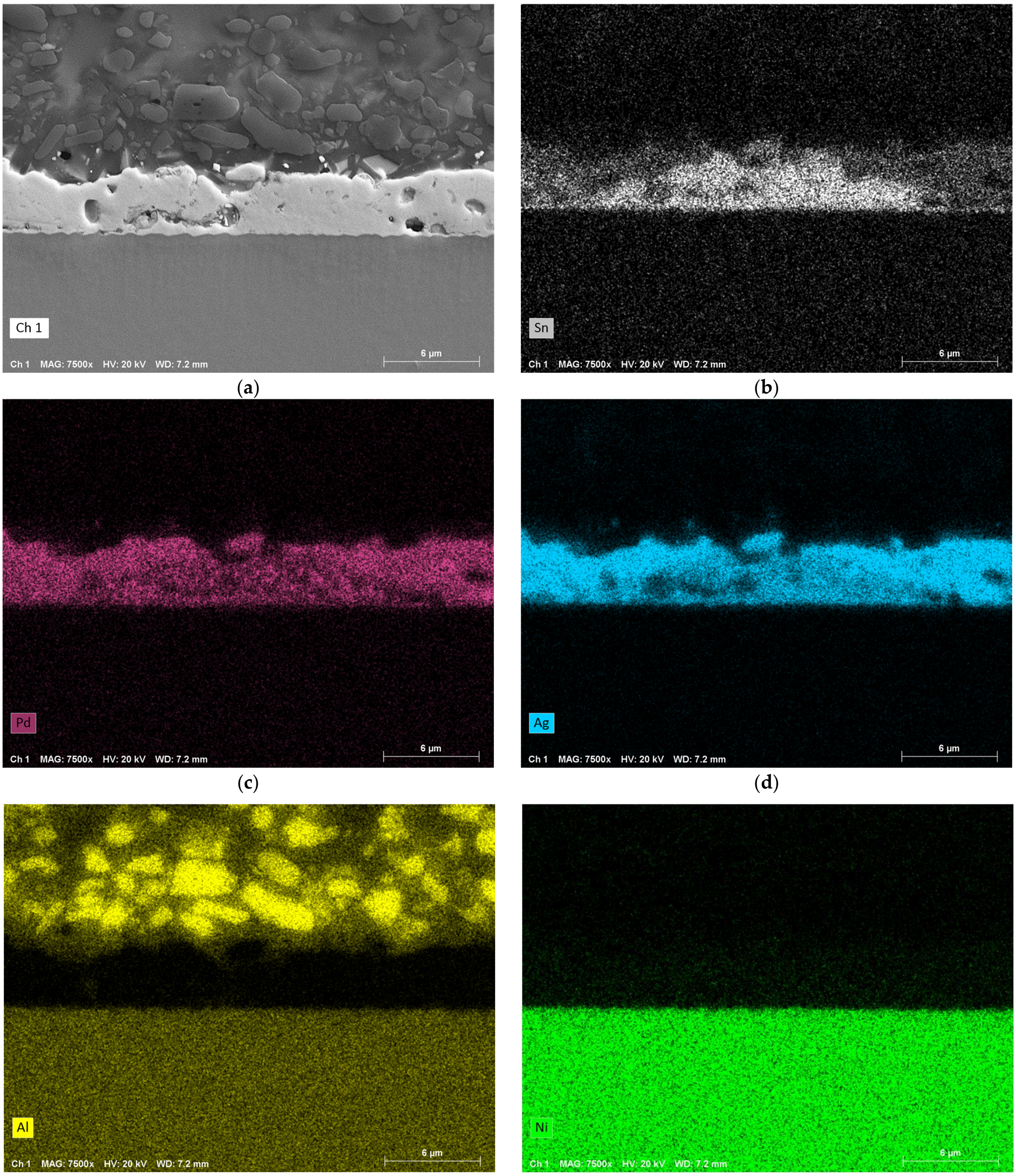

(**a**) (**b**)

(**c**) (**d**)

(**e**) (**f**)

Figure 12. EDX analysis of a sample that was bonded under a pressure of approximately 22 MPa (bottom: RMS; top: LTCC; center: intermixing zone). (**a**) SEM image in SE mode. (**b**) EDX map of Sn. (**c**) EDX map of Pd. (**d**) EDX map of Ag. (**e**) EDX map of Al. (**f**) EDX map of Ni. Magnification: 7500×.

Figure 10 illustrates the EDX analysis for a bonding pressure of 2 MPa. Due to the low pressure, the bonding zone is quite large and some unfilled gaps have formed. The three EDX maps show that Sn has not diffused into other areas after the exothermic reaction and remains confined to its original area. However, the metallization appears to have separated from the LTCC, as Pd and Ag are found to be almost uniformly distributed throughout the intermixing zone. Further, very small amounts of Al and Ni from the RMS have diffused into this layer. There is no difference in the concentration of these elements between the interfaces LTCC/solder or solder/RMS.

At a higher pressure of 11 MPa (Figure 11), the intermixing zone has shrunk to just over half its previous size. As previously observed, small amounts of Al and Ni from the RMS have diffused into the solder layer. The elements Sn, Pd, and Ag have again fully mixed together, but there is now a thin layer at the interface LTCC/solder with a lower concentration of Sn and higher concentration of Pd and Ag. No change can be observed at the interface solder/RMS.

With a further increase in pressure to 22 MPa (Figure 12), the intermediate layer shrinks further. While Al and Ni behave as in the previous case, the behavior of the other elements changes. Sn, Pd and Ag still intermix, but there are regions with high concentrations of Sn and low concentrations of Pd and Ag, and vice versa.

4. Discussion

The results of the configurations studied demonstrate that the bonding pressure during reactive bonding has a significant impact on the quality of the bonding zone. Furthermore, there are also differences between full-area and structured samples.

The light microscopic images reveal that insufficient bonding pressure leads to poor results. Numerous gaps form between the RMS and the metallization of the LTCC, with localized accumulations of solder. These gaps likely arise because the volume of the RMS shrinks by up to 12% after the transformation [24]. These gaps reduce the effective contact area between the RMS and the metallization, leading to poorer thermal conductivity [21]. It is assumed that this reduction also increases the electrical contact resistance and decreases the mechanical stability, both of which should be avoided to maintain a reliable connection. The application of pressure during the bonding process generally proves effective in reducing these gaps. However, in combination with the high temperatures exceeding 800 °C that occur during the exothermic reaction, significant thermo-mechanical stresses arise within the RMS due to the differing CTEs of Al (α_{Al} = 23×10^{-6} K^{-1}) and Ni (α_{Ni} = 13×10^{-6} K^{-1}), ultimately leading to the formation of cracks. These cracks mostly remain unfilled, as the solder tends to adhere to the metallization. Excessive pressures above 30 MPa in the case of full-area samples, on the other hand, are detrimental to the process and should be avoided. They are responsible for the destruction of the metallization or even for cracks in the ceramic material, probably caused by the initial expansion of the RMS during the exothermic reaction.

The comparison between full-area and samples with interconnects also reveals some differences. As in the case of the full-area samples, increasing pressure results in more cracks in the RMS for the structured samples. However, these cracks are more frequently filled with solder in the unmetallized areas, as Sn does not adhere to the ceramic and is drawn into the cracks by the combined effects of surface tension and capillary action, thereby additionally stabilizing the RMS. Furthermore, despite significantly higher pressures of up to 400 MPa, fewer damages were found. This is likely because, on the one hand, the pressure is concentrated on the small, metallized pads, while most of the RMS experience effectively no load due to the lack of contact (compare Figure 5). On the other hand, the RMS can expand into these tiny unmetallized gaps between it and the LTCC during the exothermic reaction, resulting in less stress.

The EDX analysis of the fully metallized samples shows that a certain pressure must be maintained for proper bonding. At low pressure of 2 MPa, there is still a gap between the RMS and the chip or substrate surface. Therefore, it seems there is an accumulation of solder at individual contact points, driven by surface tension. It is believed that the large amounts of solder at these points are able to completely dissolve the metallization. Another possible reason for this could is the significantly lower thermal conductivity of LTCC (3.3 $W \cdot m^{-1} \cdot K^{-1}$) compared to silicon (150 $W \cdot m^{-1} \cdot K^{-1}$) or copper (380 $W \cdot m^{-1} \cdot K^{-1}$), which leads to less heat being conducted away from the reaction zone. As a result, the individual layers are likely to approach the maximum reaction temperature of the RMS more closely than in other systems. At higher pressures of 11 MPa and 22 MPa, such dissolution of the metallization was not observed. Although a large portion dissolves into the solder layer, a strip with a comparatively high concentration remains intact, and there is full-area contact across the entire bonding zone (compare Figures 7b and 7c). Finally, it can be observed that Al and Ni from the RMS diffuse evenly into the solder layer, although in low concentrations.

5. Conclusions

The use of an RMS as a localized heat source is already a well-established process in bonding silicon or metals. However, transferring this technology to ceramic LTCC substrates is complicated due to their specific properties, such as lower thermal conductivity and higher roughness. One aspect that greatly influences the bonding process is the applied bonding pressure. Therefore, LTCC samples with full-area and partial Pd/Ag metallization were bonded using various pressures between 2 MPa and 400 MPa, and cross-sections of the bonding zones were examined by light microscopy, SEM, and EDX. The analyses indicate an optimal pressure range for the bonding process, likely in the range between 10 MPa and 20 MPa.

For samples with full-area metallization, low bonding pressures result in poor wetting behavior of the solder, which accumulates in a few localized areas. Large-area gaps are observed, reducing the effective contact area between the chip and the substrate, thereby negatively affecting the mechanical stability and contact resistance. Conversely, excessive pressure improves the adhesion of the metallization to the RMS but causes it to detach from the LTCC base material and increases the number of cracks in the RMS. Additionally, pressures exceeding 30 MPa increase internal stress within the RMS, causing it to break into separate sections. Furthermore, such high pressures appear to enhance the dissolution of the metallization within the solder, likely reducing the chance of forming a proper IMC.

The EDX analysis supports the hypothesis of an optimal pressure range. At 2 MPa, the elements Pd and Ag from the metallization dissolve nearly completely into the solder due to the inhomogeneous distribution of the solder. At a slightly higher pressure of 11 MPa, this intermixing also occurs, but the metallization itself remains intact and there is a full-area contact across the entire bonding zone. Further, the intermixing layer between the RMS and the LTCC is more densely packed. At 22 MPa, similar observations are made, with areas showing accumulations of Sn and lower concentrations of Pd and Ag, and vice versa.

For the samples with interconnects, high pressures do not seem to have as severe an impact. Although more cracks are formed in the RMS with increasing pressure, neither complete fragmentation of the RMS nor cracks in the LTCC occur even at extremely high pressures of up to 400 MPa. Due to the partial metallization, there are small gaps between the LTCC and the RMS, into which the RMS can likely expand during the exothermic reaction before subsequently shrinking to its final form.

However, not only the bonding pressure but also the temperature during the exothermic reaction has a significant influence on the intermixing of the particular layers and the formation of cracks within the RMS. Additionally, a thicker solder layer may also help to fill any resulting cracks, though the range of different types of commercially available reactive foils is very limited. Alternatively, direct deposition of such reactive layers onto the substrate or chip is possible, allowing for the variation in individual parameters, such as stack or nanolayer thickness, or solder thickness. Future research could therefore investigate the combined influence of these parameters and the bonding pressure to further optimize the bonding process.

Author Contributions: Conceptualization, E.W., N.J. and S.W.; methodology, E.W., N.J. and S.W.; investigation, E.W. and N.J.; resources, J.M. and S.W.; writing, E.W.; review and editing, E.W. and S.W.; supervision, J.M. and S.W.; funding acquisition, J.M. and S.W. All authors have read and agreed to the published version of the manuscript.

Funding: This research was funded by Deutsche Forschungsgemeinschaft (DFG), grant number 426204742.

Data Availability Statement: The original contributions presented in this study are included in the article. Further inquiries can be directed to the corresponding author.

Acknowledgments: The authors would like to offer particular thanks to A. Ruh for his support in microscopical analysis and in editing graphics, and to B. Müller for his support in sample preparation (LTCC manufacturing) at the Center of Micro- and Nanotechnologies (ZMN), a DFG-funded core facility (grant numbers 233759584 and 324659519) at TU Ilmenau.

Conflicts of Interest: The authors declare no conflicts of interest.

References

1. Zhang, J.; Wu, F.S.; Zou, J.; An, B.; Liu, H. Al/Ni Multilayer Used as a Local Heat Source for Mounting Microelectronic Components. In Proceedings of the 2009 International Conference on Electronic Packaging Technology & High Density Packaging (IEEE), Beijing, China, 10–13 August 2009.
2. Levin, J.P.; Rude, T.R.; Subramanian, J.; Besnoin, E.; Weihs, T.P.; Knio, O.M.; Van Heerden, D. Room Temperature Lead-Free Soldering of Microelectronic Components using a Local Heat Source. In Proceedings of the ASM Materials Solutions Conference & Exposition, Columbus, OH, USA, 18–21 October 2004.
3. Boettge, B.; Braeuer, J.; Wiemer, M.; Petzold, M.; Bagdahn, J.; Gessner, T. Fabrication and characterization of reactive multilayer systems for low-temperature bonding in microsystem technology. *J. Micromech. Microeng.* **2010**, *20*, 064018. [CrossRef]
4. Sen, S.; Lake, M.; Kroppen, N.; Farber, P.; Wilden, J.; Schaaf, P. Self-propagating exothermic reaction analysis in Ti/Al reactive films using experiments and computational fluid dynamics simulation. *Appl. Surf. Sci.* **2017**, *396*, 1490–1498. [CrossRef]
5. Adams, D.P. Reactive multilayers fabricated by vapor deposition: A critical review. *Thin Solid Film.* **2015**, *576*, 98–128. [CrossRef]
6. Gavens, A.J.; Van Heerden, D.; Mann, A.B.; Reiss, E.; Weihs, T.P. Effect of intermixing on self-propagating exothermic reactions in Al/Ni nanolaminate foils. *J. Appl. Phys.* **2000**, *87*, 1255–1263. [CrossRef]
7. Grigoryan, A.E.; Elistratov, N.G.; Kovalev, D.Y.; Merzhanov, A.G.; Nosyrev, A.N.; Ponomarev, V.I.; Rogachev, A.S.; Khvesyuk, V.I.; Tsygankov, P.A. Autowave Propagation of Exothermic Reactions in Ti-Al Thin Multilayer Films. *Dokl. Phys. Chem.* **2001**, *381*, 283–287. [CrossRef]
8. Reiss, M.E.; Esber, C.M.; Van Heerden, D.; Gavens, A.J.; Williams, M.E.; Weihs, T.P. Self-propagating formation reactions in Nb/Si multilayers. *Mater. Sci. Eng. A* **1999**, *261*, 217–222. [CrossRef]
9. Tanaka, S.; Kondo, K.; Habu, H.; Itoh, A.; Watanabe, M.; Hori, K.; Esashi, M. B/Ti multilayer reactive igniter for micro solid rocket array thruster. In Proceedings of the 2017 IEEE 20th International Conference on Micro Electro Mechanical Systems (MEMS), Hyogo, Japan, 21–25 January 2007.
10. Rzyman, K.; Moser, Z. Enthalpies of Formation of AlNi: Experiment Versus Theory. *J. Phase Equilibria* **1998**, *19*, 106–111. [CrossRef]
11. Qiu, X.; Wang, J. Bonding silicon wafers with reactive multilayer foils. *Sens. Actuators A Phys.* **2008**, *141*, 476–481. [CrossRef]
12. Qiu, X.; Wang, J. Reactive Multilayer Foils for Silicon Wafer Bonding. *Mater. Res. Soc. Symp. Proc.* **2006**, *968*, 206. [CrossRef]
13. Simões, S.; Ramos, A.S.; Viana, F.; Vieria, M.T.; Vieria, M.F. Joining of TiAl to Steel by Diffusion Bonding with Ni/Ti Reactive Multilayers. *Metals* **2016**, *6*, 96. [CrossRef]
14. Jantunen, H.; Kangasvieri, T.; Vähäkangas, J.; Leppävuori, S. Design aspects of microwave components with LTCC technique. *J. Eur. Ceram.* **2003**, *23*, 2541–2548. [CrossRef]
15. Matters-Kammerer, M.; Mackens, U.; Reimann, K.; Pietig, R.; Hennings, D.; Schreinemacher, B.; Mauczok, R.; Gruhlke, S.; Martiny, C. Material properties and RF applications of high *k* and ferrite LTCC ceramics. *Microelectron. Reliab.* **2006**, *46*, 134–143. [CrossRef]

16. Schulz, A.; Bartsch, H.; Gutzeit, N.; Matthes, S.; Glaser, M.; Ruh, A.; Müller, J.; Schaaf, P.; Bergmann, J.P.; Wiese, S. Characterization of Reactive Multilayer Systems deposited on LTCC featuring different surface morphologies. In Proceedings of the MikroSystemTechnik Congress 2021, Ludwigsburg, Germany, 8–10 November 2021.
17. Schulz, A.; Ruh, A.; Wiese, S.; Müller, J. Characterization of Reactive Multilayer Systems deposited on LTCC screen printing pastes featuring different surface morphologies suitable for reactive joining applications. In Proceedings of the Ceramic Interconnect and Ceramic Microsystems Technologies (CICMT) 2022, Wien, Austria, 13–15 July 2022.
18. Wiss, E.; Schulz, A.; Ruh, A.; Jaekel, K.; Müller, J.; Wiese, S. Morphologies of Reactive Nanolayer Stacks Sputtered on Ceramic Low-Temperature Cofired Ceramic Substrates Having a Micrometer-Scale Surface Roughness. *Adv. Eng. Mater.* **2024**, *27*, 2302284. [CrossRef]
19. Yuile, A.; Schulz, A.; Wiss, E.; Müller, J.; Wiese, S. The Simulated Effect of Adding Solder Layers on Reactive Multilayer Films Used for Joining Processes. *Appl. Sci.* **2022**, *12*, 2397. [CrossRef]
20. Wang, J.; Besnoin, E.; Knio, O.M.; Weihs, T.P. Investigating the effect of applied pressure on reactive multilayer foil joining. *Acta Mater.* **2004**, *52*, 5265–5274. [CrossRef]
21. Kanetsuki, S.; Miyake, S.; Kuwahara, K.; Namazu, T. Influence of bonding pressure on thermal resistance in reactively-bonded solder joints. *Jpn. J. Appl. Phys.* **2016**, *55*, 06GP17. [CrossRef]
22. Schumacher, A.; Gaiß, U.; Knappmann, S.; Braun, S.; Pflug, E.; Roscher, F.; Vogel, K.; Hertel, S.; Kähler, D.; Reinert, W. Assembly and Packaging of Micro Systems by Using Reactive Bonding Processes. In Proceedings of the 2015 European Microelectronics Packaging Conference (EMPC), Friedrichshafen, Germany, 14–16 September 2015.
23. Wiss, E.; Jaziri, N.; Yuile, A.; Müller, J.; Wiese, S. Experimental Study on Reactive Joining Processes on LTCC Substrates. In Proceedings of the 2024 IEEE 10th Electronics System-Integration Technology Conference (ESTC), Berlin, Germany, 11–13 September 2024.
24. Namazu, T.; Ohtani, K.; Yoshiki, K.; Inoue, S. Crack propagation direction control for crack-less solder bonding using Al/Ni flash heating technique. In Proceedings of the 2011 16th International Solid-State Sensors, Actuators and Microsystems Conference (IEEE), Beijing, China, 5–9 June 2011.

5.9 Paper 9: Concept of a Mechanical Test Setup for Packaging Materials Using Digital Image Correlation Methods

5.9.1 Veröffentlichungshinweise

Erik Wiss, David Barth, Steffen Wiese

Chair of Microintegration and Reliability, Faculty of Natural Sciences and Technology, Saarland University, Saarbrücken, Germany

2021 22nd International Conference on Thermal, Mechanical and Multi-Physics Simulation and Experiments in Microelectronics and Microsystems (EuroSimE)

Die Originalveröffentlichung ist abrufbar unter:
https://doi.org/10.1109/EuroSimE52062.2021.9410859

5.9.2 Synopse

Diese Veröffentlichung, die aus der Masterarbeit des Autors hervorging, beschreibt die Konzeption und Entwicklung eines Versuchsaufbaus zur mechanischen Charakterisierung elektrischer Verbindungen. Die Motivation ergibt sich aus der Notwendigkeit, die Stabilität und Zuverlässigkeit solcher Verbindungen zu bewerten. Ziel der Arbeit war die Entwicklung eines modularen, flexibel anpassbaren Systems, das mit überschaubarem Aufwand auf unterschiedliche Probenkörper angepasst werden kann.

Hierzu wurden zunächst die maximal zu erwartenden mechanischen Belastungen abgeschätzt und entsprechend geeignete Komponenten ausgewählt. Die mechanische Beanspruchung erfolgt über einen bürstenlosen Gleichstrommotor, während ein dreiachsiger Kraftsensor sowohl die Zugkraft als auch das auf die Probe wirkende Drehmoment erfasst. Eine integrierte Thermokammer ermöglicht die Durchführung der Experimente auch bei höheren Temperaturen. Ein Stereo-Zoom-Mikroskop nimmt während der Deformation Bilder zur Auswertung mittels digitaler Bildkorrelation (DIC, **D**igital **I**mage **C**orrelation) auf. Aus den so gewonnenen Spannungs-Dehnungs-Diagrammen lassen sich mechanische Kennwerte wie das Elastizitätsmodul ableiten. An strukturierten Cu-Folien wurde die Eignung des Aufbaus für Zug- und Ermüdungsversuche demonstriert.

Die Ergebnisse zeigen, dass der Aufbau geeignet ist, mechanische Eigenschaften von Proben zu charakterisieren. Allerdings ist er aufgrund seiner langsamen Bewegung nur bedingt für zyklische Ermüdungsversuche geeignet.

Im Kontext des Gesamtprojekts leistet diese Veröffentlichung einen Beitrag zur Beantwortung der Frage, wie robust und stabil die erzeugten Fügeverbindungen sind.

5.9.3 Vollständiger Artikel

Concept of a Mechanical Test Setup for Packaging Materials Using Digital Image Correlation Methods

E. Wiss, D. Barth, S. Wiese
Saarland University, Chair of Microintegration and Reliability
Saarbruecken, Germany
erik.wiss@uni-saarland.de

Abstract

This paper presents a concept for a mechanical testing apparatus for electronic packaging materials that benefits from the usage of digital image correlation (DIC) for strain measurement. In contrast to similar test setups, which use a CCD-microscope as an attachment to the mechanical test setup, the new concept tries to attach the mechanical test setup to a professional research microscope. The intention is to improve the projection of the object field to the CCD sensor array of the microscope-camera, and thus to improve the strain measurement of miniaturized samples. To be able to perform experiments at higher temperatures a suitable temperature-controlled test chamber was also designed. The paper shows the realization of the test setup and presents the first experiments with suitable specimen that will also be discussed.

1. Introduction

In the course of increasing mechanization, new electronic products are facing new challenges. They should be as compact as possible and offer as many functions as possible in the smallest of spaces. This leads to increased demands on the electronics packaging because the interconnection between the individual components needs to shrink to suitable dimensions too. Such small-dimensioned materials show a deviant behavior than larger ones (e.g., microplates with a thickness in the range of the grain size [1]). Having an accurate knowledge of their properties like the Young's modulus is required to achieve reliable data from FEM simulations. Most of those simulations deal with electrical, thermal and thermo-mechanical problems [2], but they are increasingly used in the area of electronic packaging.

In [3] a thermo-mechanical tester with a DC motor driven stage and an environmental chamber was already presented. It can be used in six axis (three orthogonal translations and three rotations) and measures the displacement in a capacitive way. Another type of setups was realized using a stepper motor actor [4-6], which offers a higher force range. Furthermore, the digital image correlation method was successfully employed for the evaluation of the deformation of the samples during the experiments. Other authors used laser extensometers for displacement measurements on small samples [7,8]. This requires an accurate patterning of marks on the sample which can be very time-consuming. In [9] photoacoustic measurement with a modulated laser signal was used to determine the mechanical properties of thin film probes.

The new test setup should provide the ability to run experiments without spending lots of times in sample preparation. Because of their small dimensions a conventional (capacitive or inductive) distance measurement is difficult to implement, especially without destroying or damaging the sample. Furthermore, they can only detect global shifts. A contactless method like the digital image correlation can also detect local shifts and is easy to implement, because it only needs a camera and a computer. It compares two consecutive images that are taken during the experiment for the shift of a grey scale pattern and calculates the strain of the material. In combination with the measured forces, the occurring stresses can be determined.

Most of the existing testing machines, that are using a conventional camera or a CCD-microscope, are intended to examine only large samples. In the new concept a stereo-zoom-microscope with a maximum magnification of more than 200 times is used to open up new possibilities. The magnification can be adjusted to receive an optimum object field size for different types of samples.

The new setup should be able to perform both tensile tests and cyclic fatigue tests. For this reason, a suitable actor has to be found. Setups with a piezoelectrical actor can exert high forces at high frequencies of a few thousand Hz but their operating displacement is in a small range of micrometers. In contrast stepper motor driven testers can perform large movements which are mainly limited by the available space, but their movement may not be as smooth as desired which could cause damage to the sample, especially if it is very small. Testers which are driven by an electromagnetic coil can perform large movements at high speeds, but they cannot generate such high forces as the other actor types. Additionally, there is a risk of overheating. Nowadays, DC motors combine all the features like large travel ranges, high speed and high accuracy. Because of that they seem to be a good alternative to the other motor types so one of those was used for the new setup.

The whole construction was developed to be an attachable part to the microscope. This is necessary because the samples cannot be exchanged while the setup is under the microscope because there is not enough space. Furthermore, it provides the flexibility to use the microscope as a conventional one itself and offers an easy exchange for other test setups by loosen a handful of screws (e.g., for another type of actor). For those reasons, a corresponding substructure made up of translation stages was designed to attach the mechanical test setup. The entire experimental setup is controlled via LabVIEW.

2. Mechanical Test Setup

2.1 Overview

A large optical aluminum breadboard (size 1200 mm x 600 mm) was used as a ground plate. All the components were constructed around the microscope which was set to the center of the plate. To get a better understanding of the following steps, an overview about the test setup is shown in figure 1.

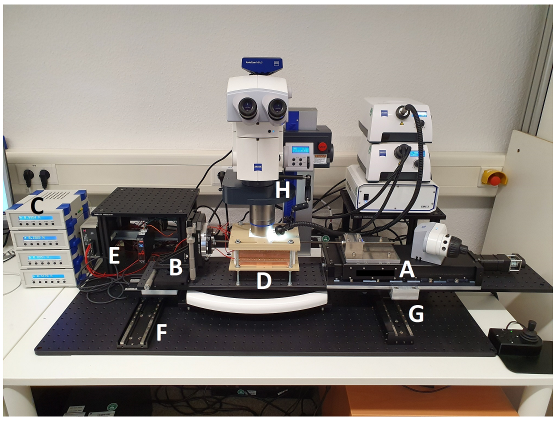

Figure 1: Overview of the realized test setup.

The components in the figure are labeled as follows:

A: Actor
B: Force Measurement Sensor
C: Measurement Amplifiers
D: Thermal Chamber
E: Temperature Controller of the Thermal Chamber
F: Non-motorized Translation Stages
G: Motorized Translation Stages
H: Stereo-Zoom-Microscope with Illumination

2.2 Actor

The main component of the whole setup is the actor which exercises the force on the sample. Because of the disadvantages of other motor types (that were already discussed in the introduction) a BLDC motor driven translation stage was used. It has a displacement of 200 mm, a maximum force of 220 N, a resolution of 2 µm and a maximum speed of 150 mm/s. To connect the actor to the computer, a USB controller was used.

To transmit the movement and thereby the force to the sample, an aluminum block was milled. It has four vertical holes to mount it on the actor and a horizontal one through which a threaded bar, that is fixed by hex nuts and washers on each side, can be inserted. The threaded bar ends in the thermal chamber where a clamp is attached.

2.3 Force Measurement Sensor

To be able to calculate the mechanical properties like the Young’s modulus, it is necessary to know the force that was acting on the sample. For this purpose, a three-axis force sensor was chosen. It can measure a force up to 200 N in pull direction and a torque up to 4 Nm in the other directions with an accuracy of 0,1 %. This features the advantage to detect disruptive interferences (e.g., skewed mounting of the sample).

It was mounted on a 90° adapter to connect it to the breadboard. For exact aligning two small breadboards that can be displaced via a micrometer screw were placed between the sensor and the adapter, and between the adapter and the breadboard. Similar to the actor, a threaded bar is fixed to the sensor by hex nuts and washers on each side. The other end of the bar ends in the thermal chamber where the second clamp is attached.

The four channels of the sensor are connected to four measurement amplifiers. Those are connected to the computer via a terminal-block and a multifunction PCIe-card, so that they can be easily controlled via LabVIEW.

2.4 Thermal Chamber

There are some applications in which electronic products are used at high ambient temperatures (e.g., in the automotive section). Most material parameters are temperature-dependent why the experiments have to be done at different temperatures. For this reason, a thermal chamber was developed which can heat up to 150 °C.

Such a thermal chamber was already used in another experimental setup of the chair [10]. This first version was completely made out of PTFE, which is easy to machine but also tends to thermically induced stress. To avoid such deformations a heat resistant glass-fibre-reinforced polymer was used for the lower and upper shell. The top shell consists of three layers with double glazing to avoid heat haze effects [11]. The walls were made double-walled for better insulation and were still made out of PTFE. Figure 2 shows the assembled thermal chamber.

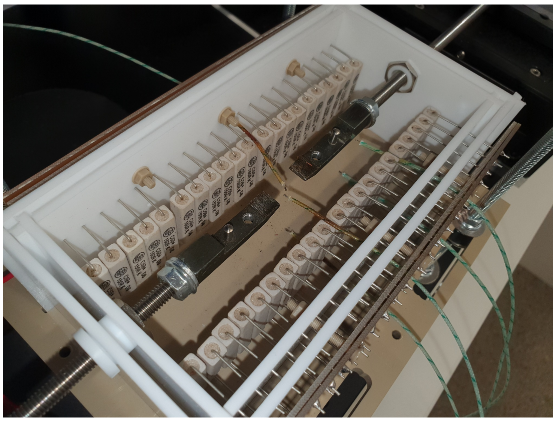

Figure 2: Assembled thermal chamber with some thermocouples at different positions.

2.5 Translation Stages

To maintain the possibility of using the microscope as a conventional itself and to enable an easy exchange of the setup the whole construction was developed as an attachable part. For this reason, a substructure made up of translation stages was designed to attach the mechanical test setup, so that it can be moved in both x- and y-direction. Furthermore, the sample can be clamped more easily by moving the experimental setup next to the user, and the sample can be positioned accurately under the microscope.

On the right side two motorized translation stages were used. They are responsible for the movement of the setup. On the opposite side two non-motorized stages that serve as support bearings were placed. To allow movements in both x- and y-direction two stages were stacked on both sides. Before suitable translation stages can be chosen, the total load that must be moved has to be estimated. The masses of the individual components are shown in table 1.

Table 1: Estimated load of the setup.

Component	Actor	Sensor	Thermal Chamber	Bread-board
Mass	9 kg	2 kg	1 kg	4,5 kg

The total mass is about 16,5 kg with the actor being the heaviest part with 9 kg why it was placed above the motorized stages. The other components can be assumed to be uniformly distributed on the breadboard. Two motorized translation stages with a maximum load of 300 N and a maximum speed of 20 mm/s were chosen. They have a maximum travel range of 100 mm in x- and 200 mm in y-direction. As counterparts two translation stages without a motor were chosen. Due to a slight offset of the mounting holes those with a maximum travel range of 100 mm in x- and 300 mm in y-direction had to be chosen. To allow gliding their spindles were removed.

Like the actor the motorized stages are connected via a USB controller to the computer. In addition, a joystick was used to be able to move the setup manually.

2.6 Connecting the Translation Stages

Both stacks of stages were connected via a large breadboard of 1200 mm x 150 mm. Indeed, the mounting holes of the actor are at a distance of the board width but using a larger breadboard with a width of 300 mm would have increased the weight unnecessarily. Instead of that some self-made aluminum adapters with self-drilled mounting holes were used to screw the parts together.

On the right side a plate with a wing on the front and the back was screwed on the upper motorized translation stage. The actor was mounted on another aluminum adapter which was in turn connected to the breadboard. This second adapter has also two wings by which it can be connected to the lower adapter.

On the left side only one adapter was necessary to compensate the height difference that has arisen due to the different heights of the tables and the use of the adapters. It was screwed to the upper non-motorized table, and the breadboard was screwed to the adapter.

This substructure offers two advantages: First, the setup can be moved in two directions to provide easier sample clamping and positioning, and to create space for using the microscope itself. Second, only four screws on each side have to be loosened to remove the whole setup and exchange it with another one.

3. Experiment

3.1 Specimen Design

To validate the operability of the mechanical test setup a tensile test should be performed. For this purpose, a LPKF S103 PCB prototyping machine was used to mill two different samples out of a 35 µm thick copper foil. This material was chosen because the authors already had some experience with it. The manufacturing of the specimen is described in detail in [12], and its design is shown in Figure 3.

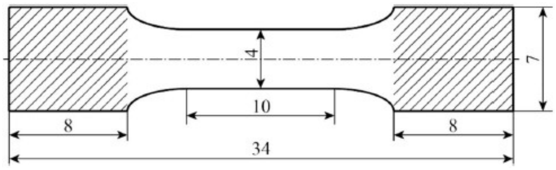

Figure 3: Dog bone specimen design with relieved gauge of 4 mm, milled out of a 35 µm thick copper foil [12].

The dog bone specimen design, which was first used in [13], was chosen because it reduces the impact of the grip forces on the stress distribution [12]. Furthermore, FEM simulations showed that an inhomogeneous stress distribution along the sample can be mostly avoided with this design.

The sample has an overall length of 34 mm with an overall width of 7 mm. At both ends there are comparatively big areas by 7 mm x 8 mm to avoid slippages and to provide easier clamping and positioning. The width of the gauge itself is reduced to 4 mm in one sample, and to 1 mm in another one. Thanks to the possible maximum magnification of the stereo-zoom-microscope a sufficient observation field for the DIC technique is given.

3.2 Experimental Procedure (LabVIEW)

The entire experiment control was realized in LabVIEW. The setup can be moved with one button to the front to clamp the sample, and back under the microscope with another one. After that the setup can be exactly positioned with the joystick of the translation stages. Then, the microscope has to be focused on the probe to receive sharp images which will be used for DIC.

Before the experiment can be started, some important parameters have to be set:

- Velocity: An actor speed of 1 RPM (lowest possible setting) is a good choice for tensile tests. For fatigue tests the maximum speed of 1500 RPM should be used.
- Displacement: This value sets the distance that should be driven in fatigue tests.
- Recording interval: This determines the distance the sample may be displaced until the next image is recorded. For the following tests a value of 5 µm was a good choice.

After setting these parameters the test can be started. For safety reasons, the test stops automatically if the force gets too high (to prevent sensor damage) or if the sample breaks. While the experiment is running the images and the measured force values are saved automatically. The following chapters show the results of tensile tests with two different samples and one fatigue test.

3.3 Evaluation in MATLAB

After finishing the experiment, the evaluation can be started. It is realized through a MATLAB-script that was written by Mehdi Elasmi in 2013 [14] and refined by Joseph Al Ahmar. After loading the images, they are converted automatically to grayscale ones and the user choses an image section that should be investigated (region of interest, figure 4) i.e., for which the strains should be calculated.

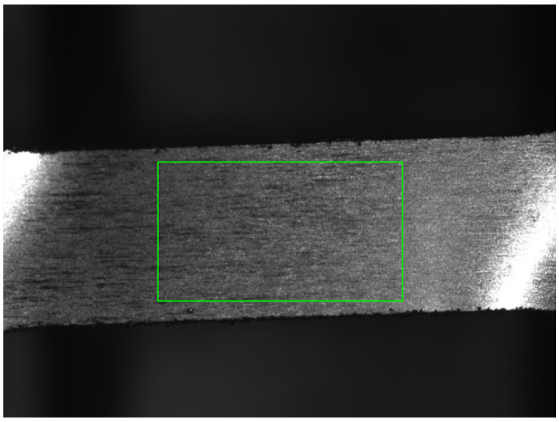

Figure 4: Image of the sample, converted to grayscale. The rectangular selection is the chosen region of interest.

After that the script compares two succeeding pictures by analyzing the movement of a random dot pattern on the samples surface. Depending on the kind of samples it might be necessary to bring up a special pattern (e.g., using white chalk spray and graphite spray). Here the surface of the samples was good enough to skip these steps. Combined with the measured force values it is possible to plot the corresponding stress-strain curves. Finally, analyzing the values out of the linear-elastic range (maximum 0,2 % strain) the Young's modulus can be calculated.

3.4 Tensile Test

In the first test a sample with a 4 mm gauge was used. The pictures were taken after each movement of 5 µm. The evaluation with the MATLAB DIC script leads to the following figure 5:

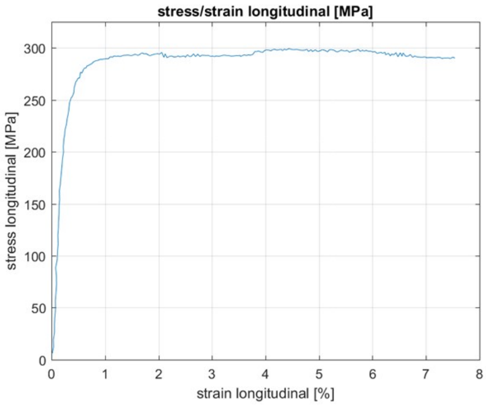

Figure 5: Stress-strain curve of the 4 mm gauge.

This stress-strain curve seems to be realistic: At small strains there is a high raise in stress, which merges in an almost constant range. Figure 6 shows the plot reduced to the linear-elastic range:

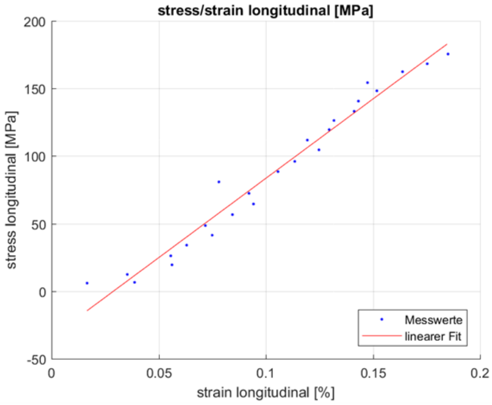

Figure 6: Stress-strain curve of the 4 mm gauge, reduced to the linear-elastic range.

The dots correspond to the measured and calculated values while the continuous line represents a linear fit. The rise of the linear fit is the Young's modulus and is 117,4 GPa in this case. Depending on the orientation of the copper the Young's Modulus is in the range of 67 … 190 GPa [15] which means that there is a good accordance.

3.5 Capability for Fatigue Tests

To determine the eligibility of the test setup for fatigue tests one sample was tested while the actor was moved in a cycling way. The speed of the BLDC motor was set to its maximum and the range was set to 20 µm. Only a few cycles were done, and the time-displacement-diagram was plotted. The time range 6000 to 7000 ms is shown in figure 7.

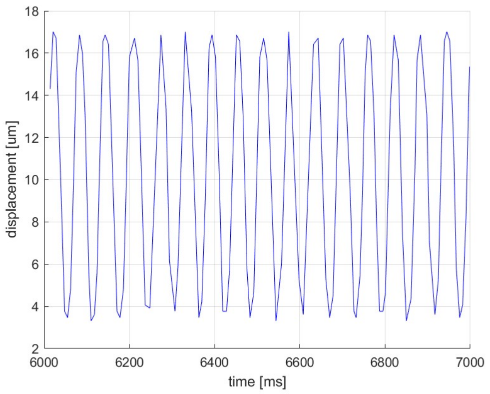

Figure 7: Time-displacement curve of a fatigue test

Counting the slopes leads to 16 cycles per second i.e., 1000 cycles per minute. This results in the following estimated times for fatigue tests, assuming a maximum of 10^7 cycles until the sample breaks:

Table 2: Estimated times for fatigue tests dependent on the number of load changes

Number of Load Changes	10^3	10^4	10^5	10^6	10^7
Time	1 min	10 min	1,67 h	16,67 h	166,67 h

This means that a number of load changes up to 10^5 could be done in sufficient short time. Beyond that limit the test procedure takes too much time for a larger series of tests. Furthermore, a higher speed would be desirable to complete at least one single test in one working day. Thanks to the attachable design a second test setup with another kind of actor (like a piezoelectrical one) could be developed and easily exchanged for such type of tests.

4. Conclusions

A new concept of a mechanical test setup for tensile and fatigue tests was presented in this paper. The centerpiece of the setup is a stereo-zoom-microscope which offers the possibility to investigate not only large-dimensioned samples but also small-dimensioned ones. The modular construction does not only offer the possibility to use the microscope for regular work but also the easy exchange of the setup with other setups. A first tensile test proved that the results are in good agreement with known values, why the setup can be considered as a valuable instrument for mechanical experiments.

Acknowledgments

The research was funded by the Deutsche Forschungsgemeinschaft (DFG, German Research Foundation) – Project-ID 426204742.

References

1. Köhler, B.; Bomas, H.; Zoch, H.-W.; Stalkopf, J.: Werkstoffprüfung an Mikroproben und -halbzeugen. *Materials Testing*. 2010, vol. 52, no. 11-12, pp. 759-764.
2. Liu, S.; Liu, Y.: Modeling and Simulation for Microelectronic Packaging Assembly: Manufacturing, Reliability and Testing. *John Wiley & Sons*. Singapore, 2011.
3. Lu, M.; Qian, Z.; Ren, W.; Liu, S.; Shangguan, D.: Investigation of electronic packaging materials by using a 6-axis mini thermo-mechanical tester. *International Journal of Solids and Structures*. 1999, vol. 36, no. 1, pp. 65-78.
4. Metasch, R.; Klemm, A.; Röllig, M.; Zerna, T.: Messverfahren zur thermo-mechanischen Charakterisierung von Werkstoffen der Hochtemperatur-AVT. Eds.: DVS / GMM, *GMM-Fb. 84: Elektronische Baugruppen und Leiterplatten – EBL 2016*, 16.-17.02. Fellbach, Germany, 2016.
5. Yuile, A.; Wiese, S.: The influence of thermal ageing on the flow-stress of copper traces on PCB's. *Microelectronics Reliability*. 2019, vol. 99, pp. 197-202.
6. Kraemer, F.; Roellig, M.; Metasch, R.; Wiese, S.; Al Ahmar, J.; Meier, K.: Experimental determination of the Young's modulus of copper and solder materials for electronic packaging. *Microelectronics Reliability. 2018.* vol. 91, pp. 251-256.
7. Müller, W. H.; Worrack, H.; Sterthaus, J.; Villain, J.; Wilden, J.; Juritza, A.: How to extract continuum materials properties for (lead-free) solders from tensile tests and nanoindentation experiments. *Microsystem technologies*. 2009, vol. 15, no. 1, pp. 45-55.
8. Villain, J.; Brueller, O. S.; Qasim, T.: Creep behaviour of lead free and lead containing solder materials at high homologous temperatures with regard to small solder volumes. *Sensors and Actuators A: Physical*. 2002, vol. 99, no. 1-2, pp. 194-197.
9. Dual, J.; Simons, G.; Villain, J.; Vollmann, J.; Weippert, C.: Mechanical properties of MEMS structures. *Proceedings of ICEM12*. 2004.
10. Wiese, S.; Kraemer, F.; Al Ahmar, J.: The onset of plastic flow in copper materials used for ridged and flexible PCB. *2017 18th International Conference on Thermal, Mechanical and Multi-Physics Simulation and Experiments in Microelectronics and Microsystems (EuroSimE).* Dresden, Germany, 2017, 5 p.
11. Yuile, A.; Schwerz, R.; Roellig, M.; Metasch, R.; Wiese, S.: Heat haze effects in thermal chamber

tensile tests on Digital Image Correlation. *2018 19th International Conference on Thermal, Mechanical and Multi-Physics Simulation and Experiments in Microelectronics and Microsystems (EuroSimE).* Toulouse, France, 2018, 7 p.

12. Wiese, S.; Bruch, D.; Elasmi, M.; Kraemer, F.; Al Ahmar, J.: Experimental Design for Tensile Tests on PCB Copper Traces for Board Level Packaging. *2016 17th International Conference on Thermal, Mechanical and Multi-Physics Simulation and Experiments in Microelectronics and Microsystems (EuroSimE).* Montpellier, France, 2016, 7 p.
13. Wiese, S.; Kraemer, F.: Adequate Mechanical Copper Modelling for 2nd Level Interconnect Structures. Experimental Design for Tensile Tests on PCB Copper Traces for Board Level Packaging. *2015 16th International Conference on Thermal, Mechanical and Multi-Physics Simulation and Experiments in Microelectronics and Microsystems (EuroSimE).* Budapest, Hungary, 2015, 7 p.
14. Elasmi, M.: Entwurf und Aufbau einer Experimentalvorrichtung zur Bestimmung werkstoffmechanischer Eigenschaften von Verkapselungsmaterialien für PV-Module. *Bachelor Thesis, Saarland University, Chair of Microintegration and Reliability.* Saarbrücken, 08.04.2013.
15. Fu, H.-H.; Benson, D. J.; Meyers, M. A.: Analytical and Computational Description of Effect of Grain Size on Yield Stress of Metals. *Acta Materialia.* 2001, vol. 49, no. 13, pp. 2567-2582.

5.10 Paper 10: The Effect of Multiple Solder Reflows on the Formation of Cu_6Sn_5 Intermetallics and the Decomposition of SnAg3.0Cu0.5 Solder Joints in the Framework of Rework and Reuse of MLCC Components

5.10.1 Veröffentlichungshinweise

Erik Wiss, Steffen Wiese

Chair of Microintegration and Reliability, Faculty of Natural Sciences and Technology, Saarland University, Saarbrücken, Germany

Metals (2024), 14.9, 986

Die Originalveröffentlichung ist abrufbar unter:
https://doi.org/10.3390/met14090986

5.10.2 Synopse

Diese Veröffentlichung beschreibt die Auswirkungen mehrfacher Reflow-Prozesse im Rahmen der Nachbearbeitung und Wiederverwendung elektronischer Bauteile. Die Motivation ergibt sich aus der Notwendigkeit, genaue Kenntnisse über die auftretenden Veränderungen der jeweiligen Eigenschaften zu erlangen. Ziel der Arbeit war die Entwicklung einer Methodik zur systematischen Analyse elektrischer, mechanischer und mikrostruktureller Veränderungen von Lötverbindungen infolge mehrfacher Reflow-Prozesse.

Hierzu wurden Keramikkondensatoren (MLCC) mit unterschiedlichen Dielektrika auf Testplatinen mit Cu-Metallisierung aufgelötet und bis zu acht Reflow-Prozessen unterzogen, um ein Aus- und Wiedereinlöten der Komponenten zu simulieren. Die Kapazität wurde nach jedem Zyklus über eine Vier-Leiter-Messung erfasst. Nach 1, 2, 4 und 8 Lötvorgängen wurden Querschliffe angefertigt und eine metallurgisch auf IMP-Wachstum und Elementverteilung analysiert.

Zur Überprüfung der mechanischen Integrität der Lötstellen wurde das Testsystem aus Paper 9 modifiziert, um Widerstände nach 1, 2, 4 und 8 Reflow-Zyklen von einer kleinen Leiterplatte abzuscheren. Während des Versuchs wurden die Lötstellen mit einer Brückenschaltung auf ihre Integrität überwacht. Nach der Detektierung eines Defekts wurde der Versuch automatisch gestoppt und die Proben metallurgisch analysiert.

Die Ergebnisse zeigen, dass die entwickelte Methodik dazu geeignet ist, die infolge mehrfacher Reflow-Zyklen hervorgerufenen Kapazitätsänderungen von MLCC-Bauteilen quantitativ zu erfassen. Die metallurgische Analyse der Lötstelle ergab, dass sich die IMP an den Grenzflächen zwischen Lot und MLCC-Metallisierung sowie zwischen Lot und Leiterplattenmetallisierung zwar mit unterschiedlicher Morphologie, aber dennoch mit vergleichbarer Wachstumsrate ausbilden.

Bei den Scherversuchen konnte keine signifikante Veränderung der maximalen Scherkraft über die Anzahl der Reflow-Zyklen hinweg gefunden werden. Die mikroskopische Auswertung der Bruchflächen ergab jedoch, dass die fortschreitende Ausbildung der IMP die Adhäsion zwischen Lot und Bauteilmetallisierung so stark erhöht, dass sie die Adhäsion zwischen Bauteilmetallisierung und Keramikkörper des Bauteils übersteigt.

Im Kontext des Gesamtprojekts dient die hier vorgestellte Methodik als Grundlage für die später noch zu erfolgende Charakterisierung reaktiv gefügter Verbindungen.

metals

IMPACT FACTOR 2.6

CITESCORE 4.9

Article

The Effect of Multiple Solder Reflows on the Formation of Cu_6Sn_5 Intermetallics and the Decomposition of SnAg3.0Cu0.5 Solder Joints in the Framework of Rework and Reuse of MLCC Components

Erik Wiss and Steffen Wiese

Special Issue
Research on Green and Environmentally Friendly Lead-Free Solder and Advanced Interconnect Technology in Electronic Packaging

Edited by
Prof. Dr. Limin Ma

MDPI

https://doi.org/10.3390/met14090986

metals

Article

The Effect of Multiple Solder Reflows on the Formation of Cu_6Sn_5 Intermetallics and the Decomposition of SnAg3.0Cu0.5 Solder Joints in the Framework of Rework and Reuse of MLCC Components

Erik Wiss and Steffen Wiese *

Chair of Microintegration and Reliability, Faculty of Natural Sciences and Technology, Saarland University, 66123 Saarbrucken, Germany; erik.wiss@uni-saarland.de
* Correspondence: s.wiese@mx.uni-saarland.de; Tel.: +49-681-302-71820

Abstract: A rework of electronic assemblies and the reuse of electronic components are the most effective ways to reduce electronic waste. Since neither components nor substrates were developed with the intention of multiple usage, the question of how the integrity of lead-free solder joints is affected by multiple reflow operations is crucial for the implementation of any reuse strategy. Therefore, various types of 1206 multilayer ceramic capacitors (MLCCs) differing in their capacitance value and dielectric type (X5R, X7R, Y5V, NP0) were soldered on test printed circuit boards (PCBs) having a pure Cu-metallization surface in order to investigate the intermetallic reactions during multiple reflows. The metallization system on the MLCC-component side consisted of a thick film of Ni covered by galvanic-deposited Sn. The reflow experiments were conducted using a hypoeutectic SnAgCu solder. The results show the formation of a Cu_6Sn_5 intermetallic phase on both metallizations, which grows homogeneously with the number of reflows. Moreover, an ongoing decomposition of the solder into Ag-enriched and depleted zones was observed. The effect of these microstructural changes on the functionality of the solder joint was investigated by mechanical shear experiments and electrical four-point capacitance measurements.

Keywords: Cu_6Sn_5 intermetallic; intermetallic morphology; reflow; solder; SnAg3.0Cu0.5; multiple reflows; reuse; MLCC; shear test

Citation: Wiss, E.; Wiese, S. The Effect of Multiple Solder Reflows on the Formation of Cu_6Sn_5 Intermetallics and the Decomposition of SnAg3.0Cu0.5 Solder Joints in the Framework of Rework and Reuse of MLCC Components. *Metals* **2024**, *14*, 986. https://doi.org/10.3390/met14090986

Academic Editor: Chonghe Li

Received: 31 July 2024
Revised: 23 August 2024
Accepted: 25 August 2024
Published: 29 August 2024

1. Introduction

The increasing concern about the large number of end-of-life (EoL) electronics is discussed in different ways. While one group of authors focuses on the effective recovery of raw materials from electronic scrap [1–3] by different recycling methods, such as thermo-mechanical dismantling [4,5] or chemical disassembly [6], other authors consider the reuse of functioning components with significant remaining useful life (RUL) [7]. Desoldering processes, which are established for the rework of electronic assemblies such as printed circuit boards (PCBs), are mostly considered a technically feasible disassembly method for the reuse of components [8]. Some studies consider the effects of thermal [9,10] or mechanical loading [9,11] during the desoldering process. Since neither components nor substrates were developed with the intention of multiple usage, the question of how the integrity of lead-free solder joints is affected by multiple reflow operations is crucial for any reuse strategy.

Although the effects of multiple reflows on the microstructural and functional changes of solder interconnects are the subject of numerous publications, the reuse of component scenarios was not the subject of these studies. Nonetheless, the procedures and effects described in the existing literature guide the experimental program of the current study. The evolution of the shear strength and the electrical resistance of BGA solder balls after multiple reflows were investigated in [12,13], whereas the studies reported in [12–16] looked into interfacial reactions and their effect on the shear strength of solder bumps with respect to the number of reflows as well as the effect of specific oxide additions (TiO_2) on intermetallic compound (IMC) growth on the Cu/solder interface [17]. Other studies focused on the shape and evolution of the Cu/solder-IMC morphology in Sn–x/Cu solder bumps after different numbers of reflow cycles [18–20], on the shape and thickness of solder/metallization-IMC in respect of different PCB surface finishes [21], and on the solder wettability and creep properties in dependence of the number of reflows [22].

Beside these predominately material science-centered studies, there are a smaller number of engineering-oriented investigations that are trying to examine the technology-related consequences of solder profile adjustments in multiple reflow operations in electronic manufacturing. Branzei and coworkers [23] worked on the optimization of reflow vapor phase soldering processes. The specimen consisted of a test PCB with surface-mounted device (SMD) 1206 zero-ohm resistors soldered to it. A similar specimen was used by Wirth and coworkers [24], who focused on the peak temperature and the time above liquidus in a traditional reflow process. In both studies, the shear strength and the IMC thickness were taken as parameters to evaluate the chosen reflow profile. The effects of soldering profiles on the functionality of multilayer ceramic capacitor (MLCC) components having X7R and Z5U dielectrics were the subject of studies by Jánó and coworkers published in [25,26]. While a significant effect of the soldering method and profile on the component parameters was shown, no further investigation into the mechanical and microstructural properties of the solder joints was undertaken.

In the framework of reuse of MLCCs by desoldering such components from an EoL-PCB and resoldering these components on a new PCB, ceramic capacitors are the more critical passive SMD components compared to resistors because the functionality of their ferroelectric body material may depend on acting external forces. Such forces may arise from residual stresses that are built up during de- and resoldering processes [10]. Therefore, the interfacial reactions of solder joints and their effect on the electrical and mechanical functionalities of MLCCs are of great interest for any reuse strategy. Thus, this study focuses on the specifics of the asymmetrical metallization system of soldered MLCCs with respect to the effects of multiple reflows. The investigated metallization system consists of pure copper on the side of the printed circuit boards (PCB), whereas on the MLCC-component side there is a thick film of Ni-metallization covered by a galvanic-deposited Sn layer. Also, the dependence of the MLCC's capacitance on the number of conducted reflow cycles is key to this investigation in order to evaluate the component functionality for the reuse case. A third important aspect deals with the solder joint's mechanical functionality for the given metallization system.

2. Materials and Methods

2.1. Sample Preparation

In order to investigate the effects of multiple solder reflow cycles on solder joints and passive SMD components, different samples were manufactured. For the first test, a PCB of size 160 mm × 100 mm was designed to hold eight MLCCs of size 1206 (length 3.2 mm and width 1.6 mm). Each pair of two soldering pads is connected to four additional pads to enable four-wire measurements of the capacitance of the MLCCs. The measurements have been carried out after every reflow cycle, up to a total of eight cycles. After machining the PCBs using a drilling machine, ProtoMat S103 (LPKF, Garbsen, Germany), the oxide layers of the PCB surface were removed with a rough pad to allow proper wetting of the solder paste. One piece of the manufactured test board is shown in Figure 1. The employed solder paste, a LOCTITE GC 10 SAC305T4 (Henkel, Düsseldorf, Germany) with a melting point of 217 °C, is a type 4 paste with a particle size distribution of 20 to 38 µm and a specified composition of 96.5 wt% Sn, 3.0 wt% Ag, and 0.5 wt% Cu, which is mixed homogeneously with a resin-based, halogen-free flux. The exact composition was not analyzed because the composition of the individual solder pad depots would vary in any case, given their relatively small volume. A compressed air dispenser, DX-250 (OKI, Cypress, CA, USA), was used for the deposition of the paste onto the solder pads. In the final step, the MLCC components, which will be used for testing (samples), were placed with a manual pick-and-place system, ProtoPlace S (LPKF). The soldering process was made in an N_2 protective atmosphere using LPKF's batch reflow oven with the accompanying software FlowShow (version 2.10) to record the temperature profiles of the subsequent reflow processes.

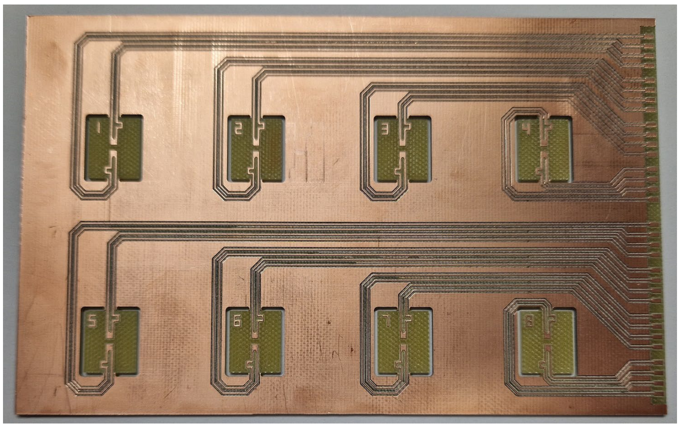

Figure 1. Layout of the electrical test-board (length 160 mm and width 100 mm) having a capacity to carry eight samples (C1–C8, solder pad layout for MLCC with 1206 size). Each pair of the MLCC soldering pads is connected to four pads on the right edge of the PCB to enable precise four-wire measurements of the MLCC's capacitances.

Table 1 shows the component types of MLCCs that were used for both the electrical measurements and the metallurgical analysis. Every type of component has the same size 1206, but they differ in their dielectric and thus in their properties, such as their operating temperature range and temperature-dependent change in capacitance. While the type X7R offers a large operating temperature range and an acceptable temperature coefficient, the type X5R can offer larger capacities. Type Y5V is very sensitive to temperature changes, which is why it is normally only used in circuits that can be operated at or near room temperature. Type NP0 is almost independent of the operating temperature, but it offers only low capacities at a high cost. Eight MLCCs of the same component type (C1–C8) were mounted on each test-board, resulting in a total of 32 samples (8 MLCC × 4 dielectric types). While the X5R and X7R MLCCs are from KEMET (Fort Lauderdale, FL, USA), the Y5V and NP0 are from Yageo (New Taipei City, Taiwan). For the metallurgical analysis, another test-board was used. It consists only of solder pads for the MLCCs, without additional pads to accommodate more MLCCs on one board. A total of four samples were used for the X7R component type.

Table 1. Summary of the different MLCC types that were used for the measurements.

Component Type	Dielectric	Nominal Capacitance	Maximum Temperature Coefficient	Number of Samples for Electrical Tests	Number of Samples for Metallurgical Analysis
KEMET C1206C106K4PAC7800+	X5R	10 µF ± 10%	±1071 ppm/K	8	0
KEMET C1206C474K5RACTU	X7R	470 nF ± 10%	±833 ppm/K	8	4
Yageo CC1206ZPY5V7BB475	Y5V	4.7 µF ± 20%	−7130 ... +1913 ppm/K	8	0
Yageo CC1206JRNPO9BN681	NP0	680 pF ± 5%	±30 ppm/K	8	0

In order to investigate the influence of multiple reflow cycles on the mechanical stability of the solder joints, a simple shear test was conducted. Therefore, small PCBs that can take up a single resistor were manufactured (see Figure 2). The resistors, model

RK73B2BTTD100J (KOA, Tokyo, Japan) with a resistance of 10 Ω, were soldered onto the pads in the same procedure as the MLCCs. Two additional pads allow in-situ monitoring of the health state of the solder joints. In each case, six samples were exposed to one, two, four, or eight reflow cycles (see Table 2).

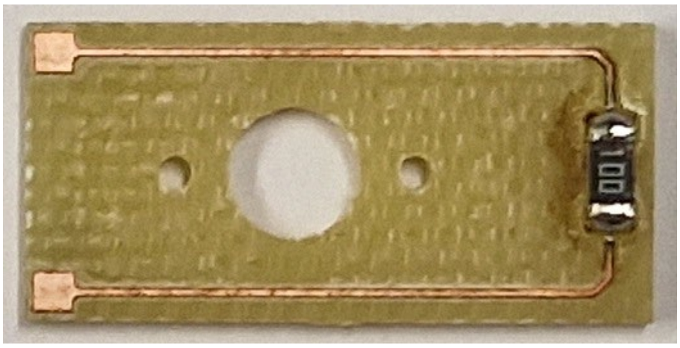

Figure 2. Layout of a test-PCB for the samples that were subjected to a shear test. The pads are connected to two additional pads on the left side of the PCB to allow in-situ monitoring of the solder joint health state during the mechanical test. The three holes in the middle are used to align and attach the samples to the holder of the testing machine.

Table 2. Summary of the resistors that were used for the shear test.

Component Type	Number of Reflow Cycles	Nominal Resistance	Temperature Coefficient	Number of Samples for Shear Tests and Metallurgical Analysis
KOA RK73B2BTTD100J	1	10 Ω ± 5%	±200 ppm/K	6
KOA RK73B2BTTD100J	2	10 Ω ± 5%	±200 ppm/K	6
KOA RK73B2BTTD100J	4	10 Ω ± 5%	±200 ppm/K	6
KOA RK73B2BTTD100J	8	10 Ω ± 5%	±200 ppm/K	6

2.2. Reflow Process

The samples were soldered in a batch reflow oven, ProtoFlow S (LPKF), into a nitrogen-protective atmosphere. Depending on the heat capacity of the components and substrates to be soldered, the reflow profile needs to be chosen in an appropriate manner to ensure that all solder joints melt during every reflow process. Therefore, the solder paste manufacturer gives various recommendations that differ in the preheat time, the heating rate, the peak time, and the peak temperature. First attempts showed that good results could be achieved using a preheat phase of 160 °C for 70 s to heat up the components uniformly and activate the flux, and a peak phase of 250 °C for 80 s. While the heating rate of approximately 0.95 °C/s could not be changed, the cooling rate was set to approximately 1.56 °C/s. Note that the temperatures are the air temperature and not the substrate temperature. The time-temperature curve of the reflow profile is shown in an idealized form without noise in Figure 3.

In the case of the MLCC samples, the capacitance values were measured after every reflow cycle. After every reflow, a sufficiently long cooling time was chosen to bring the samples securely to room temperature in order to minimize the potential temperature error for the capacitance measurement on MLCCs. In the case of the resistor samples for mechanical functionality, the respective shear test was started when the stated number of reflow cycles (see Table 2) had been carried out.

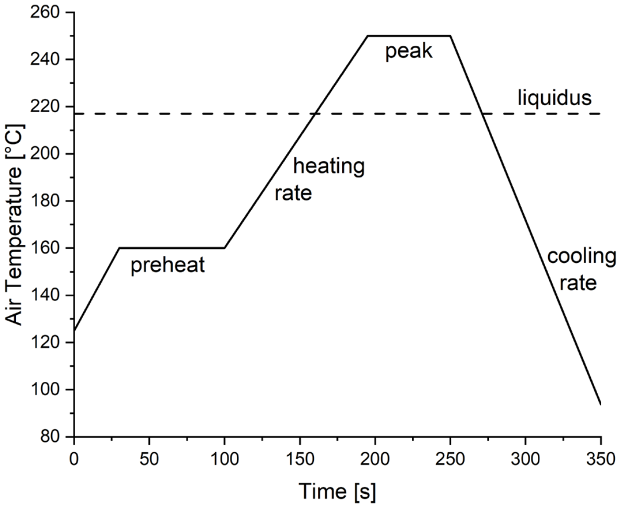

Figure 3. Time-temperature curve of the reflow profile that was used for the experiments. The graph summarizes the recordings of the subsequent reflow process in a typical and idealized form (without noise). Every reflow process had an identical profile. The reflow soldering has been carried out in a batch reflow oven, ProtoFlow S (LPKF), using a nitrogen-protective atmosphere.

2.3. MLCC Measurements

The MLCC measurements were realized using an LCR meter E4980AL (Keysight, Santa Rosa, CA, USA) and a specially developed measurement adapter (see Figure 4). The measurement device is connected to this adapter using four BNC connectors, which are adapted to four pin heads. Its grid exactly matches one of the Cu pads on the MLCC board, allowing easy measurement of the capacitance and resistance values. After the pin heads have contact with the Cu pads, the measurement is initiated by a manual trigger on the device.

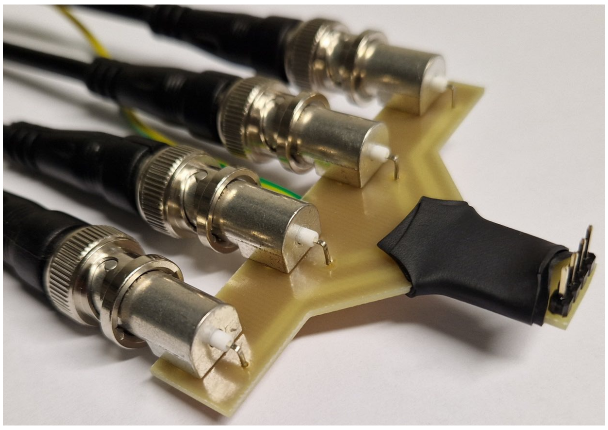

Figure 4. Specially developed measurement adapter that is connected to the measurement device via four BNC connectors, which bring the shielded measurement connections to the adapter. These measurement connections are redistributed by the PCB to four pin heads, whose grid exactly matches one of the Cu pads. After the pin heads have been brought into contact with the pads, the measurement is initiated (manual trigger).

The capacitance of the used MLCCs is less than or equal to 10 µF, which is why the parallel measurement mode with a voltage of 1 V was chosen. In this mode, the series resistance R_s and the series inductance L_s, which are mainly derived from the resistance of the measurement wires and the capacitor plates, are ignored. Only the parallel resistance R_p, mainly caused by polarization losses, and the capacitance are measured. The equivalent circuit diagram of a real capacitor is shown in Figure 5.

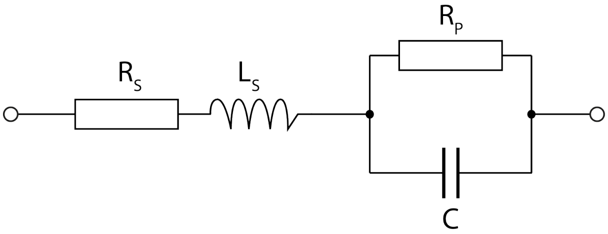

Figure 5. Equivalent circuit diagram of a real capacitor, consisting of a series resistance R_s, a series inductance L_s, a parallel resistance $R_{p,}$ and the capacitance C, adapted from [27].

In accordance with the international standard norm IEC 60384-1 [28], a frequency of 1 kHz was chosen for the X5R, X7R, and Y5V MLCCs (1 nF $\leq$ C $\leq$ 10 µF), while a frequency of 300 kHz instead of 1 MHz had to be used for the NP0 MLCCs (C $\leq$ 1 nF) due to the limitations of the measurement device. An overview of the measurement settings is shown in Table 3. The measurements, which were conducted after every reflow cycle, were averaged over five net power line cycles (NPLCs) to minimize interfering noises and thus stabilize the results. After five reflow cycles, the measurements had to be paused until the next day.

Table 3. Summary of the measurement settings that were used for the different MLCCs.

Model	Dielectric	Nominal Capacitance	Measurement Voltage	Measurement Frequency	NPLC
KEMET C1206C106K4PAC7800+	X5R	10 µF ± 10%	1 V	1 kHz	5
KEMET C1206C474K5RACTU	X7R	470 nF ± 10%	1 V	1 kHz	5
Yageo CC1206ZPY5V7BB475	Y5V	4.7 µF ± 20%	1 V	1 kHz	5
Yageo CC1206JRNPO9BN681	NP0	680 pF ± 5%	1 V	300 kHz	5

2.4. Mechanical Test Setup

The shear tests were conducted on a slightly modified mechanical test setup that was developed to conduct mechanical tests on packaging materials (specialized samples), i.e., tensile tests on PCB Cu-trace sheet material [29], or electronic components, i.e., cyclic bending experiments on QFN samples that were soldered on a PCB [30]. The setup is built around a stereo zoom microscope, SteREO Discovery.V20 (Zeiss, Oberkochen, Germany), with two attached cameras to allow the possibility of image acquisition during the mechanical experiments for further evaluation using digital image correlation (DIC) methods, which is important to analyze complex deformation states as in the case of the bending of the soldered QFN samples [30]. In this study, no use of the DIC method was made because, in order to evaluate the bonding strength as a parameter of mechanical functionality, no deformation information was needed. The shear test conducted on the MLCC components refers only to the fracture strength of the weaker of the two solder joints. The setup is shown in Figure 6.

A threaded rod is mounted on a motor-driven linear table (A), which can provide a load of up to 200 N. At the other end, a shear chisel made of a small piece of PCB material with a removed Cu layer is attached to a holder, transferring the load of the actuator to the sample (see Figure 7). This special, non-conductive chisel was chosen because a metal one would possibly short-circuit the Cu pads to which the resistor was soldered and thus prevent correct crack detection within the solder joints. On the opposite side, the prepared sample is clamped under the microscope (D) in another sample holder, which is attached to a three-dimensional force sensor (B) K3R110 (ME-Meßsysteme, Hennigsdorf, Germany) in order to record not only the force in the shear direction but also any torques. The sensor is connected via amplifiers (C) GSV-2TSD-DI (ME-Meßsysteme) to a multifunction I/O device PCIe-6341 (National Instruments, Austin, TX, USA). The crack detection circuit (E) monitors the output voltage of an operational amplifier in whose positive input path the pads of the resistor samples are inserted. A crack in one of the solder joints results in a change in the measured voltage and thus indicates a failure. The setup is controlled by LabVIEW (National Instruments).

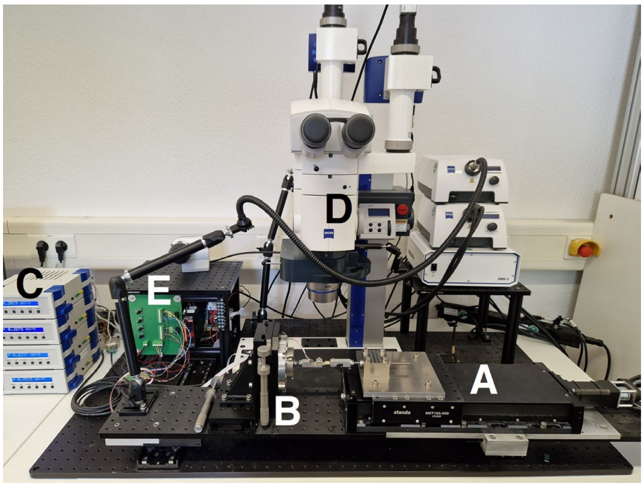

Figure 6. Overview of the mechanical test setup presented in [29,30]. The main components of the setup are labeled as follows: A: Actuator. B: Three-axis force sensor. C: Measurement amplifiers (for force sensors). D: Stereo zoom microscope with illumination units. E: Crack detection circuit.

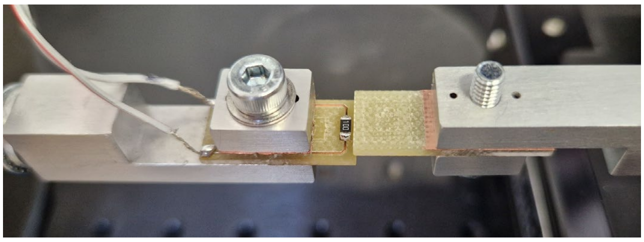

Figure 7. Detailed view of the experimental setup. The displacement of the actuator and thus a force are transferred to the resistor via a small PCB, which is electrically isolated to not influence the electrical measurement. A crack formation within one of the solder joints results in an interruption of the electrical pathway between the two wires on the left side, which are connected to the crack detection circuit.

All shear tests have been conducted with a cross-head speed of 0.1 mm/s, which corresponds to the international standard norm IEC 62137-1-2 [31]. Although the estimated shear rate of 1/s is relatively high, similar cross-head speeds were chosen by other studies, i.e., 0.1 mm/s [14], 0.2 mm/s [12,15], 0.3 mm/s [24], and 0.5 mm/s [26]. These shear rates do not represent the usual thermal cyclic loading appropriately. In that respect, the practice of conducting shear tests seems to be a bit controversial. Obviously, under these conditions, the standard shear test is unable to determine the comprehensive mechanical behavior or the long-term reliability of solder joints. The determination of these properties requires creep tests and thermal cycle tests. However, such experiments take a very long time to be carried out. Moreover, creep experiments cannot be conducted on the presented specimens because the stiffness of the PCB base material is very time-dependent. The high shear rate of the standard shear test helps to suppress the viscoelastic PCB base material behavior influence on the shear strength results, except for shock resistance testing. The latter requires much higher shear rates in the range of 100–2000 mm/s, as used in [32].

In this study, the shear tests were conducted after one, two, four, and eight reflow cycles, with a total of six samples per condition (6 × 4 = 24 samples).

2.5. SEM and EDX Analysis

To allow scanning electron microscopy (SEM) and energy dispersive X-ray spectroscopy (EDX) analysis, the samples had to be prepared in a specific way using several preparation steps. First step: the diced samples were embedded in epoxy using the EpoFix kit (Struers, Ballerup, Denmark) and cut with an ISOMET 4000 precision saw (Buehler, Lake Bluff, IL, USA). Second step: after hardening, the samples were ground on SiC foils with different grits of 500 and 1200 on a LabPol-25 (Struers). Third step: polishing using various diamond suspensions having 9 µm, 3 µm, and 1 µm particle sizes on a Tegramin-25 (Struers). Fourth step: final polishing with a colloidal silicon oxide on a Saphir Vibro (ATM Qness, Mammelzen, Germany) vibratory polishing machine, resulting in an extremely even surface with ultra-low roughness. Fifth step: the prepared samples were coated with a very thin carbon film using a Q150T Coater (Quantum Design, Pfungstadt, Germany) to avoid charging effects during the SEM operation and to not disturb the EDX analysis. The target thickness of the carbon film was 20 nm to retain the even surface of the samples. The SEM and EDX analyses were realized using an EVO MA15 (Zeiss) with an LaB_6 cathode, an accelerating voltage of 20 kV and a beam current of 40 µA, and an XFlash detector (Bruker, Billerica, MA, USA) with an energy resolution of 123 eV. The images were taken in secondary electrons (SE) mode. In the case of the MLCCs, the analysis has been carried out at almost the same location between the MLCC termination and the Cu pad underneath (see Figure 8). For a more accurate analysis, line scans that start at the termination of the MLCC component and end at the Cu pad were performed (see Figure 9). In the case of the resistors that were subjected to the shear test, one side of the ragged component was analyzed. Additionally, a more detailed picture of the location above the Cu pad was analyzed.

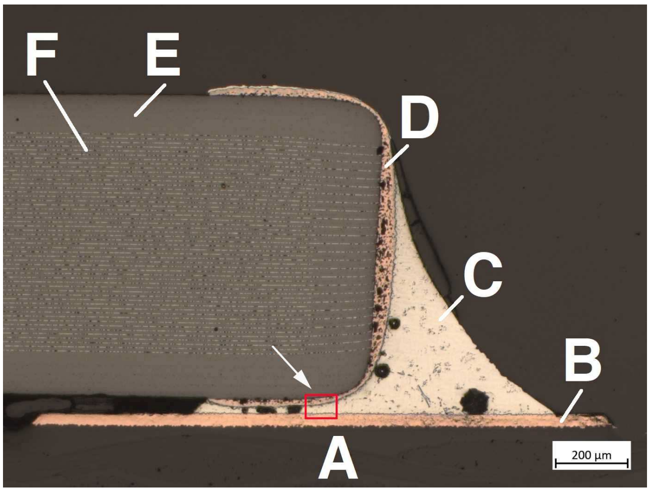

Figure 8. Light microscopy image of an X7R MLCC (Magnification: 5×). The red box between the MLCC and the Cu pad marks the location of the SEM and EDX analysis. A: PCB base material. B: Cu pad of the PCB. C: Solder joint. D: Cu metallization and Ni termination. E: MLCC ceramic body. F: Inner electrodes.

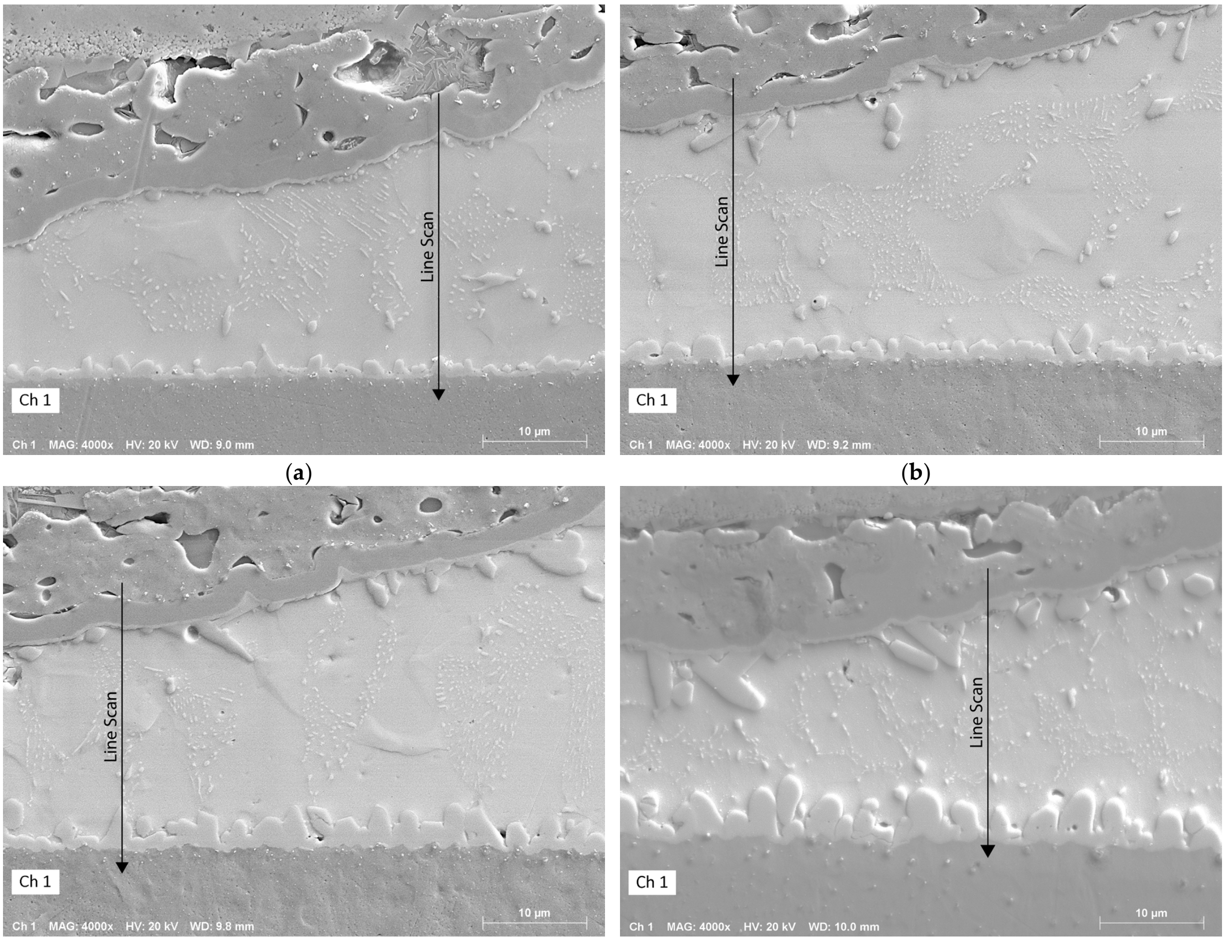

(**a**) (**b**)

(**c**) (**d**)

Figure 9. SEM images in SE mode with an enlarged view of the red box area of Figure 8. Path along which the line scans were performed after the (**a**) first, (**b**) second, (**c**) fourth, and (**d**) eighth reflow cycles, starting within the Ni-thick film layer (termination) of the MLCC and ending in the Cu metallization of the PCB.

3. Results

3.1. IMC Formation

The IMC formation at the solder/Cu interface was analyzed by EDX. Although only diffraction methods are able to unambiguously identify IMCs by their crystal properties, the tight framework of reflow experiments in a clearly defined temperature range makes the EDX analysis a more suitable and convenient tool, given its unexpensive sample preparation and thus higher throughput to achieve more statistical confidence in the overall picture. Figures 10–13 show a detail of the solder meniscus (see Figure 8) as SEM photographs in SE mode and as an EDX map. The composite map, which contains counts for the elements Ni, Cu, Ag, and Sn, is also displayed for the individual elements in order to more clearly show where the four elements intermix with each other and where the elements are separated from each other. Additionally, Figure 14 shows the composition of the four elements and the separated Ag concentration along a path, starting from the MLCC termination and ending in the Cu metallization of the PCB (see Figure 9).

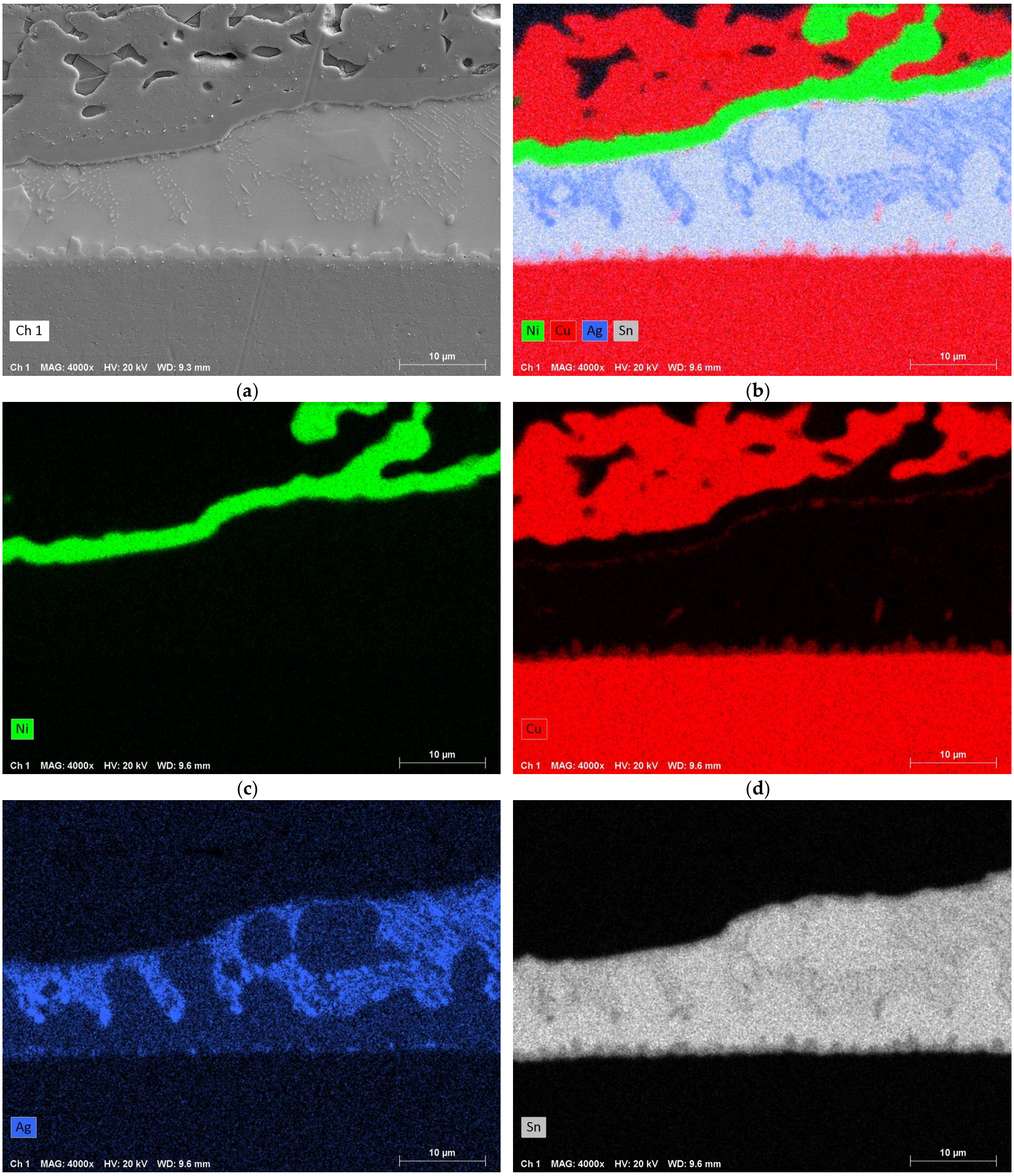

(**a**) (**b**) (**c**) (**d**) (**e**) (**f**)

Figure 10. EDX analysis of an X7R MLCC after the first reflow cycle with a magnification of 4000×. (**a**) SEM image in SE mode. (**b**) Combined EDX maps of Ni, Cu, Ag, and Sn. (**c**) EDX map of Ni. (**d**) EDX map of Cu. (**e**) EDX map of Ag. (**f**) EDX map of Sn.

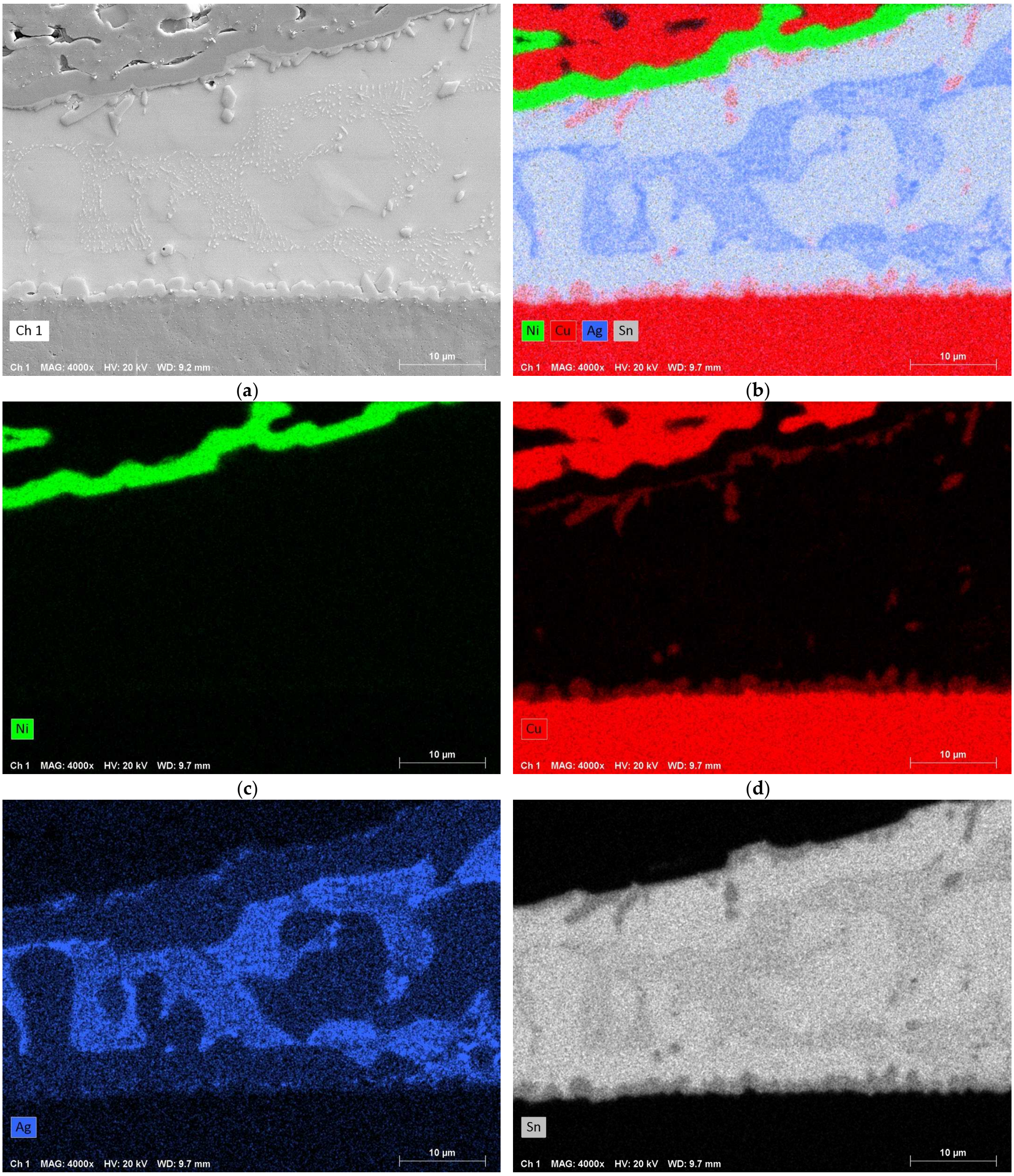

(**a**) (**b**)

(**c**) (**d**)

(**e**) (**f**)

Figure 11. EDX analysis of an X7R MLCC after the second reflow cycle with a magnification of 4000×. (**a**) SEM image in SE mode. (**b**) Combined EDX maps of Ni, Cu, Ag, and Sn. (**c**) EDX map of Ni. (**d**) EDX map of Cu. (**e**) EDX map of Ag. (**f**) EDX map of Sn.

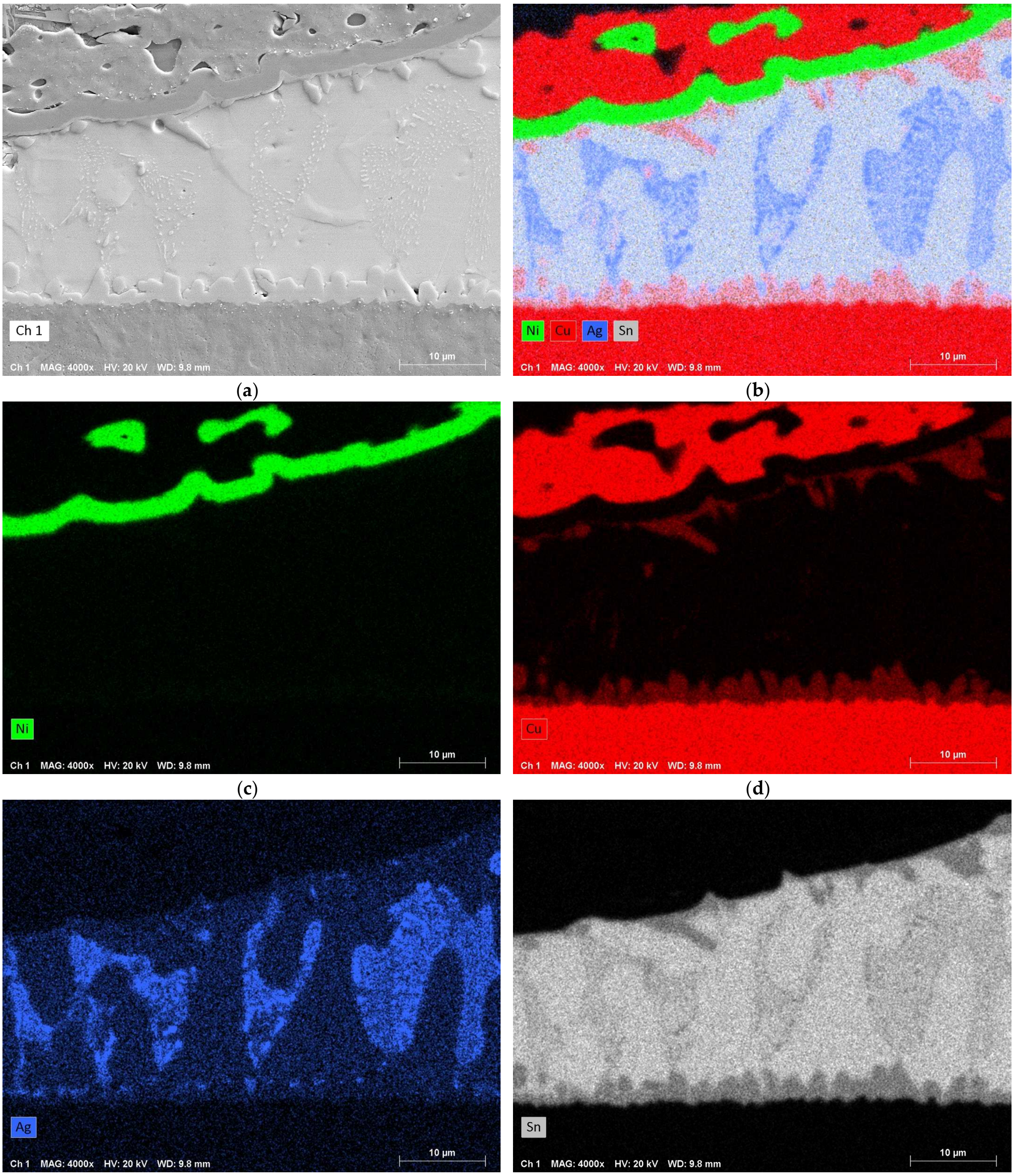

(**a**) (**b**) (**c**) (**d**) (**e**) (**f**)

Figure 12. EDX analysis of an X7R MLCC after the fourth reflow cycle with a magnification of 4000×. (**a**) SEM image in SE mode. (**b**) Combined EDX maps of Ni, Cu, Ag, and Sn. (**c**) EDX map of Ni. (**d**) EDX map of Cu. (**e**) EDX map of Ag. (**f**) EDX map of Sn.

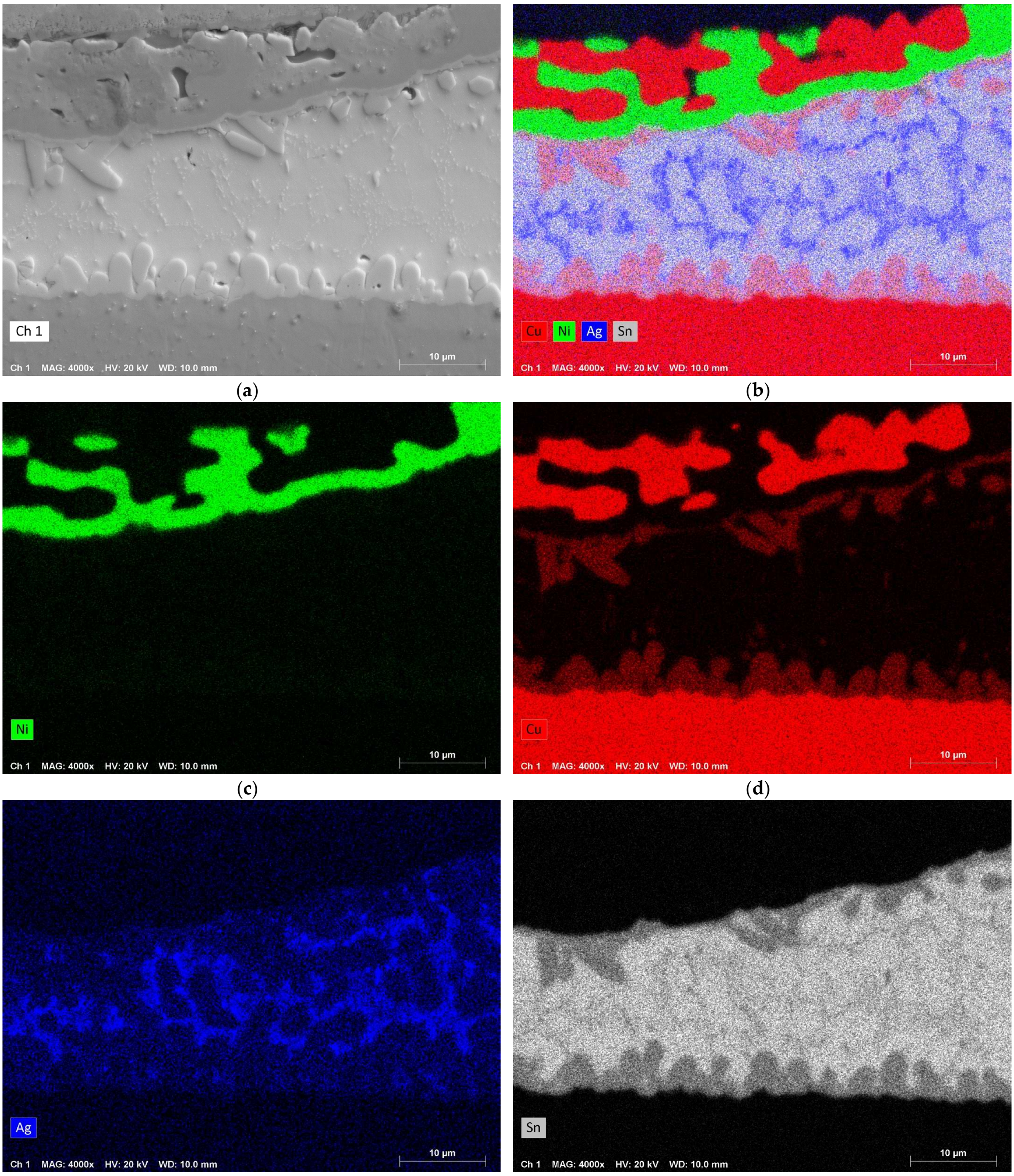

(**a**) (**b**) (**c**) (**d**) (**e**) (**f**)

Figure 13. EDX analysis of an X7R MLCC after the eighth reflow cycle with a magnification of 4000×. (**a**) SEM image in SE mode. (**b**) Combined EDX maps of Ni, Cu, Ag, and Sn. (**c**) EDX map of Ni. (**d**) EDX map of Cu. (**e**) EDX map of Ag. (**f**) EDX map of Sn.

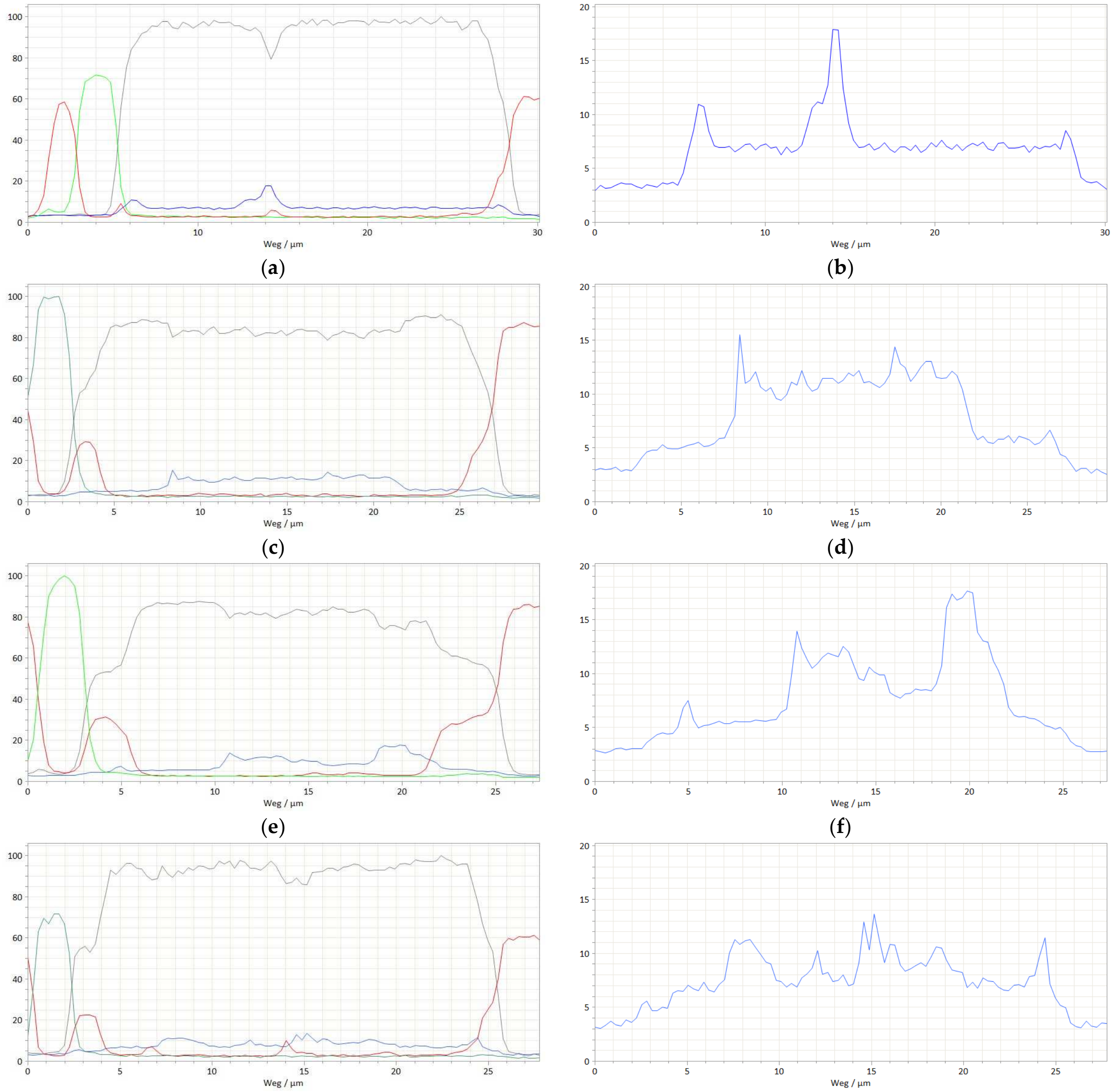

(**a**) (**b**) (**c**) (**d**) (**e**) (**f**) (**g**) (**h**)

Figure 14. Line scan overviews along the given path (compare Figure 9) of an X7R MLCC after the (**a**,**b**) first, (**c**,**d**) second, (**e**,**f**) fourth, and (**g**,**h**) eighth reflow cycle, showing the evolution of the Cu_6Sn_5 IMC (left-hand side) and the distribution of Ag within the solder (right-hand side), standardized to a total concentration of 100% (y-axis). Green: Ni. Red: Cu. Gray: Sn. Blue: Ag. While a continuous IMC layer has already formed at the interface solder/PCB metallization after the first reflow cycle, it takes four reflow cycles to form a proper IMC layer at the interface solder/component termination. During several reflow cycles, the Ag depletion zones at the interfaces diminish, and the Ag seems to distribute more and more uniformly within the solder paste. The depicted diagrams were taken directly from the EDX software QUANTAX ESPRIT (version 2.0) without editing. The ordinate shows the concentration in %, and the abscise ('Weg/µm') shows the distance along the scanning path. The algorithm of the used EDX software seems not always to be able to standardize the total concentration to 100%, which causes the differences in the tin concentration in the center of the solder joints.

Figure 10 shows the IMC formation after the first reflow (=solder paste is melted and reacts for the first time with the PCB- and component metallization). While the interface solder/PCB-metallization shows a tightly packed Cu_6Sn_5 IMC layer formation with a thickness of a few micrometers, there has only been a sparse growth of small individual Cu_6Sn_5 IMC cells at the interface solder/component metallization.

After the second reflow (the solder joint is remelted and reacts with the IMC on both interfaces, solder/PCB and solder/component metallization), a significant growth of the Cu_6Sn_5 IMC at the interface solder/component metallization can be observed (Figure 11). Although this compound is still not a coherent layer on top of the Ni diffusion barrier of the component, its appearance is much more pronounced than after the first reflow. This effect of the subsequent formation of Cu_6Sn_5 IMC (on the solder/PCB side after the first reflow and on the solder/component side after the second reflow) can be very well recognized from the results of the EDX line scans depicted in Figure 14. While there is a notable overlap area where the Sn-line and the Cu-line cross each other on the right-hand side of Figure 14a (at 28 µm), there is only a small Cu-line peak on the left-hand side (at 5.5 µm). In contrast, Figure 14c shows two distinct overlap areas for the Sn-line and Cu-line on the left-hand side (at 3.5 µm) and on the right-hand side (at 26.5 µm). The same picture is shown in the diagrams in Figure 14e,g, which depict the line scans for the sample after four and eight reflow cycles.

If the microstructure of the solder joint is compared between the first and second reflows, a large contrast in the distribution of Ag can be observed. While after the first reflow, an Ag depletion zone can only be observed on top of the Cu_6Sn_5 IMC at the interface solder/PCB metallization (Figure 10), this Ag depletion zone can be observed on both interfaces (solder/PCB and solder/component metallization) after the second reflow (Figure 11). The Ag-depleted zone diminishes with the number of reflows, and the Ag distribution becomes more and more equal (Figure 14b,d,f,h), as the pure beta-tin areas and the mixed Ag_3Sn/Sn areas continuously shrink (Figures 12 and 13). This effect of the subsequent decomposition of the SnAg3.0Cu0.5 solder is also indicated by the results of the EDX line scans depicted in Figure 14. The enlarged Ag-line scan after the first reflow (Figure 14b) shows two peaks (at 6 µm and 14 µm), which are closer to the component side. Particularly, the peak at 6 µm is directly on the solder/component interface. In contrast, the Ag-line scan after the second reflow (Figure 14d) shows a pronounced plateau (from 8 µm to 22 µm), which is away from either interface (to the PCB or the component). The Ag-line scan after the fourth reflow (Figure 14f) shows peaks at both interfaces (at 5 µm and 20 µm) as well as a central peak (from 10 µm to 16 µm), while the Ag-line scan after the eighth reflow (Figure 14h) shows a plateau reaching from one interface to the other one (from 5 µm to 24 µm).

After four reflow cycles, a Cu_6Sn_5 IMC layer has formed that covers the Ni diffusion barrier of the component nearly entirely (Figure 12). The further growth of this Cu_6Sn_5 IMC on the component side is different from that on the PCB side. While the PCB side Cu_6Sn_5 IMC has a spherical morphology in accordance with the fundamental growth kinetics reported in [19], the further growth of the component side Cu_6Sn_5 IMC occurs in single locations with a rather dendritic morphology (Figure 13). Therefore, it is very difficult to determine the IMC thickness at the solder/component metallization interface. The results of the IMC thickness characterization are displayed in the diagrams in Figure 15. It was observed that the initial thickness of the Cu_6Sn_5 IMC that grows on the Cu metallization of the PCB is approximately 2 µm, while the continuous layer of the Cu_6Sn_5 IMC on the Ni metallization on the component side never exceeds 1 µm. However, the average Cu_6Sn_5 IMC layer thickness is similar on both sides, beginning with the second reflow. The EDX line scans depicted in Figure 14 indicate that the Cu_6Sn_5 IMC on both interfaces is widening during the first couple of reflows. As the Cu-line peaks in Figure 14g show, the Cu_6Sn_5 IMCs seem to be present not only on the interfaces but also in the center of the solder joint after a larger number of reflows. The presence of Cu_6Sn_5 IMC particles within the solder material can also be concluded from the EDX mapping depicted in Figure 13.

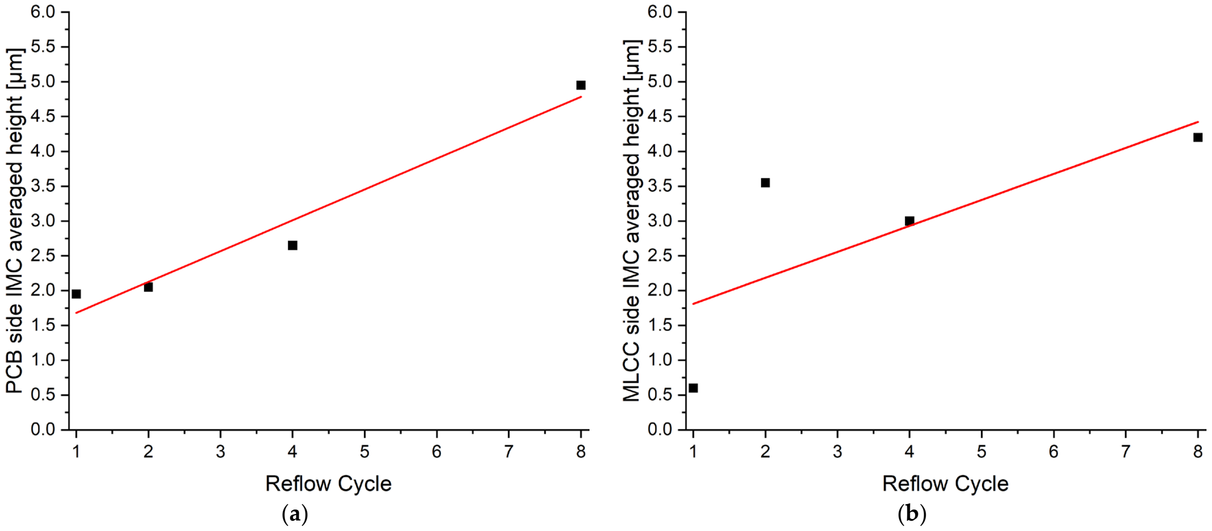

Figure 15. Averaged height of the Cu6Sn5 IMC at the interface between (**a**) the solder paste and the PCB metallization (R^2 = 0.96), and (**b**) the solder paste and the MLCC component (R^2 = 0.54). As the values were only measured after one, two, four, and eight reflow cycles, the remaining values were interpolated using a linear fit.

The formation of the Ni-layer in the EDX-mappings of Figures 10b, 11b, 12b and 13b appears to be irregular because parts of the Ni layer are situated underneath the Cu-layer of the MLCC. The most extreme case is shown in Figure 13b, where the Ni layer can be found directly on the interface to the $BaTiO_3$ body. It seems that the viscous Ni thick film paste (which shows no porosity) was optimized to fill in all the pores of the Cu thick film paste, which was supposedly optimized for other properties, i.e., adhesion to the $BaTiO_3$ body. What can be observed from all EDX-mappings is that the dipping process for the fabrication of MLCC terminals produces a closed Ni-layer on top of the Cu-layer and thus protects the Cu-layer from any reaction with the liquid Sn during soldering.

3.2. Capacitance Measurements

The samples of the KEMET C1206C106K4PAC7800+ (dielectric X5R, size 1206, nominal capacitance 10 µF ± 10%) were measured in parallel mode over 5 NPLCs using a voltage of 1 V and a frequency of 1 kHz. The Cycle-Capacitance diagram of eight samples (C8 for four reflow cycles and C1-C7 for eight reflow cycles) is shown in Figure 16.

As can be seen from the diagram, all X5R MLCCs show similar changes in their electrical functionality during multiple reflow cycles. No matter how many reflow cycles were conducted, all the measured values remain within the capacitance range specified by the manufacturer (9–11 µF). The biggest increase in the capacitance between two reflow cycles occurs after the second one (3–5.5%), with further changes between −2.5% and 3.5%. The reason for the large increase in capacitance between the first two reflow cycles remains unclear, but the solder joint may be one possible reason. After the sixth reflow cycle, the values remain quasi-constant, with small changes between −0.5% and 0.5%. Referring back to the initial value, the largest average change was reached after the eighth reflow cycle (averaged 5.2%), but it is only a slight increase when compared to the second one (averaged 4.6%). It can be assumed that the small, minimal turning point after the fifth reflow cycle is caused by the interruption of measurements due to any relaxation processes within the materials.

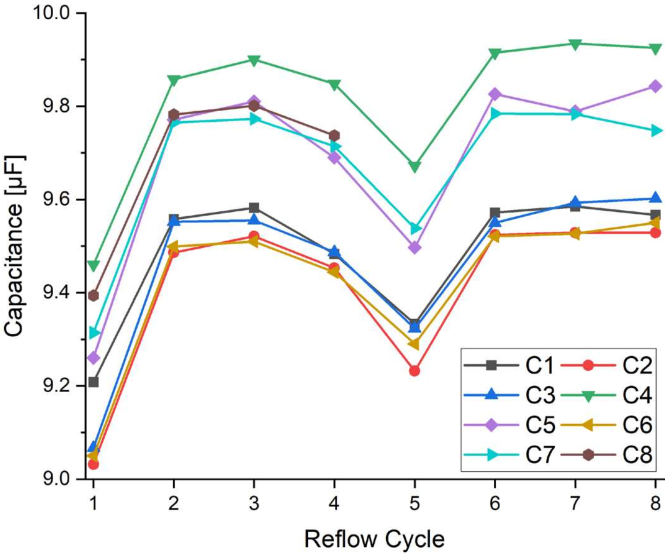

Figure 16. Cycle-Capacitance diagram of the measured values of KEMET C1206C106K4PAC7800+ (dielectric X5R, size 1206, nominal capacitance 10 µF ± 10%) for eight reflow cycles. The values behave in a similar way, including an increase after the first two reflow cycles, a decrease between the third and the fifth one, and further increases during the last three ones.

The samples of the KEMET C1206C474K5RACTU (dielectric X7R, size 1206, nominal capacitance 470 nF ± 10%) were measured in parallel mode over 5 NPLCs using a voltage of 1 V and a frequency of 1 kHz. The Cycle-Capacitance diagram of eight samples (C8 for four reflow cycles and C1–C7 for eight reflow cycles) is shown in Figure 17.

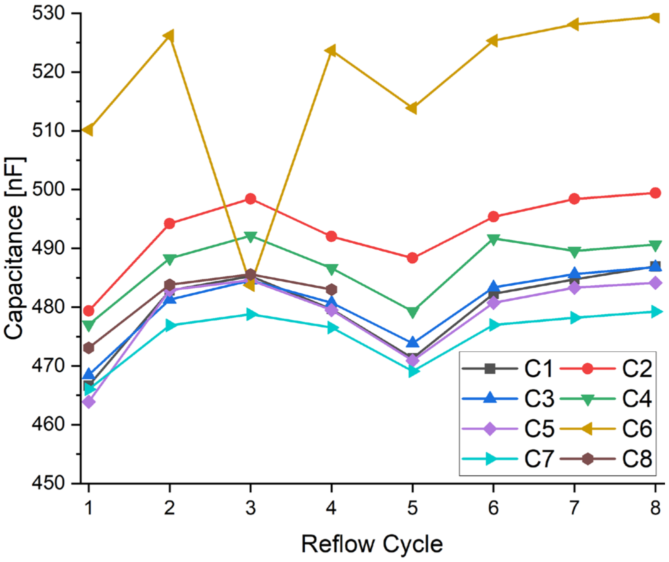

Figure 17. Cycle-Capacitance diagram of the measured values of KEMET C1206C474K5RACTU (dielectric X7R, size 1206, nominal capacitance 470 nF ± 10%) for eight reflow cycles. Except for sample number 6, the values behave in a similar way, including an increase after the first two reflow cycles, a decrease between the third and the fifth one, and further increases during the last three ones.

With the exception of C6, whose capacitance value is already outside the capacitance range specified by the manufacturer (423–517 nF) after two reflow cycles, the other samples remain within the range. As in the case of the X5R MLCCs, the X7R MLCCs show similar changes, with the biggest increase after the second reflow cycle (2.2–4.2%), with further changes between −1.8% and 2.6%. As before, the values remain quasi-constant after the sixth reflow cycle (−0.6% and 0.8%), with a maximum variation after the eighth reflow cycle (averaged 3.8% compared to 2.9% after the second one).

The samples of the Yageo CC1206ZPY5V7BB475 (dielectric Y5V, size 1206, nominal capacitance 4.7 µF ± 20%) were measured in parallel mode over 5 NPLCs using a voltage of 1 V and a frequency of 1 kHz. The Cycle-Capacitance diagram of eight samples (C8 for four reflow cycles and C1-C7 for eight reflow cycles) is shown in Figure 18.

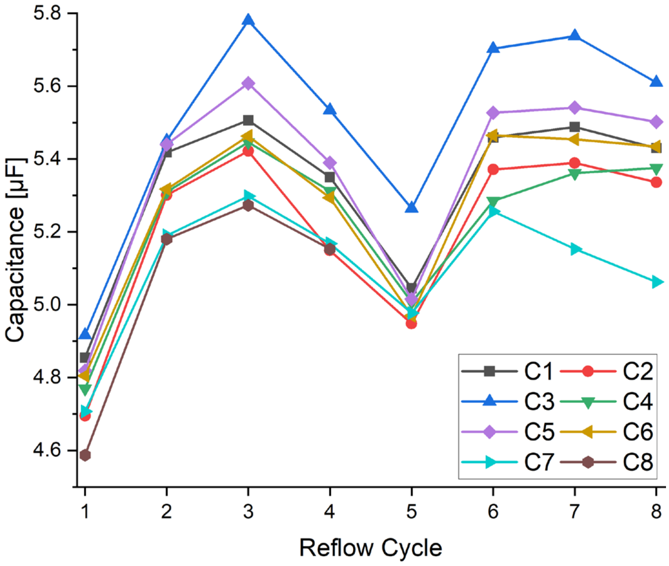

Figure 18. Cycle-Capacitance diagram of the measured values of Yageo CC1206ZPY5V7BB475 (dielectric Y5V, size 1206, nominal capacitance 4.7 µF ± 20%) for eight reflow cycles. The values behave in a similar way, including an increase after the first two reflow cycles, a decrease between the third and the fifth one, and further increases during the last three ones.

With the exception of C3, whose capacitance value is already outside the capacitance range specified by the manufacturer (3.76–5.64 µF) after three reflow cycles, the other samples remain within the range, albeit at the upper limit. The basic shape of the changes in capacitance of the Y5V MLCCs is similar to the first two types, but the relative changes are much greater. After the second reflow cycle, the values increase by 9.5% to 13%, with further changes between −7% and 10%. Again, the values remain comparatively constant, with small changes between −2% and 1.5% after the sixth reflow cycle. The largest averaged change is reached after the third reflow cycle with 14.8%, while it is only 12.4% after the eighth reflow cycle.

The samples of the Yageo CC1206JRNPO9BN681 (dielectric NP0, size 1206, nominal capacitance 680 pf ± 5%) were measured in parallel mode over 5 NPLCs using a voltage of 1 V and a frequency of 300 kHz. The Cycle-Capacitance diagram of eight samples (C8 for four reflow cycles and C1–C7 for eight reflow cycles) is shown in Figure 19.

Without exception, the measured values of the NP0 MLCCs remain almost constant and thus in the specified capacitance range specified by the manufacturer (646, 714 pF). They exhibit the highest robustness against the temperature effects of the soldering processes. The change in capacitance values between two reflow cycles and the changes referenced to the initial value vary in a range between −0.2% and 0.2%. Table 4 summarizes the results of all the capacitance measurements. While the changes in the X5R and X7R types are mid-range, the Y5V experiences the highest changes. At NP0, nearly no change in capacitance could be observed.

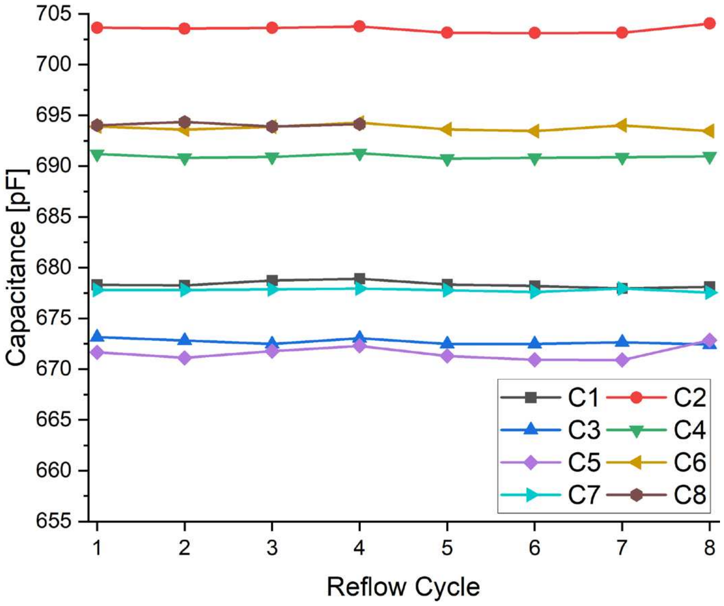

Figure 19. Cycle-Capacitance diagram of the measured values of Yageo CC1206JRNPO9BN681 (dielectric NP0, size 1206, nominal capacitance 680 pF ± 5%) for eight reflow cycles. The values remain mainly constant, with very small deviations.

Table 4. Summary of the measured changes in capacitance for the different MLCCs.

Component Type	Dielectric	Relative Change after Second Reflow	Relative Change between Subsequent Reflows	Largest Averaged Change Compared to Initial Value	Averaged Change after Eight Reflows Compared to Initial Value	Estimated Uncertainty of Measured Values
KEMET C1206C106K4PAC7800+	X5R	3–5.5%	−2.5–3.5%	5.3%	5.2%	±0.5%
KEMET C1206C474K5RACTU	X7R	2.2–4.2%	−1.8–2.6%	3.8%	3.8%	±0.2%
Yageo CC1206ZPY5V7BB475	Y5V	9.5–13%	−7–10%	14.8%	12.4%	±0.5%
Yageo CC1206JRNPO9BN681	NP0	−0.2–0.2%	−0.2–0.2%	0.2%	0.2%	±0.2%

3.3. Shear Tests

The results of the shear tests conducted with a cross-head speed of 0.1 mm/s are shown in Figure 20. The fracture force values were transferred to their corresponding shear strengths using the following equation:

$$\tau = F/A, \tag{1}$$

where τ is the shear strength, F is the force, and A = 1.85 mm^2 is the sum of the areas of both soldering pads (corresponding to the contact area).

Starting with a mean shear strength of 45.71 MPa, there are only slight variations during the following reflow cycles, with a minimum of 44.51 MPa after four cycles and a final value of 45.14 MPa. Even if no statistics can be derived from the experiments due to the small number of samples, the shear strength of the solder joints does not really appear to change with the number of reflow cycles.

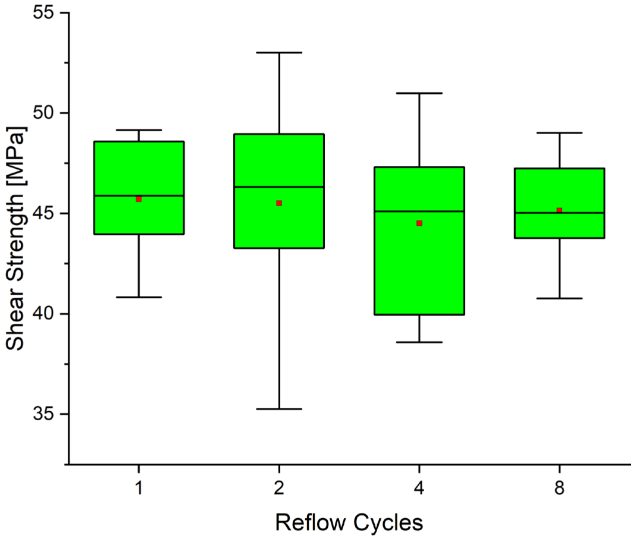

Figure 20. Results of the shear test with respect to the number of reflow cycles conducted The green box marks the first and third quartiles, the black line within the box marks the median, and the red dot marks the mean.

The tested samples were metallographically prepared to analyze the fracture path with EDX. Figures 21–24 show the results of these analyses. Each figure contains a SEM-photograph that shows the entire fracture through the solder joint and one more detailed SEM photograph that shows only the residuals of the fractured solder joint in the gap region. Corresponding EDX-mappings are depicted for both SEM photographs.

Figure 21 shows the fracture path of the shear test after one reflow cycle. It can be seen that across the entire gap region, the crack path runs along the interface to the Al_2O_3 ceramic body of the chip resistor. At the corner where the gap region ends, the crack continues its path through the meniscus of the solder joint. It can be recognized from the EDX mappings in Figure 21c,d that the Ni-thick film layer has neither adhered to the Al_2O_3 ceramic body nor to the solder. Figure 21c reveals that some residues of an Ag-metallization can still be found on the Al_2O_3 body surface.

The course of the crack path found for the shear tests after two, four, and eight reflow cycles (Figures 22–24) is very similar to that after one reflow cycle. However, in contrast to the EDX-mapping in Figure 21d, the EDX-mappings in Figures 22d, 23d and 24d show that the Ni-thick film layer adheres to the solder joint across the gap region. Moreover, the mappings show that the Ag-metallization and parts of the Al_2O_3 body can be found on top of that Ni-layer in the gap region, while the mappings depicted in Figures 22c and 24c reveal that only Al_2O_3 can be found on the opposite fracture surface, the component side. This indicates that the formation of the Cu_6Sn_5 IMC on top of the Ni thick film metallization, which occurs from the second reflow on (see Figures 11–13), increases the cohesion between solder and component metallization to a value that is higher than that for the cohesion of thick film metallization on the Al_2O_3 ceramic body of the component. Thus, the latter seems to determine the shear strength, since it is reasonable to assume that the fracture force will not increase when the crack runs through the softer solder material of the meniscus.

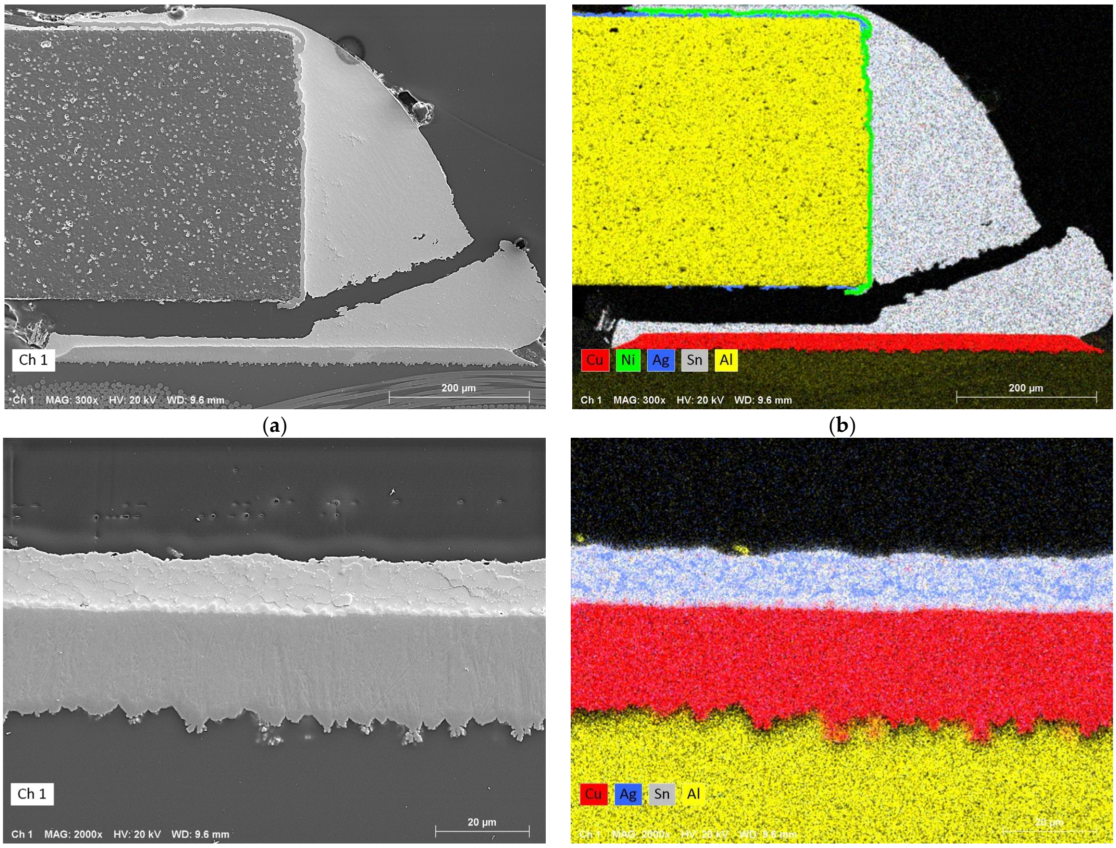

(**a**) (**b**)

(**c**) (**d**)

Figure 21. EDX analysis of a shear tested resistor after one reflow cycle. (**a**) SEM image in SE mode with a magnification of 300× and (**b**) associated combined EDX map of Cu, Ni, Ag, Sn and Al. (**c**) Detailed SEM image in SE mode of the location between the ragged resistor and the Cu pad of the PCB with a higher magnification of 2000× and (**d**) associated combined EDX map of Cu, Ag, Sn, and Al (here, the Ni barrier neither adhered to the ceramic body nor to the solder). For each pair of pictures, the same settings were used.

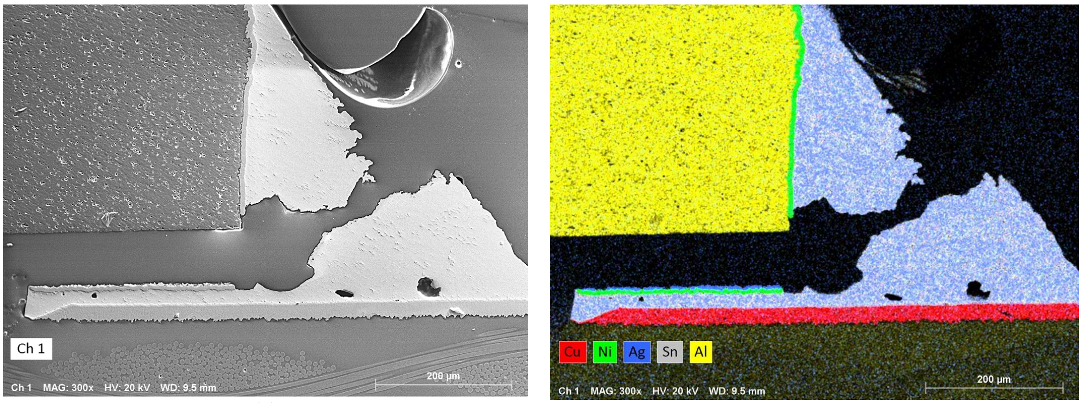

(**a**) (**b**)

Figure 22. *Cont.*

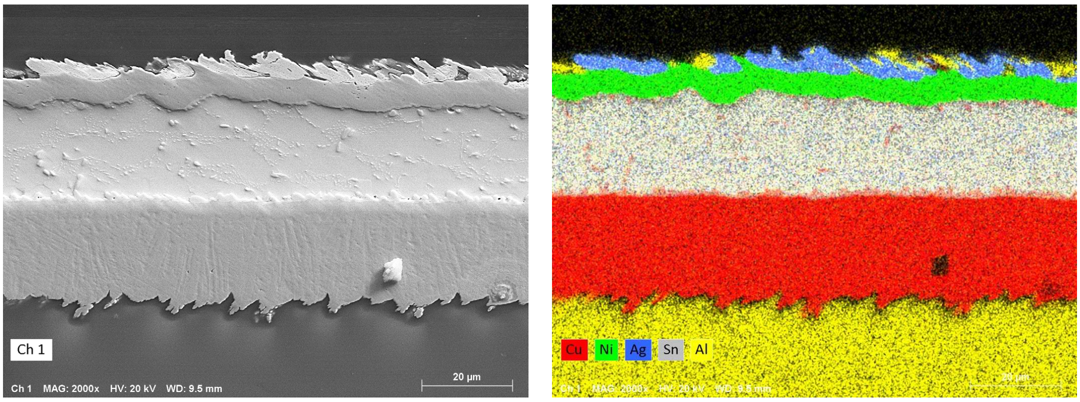

(**c**) (**d**)

Figure 22. EDX analysis of a shear tested resistor after two reflow cycles. (**a**) SEM image in SE mode with a magnification of 300× and (**b**) associated combined EDX map of Cu, Ni, Ag, Sn and Al. (**c**) Detailed SEM image in SE mode of the location between the ragged resistor and the Cu pad of the PCB with a higher magnification of 2000× and (**d**) associated combined EDX map of Cu, Ni, Ag, Sn, and Al. For each pair of pictures, the same settings were used.

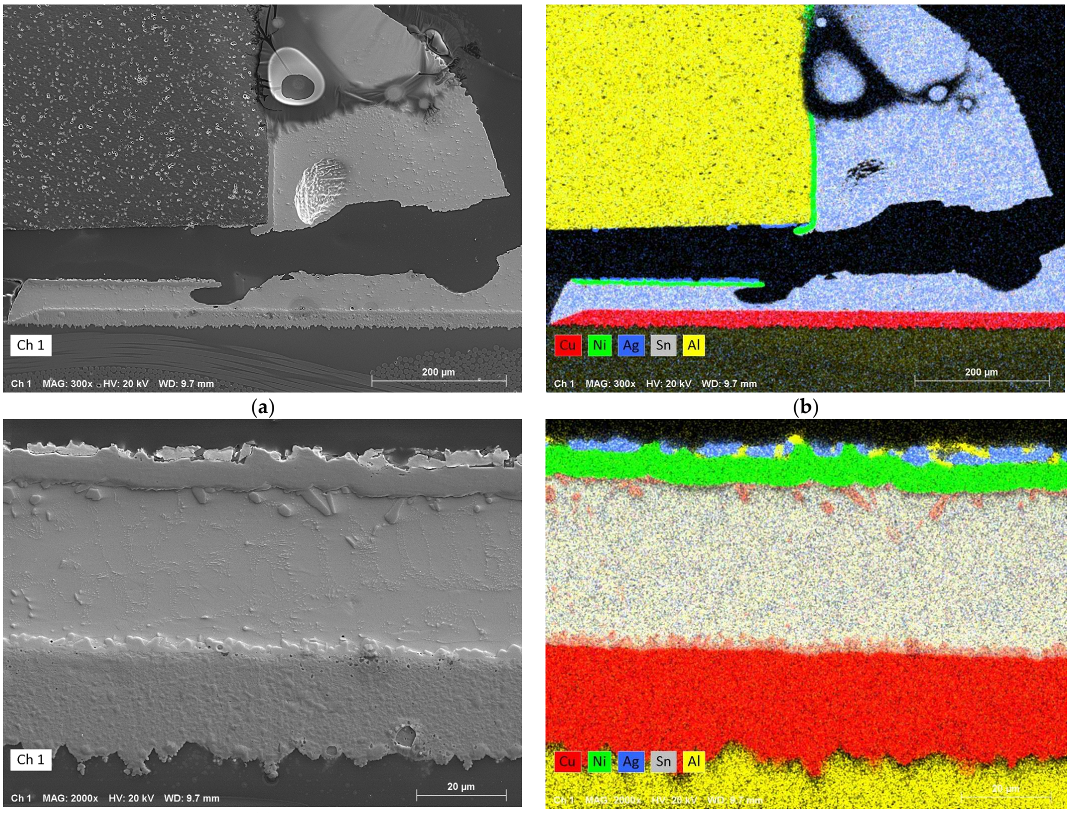

(**c**) (**d**)

Figure 23. EDX analysis of a shear tested resistor after four reflow cycles. (**a**) SEM image in SE mode with a magnification of 300× and (**b**) associated combined EDX map of Cu, Ni, Ag, Sn and Al. (**c**) Detailed SEM image in SE mode of the location between the ragged resistor and the Cu pad of the PCB with a higher magnification of 2000× and (**d**) associated combined EDX map of Cu, Ni, Ag, Sn, and Al. For each pair of pictures, the same settings were used.

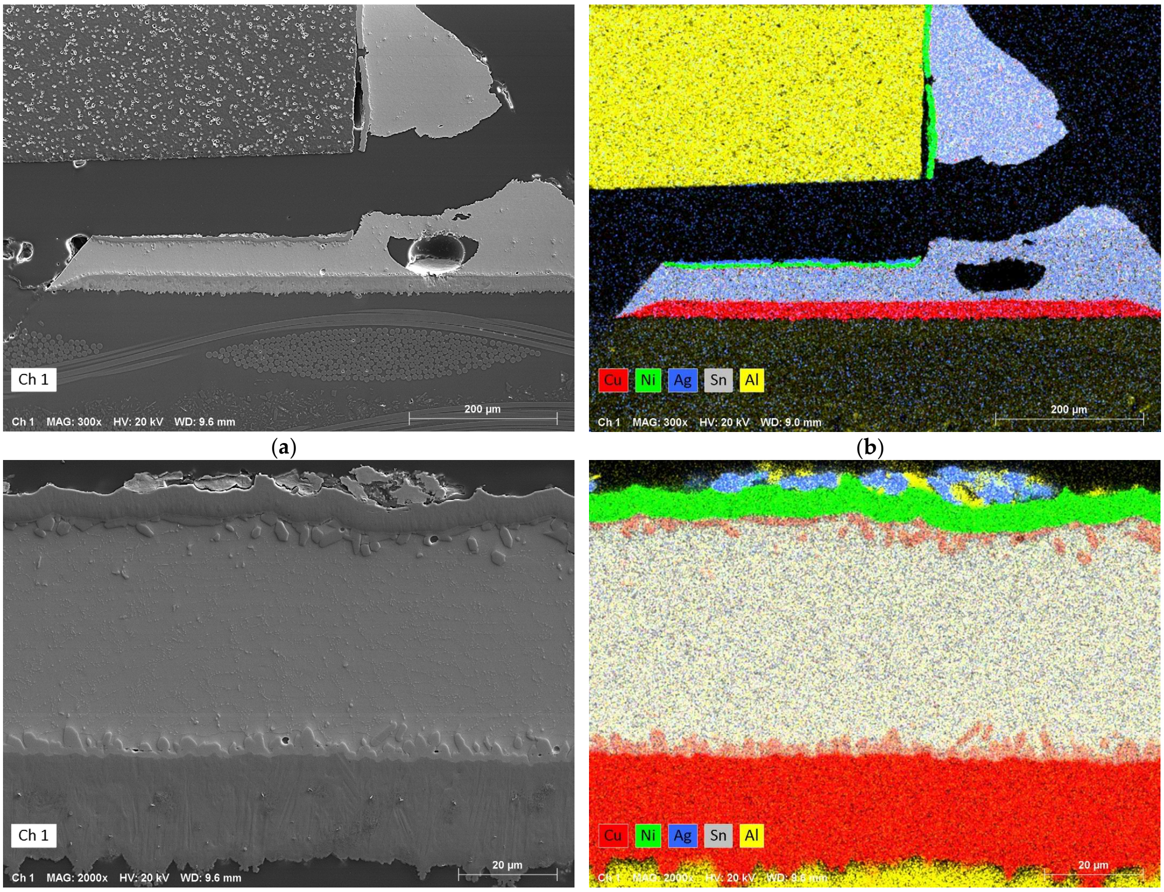

(**a**) (**b**)

(**c**) (**d**)

Figure 24. EDX analysis of a shear tested resistor after eight reflow cycles. (**a**) SEM image in SE mode with a magnification of 300× and (**b**) associated combined EDX map of Cu, Ni, Ag, Sn and Al. (**c**) Detailed SEM image in SE mode of the location between the ragged resistor and the Cu pad of the PCB with a higher magnification of 2000× and (**d**) associated combined EDX map of Cu, Ni, Ag, Sn, and Al. For each pair of pictures, the same settings were used.

This assumption is supported by the light microcopy pictures shown in Figure 25. The four pictures show the strength of the two component solder joints after one reflow (Figure 25a), after two reflows (Figure 25b), after four reflows (Figure 25c), and after eight reflows (Figure 25d). While the solder meniscus is uncracked, a crack path between the Al_2O_3 ceramic body and the solder joint across the gap region can be observed in all four cases. It needs to be noted that the effect of a stronger and weaker joint was only observed for roughly 50% of the shear test. The other 50% showed a full crack through both solder joints of the chip resistor.

The EDX mapping in Figures 21d, 22d, 23d and 24d indicates that the results from the shear tests on chip resistors can be transferred to the case of MLCCs. Although the metallization system is slightly different (Ag-Ni for chip resistors and Cu-Ni for MLCCs), the formation of the Cu_6Sn_5 IMC on the Ni-thick film/solder interface seems to be similar for both components. Thus, a comparable cohesion between the component metallization and the solder joint should be expected for the MLCCs.

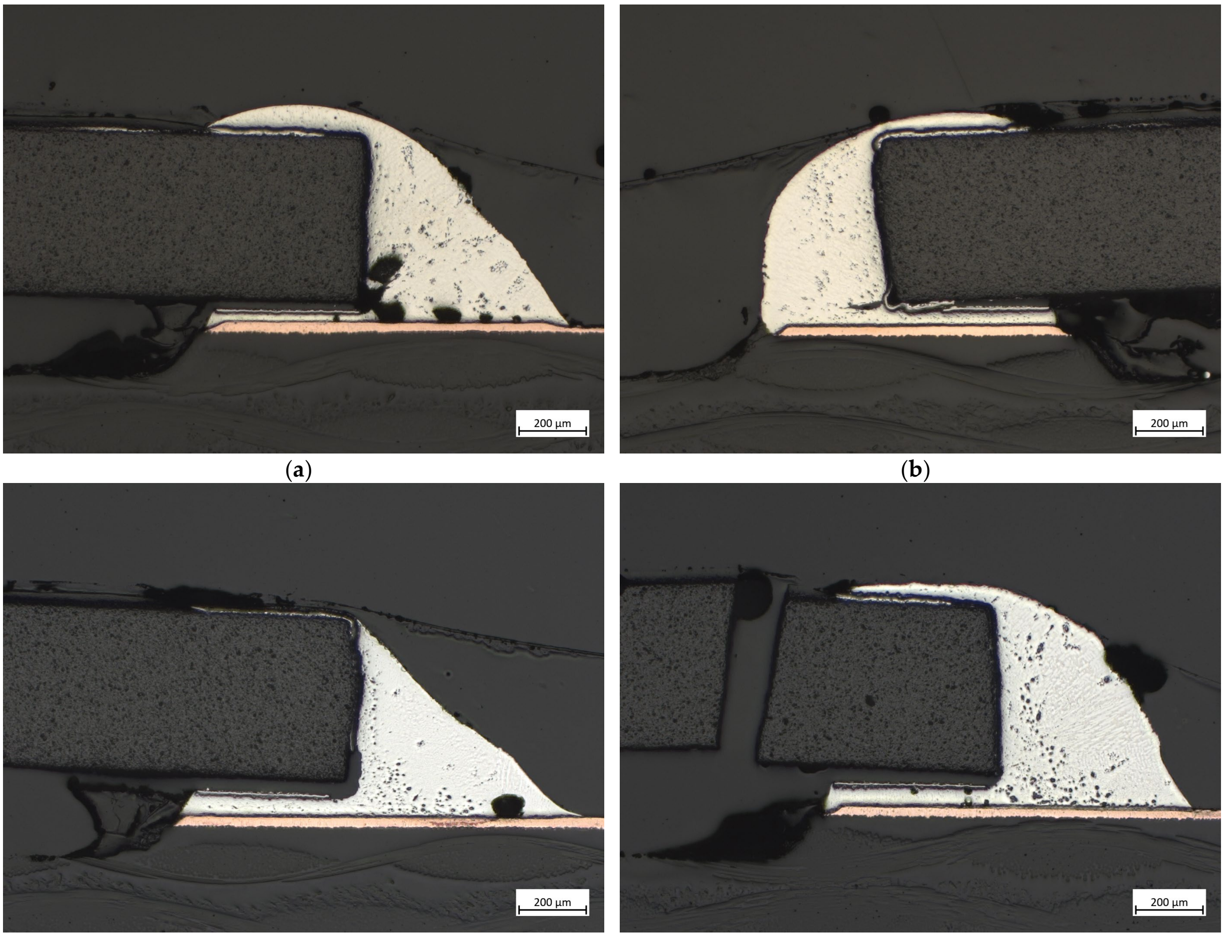

(**a**) (**b**)

(**c**) (**d**)

Figure 25. Light microscopy images with a magnification of 5× of the non-ragged side of resistors after the shear test after (**a**) one, (**b**) two, (**c**) four, and (**d**) eight reflow cycles.

4. Discussion

During a reflow cycle, the formation of a proper Cu_6Sn_5 IMC within the solder paste is necessary to achieve a strong and reliable bond between the component and the Cu metallization of a PCB. However, due to the much higher brittleness of the IMC compared to the individual materials, the thickness of this formation should be kept to a minimum. In times of significantly increased demand for a reduction in environmental pollution, the reuse of components gets more and more important. In this framework, some components will have to experience multiple reflow cycles, resulting in a small but constant increase in the IMC layer thickness, as the experiments show.

Although this average IMC layer thickness grows in a similar way on both the PCB side and component side, the morphology differs. While there seems to be linear growth on the PCB side with nearly no variability (coefficient of determination, $R^2 = 0.96$), a lot of variability compared to the linear growth can be observed on the component side ($R^2 = 0.54$). This variability is supposedly caused by the inhomogeneous, rather dendritic, growth of Cu_6Sn_5 IMC on the component side compared to the equally distributed spherical growth kinetics of the Cu_6Sn_5 IMC on the PCB side. The Cu_6Sn_5 IMC on the component side, which requires the transport of Cu from the PCB-Side trough the solder joint, might be responsible for the decomposition of the solder material, which shows in a depletion of the silver in towards the Cu_6Sn_5 IMCs. This effect is particularly pronounced after the first and second reflows, when the Cu_6Sn_5 IMCs start to form and grow. However, in order to precisely describe and understand the formation of the Cu_6Sn_5 IMC on the Ni-thick film layer and the depletion of Ag towards Cu_6Sn_5 IMC, similar experiments to those reported [19] have to be carried out.

Depending on the number of reflow cycles, the capacitance of most of the usual types of MLCC changes. After the first reflow cycle, all the measured capacitance values are still in the ranges that were specified by the respective manufacturer. Some of the samples were out of range after two (X7R) or three (Y5V) reflow cycles or increased almost to the upper limit (Y5V) after several reflow cycles. It was observed that existing differences between the MLCC samples do not change and remain. While the highest change in capacitance with 12.4% could be observed for Y5V MLCCs (class III), the change was in mid-range with 3.8% to 5.3% for X5R and X7R MLCCs (class II) and 0.2% for NP0 MLCCs (class I). The reason for the different changes in capacitance is the use of different materials as dielectrics. The X5R and X7R bodies are based on ferroelectric $BaTiO_3$ and different dopants ($\varepsilon_r = 10^3 \ldots 10^4$), which exhibit high polarizability, which in turn depends on mechanical stress, among other things. The heat input that is caused by the multiple reflow cycles evokes thermomechanical stress within the MLCC component due to the different coefficients of thermal expansion of the component, the PCB, and the solder paste. This thermomechanical stress remains as residual stress within the component, affecting the polarizability and thus the permittivity, resulting in a change in capacitance. The Y5V bodies are also based on ferroelectric $BaTiO_3$, but with other dopants to increase the polarizability and thus the permittivity and capacitance, respectively, which is why the changes are relatively the highest. In contrast, the NP0 bodies consist of a paraelectric dielectric (e.g., $CaZrO_3$), which offers a much lower permittivity ($\varepsilon_r << 10^2$) and thus much lower capacitance values, which cannot be polarized, and the capacitance remains almost constant during the experiments. The measured values are in accordance with the observations made in [25].

Up to now, it appears that the described changes in the microstructure of the solder (e.g., the change in the Ag distribution within the solder) and in the thickness of the IMC layers (from 2 µm up to 5 µm) do not seriously affect the mechanical stability of the solder joints: the measured mean shear strengths vary in the range from 44.51 MPa to 45.71 MPa (corresponding to a relative change of less than 3%) for the different reflow cycle numbers. The microscopical analysis of the samples reveals that the metallization is always detached from the body of the resistor after a crack was detected during the experiment. In the moment of the detachment, the solder paste is carried away by the breaking metallization. It can be assumed that the cohesion of the metallization/component interface is lower than the cohesion on the metallization/solder interface because the crack would otherwise run differently, most probably up to the inner end of the Cu pad. This weakness of the metallization might be a reason for the very small change in the measured shear strengths. In contrast, other publications report larger changes of approximately 10% to 20% at similar IMC layer thicknesses [15,21,23,24], or similar changes of approximately 5% at slightly higher IMC layer thicknesses of 3 µm to 8.5 µm [16]. Another important effect that could not be observed here might be the problem of detaching Cu metallization after several reflow cycles, as reported in [21].

5. Conclusions

In the context of reusing electronic components, it is necessary to have an accurate knowledge of the effects of multiple reflow cycles on the formation of IMCs and the decomposition of the solder paste used. Therefore, up to eight reflow cycles were performed on various kinds of MLCCs of size 1206 with different capacitance values and dielectric types (X5R, X7R, Y5V, and NP0). Electrical four-point capacitance measurements were performed after each cycle, showing an average increase after eight cycles of 5.2% (X5R), 3.8% (X7R), and 12.4% (Y5V), while almost no change in capacitance could be observed in the case of the NP0 MLCCs. Depending on the tolerance of the selected components, a change in capacitance due to the reuse of MLCCs may be another factor that needs to be considered during the circuit design.

After one, two, four, and eight reflow cycles, cross sections of the samples were made, and both SEM and EDX analyses were performed to investigate the changes at the Cu/solder and the component/solder interfaces. While a proper Cu_6Sn_5 IMC layer is already formed at the interface solder/PCB metallization after the first reflow cycle, there are only small individual Cu_6Sn_5 cells formed at the interface solder/component metallization. These small cells experience significant growth during the second reflow cycle, although they still do not form a coherent layer. Further reflow cycles result in a similar increase in both IMC thicknesses. At the same time, an Ag depletion zone could be found at the interface solder/PCB metallization after the first reflow cycle, resulting in a second Ag depletion zone at the interface solder/component metallization after the second reflow cycle. During the following reflow cycles, the Ag is distributed more and more within the solder and Ag-depleted zones diminish, while the pure beta-tin areas and the Ag_3Sn/Sn layers continuously shrink.

To investigate the influence of these changes on the solder joint mechanical functionality, shear tests were conducted on small PCBs with resistors of size 1206 after different numbers of reflow cycles. During the experiments, the resistance was measured continuously to detect a crack within the solder joints as soon as possible. With a minimum mean shear strength of 44.51 MPa after four cycles and a maximum shear strength of 45.71 MPa after one cycle, multiple reflow cycles do not appear to have any significant influence on mechanical robustness.

Author Contributions: Conceptualization, E.W. and S.W.; methodology, E.W. and S.W.; investigation, E.W.; writing, E.W. and S.W.; review and editing, E.W. and S.W.; supervision, S.W. All authors have read and agreed to the published version of the manuscript.

Funding: This research received no external funding.

Data Availability Statement: The original contributions presented in the study are included in the article, further inquiries can be directed to the corresponding author.

Acknowledgments: The authors would like to offer particular thanks to G. S. Dekate for assistance in electrical measurements, to D. Barth for his help in sample preparation and mechanical characterization, and to A. Ruh for his support in SEM/EDX analysis and in editing graphics.

Conflicts of Interest: The authors declare no conflicts of interest.

References

1. Goosey, M.; Kellner, R. Recycling technologies for the treatment of end of life printed circuit boards (PCBs). *Circuit World* **2003**, *29*, 33–37. [CrossRef]
2. Chancerel, P.; Meskers, C.E.M.; Hagelüken, C.; Rotter, V.S. Assessment of Precious Metal Flows During Preprocessing of Waste Electrical and Electronic Equipment. *J. Ind. Ecol.* **2009**, *13*, 791–810. [CrossRef]
3. Ramon, H.; Peeters, J.R.; Sterkens, W.; Duflou, J.R.; Kellens, K.; Dewulf, W. Techno-economic potential of recycling Tantalum containing capacitors by automated selective dismantling. *Procedia CIRP* **2020**, *90*, 421–425. [CrossRef]
4. Maurice, A.A.; Dinh, K.N.; Charpentier, N.M.; Brambilla, A.; Gabriel, J.-C.P. Dismantling of Printed Circuit Boards Enabling Electronic Components Sorting and Their Subsequent Treatment Open Improved Elemental Sustainability Opportunities. *Sustainability* **2021**, *13*, 10357. [CrossRef]
5. Wang, J.; Guo, J.; Xu, Z. An environmentally friendly technology of disassembling electronic components from waste printed circuit boards. *Waste Manag.* **2016**, *53*, 218–224. [CrossRef]
6. Jiang, P.; Harney, M.; Song, Y.; Chen, B.; Chen, Q.; Chen, T.; Lazarus, G.; Dubois, L.H.; Korzenski, M.B. Improving the end-of-Life for electronic materials via sustainable recycling methods. *Procedia Environ. Sci.* **2012**, *16*, 485–490. [CrossRef]
7. Conti, M.; Orcioni, S. Modeling of Failure Probability for Reliability and Component Reuse of Electric and Electronic Equipment. *Energies* **2020**, *13*, 2843. [CrossRef]
8. Kopacek, B. Intelligent disassembly of components from printed circuit boards to enable re-use and more efficient recovery of critical metals. In Proceedings of the 2016 Electronics Goes Green 2016+(EGG), Berlin, Germany, 6–9 September 2016; pp. 190–195.

9. Stobbe, I.; Potter, H.; Griese, H.; Fotheringham, G.; Reichl, H. Quality Challenges of Reused Components. In Proceedings of the 2004 International IEEE Conference on the Asian Green Electronics (AGEC), Hong Kong, Shenzhen, China, 7–9 January 2004; pp. 218–225.
10. Yuile, A.; Wiss, E.; Barth, D.; Wiese, S. Simulation of Mechanical Stresses in $BaTiO_3$ Multilayer Ceramic Capacitors during Desoldering in the Rework of Electronic Assemblies Using a Framework of Computational Fluid Dynamics and Thermomechanical Models. *Materials* **2024**, *17*, 2702. [CrossRef]
11. Xiang, D.; Pang, Z.; Long, D.; Mou, P.; Yang, J.; Duan, G. The Disassembly Process and Apparatus of waste Printed Circuit Board Assembly for reusing the components. *Appl. Mech. Mater.* **2014**, *457*, 474–485. [CrossRef]
12. Koo, J.M.; Lee, Y.H.; Kim, S.K.; Jeong, M.Y.; Jung, S.B. Mechanical and Electrical Properties of Sn-3.5 Ag Solder/Cu BGA Packages during Multiple Reflows. *Key Eng. Mater.* **2005**, *297*, 801–806. [CrossRef]
13. Koo, J.M.; Lee, C.Y.; Jung, S.B. Effect of Reflow Number on Mechanical and Electrical Properties of Ball Grid Array (BGA) Solder Joints. *J. Microelectron. Packag. Soc.* **2007**, *14*, 71–77.
14. Kim, D.G.; Kim, J.W.; Ha, S.S.; Noh, B.I.; Koo, J.M.; Park, D.W.; Ko, M.W.; Jung, S.B. Effect of reflow numbers on the interfacial reaction and shear strength of flip chip solder joints. *J. Alloys Compd.* **2008**, *458*, 253–260. [CrossRef]
15. Noh, B.I.; Koo, J.M.; Kim, J.W.; Kim, D.G.; Nam, J.D.; Joo, J.; Jung, S.B. Effects of number of reflows on the mechanical and electrical properties of BGA package. *Intermetallics* **2006**, *14*, 1375–1378. [CrossRef]
16. Zhong, W.H.; Chan, Y.C.; Alam, M.O.; Wu, B.Y.; Guan, J.F. Effect of multiple reflow processes on the reliability of ball grid array (BGA) solder joints. *J. Alloys Compd.* **2006**, *414*, 123–130. [CrossRef]
17. Salleh, M.M.; McDonald, S.D.; Gourlay, C.M.; Yasuda, H.; Nogita, K. Suppression of Cu_6Sn_5 in TiO_2 reinforced solder joints after multiple reflow cycles. *Mat. Des.* **2016**, *108*, 418–428.
18. Ma, H.R.; Wang, Y.P.; Chen, J.; Ma, H.T.; Zhao, N. The effect of reflow temperature on IMC growth in Sn/Cu and Sn0.7Cu/Cu solder bumps during multiple reflows. In Proceedings of the 18th International Conference on Electronic Packaging Technology (ICEPT), Harbin, China, 16–19 August 2017; pp. 1402–1405.
19. Ma, H.; Ma, H.; Kunwar, A.; Shang, S.; Wang, Y.; Chen, J.; Huang, M.; Zhao, N. Effect of initial Cu concentration on the IMC size and grain aspect ratio in Sn-xCu solders during multiple reflows. *J. Mater. Sci. Mater. Eletron.* **2018**, *29*, 602–613. [CrossRef]
20. Huang, R.; Ma, H.; Shang, S.; Kunwar, A.; Wang, Y.; Ma, H. Size effect on interface reaction of Sn–x Cu/Cu solder joints during multiple reflows. *J. Mater. Sci. Mater. Electron.* **2019**, *30*, 4359–4369. [CrossRef]
21. Liu, P.; Yao, P.; Liu, J. Effects of multiple reflows on interfacial reaction and shear strength of SnAgCu and SnPb solder joints with different PCB surface finishes. *J. Alloys Compd.* **2009**, *470*, 188–194. [CrossRef]
22. Gao, H.; Wei, F.; Sui, Y.; Qi, J. Growth behaviors of intermetallic compounds on the Sn-0.7Cu-10Bi-xCo/Co interface during multiple reflow. *Mater. Des.* **2019**, *174*, 107794. [CrossRef]
23. Branzei, M.; Plotog, I.; Miculescu, F.; Varzaru, G.; Svasta, P.; Thumm, A. Solder Joints Properties as Function of Multiple Reflow Vapor Phase Soldering Process. In Proceedings of the 35th International Spring Seminar on Electronics Technology (ISSE), Bad Aussee, Austria, 9–13 May 2012; pp. 155–160.
24. Wirth, V.; Rendl, K.; Steiner, F. Effect of Multiple Reflow Cycles on Intermetallic Compound Creation. In Proceedings of the 38th International Spring Seminar on Electronics Technology (ISSE), Eger, Hungary, 6–10 May 2015; pp. 226–230.
25. Jánó, R.; Fodor, A. Soldering Profile Optimization for Through-Hole and Surface Mounted Ceramic Capacitors. In Proceedings of the 37th International Spring Seminar on Electronics Technology (ISSE), Dresden, Germany, 7–11 May 2014; pp. 170–175.
26. Jánó, R.; Pitică, D.; Svasta, P.; Vărzaru, G. Effects of Reflow Soldering Methods on the Lifetime of Capacitors. In Proceedings of the 35th International Spring Seminar on Electronics Technology (ISSE), Bad Aussee, Austria, 9–13 May 2012; pp. 183–188.
27. Kim, M.-G.; Lee, B.H.; Yun, T.-Y. Equivalent-Circuit Model for High-Capacitance MLCC Based on Transmission-Line Theory. *IEEE Trans. Compon. Packag. Manuf. Technol.* **2011**, *2*, 1012–1020. [CrossRef]
28. *IEC 60384-1*; Fixed Capacitors for Use in Electronic Equipment—Part 1: Generic Specification. International Electrotechnical Commission: Geneva, Switzerland, 2021.
29. Wiss, E.; Barth, D.; Wiese, S. Concept of a Mechanical Test Setup for Packaging Materials Using Digital Image Correlation Methods. In Proceedings of the 22nd International Conference on Thermal, Mechanical and Multi-Physics Simulation and Experiments in Microelectronics and Microsystems (EuroSimE), Online, 19–21 April 2021; pp. 1–6.
30. Anthati, S.G.; Wiss, E.; Wiese, S. Bending Experiments on QFN Components. In Proceedings of the 25th International Conference on Thermal, Mechanical and Multi-Physics Simulation and Experiments in Microelectronics and Microsystems (EuroSimE), Catania, Italy, 7–10 April 2024; pp. 1–5.
31. *IEC 62137-1-2*; Surface Mounting Technology—Environmental and Endurance Test Methods for Surface Mount Solder Joint—Part 1–2: Shear Strength Test. International Electrotechnical Commission: Geneva, Switzerland, 2007.
32. Amli, S.F.M.; Salleh, M.A.A.M.; Aziz, M.S.A.; Yasuda, H.; Nogita, K.; Abdullah, M.M.A.B.; Nemes, O.; Sandu, A.V.; Vizureanu, P. Effects of Multiple Reflow on the Formation of Primary Crystals in Sn-3.5Ag and Solder Joint Strength: Experimental and Finite Element Analysis. *Materials* **2023**, *16*, 4360. [CrossRef] [PubMed]

5.11 Paper 11: Electrical diagnostics of passive components failure during reliability testing

5.11.1 Veröffentlichungshinweise

Erik Wiss[1], René Metasch[2], David Barth[1], Vlad Serea[1], Mike Röllig[2], Steffen Wiese[1]

[1]Chair of Microintegration and Reliability, Faculty of Natural Sciences and Technology, Saarland University, Saarbrücken, Germany

[2]Fraunhofer Institute, Testing of Electronics and Optical Methods, Dresden, Germany

2022 23rd International Conference on Thermal, Mechanical and Multi-Physics Simulation and Experiments in Microelectronics and Microsystems (EuroSimE)

Die Originalveröffentlichung ist abrufbar unter:
https://doi.org/10.1109/EuroSimE54907.2022.9758860

5.11.2 Synopse

Diese Veröffentlichung beschreibt die Entwicklung und anschließende Validierung mehrerer Messaufbauten zur elektrischen Charakterisierung niederohmiger Verbindungen (Mikro- bis Milliohmbereich) während Umweltprüfungen. Die Motivation ergibt sich aus der Notwendigkeit, die Stabilität und Zuverlässigkeit solcher Verbindungen zu bewerten. Ziel der Arbeit war die Entwicklung eines In-situ-Messaufbaus, der kontinuierlich den elektrischen Widerstand einer Vielzahl von Proben erfassen und Defekte unmittelbar nach ihrem Auftreten detektieren kann.

Hierzu wurden drei Messsysteme konzipiert und miteinander verglichen. Die beiden in Saarbrücken entwickelten Systeme nutzen zwei getrennte Messgeräte zur simultanen Strom- und Spannungsmessung sowie eine eigens entwickelte, digital umschaltbare Konstantstromquelle. Diese liefert einen hohen Messstrom von 500 mA, um ein günstiges Signal-Rausch-Verhältnis zu erzielen und einen ausreichend großen Spannungsabfall zu erzeugen. Durch die Möglichkeit zur Richtungsumkehr des Stroms können Rauschen und thermische Effekte weiter reduziert werden (Delta-Modus), sodass sich die Genauigkeit der Messung weiter erhöht. Zur Validierung der Aufbauten wurden Nullohmwiderstände auf Testplatinen aufgelötet und einem Temperaturwechseltest unterzogen.

Die Ergebnisse zeigen, dass alle drei Systeme in der Lage sind, solche niederohmigen Verbindungen mit hoher Genauigkeit von wenigen Mikroohm zu messen und das Auftreten defekter Lötstellen zuverlässig zu detektieren.

Im Kontext des Gesamtprojekts leistet diese Veröffentlichung einen Beitrag zur Beantwortung der Frage, wie sich die elektrischen Eigenschaften reaktiv gefügter Verbindungen während Umweltprüfversuchen zuverlässig überwachen lassen.

5.11.3 Vollständiger Artikel

Electrical diagnostics of passive components failure during reliability testing

E. Wiss[1)], R. Metasch[2)], D. Barth[1)], V. Serea[1)], M. Roellig[2)], S. Wiese[1)]

[1)] Saarland University, Dept. Systems Engineering
Chair of Microintegration and Reliability,
Campus C6 3, 66123 Saarbrucken, Germany
erik.wiss@uni-saarland.de, +49 681 30271820

[2)] Fraunhofer Institute for Ceramic Technologies and Systems,
Dept. Testing of Electronics and Optical Methods
Maria-Reiche-Str. 2, 01109 Dresden, Germany
rene.metasch@ikts.fraunhofer.de, +49 351 88815-557

Abstract

While the major reliability concerns in electronics packaging target often new types of semiconductor packages, passive components such as chip resistors (CR) or chip capacitors (CC) can be still responsible for a significant portion of failures that occur in electronic devices. Although passive components show generally good reliability figures, component failures may result from either a very large number of such components on a board or from unfavourable mounting positions they are placed in, e.g. close to large THT-connectors. The main challenge in performing reliability tests on passive components results from their superior robustness in comparison to semiconductor packages. Therefore efficient ways need to be used to test large quantities of such components. Thus, the focus in failure detection in passive components is on electrical diagnostics because of its speed and cost effectiveness.

In order to address the specific problems of failure detection using electrical measurements on chip resistors one need to consider not only the problems of low resistance measurements, like lead resistance, thermoelectric voltages, triboelectric voltages, non ohmic contacts and device self-heating, but also the particular issues that come with the two-pole nature of the resistor. While a solder joint on a dummy semiconductor package can be simply connected in a four-wire-"Kelvin"-scheme, any chip resistor has a current-voltage path that connects two solder joints and the resistive element in series. Thus, it is difficult to figure out, which of the three elements contributes to small changes in the measured resistance.

Test measurements were carried out using the Keithley Models 6221/2182A SMU/nanovoltmeter combination, the Keysight Model 34980A and the Keithley Model 3700A multifunction switch/measure mainframes with appropriate expansion cards to provide multichannel configurations. Measurements were executed using either the internal DMMs of the two mainframe systems or combining the switch units with external measurement devices such as the Keithley Model DAQ6510 or the Keysight Model 34461A. The DUTs were provided by special test boards that allow not only to electrically connect the chip resistors or chip capacitors to the measurement devices but also provide the possibility to separate individual components during the reliability test for further metallographic analysis. The results of the measurements on larger sets of zero-ohm resistors show that the precision and repeatability of the measurements depends fundamentally on measurement parameters such as the chosen test current as well as the measurement time. The paper will give a comparison of the different test parameters with respect to the achieved precision of the measurements. The limitations of electrical diagnostics for failure detection on passive components will be discussed.

1. Introduction

Solder fatigue is a major reliability concern in electronic assemblies. The various environmental factors causing damage of solder joint can be addressed by different types of reliability tests, such as cyclic three point bending tests [1], cyclic four point bending test [2-4], drop tests [5-7], vibration tests [8-10] and temperature cycling tests [11-21]. While all these types of tests use electric detection methods to identify occurrence of a failure at a specific load cycle, the methodology to conduct electric failure detection can be very different depending on the nature of the test and the type of the components tested. One example are electric event detectors, which are used to register intermitted openings in solder interconnects, when area array components are subjected to drop tests. Such a method would not be suitable for tests having less intense loading cycles such as temperature cycling tests, where failure detection was originally carried out with resistance measurements at room temperature in an "offline" test scheme. Specimens were taken out of the temperature cycling chambers periodically for electrical failure detection after a defined number of cycles had been applied, e.g. after every 100 temperature cycles. Although this methodology caused an unfavorable censoring of the test data, it helped on the other hand to minimize the capacity of the necessary electrical test equipment. However, the "offline" test methodology failed to securely detect damaged solder joints of area array components subjected to temperature cycles, because the multi-joint configurations of these components were able to close broken interconnects at room temperature, even when a contact opening at the lower or upper temperature of the cycling test had already occurred. Therefore, the electrical test methodology needed to be adapted to the needs of “online” or in-situ failure detection. This led to an enormous increase in the number of necessary test channels, because specimens (test boards) could no longer be analyzed sequentially.

2. Electrical failure detection methodology

The different approaches to detect failure during a thermal cycling test can be distinguished by the number of test channels needed and the precision of failure detection provided by the test method. The least expensive test methodology is the two-wire resistance measurement, which is usually employed in combination with daisy chain test structures on the specimen.

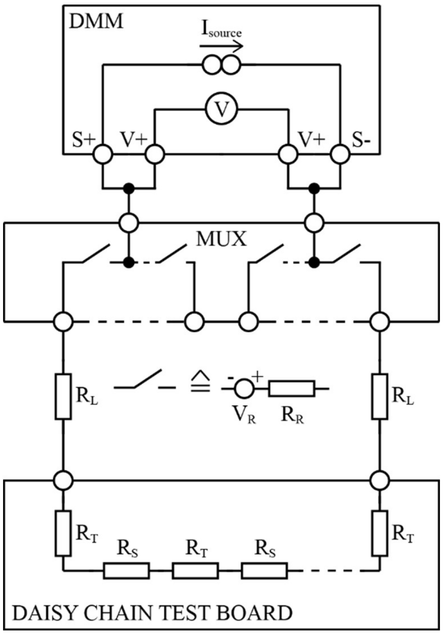

Figure 1: Two-wire resistance measurement, where V_R is the relay’s contact offset voltage, R_R is the relay’s contact resistance, R_L is the line resistance, R_T is the pcb’s trace resistance, and R_S is the solder joint resistance [22, 23]

The schematic in Fig. 1 shows the application of the two-wire method using a digital multimeter (DMM) that is connected to a test board through a multiplexer. In addition to the solder joint resistance (R_S), the resistance of the lead wires (R_L), the contact resistance of the multiplexer relays (R_R) and the resistance of conductive traces (R_T) on the test board and the components are measured by the DMM. Since the resistance of a single solder joint R_S is in the microohm range, the error caused by the parasitic resistances R_L, R_R, and R_T is able to effectively reduce the capability to detect changes in the solder joint resistance caused by damage processes, such as crack propagation [22, 23].

The most accurate method to determine a solder joint resistance is the four-wire configuration shown in Fig.2. The four-wire technique uses separate paths to excite the solder joint resistance by the measurement current and to sense the resulting voltage drop across the joint. Therefore, the parasitic resistances R_L and R_R will not affect the precision of solder joint resistance measurement, which depends only on the value of the parasitic trace resistances R_T of the test component, e.g. zero-ohm chip resistor [22-23].

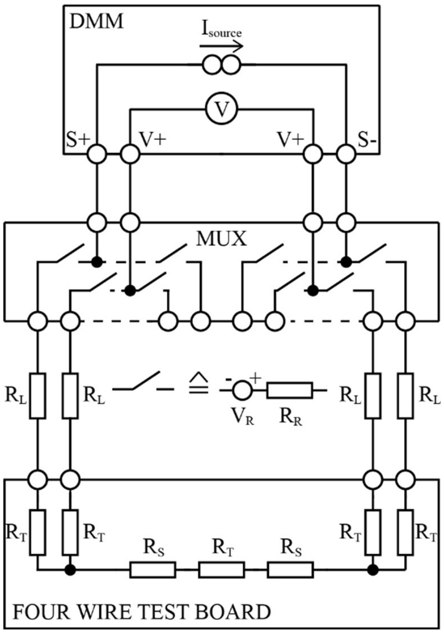

Figure 2: Four-wire resistance measurement, where V_R is the relay’s contact offset voltage, R_R is the relay’s contact resistance, R_L is the line resistance, R_T is the pcb’s trace resistance, and R_S is the solder joint resistance [22, 23]

Other significant errors to a low resistance measurement might be introduced by offset voltages such as the internal instrument zero offset, thermal zero drift, thermoelectric EMFs, radio frequency interference (RFI) induced voltages, electromagnetic inference (EMI) induced voltages, line cycle interference induced voltages, ground loop induced voltages, common-mode current induced voltages or common-mode reversal induced voltages. Although these voltages are very small (microvolt range), they add up in the low voltage path where the voltmeter is connected to the device under test (DUT). In order to enable a high-resolution resistance measurement these additional offset voltages need to be effectively reduced by a number of different measures, such as cable shielding, auto zeroing, signal filtering, and the current reversal method [22-27].

3. Test system design

The outcome of electrical failure detection during a thermal cycling reliability experiment depends on the performance on the measurement hardware. In order to select appropriate test equipment and put it together to a suitable test system, the targeted accuracy and the necessary channel number need to be determined. Additional features such as sensor interfaces, communication protocols or expandability may also be of importance [29, 30].

The selection of the measurement equipment depends on the approximate value of a single solder joint resistance. The different investigations [31-43], that have used resistance measurements to either characterize crack propagation in joints or to determine intrinsic electrical properties of solders and intermetallics, show a wide band ranging from microohm value to milliohm values. Different types of solder joints were used in the various studies. The smallest value (17 … 60 µΩ) was found for rectangular 2x2x0.05 mm³ solder joints [35,43], the largest value (2.5 mΩ) was detected on solder balls having a diameter of approx. 80 µm [42].

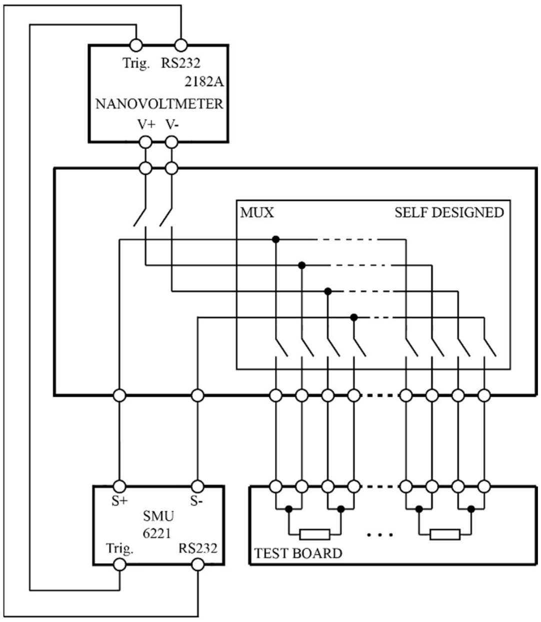

Figure 3: Test System #1 configuration using Keithley Models 6221/2182A for precise low level resistance measurements in delta mode at a reversible source current of ±100 mA. DUT channel switching is provided by a PC-controlled homebrew multiplexer device.

The selection of the multiplexer solution depends on a number of different arguments. Beside the number of DUTs to be tested, it is important to know at what voltage and current levels the tests are conducted and if the interference between different DUTs is of interest (as for instance for pin-to-pin behavior in connector tests). Since medium to high current levels are preferable for low level resistance measurements, switches can either be realized by armature relays or by reed relays. The later have a slightly higher contact voltage but allow more switching operations due to the reduced contact oxidation [29, 30].

The first test system design is schematically depicted in figure 3. The core part consists of a high-resolution resistance measurement, that uses the so called delta mode method and is set up by a combination of a nanovoltmeter device (Keithley 8212) and a low noise source measure unit (SMU, Keithley 6221). Both devices are connected by a RS232 interface to communicate with each other autonomously.

Since the model 6221 SMU is able to create a reversible current of up to 100 mA trough the DUT and the model 2182A nanovoltmeter has a resolution of 10 nV, the system would be able to achieve resistance measurement sensitivity of down to 100 nΩ. This requires the compensation of all erroneous offset voltages in the sense path by a programmed current reversal in the source path. After the first measurement is taken with positive current flow through the DUT, a second measurement is taken with the opposite current flow. To calculate the resistance these two measurements are subtracted from each other [29]:

$$R_{Delta\ Mode} = \frac{U^{(+)} - U^{(-)}}{I^{(+)} - I^{(-)}}$$

$U^{(+)}$ … *voltage at positve source current*
$U^{(-)}$ … *voltage at negative source current*
$I^{(+)}$ … *positve source current*
$I^{(-)}$ … *negative source current*

As a consequence of the fully autonomous operation of the resistance measurement instruments (Model 2182A/ Model 6221) and the very low switching speed requirements a homebrew solution was chosen for the multiplexer. The design uses armature telecom relays and is controlled via a DIO-card from the same PC that collects the resistance data from the measurement instruments. A self-made multiplexer solution helps not only to reduce the overall system cost and it also enables the possibility to design an efficient interface for complex wiring of larger DUT numbers that may contain hundreds of individual wires to be connected.

However, homebrew multiplexer solutions have certain limitations. They will mostly be fixed to the switching task, that they were designed for. The integration of other devices, such as temperature sensors, through the multiplexer becomes usually difficult. Although a PT-100 temperature sensor has the same connection scheme as the solder joint DUT, it needs a much lower sourcing current and delivers higher voltages, which would require a permanent reconfiguration of the measurement devices through the IEEE-488 bus.

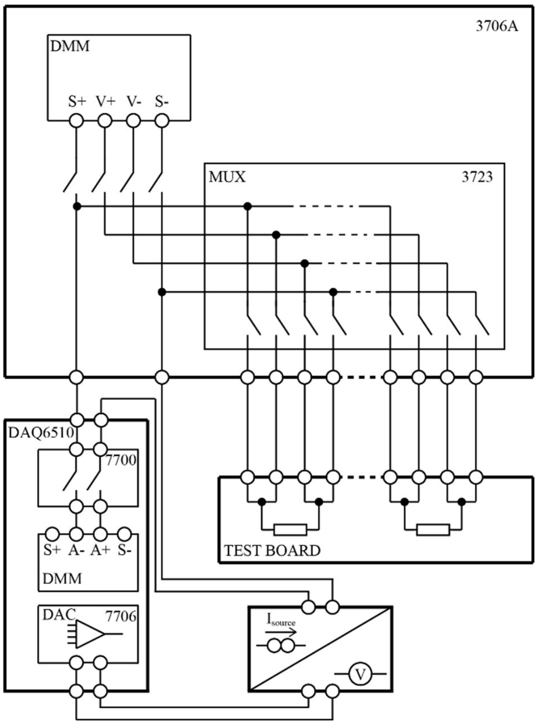

Figure 4: Test System #2 configuration makes use of the LXI-based Keithley model 3706A switch mainframe with an integrated 7.5 digit DMM for low level voltage measurements. Synchronized current measurements are conducted by a LXI-based DAQ6510 6.5 digit DMM. A reversed source current of ±500 mA is generated by a homebrew bidirectional current source.

Since electrical solder fatigue monitoring during temperature cycling experiments entails the permanent registration of test temperatures at various locations in the thermal cycling chamber, the system design tasks comprise synchronized integration of solder resistance and test temperature measurements. Modern LXI-based Switch/Multimeter Systems enable not only a tight integration of the various types of measurement tasks, they also provide excellent expansion capabilities by the connection with other LXI-based-Instruments through the high throughput data transfer and IEEE-1588 clock synchronization [29, 44].

The second test system design uses LXI-based solution and is schematically depicted in figure 4. The core part consists of a Keithley 3706A mainframe with an integrated DMM and six slots for a variety of plug-in cards. The 7.5 digit built in DMM offers a 26 bit A/D conversion with a 10 nV resolution for voltage measurements. However the amplification of low level input signals is limited to a 100 mV minimum range with a 9 ppm precision, whereas the model 2182 offers a 10 mV range with a 4 ppm precision for µV-signals. A type 3723 multiplexer card is internally connected to the DMM. It uses reed relays to switch between the different DUTs in four-wire mode. An external DAQ6510 data acquisition system is connected to the 3706A mainframe via the LXI-bus. It provides two slots for plug in cards and a 6.5 digit built in DMM, that offers a 1 µA resolution with a basic 35 ppm precision in the 1 A current measurement range and 10 mK resolution with a 60 mK precision for four-wire RTD measurements. The current measurement is switched trough the DMM by a type 7700 multiplexer card. A type 7706 all in one card provides 10 channels for RTD measurements and a DAC output to control an external current source. The homebrewed bidirectional current source is able to deliver up to ±500 mA through the source path of the DUT. To measure the solder joint resistance a reversible current is driven through the source path. Synchronized voltage and current measurement are conducted by the model 3706A internal DMM and the model 6510 DMM respectively. The solder joint resistance is calculated similarly to the delta method from the voltage and current measurements, that are taken for every positive and negative current source cycle.

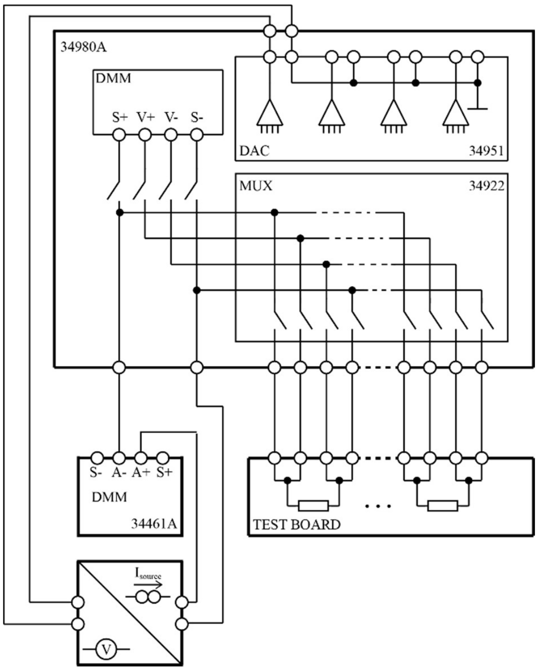

Figure 5: Test System #3 configuration makes use of the LXI-based Keysight model 34980A switch mainframe with an integrated 6.5 digit DMM for low level voltage measurements. Synchronized current measurements are conducted by an LXI-based Keysight 34461 6.5 digit DMM. A reversed source current of ±500 mA is generated by a homebrew bidirectional current source.

The third test system design is also using an LXI-based solution and is schematically depicted in figure 5. The core part consists of a Keysight 34980A mainframe with an integrated DMM and eight slots for plug in cards. The 6.5 digit built in DMM offers a 22 bit A/D conversion with a 100 nV resolution and a basic 40 ppm precision for voltage measurements. A type 34922 multiplexer card is internally connected to the DMM. It uses armature relays to switch between the different DUTs in four-wire mode. The RTD sensors for temperature measurement are also connected via the 34922 card. A type 34951 four channel D/A converter card provides a DAC output to control an external current source. The homebrewed bidirectional current source is able to deliver up to ±500 mA through the source path of the DUT. An external Keysight 34461A 6.5 digit DMM is connected to the 34980A mainframe via the LXI-bus. It provides a 1 µA resolution with a basic 10 ppm precision in the 1 A current measurement range. The solder joint resistance is measured in a reversible current mode similarly to the second test setup.

3. Test system evaluation

In order to evaluate the usability of the equipment to determine the solder joint resistance precisely, test measurements have been taken on all three test systems. All test configurations consisted of zero-ohm chip resistors, that were soldered to a pcb test board with a four-wire connection scheme. For the test setup #1 a -55 °C to 150 °C thermocycle test (TCT) was carried out on 1206 chip resistors. The results were corrected for the average resistance increase per cycle during the TCT, so that the corrected measurement data runs strictly horizontally along the initial value of the zero-ohm resistor. A set of N = 50 data points was selected for statistical analysis. These datapoints correspond to measurements that were taken at the upper temperature of 150 °C of the TCT. Figure 6 depicts the data. The mean is about 20 mΩ, which corresponds to the internal trace resistance of the zero-ohm chip resistor. The entire scatter spans of an interval of approximately 9 µΩ, the standard deviation is about ±2 µΩ.

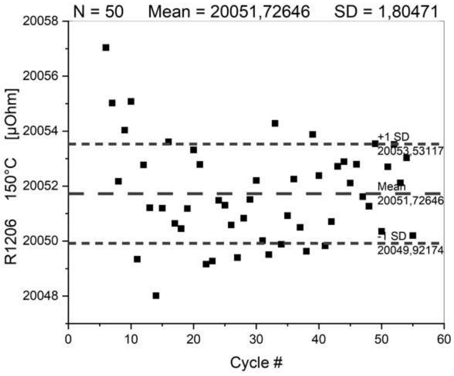

Figure 6: Results of resistance measurements on 1206 zero-ohm chip resistors at 150 °C undergoing a thermal cycling Test -55 °C/150 °C using test system #1

For the test setup #2 a -40 °C to 150 °C thermocycle test (TCT) was carried out on 2512 chip resistors. The results were corrected for the average resistance increase per cycle during the TCT was corrected similarly to the data of test setup #1. A set of N = 50 data points was selected for statistical analysis. These datapoints correspond to measurements that were taken at the upper temperature of 150 °C of the TCT. Figure 7 depicts the data. The mean is about 9 mΩ, which corresponds to the internal trace resistance of the zero-ohm chip resistor. The entire scatter spans of an interval of approximately 9 µΩ, the standard deviation is about ±2 µΩ.

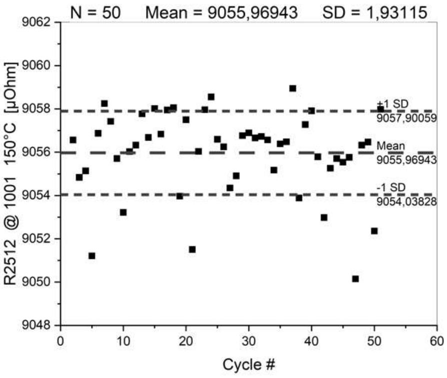

Figure 7: Results of resistance measurements on 2512 zero-ohm chip resistors at 150 °C undergoing a thermal cycling Test -55 °C/150 °C using test system #2

For the test setup #3 a -40 °C to 150 °C thermocycle test (TCT) was carried out on 2512 chip resistors. The results were corrected for the average resistance change per cycle during the TCT was corrected similarly to the data of test setup #1. A set of N = 45 data points was selected for statistical analysis. These datapoints correspond to measurements that were taken at the upper temperature of 150 °C of the TCT.

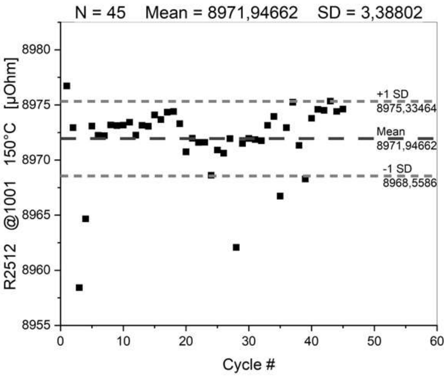

Figure 8: Results of resistance measurements on 2512 zero-ohm chip resistors at 150 °C undergoing a thermal cycling Test -55 °C/150 °C using test system #3

Figure 8 depicts the data. The mean is about 9 mΩ, which corresponds to the internal trace resistance of the zero-ohm chip resistor. The entire scatter spans of an interval of approximately 19 µΩ, the standard deviation is about ±3 µΩ.

4. Conclusions

The specific problems of failure detection using electrical measurements on chip resistors need to consider issues that come with the two-pole nature of the resistor. The internal trace resistance of a zero-ohm resistor is orders of magnitude higher than the corresponding solder joint resistance. Moreover, other problems of low resistance measurements, like lead resistance, thermoelectric voltages, triboelectric voltages, non ohmic contacts and ground loop induced voltages may add to the measurement error. Three different tests setups basing on either the Keithley Models 6221/2182A SMU/nanovoltmeter combination, or the Keysight 34980A and the Keithley 3700A multifunction switch/measure mainframes have been tested for the particular task. The results show that all three systems have the capability to determine the solder joint resistance during a thermal cycling test with a one-digit microohm precision, which is an acceptable level given the typical resistance values of chip resistor solder joints.

Acknowledgments

The authors would like to offer particular thanks to Andreas Ruh for his help in processing the measurement data and preparing the drawings for the paper. This research work was supported by funding from the Deutsche Forschungsgemeinschaft (DFG, German Research Foundation)—Project-ID 426204742.

References

1. J. D. Wu, S. H. Ho, P. J. Zheng, C. C. Liao and S. C. Hung, “An experimental study of failure and fatigue life of a stacked CSP subjected to cyclic bending”, IEEE Proceedings 51st Electronic Components and Technology Conference (2001), pp. 1081-1086.
2. K. Harada, S. Baba, Q. Wu, H. Matsushima, T. Matsunaga, Y. Ucgai and M. Kimura, “Analysis of solder joint fracture under mechanical bending test”, IEEE Proceedings 53rd Electronic Components and Technology Conference (2003), pp. 1731-1737.
3. L. L. Mercado, B. Phillips, S. Sahasrabudhe, J. P. Sedillo, D. Bray, E. Monroe, K. J. Lee and G. Lo, “Use-condition-based cyclic bend test development for handheld components”, IEEE Proceedings 54th Electronic Components and Technology Conference (2004), pp. 1279-1287.
4. I. Kim and S. Lee, “Reliability and Failure Analysis of Lead-Free Solder Joints for PBGA Package Under a Cyclic Bending Load”, IEEE Transactions on Components and Packaging Technologies, vol. 31 (2008), pp. 478-484.
5. F. Kraemer, S. Rzepka, J. Lienig, “Lifetime Modeling for Jedec Drop Tests”, Proceedings of the 2009 International Conference on Thermal, Mechanical and Multi-Physics Simulation and Experiments in Microelectronics and Microsystems (EuroSimE), Delft (NL), April 27-29, 2009, pp. 309-317.
6. F. Kraemer, S. Wiese, S. Rzepka, J. Lienig, “BGA Lifetime Prediction in Jedec Drop Tests Accounting for Copper Trace Routing Effects”, Proc. of the 2010 EuroSimE, Bordeaux(F), April 26-28, 2010, p. 1-8.
7. M. Alajoki, Luu Nguyen, Jorma Kivilahti, “Drop test reliability of wafer level chip scale packages”, IEEE Proc. Electronic Components and Technology, (ECTC), 2005, pp. 637-644 .
8. K. Meier, M. Roellig, A. Schiessl and K. Wolter, “Life time prediction for lead-free solder joints under vibration loads”, in 12th Intl. Conf. on Thermal, Mechanical & Multi-Physics Simulation and Experiments in Microelectronics and Microsystems, 2011, pp. 1-8.
9. F. Liu and G. Meng, “Random vibration reliability of BGA lead-free solder joint”, Microelectronics Reliability, vol. 54 (2014), pp. 226-232.
10. D. Yu, A. Al-Yafawi, T. T. Nguyen, S. Park and S. Chung, “High-cycle fatigue life prediction for Pb-free BGA under random vibration loading”, Microelectronics Reliability, vol. 51 (2011), pp. 649-656.
11. W. Engelmaier, “BGA and CGA solder attachments: results of low-acceleration reliability tests and analysis”, Proceedings of 1995 Japan International Electronic Manufacturing Technology Symposium, 1995, pp. 218-227.
12. J.-P. M. Clech, D. M. Noctor, J. C. Manock, G. W. Lynott and F. E. Baders, “Surface mount assembly failure statistics and failure free time”, 1994 Proceedings. 44th Electronic Components and Technology Conference, 1994, pp. 487-497.
13. Tae-Kyu Lee, Hongtao Ma, Kuo-Chuan Liu, and Jie Xue, “Impact of Isothermal Aging on Long-Term Reliability of Fine-Pitch Ball Grid Array Packages with Sn-Ag-Cu Solder Interconnects: Surface Finish Effects”, J. Electronic Materials, vol. 39 (2010), pp. 2564-2573.
14. E. George, M. Osterman, M. Pecht, and R. Coyle, “Effects of Extended Dwell Time on Thermal Fatigue Life of Ceramic Chip Resistors”, Proc. International Symposium on Microelectronics, San Diego, CA, January 2012.
15. Richard Coyle, Keith Sweatman, and Babak Arfaei, “Thermal Fatigue Evaluation of Pb-Free Solder Joints: Results, Lessons Learned, and Future Trends”, JOM, vol. 67 (2015), pp. 2394–2415.
16. Y. Qi, R. Lam, R. H. Ghorbani, P. Snugovsky and J. K. Spelt, “Temperature profile effects in accelerated thermal cycling of SnPb and Pb-free solder joints”, J. Microelectron. Rel., vol. 46 (2006), pp. 574-588.
17. J. C. Suhling, H.S. Gale, R.W. Johnson, M.N. Islam, T. Shete, P. Lall, M.J. Bozack, J.L. Evans, Ping Seto, T. Gupta, and J.R. Thompson, “Thermal cycling

reliability of lead free solders for automotive applications", The Ninth Intersociety Conference on Thermal and Thermomechanical Phenomena In Electronic Systems, vol.2 (2004), pp. 350-357.

18. Joseph M. Juarez, Jr., Polina Snugovsky, Eva Kosiba, Zohreh Bagheri, Subramaniam Suthakaran, Michael Robinson, Joel Heebink, Jeffrey Kennedy, and Marianne Romansky, "Manufacturability and Reliability Screening of Lower Melting Point Pb-Free Alloys Containing Bismuth", J. Microelectronics and Electronic Packaging, Vol. 12 (2015), pp. 1-28.
19. F. X. Che and J. H. L. Pang, "Fatigue Reliability Analysis of Sn–Ag–Cu Solder Joints Subject to Thermal Cycling", IEEE Transactions on Device and Materials Reliability, vol. 13 (2013), pp. 36-49.
20. J. Lau, Ming Li, Lei Yang, Margie Li, Qing Xiang Yong, Zhong Cheng, Tony Chen, Iris Xu, Nelson Fan, Eric Kuah, Zhang Li, Kim Hwee Tan, Y.M. Cheung, Eric Ng, Penny Lo, Wu Kai, Ji Hao, Rozalia Beica, Koh Sau Wee, Jiang Ran, Cao Xi, Sze Pei Lim, N.C. Lee, Cheng-Ta Ko, Henry Yang, Y.H. Chen, Mian Tao, Jeffery Lo, Ricky Lee, "Reliability of Fan-Out Wafer-Level Packaging with Large Chips and Multiple Re-Distributed Layers", IEEE-Proc. 68th Electronic Components and Technology Conference (ECTC), 2018, pp. 1574-1582.
21. G. Sharma, N. Lakhera, M. Benson and A. J. Mawer, "Advanced Fan Out Wafer Level Package Development for Small form Factor and High-Performance Microcontroller Applications", 2019 International Wafer Level Packaging Conference (IWLPC), 2019, pp. 1-6.
22. Application Note, "Achieve Accurate Resistance Measurements with the 34980A Multifunction Switch Measure Unit", Keysight Technologies, December 5, 2017, 5991-2788EN, 7 p.
23.Keithley Instruments, "Making precision low voltage and low resistance measurements", E-Handbook.; Keithley Instruments Inc.: Cleveland, OH (2013), 22 p.
23. D. Cigoy, "Troubleshooting low voltage measurement problems", Keithley Instruments Inc.: Cleveland, OH (2010), 5 p.
24. Application Note 200, "Understanding low voltage measurements", Keithley Instruments Inc.: Cleveland, OH (2001), 2 p.
25. C. Miller, "Techniques for reducing resistance measurement uncertainty: DC current reversals vs. classic offset compensation", White paper, Keithley Instruments Inc.: Cleveland, OH (2000), 8 p.
26. D. Kirsop and J. Yeager, "Design considerations in low level analog test systems", IEEE Conference on Systems Readiness Technology, 'Advancing Mission Accomplishment', 1990, pp. 577-582.
27. Keithley Instruments, "Low Level Measurements Handbook. Precision DC Current, Voltage and Resistance Measurements", 7th ed.; Keithley Instruments Inc.: Cleveland, OH (2013), 245 p.
27. J. Muniesa and J. Mousson, "Effect of Measurement Conditions on Low-Level Contact Resistance", in IEEE Transactions on Components, Hybrids, and Manufacturing Technology, vol. 7 (1984), pp. 81-83.
28. H. Ikeda, K. Ishida and K. Shirako, "Automated measurement of current dependency of contact resistance in low current level switches", in IEEE Transactions on Instrumentation and Measurement, vol. IM-36, no. 2, pp. 390-393, June 1987.
29. Keithley Applications Guide #3252, "Techniques for multi-channel testing and data acquisition", Keithley Instruments Inc.: Cleveland, OH (2014), 39 p.
30. D. Cigloy, J. Janesch,. "Switching Handbook – A Guide to Signal Switching in Automated test Systems", 6th ed.; Keithley Instruments Inc.: Cleveland, OH (2008), 194 p.
31. R. Wrona, Z. Drozd and M. Szwech, "Resistance Measurements of BGA Contacts During Reliability Tests", IEEE Proc. 29th International Spring Seminar on Electronics Technology, 2006, pp. 184-187.
32. R. Dudek, W. Faust, J. Vogel and B. Michel, "A comparative study of solder fatigue evaluated by microscopic in-situ analysis, on-line resistance measurement and FE calculations", EuroSimE 2005. Proceedings of the 6th International Conference on Thermal, Mechanical and Multi-Physics Simulation and Experiments in Micro-Electronics and Micro-Systems, 2005, pp. 610-617.
33. K. Meier, M. Ochmann, K. Bock, D. Leslie and A. Dasgupta, "Low Temperature Vibration Reliability of Lead-free Solder Joints", IEEE Proc. 70th Electronic Components and Technology Conference (ECTC), 2020, pp. 801-806.
34. J. F. J. M. Caers, X. J. Zhao, E. H. Wong, S. K. W. Seah, C. S. Selvanayagam, W. D. van Driel, N. Owens, M. Leoni, L. C. Tan, P. L. Eu, Yi-Shao Lai, Chang-Lin Yeh, "A Study of Crack Propagation in Pb-Free Solder Joints", in IEEE Transactions on Electronics Packaging Manufacturing, vol. 33 (2010), pp. 84-90.
35. J. Zhang, S. van der Zwaag, H. W. Zeijl and G. Q. Zhang, "On the use of high precision electrical resistance measurement for analyzing the damage development during accelerated test of Pb-free solder interconnects", Proc. IEEE 63rd Electronic Components and Technology Conference (ECTC), 2013, pp. 192-199.
36. J. Lin, Y. Lei, H. Zhao, Z. Wu and L. Lu, "Investigation on failure behaviour of solder joint during thermal fatigue", Proc. 16th IEEE International Symposium on the Physical and Failure Analysis of Integrated Circuits, 2009, pp. 455-459.
37. Alfred Yeo, Bernd Ebersberger, Charles Lee, "Consideration of temperature and current stress testing on flip chip solder interconnects", Microelectronics Reliability, vol. 48 (2008), pp. 1847-1856.
37. Guo, F., Lee, J.G., Hogan T., Subramanian K.N., "Electrical conductivity changes in bulk Sn, and

eutectic Sn-Ag in bulk and in joints, from aging and thermal shock", J. Mater. Res., vol. 20 (2005), pp. 364-374.

38. Cook, B.A., Anderson, I.E., Harringa, J.L., Kang S.K., "Isothermal aging of near-eutectic Sn-Ag-Cu solder alloys and its effect on electrical resistivity", J. Electron. Mater. vol. 32 (2003), pp. 1384–1391.
39. B. Liu, F. Guo, "Electrical conductivity changes of bulk tin and Sn-3.0Ag-0.5Cu in bulk and in joints during isothermal aging", International Journal of Minerals, Metallurgy, and Materials, vol. 17, (2010), pp. 453-458.
40. R. Wrona and Z. Drozd, "Calculation of BGA contact resistance by using the contacts volume method", IEEE Proc. 31st International Spring Seminar on Electronics Technology, 2008, pp. 37-40.
42. A. Yeo, W. F. Lam and C. Lee, "Development of Novel Joint Resistance Modeling Technique for Flip Chip Interconnection Systems", Proc. 31th IEEE/CPMT International Electronics Manufacturing Technology Symposium, 2006, pp. 115-119.
43. Jing Zhang, "Fast Qualification of Solder Reliability in Solid-State Lighting System", Dissertation, TU Delft, 2015.
44. D. Pleasant, White Paper No.2, LXI Triggering, Revision 1.0, December 1st, 2005.

6 Diskussion

6.1 Abscheidung des RMS und Oberflächenmorphologien

6.1.1 Analysemethodik und Ergebnisse

Um die Wechselwirkung zwischen verschiedenen Oberflächenmorphologien keramischer LTCC-Substrate und der Struktur sowie den Eigenschaften abgeschiedener RMS zu untersuchen, wurden in Paper 1 und 3 die Oberflächen von LTCC-Substraten vor der Abscheidung des RMS mit verschiedenen Methoden modifiziert. Während bei manchen Proben die Rauheit mittels CMP reduziert wurde, wurde die Rauheit anderer Proben mit einem Laser gezielt erhöht. Zur Nachbildung mikroelektronischer Verbindungen wurden laserbearbeitete Proben zusätzlich auch mit einer elektrisch leitfähigen Pd/Ag-Metallisierung (5 µm) und einer zusätzlichen Lotschicht (2 µm) versehen. Die Rauheit der resultierenden Oberflächen wurde mit einem LSM bestimmt und anschließend die RMS abgeschieden. Die Morphologie der Schichten wurde im REM analysiert, während die Reaktionseigenschaften (Spitzentemperatur und Reaktionsgeschwindigkeit) nach elektrischer Zündung mit einem Pyrometer und einer Hochgeschwindigkeitskamera bestimmt wurden. Tab. 7 zeigt die ermittelten Werte in Bezug auf den Mittenrauwert R_a [68, 69, P3], während Tab. 8 bei ausgewählten Proben die ermittelten Werte in Bezug zu den Abbott-Parametern Kernrautiefe S_k, reduzierte Spitzenhöhe S_{pk} und reduzierte Talhöhe S_{vk} setzt [68, 69, P1], die weitere Informationen über die Probenoberflächen liefern.

Tabelle 7: Vergleich der Mittenrauwerte, Spitzentemperaturen und Reaktionsgeschwindigkeiten verschiedener Probenkonfigurationen nach unterschiedlicher Oberflächenbehandlung [68, 69, P3].

Probe	**ohne Metallisierung**					**mit Metallisierung**		
	CMP 1	**CMP 2**	**Ref.**	**Laser 1**	**Laser 2**	**Ref.**	**Laser 1**	**Laser 2**
Mittenrauwert R_a in nm	105	257	390	572	873	525	537	773
Spitzentemperatur in °C	1067	1062	1092	811	803	854	847	739
Reaktionsgeschwindigkeit in m/s	5,1	4,7	5,1	3,7	2,9	3,7	2,8	2,2

Tabelle 8: Vergleich der Abbott-Parameter Kernrautiefe, reduzierter Spitzenhöhe, reduzierter Talhöhe, Spitzentemperatur und Reaktionsgeschwindigkeit verschiedener Probenkonfigurationen nach unterschiedlicher Oberflächenbehandlung [68, 69, P1].

Probe	**Referenz**	**Laser**	**Laser + Pd/Ag**	**Laser + Pd/Ag + Sn**
Kernrautiefe S_k in µm	1,4097	1,9667	2,8483	2,9521
reduzierte Spitzenhöhe S_{pk} in µm	0,6138	0,8175	1,1915	1,5055
reduzierte Talhöhe S_{vk} in µm	0,5187	0,6621	1,0783	1,0375
Spitzentemperatur in °C	1092	803	739	838
Reaktionsgeschwindigkeit in m/s	5,0	2,9	2,2	2,4

Abb. 12 zeigt REM-Aufnahmen mit kleiner und großer Vergrößerung der unbearbeiteten Probe, Abb. 13 nach Laserablation, Abb. 14 nach Laserablation mit Pd/Ag-Metallisierung und Abb. 15 nach Laserablation mit Pd/Ag-Metallisierung und Lotschicht. Von den Proben nach CMP wurden keine Querschliffe angefertigt. Die Auswirkungen der verschiedenen Rauheiten auf die abgeschiedenen RMS geht aus diesen Abbildungen deutlich hervor.

Auf dem unbearbeiteten LTCC-Substrat mit einer Rauheit von 390 nm (Abb. 12) bildet das abgeschiedene RMS die Topologie des Substrats nahezu gleichmäßig nach. Die einzelnen Schichten sind in der gesamten Fläche unterbrechungsfrei miteinander verbunden. Nach der Zündung wurde eine Spitzentemperatur von 1092 °C und eine Reaktionsgeschwindigkeit von 5,1 m/s gemessen. CMP reduziert die Rauheit auf 105–257 nm, ohne die Reaktionseigenschaften signifikant zu beeinflussen (1062–1067 °C und 4,7–5,1 m/s).

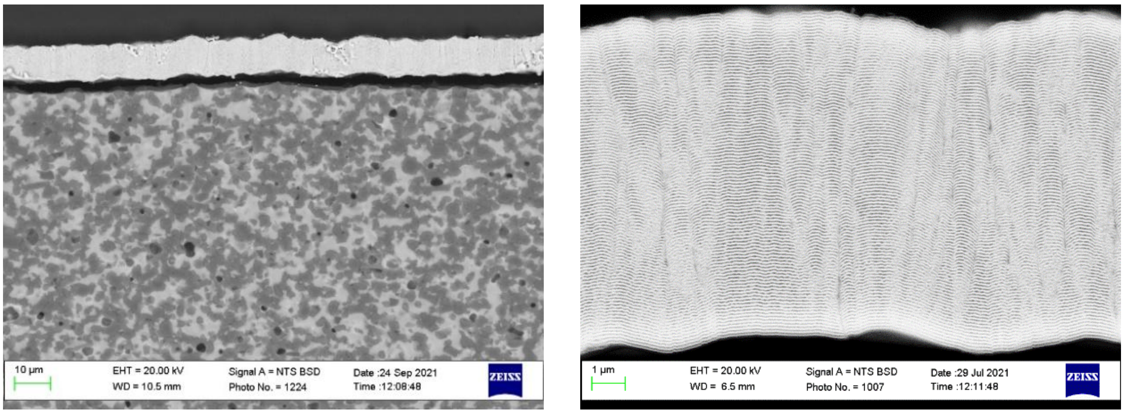

(a) **(b)**

Abbildung 12: REM-Aufnahmen im BSE-Modus eines RMS, das auf ein unbearbeitetes LTCC-Substrat abgeschieden wurde [P1]. Die Morphologie des RMS imitiert die Oberfläche der LTCC nahezu vollständig ohne Unterbrechungen in der Struktur. Vergrößerung: (a) 2000x, (b) 18 500x.

Signifikante Änderungen ergeben sich durch eine Erhöhung der Rauheit infolge der Laserablation, die zu einem lokalen Materialabtrag führt (vgl. Abb. 13). Dadurch entstehen Höhengradienten auf dem Substrat, die die Abscheidung eines durchgängig verbundenen RMS verhindern. Stattdessen wird das RMS in einzelne säulen-förmige Bereiche separiert, die nicht vollständig miteinander verbunden sind. Durch die Laserablation wurden die Spitzentemperaturen auf 803–811 °C und die Reaktionsgeschwindigkeiten auf 2,9–3,7 m/s reduziert.

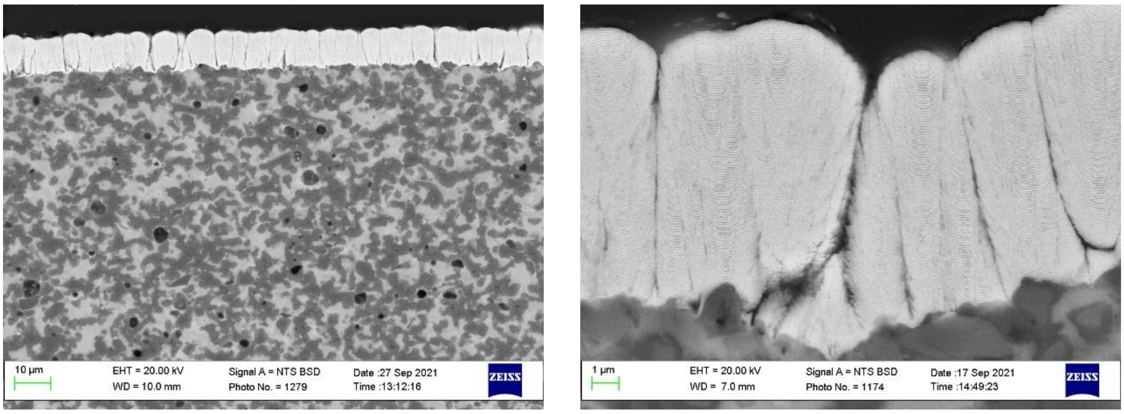

(a) **(b)**

Abbildung 13: REM-Aufnahmen im BSE-Modus eines RMS, das auf ein laserbearbeitetes LTCC-Substrat abgeschieden wurde [P1]. Durch den Materialabtrag auf dem Substrat entstehen Höhengradienten, die die Abscheidung eines durchgängig verbundenen RMS verhindern. Stattdessen bilden sich einzelne Bereiche, die durch kleine Lücken voneinander getrennt sind. Vergrößerung: (a) 2000x, (b) 15 000x.

Ähnliche Effekte konnten durch das Hinzufügen einer Pd/Ag-Metallisierung (vgl. Abb. 14) und einer zusätzlichen Lotschicht (vgl. Abb. 15) beobachtet werden. Mit Spitzentemperaturen von 739–854 °C und Reaktionsgeschwindigkeiten von 2,2–3,7 m/s liegen die Werte bei diesen Proben unter denen der anderen Varianten.

Während das RMS bei unbearbeiteten LTCC-Substraten zu einer nahezu vollständigen Ablösung vom LTCC-Substrat tendiert, konnte bei den laserbearbeiteten Proben eine verbesserte Adhäsion beobachtet werden.

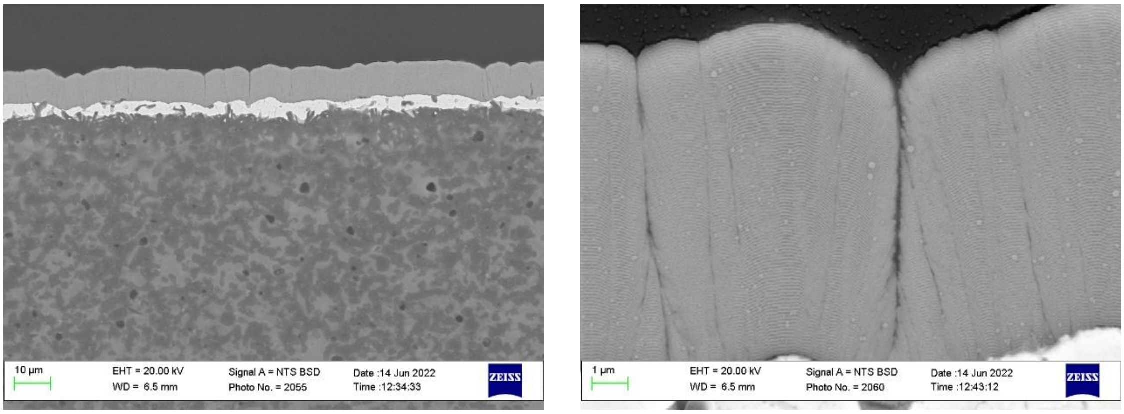

(a) **(b)**

Abbildung 14: REM-Aufnahmen im BSE-Modus eines RMS, das auf ein laserbearbeitetes LTCC-Substrat mit Pd/Ag-Metallisierung abgeschieden wurde [P1]. Die Metallisierung bewirkt bereits eine Erhöhung der Rauheit, die durch die vorherige Laserablation weiter gesteigert wird. Wie zuvor ist das RMS in einzelne Bereiche getrennt. Vergrößerung: (a) 2000x, (b) 20 000x.

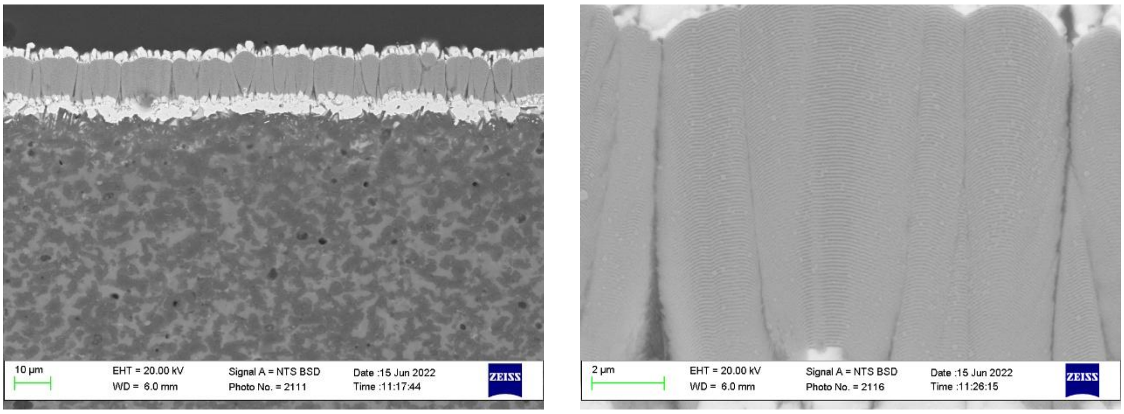

(a) **(b)**

Abbildung 15: REM-Aufnahmen im BSE-Modus eines RMS, das auf ein laserbearbeitetes LTCC-Substrat mit Pd/Ag-Metallisierung und zusätzlicher Lotschicht abgeschieden wurde [P1]. Die Morphologie des RMS imitiert die Oberfläche der LTCC nahezu vollständig. Es können keine Unterbrechungen in der Struktur gefunden werden. Vergrößerung: (a) 2000x, (b) 20 000x.

6.1.2 Schlussfolgerungen

1. Die Morphologie der abgeschiedenen RMS variiert stark in Abhängigkeit von der Substratstrukturierung. Auf unbearbeiteten Oberflächen konnte die Abscheidung kontinuierlicher Schichten beobachtet werden (siehe Abb. 12), die die Topographie des Substrats nahezu vollständig nachbilden. Es ist anzunehmen, dass bei mittels CMP bearbeiteten Oberflächen identische Effekte beobachtet werden können. Im Gegensatz dazu bilden sich auf laserbearbeiteten Substraten diskontinuierliche, unterbrochene Schichten (siehe Abb. 13, 14 und 15). Diese führen zu unterschiedlichen Reaktionseigenschaften und erhöhen die Adhäsion des RMS auf dem LTCC-Substrat durch eine lokale Verankerung. Die verbesserte Adhäsion erhöht zudem die effektive Kontaktfläche zwischen den einzelnen Schichten, was sich positiv auf die thermischen, elektrischen und mechanischen Eigenschaften der Verbindung auswirkt. Ein optimierter Fügedruck (vgl. Kapitel 6.3 und 6.4) kann diese Eigenschaften weiter verbessern.
2. Die Oberflächenmorphologie der LTCC-Substrate hat einen signifikanten Einfluss auf die Reaktionseigenschaften der abgeschiedenen RMS und es besteht ein Zusammenhang zwischen Spitzentemperatur und Reaktionsgeschwindigkeit. Die unbearbeiteten und die mittels CMP bearbeiteten LTCC-Substrate weisen die höchsten Spitzentemperaturen und Reaktionsgeschwindigkeiten aller untersuchten Konfigurationen auf. Die in beiden Varianten vollständig miteinander verbundenen Schichten des RMS ermöglichen ein ungebremstes Fortschreiten der Reaktion. Im Gegensatz dazu führt die Laserablation zur Bildung einzelner voneinander getrennter Bereiche. An jeder Kante pausiert die Reaktion für kurze Zeit, ehe die freigesetzte Wärme die Zündung im Nachbarsegment wieder initiiert. Diese verringerte Spitzentemperatur und Reaktionsgeschwindigkeit wirken sich positiv auf den Fügeprozess aus, da das LTCC-Material so mehr Zeit hat, die entstehende Wärme abzuleiten, ohne lokal zu überhitzen.

6.2 Simulationen

6.2.1 Modellierung und Ergebnisse

Die ersten Simulationen zielten darauf ab, ein Modell mit integrierten Pt-Sensoren zur Messung von Reaktionsgeschwindigkeit und Temperatur zu entwickeln, sowie den Einfluss einer zusätzlichen Sn-Schicht auf die entstehenden Temperaturen zu untersuchen (vgl. Paper 2). Hierzu wurde ein Modell bestehend aus einer LTCC (570 µm), einer Isolationsschicht (35 µm) und einem RMS (30 µm) verwendet, das mit einem zweiten Modell mit einer zusätzlichen Sn-Schicht (200 µm) und einem Si-Chip (400 µm) verglichen wurde (siehe Abb. 16). Als Reaktionsgeschwindigkeit wurde 1 m/s gewählt. In die LTCC wurden in horizontaler Anordnung mit 1 mm Abstand insgesamt drei Pt-Sensoren, je 300 µm lang und 10 µm dick, integriert.

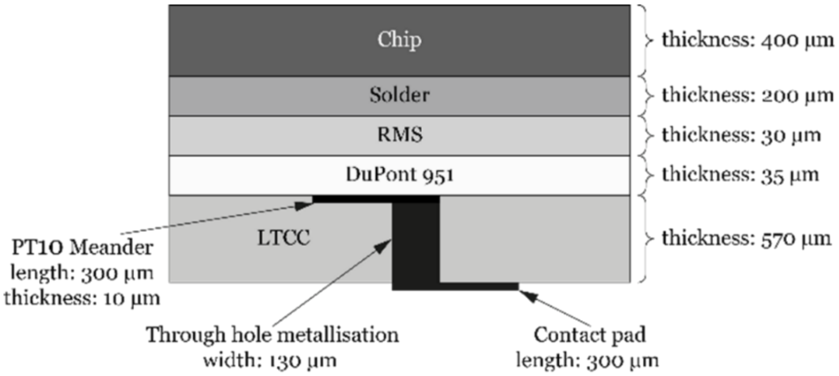

Abbildung 16: Skizzierter Querschnitt des Modells mit integrierten Pt-Sensoren [P2].

Abb. 17 zeigt die zeitliche Temperaturentwicklung des Modells mit Si-Chip und Sn, Abb. 18 die des Modells ohne Si-Chip und Sn. Gezeigt werden jeweils die Temperaturen an den Pt-Sensoren, sowie ein Vergleich der Temperaturen am zweiten Pt-Sensor mit denen innerhalb des RMS und – falls vorhanden – der Sn-Schicht. Im Modell mit Sn erreichen die Pt-Sensoren mit zeitlichem Verzug eine Maximaltemperatur von knapp unter 100 °C, während im RMS ca. 150 °C und in der Sn-Schicht ca. 280 °C erreicht werden. Im Modell ohne Sn erreichen die Pt-Sensoren eine Maximaltemperatur von 250 °C, während im RMS eine Temperatur von rund 430 °C erreicht wird.

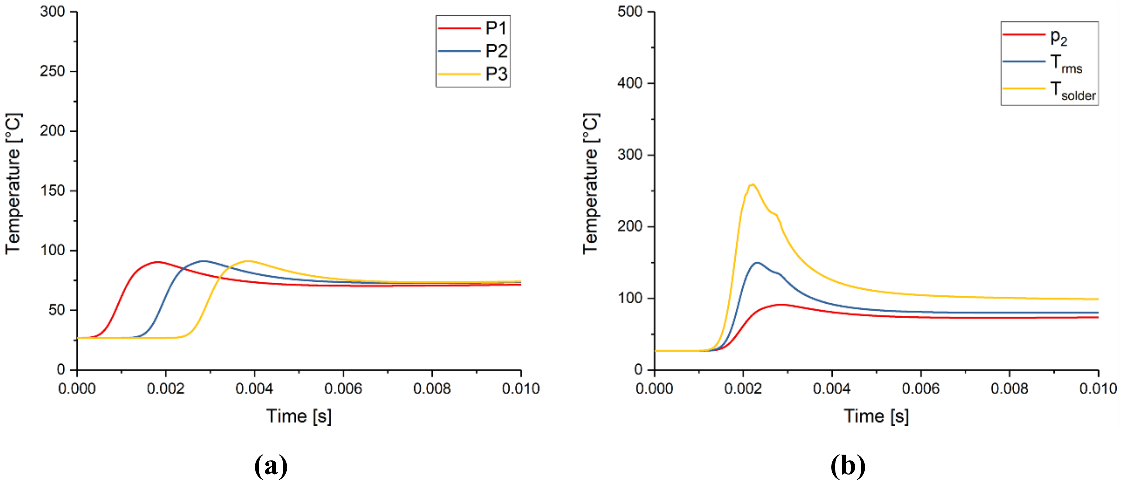

Abbildung 17: Zeit-Temperatur-Diagramme des Modells aus Si-Chip, Sn-Schicht, RMS, Isolationsschicht und LTCC mit integrierten Pt-Sensoren [P2]. (a) Vergleich der Temperaturen der drei Pt-Sensoren. (b) Vergleich der Temperaturen der Sn- und RMS-Schicht mit Pt-Sensor 2.

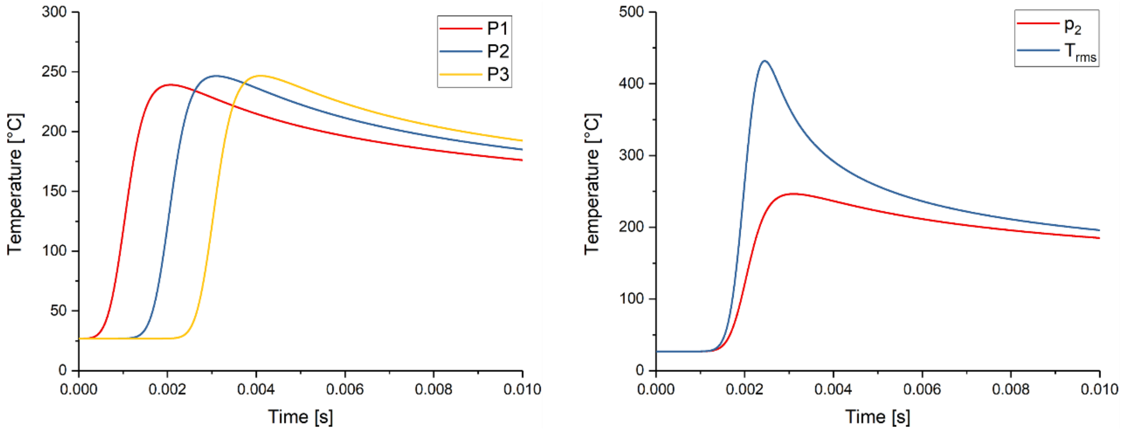

(a) **(b)**

Abbildung 18: Zeit-Temperatur-Diagramme des Modells aus RMS, Isolationsschicht und LTCC mit integrierten Pt-Sensoren [P2]. (a) Vergleich der Temperaturen der drei Pt-Sensoren. (b) Vergleich der Temperaturen der Sn- und RMS-Schicht mit Pt-Sensor 2.

Im nächsten Schritt wurde das Modell um eine dreidimensionale Sensor-Anordnung mit insgesamt 9 Sensoren erweitert (vgl. Paper 3 und [67]). Die Modelle entsprechen im Wesentlichen dem vorherigen, jedoch wurde die Dicke der LTCC auf 825 µm und in [67] zusätzlich die Dicke des RMS auf 40 µm angepasst. Simulationen wurden mit und ohne Si-Chip und Sn-Schicht bei einer Reaktionsgeschwindigkeit von 1 m/s [P3, 67] und 10 m/s [67] durchgeführt. Aufgrund der unterschiedlichen Dicken der verwendeten RMS werden zur besseren Vergleichbarkeit die Ergebnisse aus [67] vorgestellt.

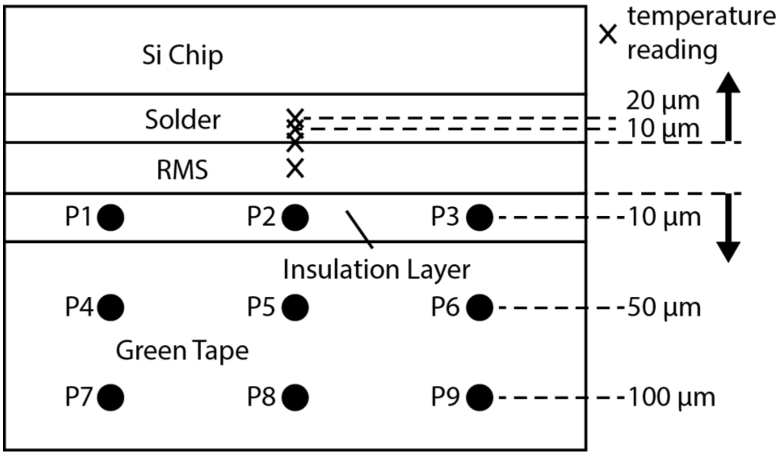

Abbildung 19: Querschnitt des Modells mit dreidimensionaler Sensor-Anordnung [P3]. © 2023 IEEE

Abb. 20 und 21 zeigen die zeitliche Temperaturentwicklung der beiden Modelle mit der dreidimensionalen Sensor-Anordnung für Reaktionsgeschwindigkeiten von 1 m/s und 10 m/s [67]. Wie zuvor lässt sich ein signifikanter Temperaturabfall beobachten, wenn dem

Modell ein Si-Chip und eine Sn-Schicht hinzugefügt werden. Die Temperatur fällt in vertikaler Richtung mit steigendem Abstand zum RMS in allen Fällen sehr stark ab.

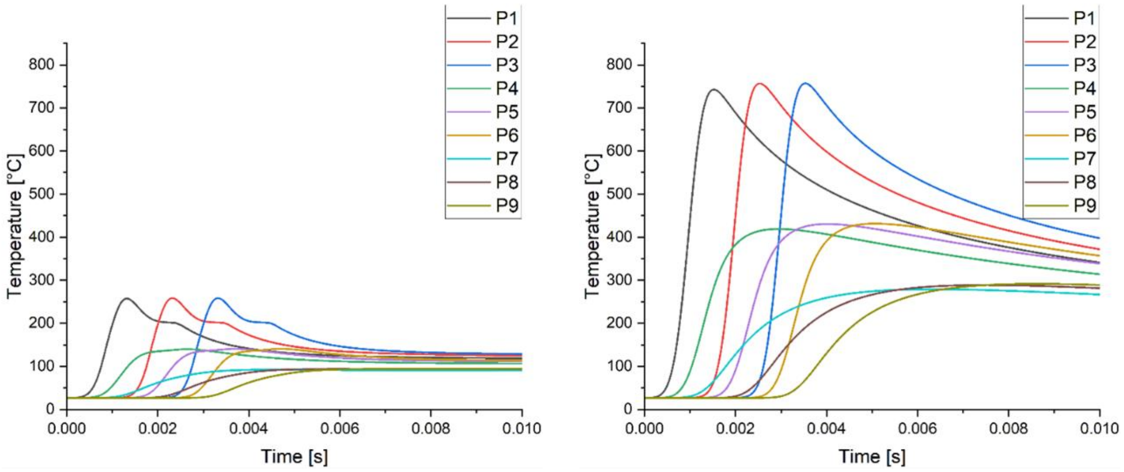

(a) **(b)**

Abbildung 20: Zeit-Temperatur-Diagramme des erweiterten Modells (a) mit und (b) ohne Si-Chip und Lotschicht für eine Reaktionsgeschwindigkeit von 1 m/s [67]. © 2024 IEEE

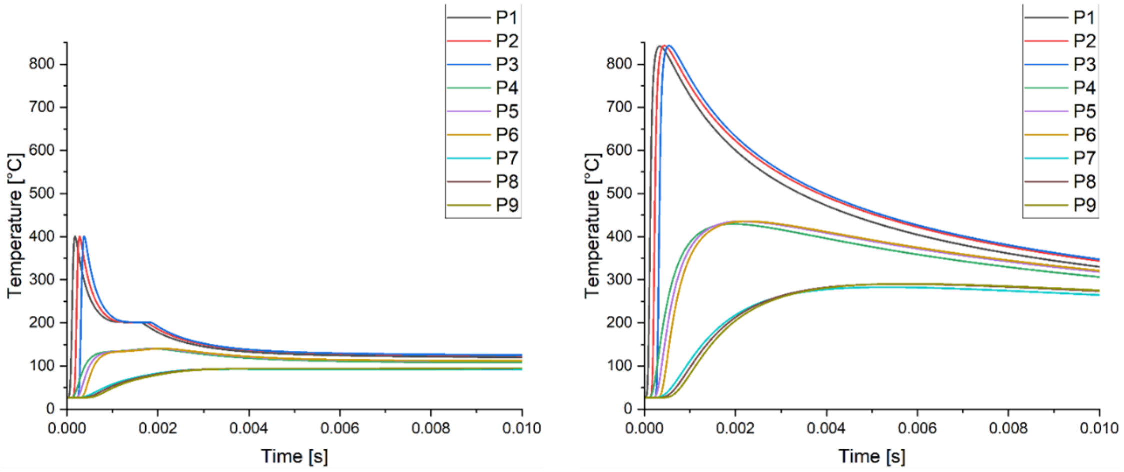

(a) **(b)**

Abbildung 21: Zeit-Temperatur-Diagramme des erweiterten Modells (a) mit und (b) ohne Si-Chip und Sn-Schicht für eine Reaktionsgeschwindigkeit von 10 m/s [67]. © 2024 IEEE

Ein anderer Ansatz zur Temperaturmessung, der in Paper 4 simuliert wurde, besteht in der Nutzung von in die LTCC integrierten Thermopaaren. Das verwendete Modell besteht aus einem RMS (10 µm), einer Sn-Schicht (2 µm), einer Ag-Metallisierung (2 µm), einer Isolierschicht (9 µm) mit Ag-Pad (7 µm) sowie einer LTCC (840 µm), in der die beiden Schenkel eines Thermopaares mit einem Durchmesser von 300 µm eingebettet sind (siehe Abb. 22).

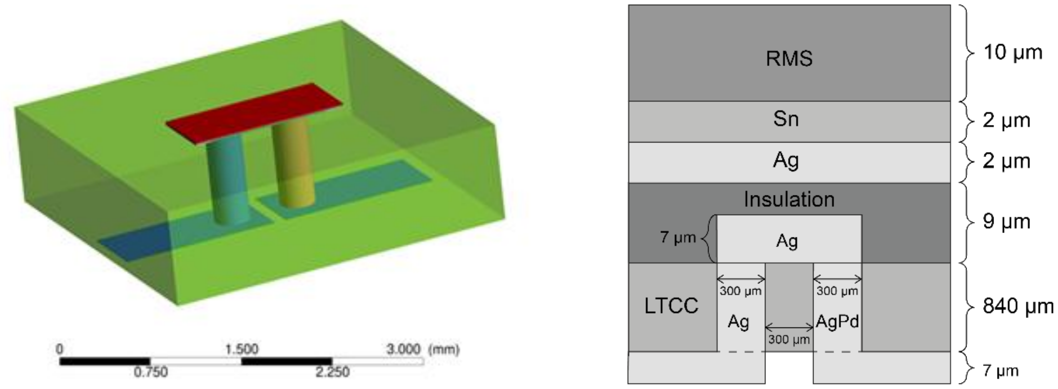

(a) (b)

Abbildung 22: (a) 3D-Ansicht und (b) skizzierter Querschnitt des CFD-Modells mit eingebettetem Thermopaar [P4]. © 2022 IEEE

Aufgrund des Seebeck-Effekts (siehe Kapitel 4.1.6) entsteht durch die exotherme Reaktion des RMS an der Kontaktstelle beider Schenkel eine elektrische Spannung, die über nach außen geführte Kontakte gemessen werden kann. Abb. 23 zeigt das Zeit-Temperatur-Diagramm von RMS, Sn-Schicht und Ag-Metallisierung sowie das Zeit-Spannungs-Diagramm. Die maximal entstehende Spannung von ca. 3,5 mV wird nach ca. 0,3 ms erreicht.

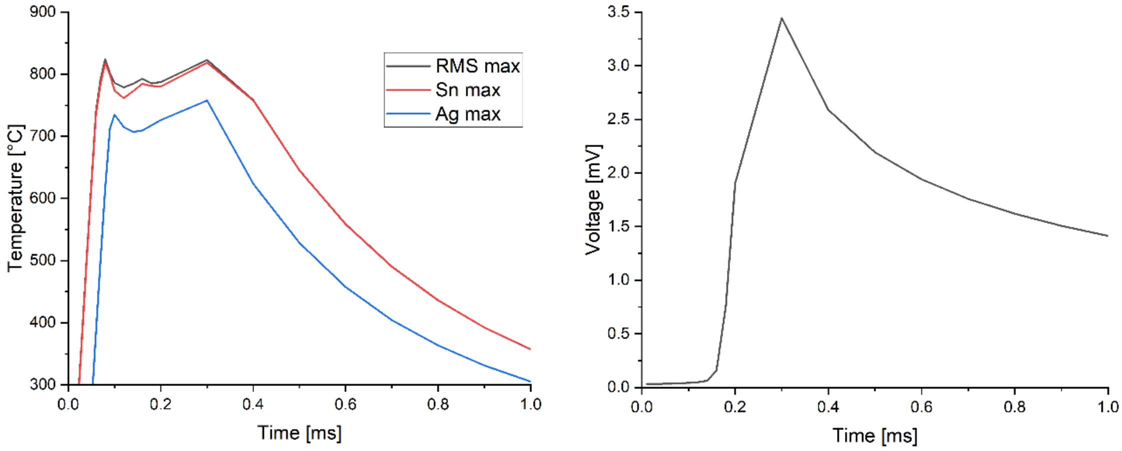

(a) (b)

Abbildung 23: (a) Zeit-Temperatur-Diagramm von RMS, Sn-Schicht und Ag-Metallisierung [P4]. (b) Aufgrund des Seebeck-Effekts induzierte elektrische Spannung zwischen den beiden Schenkeln des Thermopaars [P4]. © 2022 IEEE

Zur Validierung der PDF der Simulationen (siehe Kapitel 4.2) wurde die zeitliche Temperaturentwicklung mit den experimentell ermittelten Temperaturverläufen einer laserbearbeiteten Probe mit Pd/Ag-Metallisierung verglichen (vgl. Paper 5). Hierzu wurde ein einfaches Modell, bestehend aus einem RMS (10 µm), einer Isolationsschicht (35 µm) und einer LTCC (825 µm), verwendet (siehe Abb. 24).

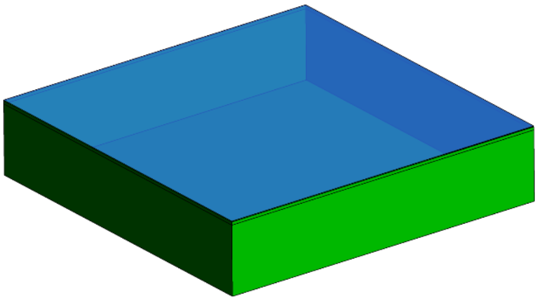

Abbildung 24: Skizze des Modells, das für einen Vergleich mit den experimentellen Daten verwendet wurde [P5]. © 2023 IEEE

Abb. 25 zeigt einen Vergleich der zeitlichen Temperaturverläufe aus Simulation und Experiment in einem gemeinsamen Zeit-Temperatur-Diagramm. Nach Korrektur eines zeitlichen Offsets von $t = -0{,}112\ ms$ ergibt sich im Bereich zwischen 0,75 ms und 2 ms ein Bestimmtheitsmaß von $R^2 > 0{,}99$. Dies deutet auf eine sehr hohe Übereinstimmung zwischen Modell und Messung hin.

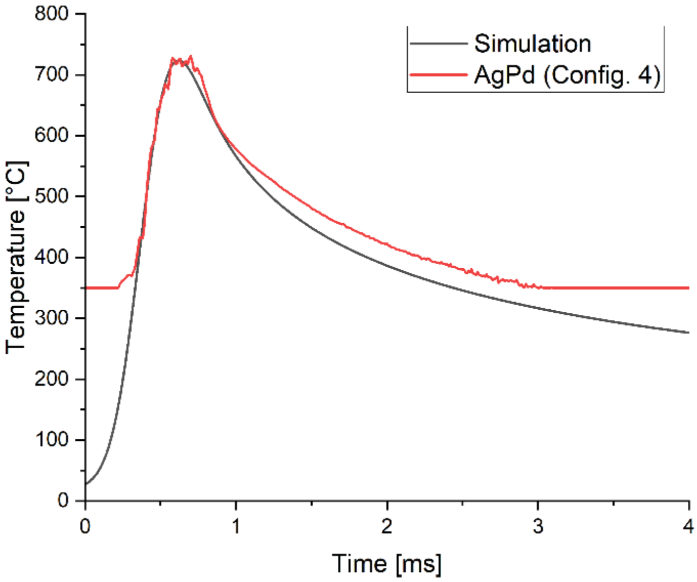

Abbildung 25: Vergleich der zeitlichen Temperaturverläufe aus Simulation und Experiment (laserbearbeitete Probe mit Pd/Ag-Metallisierung) [P5]. © 2023 IEEE

Ein Vergleich zwischen einer reaktiven Fügung von LTCC- und Si-Substraten wurde in Paper 6 hinsichtlich der maximalen Temperatur sowie des Flüssigphasenanteils im Lot durchgeführt. Das Modell besteht aus zwei der jeweiligen Substrate (800 µm), einer Ag-Metallisierung (5 µm), einer Lotschicht (5 µm) sowie einem RMS (10 µm), wie in Abb. 26 dargestellt.

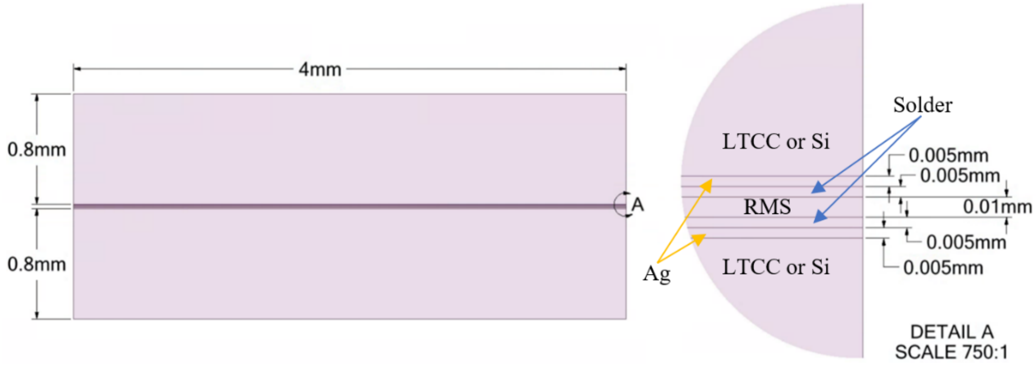

Abbildung 26: Skizze des Modells, das für den Vergleich zwischen einer reaktiven Fügung mit LTCC- und Si-Substraten verwendet wurde [P6].

Abb. 27 zeigt die zeitlichen Temperaturverläufe des LTCC/LTCC- und des Si/Si-Modells in einem gemeinsamen Zeit-Temperatur-Diagramm. Die Maximaltemperatur im RMS und in der Lotschicht erreicht beim LTCC-Stapel ca. 500 °C und ist damit rund doppelt so hoch wie beim Si-Stapel. Der horizontal verlaufende Bereich zwischen 1,2 ms und 1,5 ms des LTCC-Stapels beschreibt den Zeitraum der Phasenumwandlung, der beim Si-Stapel in einem Bruchteil der Zeit abläuft.

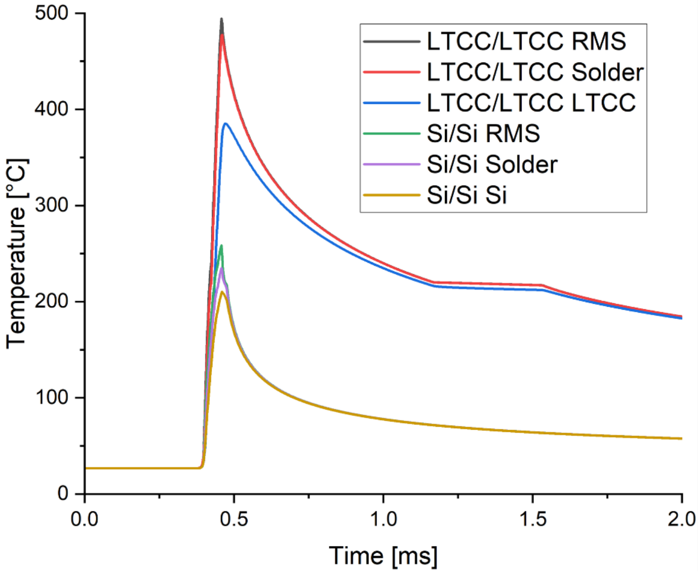

Abbildung 27: Vergleich der zeitlichen Temperaturverläufe des LTCC/LTCC- und des Si/Si-Modells [P6]. Während die Maximaltemperatur beim Si-Stapel bei ca. 250 °C liegt, liegt sie beim LTCC-Stapel aufgrund der schlechteren Wärmeleitfähigkeit bei ca. 500 °C.

Abb. 28 zeigt den zeitlichen Verlauf des Flüssigphasenanteils des Lots für den (a) LTCC- und (b) Si-Stapel. Beim Si-Stapel befindet sich zu jedem Zeitpunkt nur ein kleiner Teil des Lots in der flüssigen Phase, und das Lot ist nach 0,6 ms vollständig erstarrt. Im Gegensatz dazu befindet sich beim LTCC-Stapel zu diesem Zeitpunkt das komplette

Lot in der flüssigen Phase, und der Erstarrungsprozess ist selbst nach 1,2 ms noch nicht vollständig abgeschlossen.

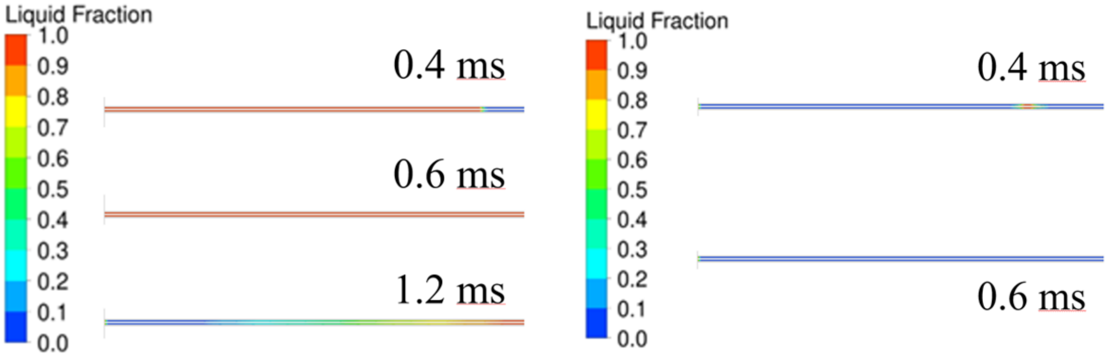

(a) (b)

Abbildung 28: Simulierter Flüssigphasenanteil des Lots beim Modell aus (a) LTCC/LTCC und (b) Si/Si zu verschiedenen Zeitpunkten [P6]. Während sich beim Si/Si-Stapel zu jeder Zeit nur ein kleiner Bereich des Lots in der flüssigen Phase befindet, erstreckt sich dieser Bereich beim LTCC/LTCC-Stapel nach 0,6 ms über das gesamte Modell.

6.2.2 Schlussfolgerungen

1. Die exotherme Reaktion eines RMS lässt sich mit CFD-Simulationen hinsichtlich ihrer Reaktionsgeschwindigkeit und Temperaturverteilung zuverlässig modellieren. Obwohl in den verwendeten Modellen vereinfachende Annahmen, wie die Vernachlässigung der Oberflächenrauheit der Substrate, getroffen wurden, stellen sie durch die Berücksichtigung physikalischer Effekte wie latenter Wärme und Phasenumwandlungen eine deutliche Weiterentwicklung gegenüber früheren Arbeiten dar [18, 70, 71]. Ein Vergleich der Wärmefreisetzung über die modellierte PDF mit experimentellen Messungen ergibt, dass diese Erweiterungen zu realistischeren Temperaturverläufen führen, die generell niedriger sind als bei früheren Modellen.
2. Es gibt eine starke Beziehung zwischen Reaktionsgeschwindigkeit und Maximaltemperatur. Eine Erhöhung der Reaktionsgeschwindigkeit von 1 m/s auf 10 m/s führt zu einem deutlichen Temperaturanstieg in den einzelnen Schichten – die Temperatur steigt im RMS um über 200 % auf ca. 820 °C an. Diese Temperatur liegt deutlich über den werkstofflichen Grenzen der eingesetzten Pd/Ag-Metallisierung, die für maximale Löttemperaturen von 230–360 °C und kurze Lötzeiten von wenigen Sekunden ausgelegt ist (siehe Kapitel 6.4). Daraus ergibt sich die Notwendigkeit einer gezielten Kontrolle der Reaktionseigenschaften.

3. Die Simulationen zeigen, dass Lotschichten ein wirksames Mittel zur Steuerung der Reaktionsgeschwindigkeit und damit der Temperaturentwicklung darstellen. Durch eine geeignete Wahl der Lotmenge kann die Wärmeabfuhr beeinflusst werden, wodurch die Reaktion gezielt gesteuert werden kann. Ähnliche Beobachtungen wurden in der Literatur berichtet [18, 72, 73].
4. In das LTCC-Material eingebettete Temperatursensoren ermöglichen eine Messung der Reaktionsgeschwindigkeit, die Messung der Maximaltemperatur ist jedoch aufgrund der Lotschichten und der latenten Wärme schwierig. Horizontal angeordnete Sensoren mit gleichem Abstand zum RMS werden mit nahezu gleichem zeitlichem Verzug von der während der exothermen Reaktion freigesetzten Wärme erreicht. Diese Signaldifferenz erlaubt einen Rückschluss auf die Reaktionsgeschwindigkeit. Da die Temperatur in vertikaler Richtung sehr stark und schnell abfällt, und zudem in großem Maße von der Dicke der Lotschicht abhängt, kann die Maximaltemperatur nur grob abgeschätzt werden. Die Nutzung von Thermopaaren [74, 75] im Gegensatz zu herkömmlichen Pt-Sensoren könnte hier weitere Fortschritte liefern. Allerdings ist hierbei zu beachten, dass die durch ein einzelnes Thermopaar generierte Spannung im niedrigen mV-Bereich liegt, was eine entsprechend stabile Auswerteschaltung erforderlich macht, um ein möglichst unverfälschtes Signal mit wenig Rauschen zu erhalten.

6.3 Fügeversuche

6.3.1 Experimentelle Vorgehensweise und Ergebnisse

In ersten Versuchen wurden LTCC-Proben (10 mm x 10 mm) unter einem Fügedruck von 1,5 MPa mit NanoFoil® (60 µm) sowie abgeschiedenen RMS gefügt. Die REM-Aufnahmen in Abb. 29 und 30 zeigen jeweils (a) eine bessere und (b) eine schlechtere Fügezone. Auffällig ist, dass die NanoFoil® nach der Zündung eine gleichmäßige Struktur aufweist, während das abgeschiedene RMS durch sein säulenförmiges Erscheinungsbild ein stark fragmentiertes Bruchbild aufweist.

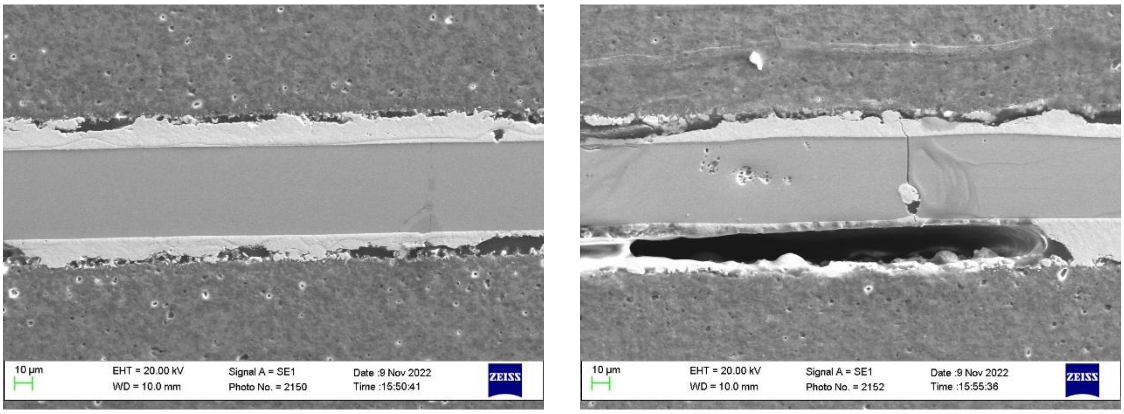

(a) **(b)**

Abbildung 29: REM-Aufnahmen im SE-Modus einer mit NanoFoil® (NF60) realisierten Fügung unter einem Druck von 1,5 MPa. Während die Probe an der Stelle (a) ein gewünschtes Aussehen mit einer gleichen Menge Lot auf beiden Seiten zeigt, hat sich an Stelle (b) die gelötete Metallisierung auf der Unterseite vom LTCC-Substrat abgelöst. Vergrößerung: 1000x.

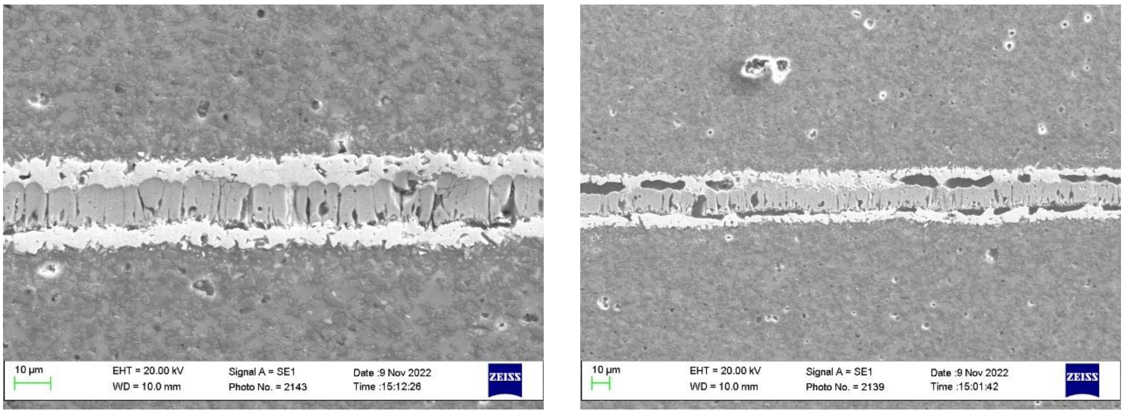

(a) **(b)**

Abbildung 30: REM-Aufnahmen im SE-Moduls einer mit abgeschiedenem RMS realisierten Fügung unter einem Druck von 1,5 MPa. Während die Probe an der Stelle (a) ein gewünschtes Aussehen mit einer gleichmäßigen Lotverteilung auf beiden Seiten zeigt, ist die Verbindung an der Stelle (b) nur unzureichend mit vielen Lücken. Vergrößerung: (a) 2000x, (b) 1000x.

Bei den besseren Fügungen (Abb. 29a und 30a) ist auf beiden Seiten der RMS eine gleichmäßige Benetzung des Lots auf der Metallisierung erkennbar. Bei den schlechteren Fügungen zeigen sich Ablöseeffekte der Metallisierung (Abb. 29b) oder Lücken zwischen RMS und Metallisierung (Abb. 30b). Es ist anzunehmen, dass die Ablösung der Metallisierung eine Folge der Kombination aus schlechter Wärmeleitfähigkeit des LTCC-Materials und der hohen Temperatur der reaktiven Folie ist. Beim abgeschiedenen RMS konnte keine solche Ablösung beobachtet werden – stattdessen führt die stellenweise schlechte Benetzung des Lots aufgrund dessen Oberflächenspannung zu lokalen Lotansammlungen. Die während der exothermen Reaktion auftretende Schrumpfung des Al/Ni-RMS um bis zu 12 %, die durch Phasenumwandlung und die damit einhergehende Neuordnung der

Atomstruktur hervorgerufen wird [25], kann durch den geringen Fügedruck nicht kompensiert werden.

In Paper 7 wurden weitere Fügeversuche mit NanoFoil® (40 µm) auf kleineren LTCC-Substraten (3 mm x 3 mm) durchgeführt, um höhere Fügedrücke von 2–44 MPa zu erzielen. Die Ergebnisse zeigen, dass ein geringer Druck zu schlechter Benetzung und somit zu schlechter Adhäsion führt, und dass ein zu hoher Druck zu einer kompletten Vermischung von Metallisierung und Lot führt. Es lässt sich annehmen, dass ein optimaler Druckbereich für reaktive Fügungen existiert. Daher wurden weitere Untersuchungen durchgeführt und die Ergebnisse in Paper 8 publiziert. Während Abb. 31 die aus mehreren Einzelbildern zusammengesetzten Gesamtbilder von mit NanoFoil® gefügten Proben mit vollflächiger Pd/Ag-Metallisierung unter Fügedrücken von 2 MPa, 11 MPa, 22 MPa und 44 MPa zeigt, zeigt Abb. 33 Proben mit strukturierter Pd/Ag-Metallisierung – ähnlich den Kontakten in mikroelektronischen Schaltungen. Abb. 32 und 34 zeigen Aufnahmen beider Probenarten mit höherer Vergrößerung.

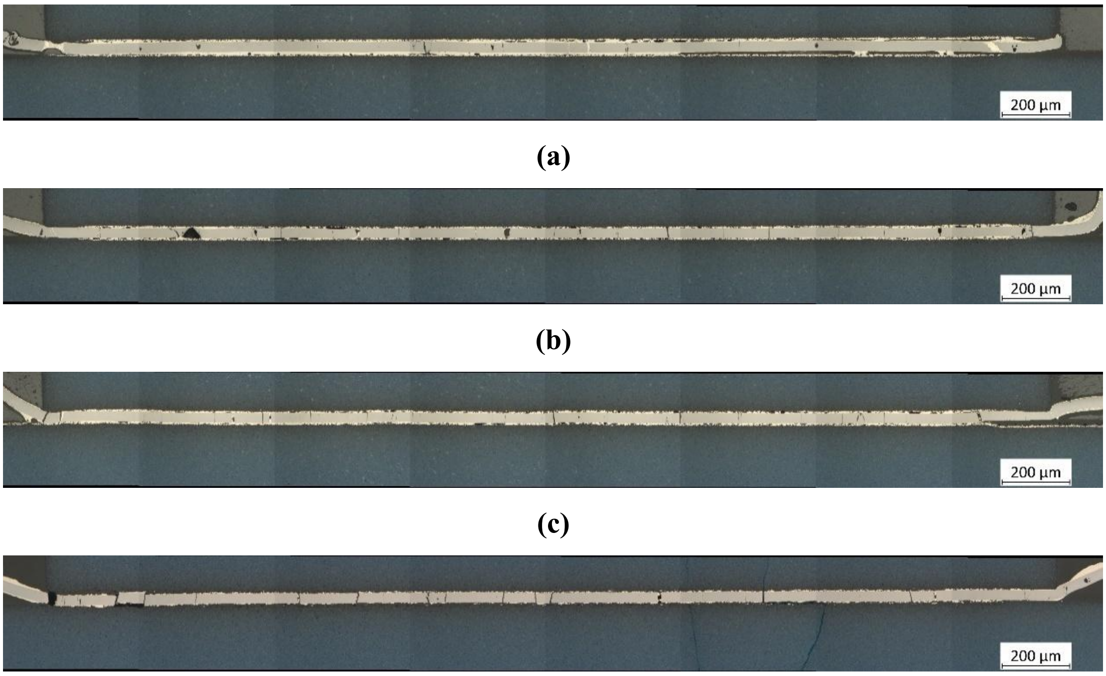

(d)

Abbildung 31: Aus mehreren Einzelbildern zusammengesetzte Gesamtbilder von Proben mit vollflächiger Pd/Ag-Metallisierung, die mit NanoFoil® unter einem Fügedruck von (a) 2 MPa, (b) 11 MPa, (c) 22 MPa und (d) 44 MPa gefügt wurden [P8]. Bei 2 MPa zeigen sich viele Lücken und eine schlechte Adhäsion zwischen Metallisierung und Lot, bei 44 MPa zeigen sich viele Brüche in der Reaktivschicht und auch im LTCC-Material. Bei 22 MPa sieht die Fügezone insgesamt am ordentlichsten aus. Vergrößerung: 20x.

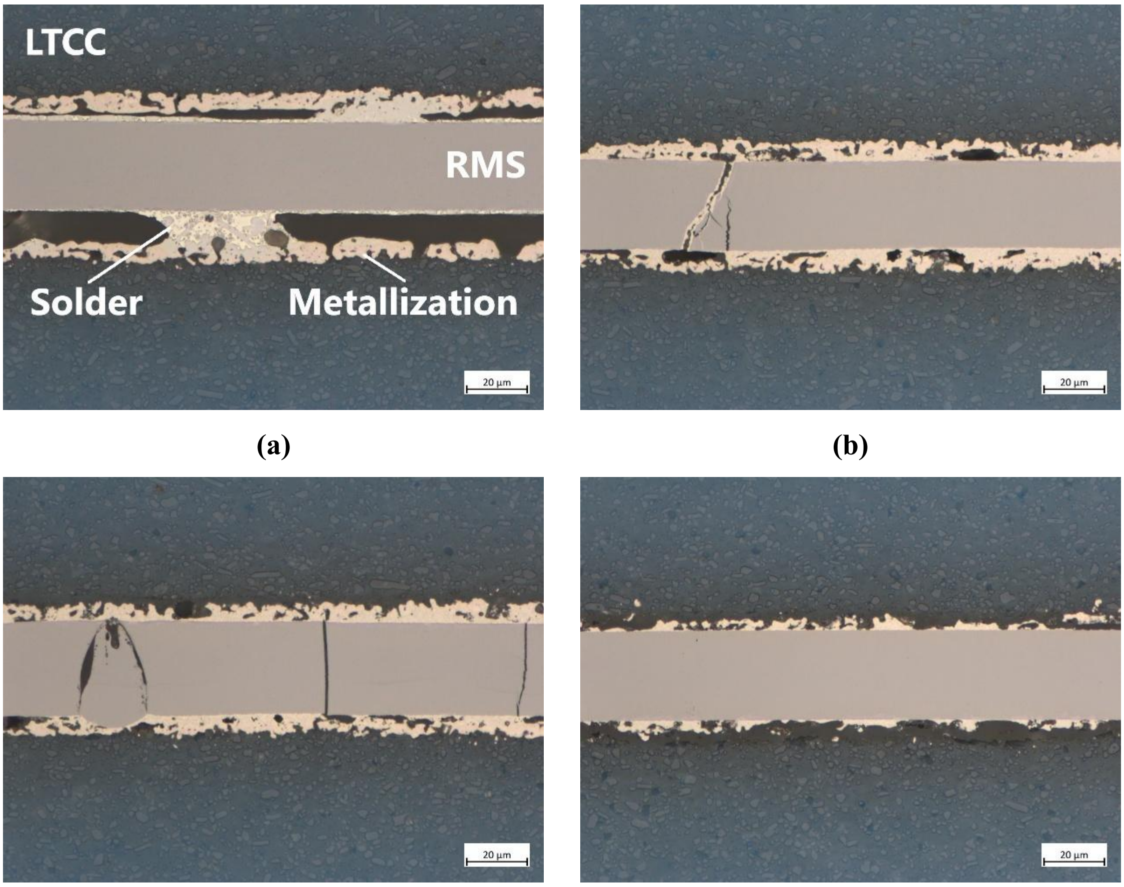

(a) (b)

(c) (d)

Abbildung 32: Detailliertere Aufnahmen der Proben aus Abb. 31, die unter einem Fügedruck von (a) 2 MPa, (b) 11 MPa, (c) 22 MPa und (d) 44 MPa mit NanoFoil® gefügt wurden [P8]. Vergrößerung: 50x.

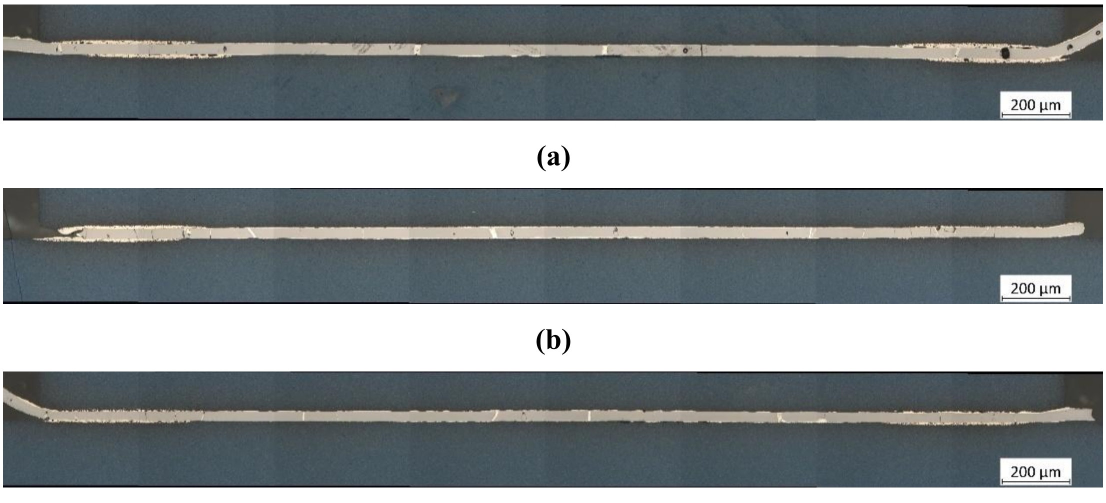

(a)

(b)

(c)

Abbildung 33: Aus mehreren Einzelbildern zusammengesetzte Gesamtbilder von Proben mit strukturierter Pd/Ag-Metallisierung, die mit NanoFoil® unter einem Fügedruck von (a) 20 MPa, (b) 200 MPa und (c) 400 MPa gefügt wurden [P8]. Bei 20 MPa zeigt sich eine annehmbare Fügestelle, während sich die Metallisierung bei 400 MPa aufzulösen beginnt. Vergrößerung: 20x.

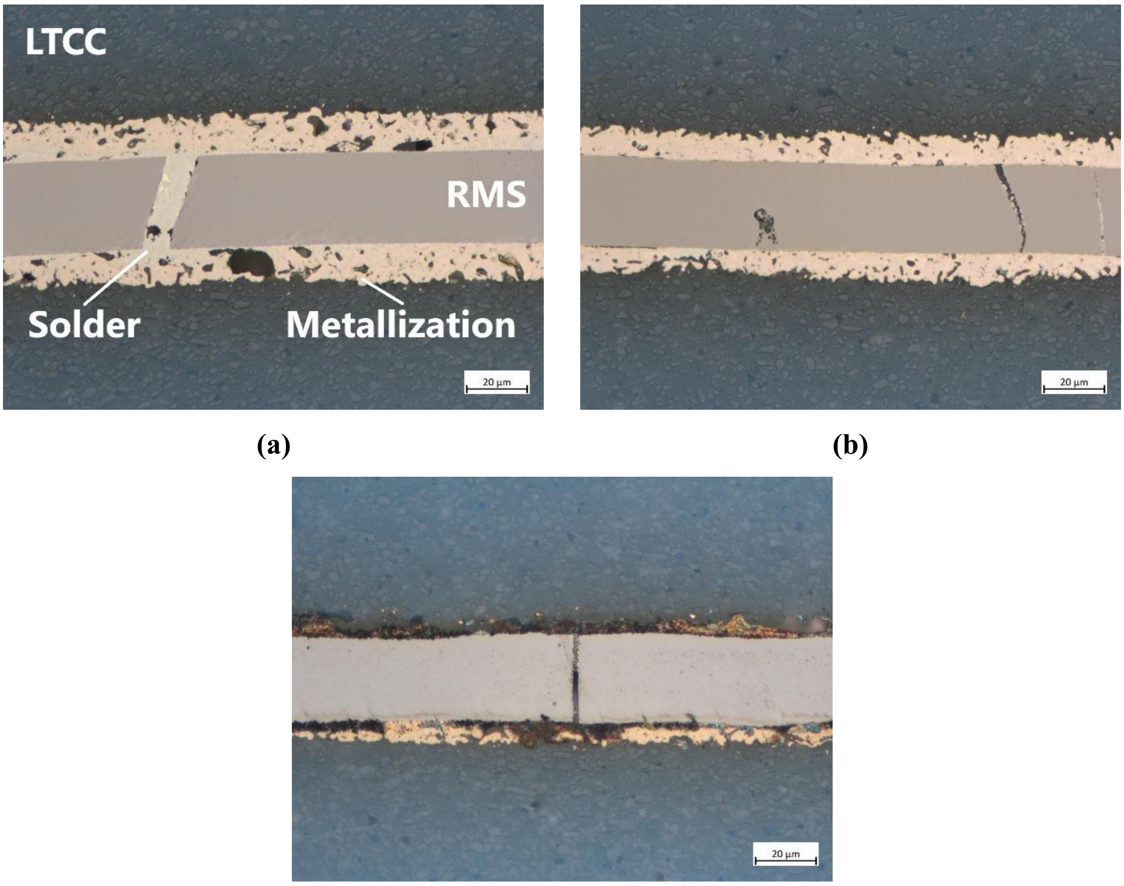

(a) (b)

(c)

Abbildung 34: Detailliertere Aufnahmen der Proben aus Abb. 33, die unter einem Fügedruck von (a) 20 MPa, (b) 200 MPa und (c) 400 MPa mit NanoFoil® gefügt wurden [P8]. Vergrößerung: 50x.

Bei den Proben mit vollflächiger Metallisierung bilden sich bei einem geringen Fügedruck von 2 MPa viele Lücken zwischen Metallisierung und Lot, deren Anzahl mit steigendem Druck abnimmt. Bei leicht höheren Fügedrücken von 11 MPa und 22 MPa erscheint die Zone zwischen RMS und Metallisierung deutlich schmaler. Bei einem hohen Druck von 44 MPa führen hohe thermomechanische Spannungen zu vielen Rissen im RMS und sogar im LTCC-Material. Obwohl die Fügedrücke im Fall der strukturierten Proben deutlich höher sind, entstehen hier weniger Risse und Beschädigungen. Dies lässt sich durch die Tatsache erklären, dass sich das RMS während der exothermen Reaktion zuerst ausdehnt, bevor es sich beim Abkühlen zusammenzieht. Im Gegensatz zu den Proben mit vollflächiger Metallisierung gibt es bei den strukturierten Proben Lücken zwischen dem LTCC-Material und dem RMS, in die es sich ohne Widerstand ausdehnen kann.

6.3.2 Schlussfolgerungen

1. Der Fügedruck beeinflusst die Wärmeableitung während der Reaktion des RMS. Der verbesserte Kontakt führt zu einem geringeren thermischen Widerstand zwischen RMS und LTCC-Material, wodurch dessen schlechtere Wärmeleitfähigkeit in gewissem Maße kompensiert wird. Zukünftige Arbeiten könnten diesen Einfluss auf Spitzentemperatur und Reaktionsgeschwindigkeit näher untersuchen, beispielsweise unter Einsatz eines Systems mit integrierten Sensoren (vgl. Paper 4).
2. Es existiert ein optimaler Druckbereich für reaktive Fügeprozesse. Ein zu geringer Druck führt zu einem unvollständigen Kontakt und zur Entstehung großflächiger Lücken. Ein zu hoher Druck führt zu einer Delamination oder Auflösung einzelner Schichten, sowie zu mechanischen Schäden im System. Unter einem idealen Druck bildet sich ein ganzflächiger Kontakt aus, der positive Auswirkungen auf die thermische und elektrische Leitfähigkeit sowie auf die mechanische Stabilität hat.

6.4 Analyse der Fügestellen

6.4.1 Analysemethodik und -ergebnisse

Zur näheren Analyse wurden von einigen Proben REM-Aufnahmen angefertigt, sowie EDX-Analysen der Elemente Sn, Pd, Ag, Al und Ni durchgeführt. Während Abb. 35 die Aufnahmen der mit abgeschiedenem RMS gefügten Proben unter einem Druck von 1,5 MPa zeigt, zeigen die Abb. 36–38 die Aufnahmen der mit NanoFoil® gefügten Proben unter einem Druck von 2 MPa (Abb. 36), 11 MPa (Abb. 37) und 22 MPa (Abb. 38). Die Farbgebung der einzelnen Elemente unterscheidet sich, da sie während der Projektlaufzeit optimiert wurde.

Im Fall des abgeschiedenen RMS (Abb. 35) ist die gelötete Metallisierung in zwei markante Bereiche unterteilt. Der Bereich nahe dem RMS weist höhere Konzentrationen von Sn und niedrigere Konzentrationen von Pd, Ag und Ni auf, während der Bereich nahe der LTCC höhere Konzentrationen von Pd und Ag, und niedrigere Konzentrationen von Sn und Ni aufweist. Diese Verteilung zeigt, dass das geschmolzene Sn geringe Mengen Pd und Ag aus der Metallisierung sowie geringe Mengen Ni aus dem RMS lösen kann und somit IMP bilden kann.

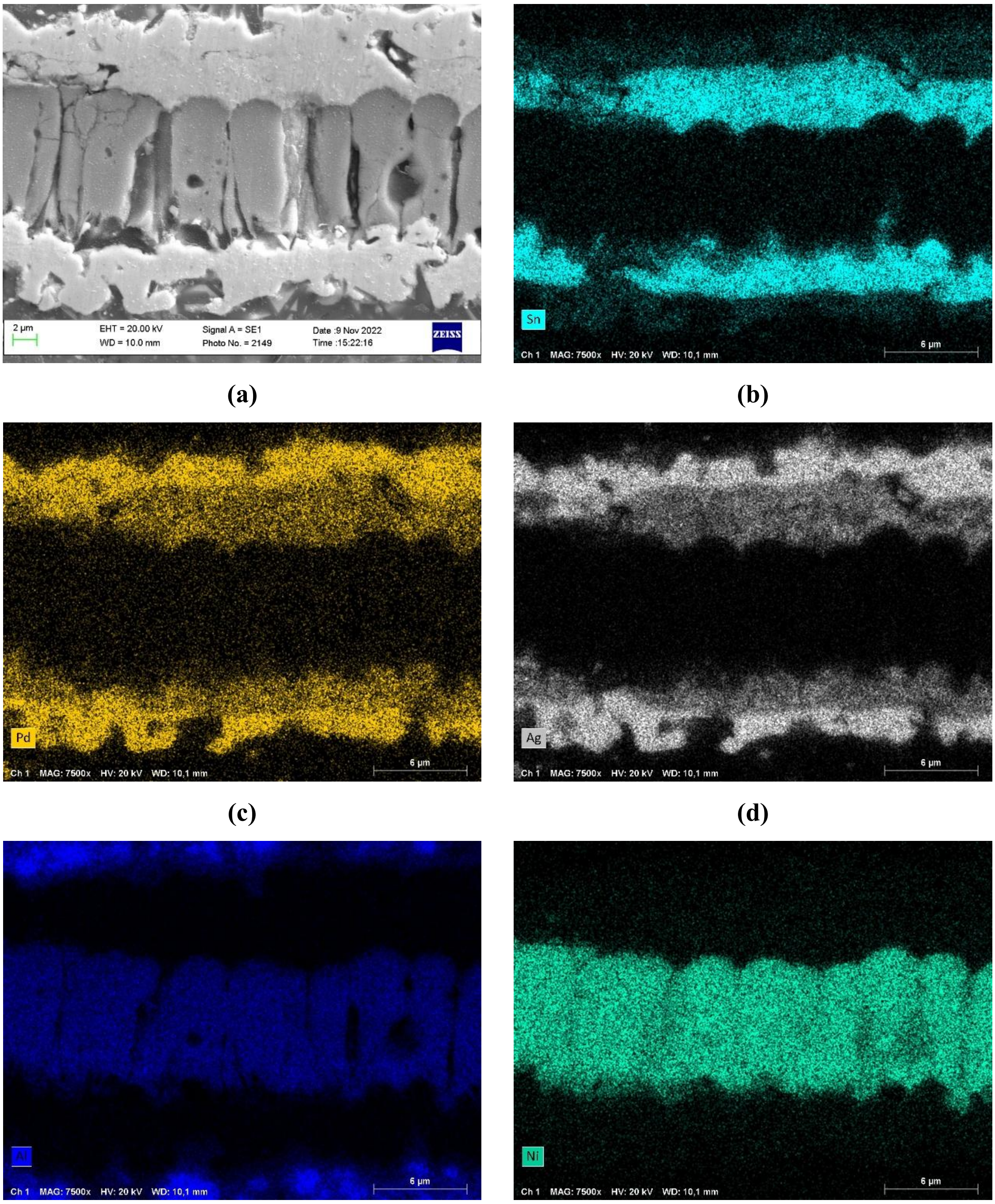

(a) (b)

(c) (d)

(e) (f)

Abbildung 35: EDX-Analyse einer mit abgeschiedenem RMS gefügten Probe mit einem Anpressdruck von 1,5 MPa. (a) REM-Aufnahme im SE-Modus. (b) Elementverteilung von Sn. (c) Elementverteilung von Pd. (d) Elementverteilung von Ag. (e) Elementverteilung von Al. (f) Elementverteilung von Ni. Vergrößerung: 7500x.

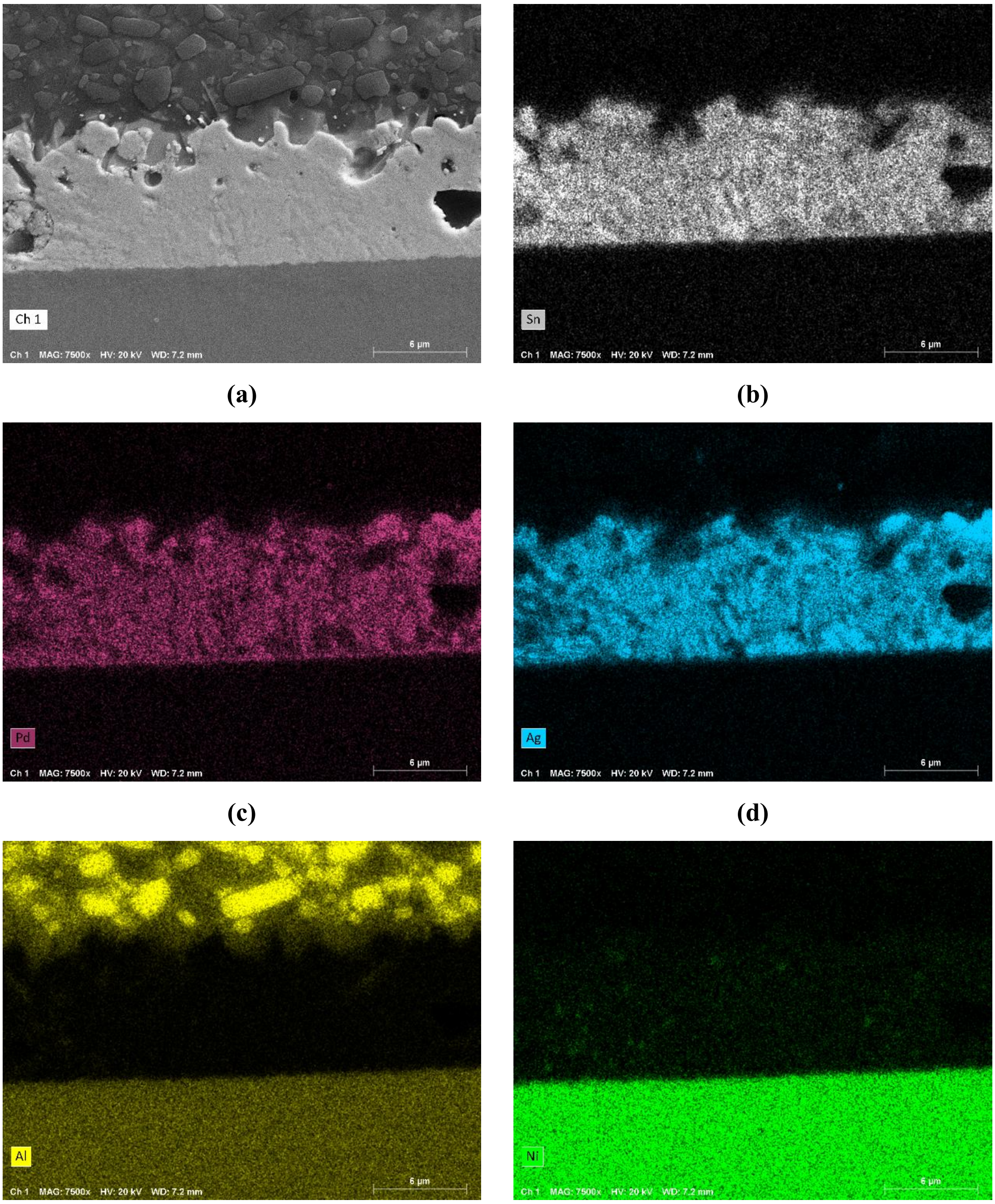

(a) (b)

(c) (d)

(e) (f)

Abbildung 36: EDX-Analyse einer mit NanoFoil® gefügten Probe mit einem Anpressdruck von 2 MPa [P8]. (a) REM-Aufnahme im SE-Modus. (b) Elementverteilung von Sn. (c) Elementverteilung von Pd. (d) Elementverteilung von Ag. (e) Elementverteilung von Al. (f) Elementverteilung von Ni. Vergrößerung: 7500x.

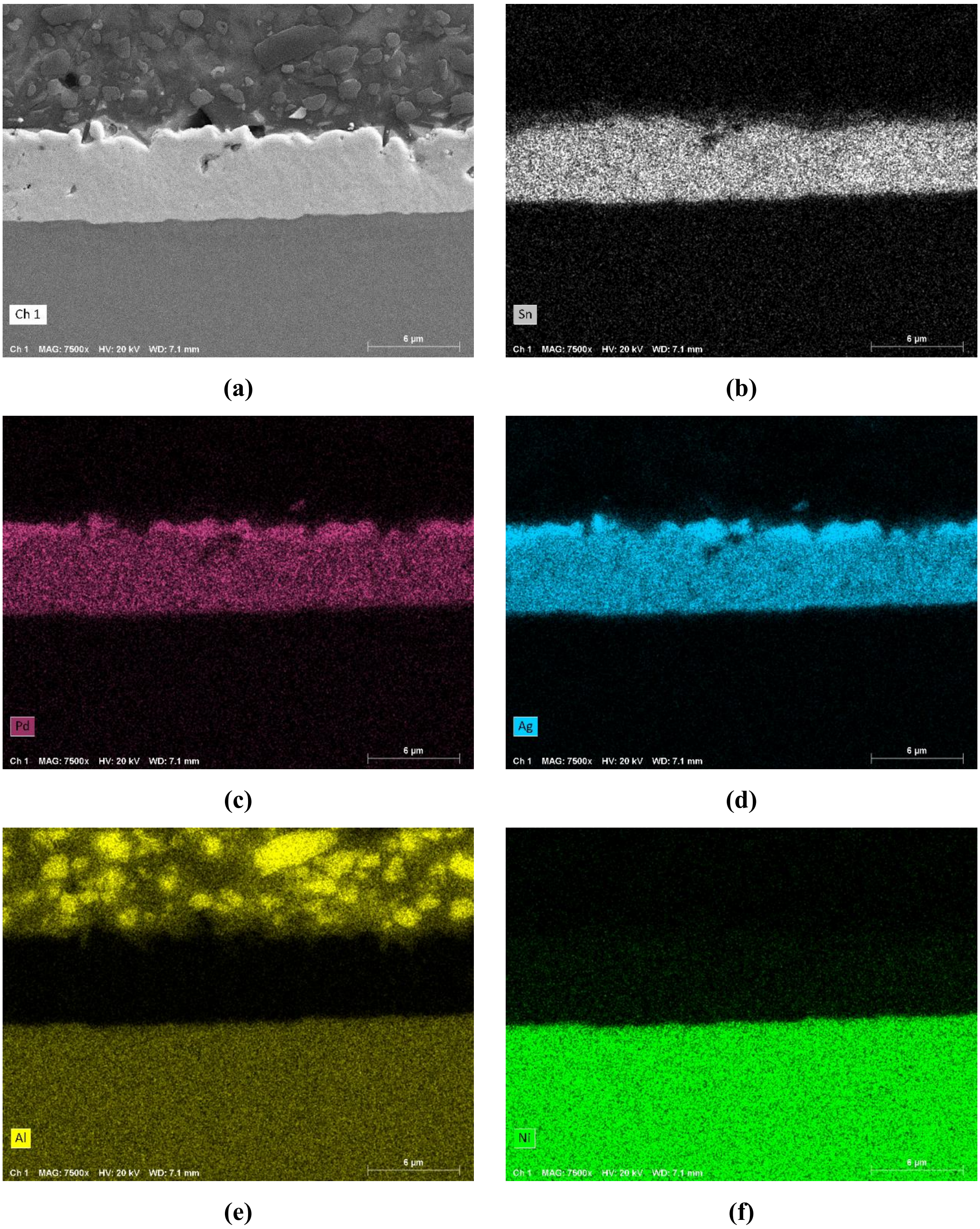

(a) (b) (c) (d) (e) (f)

Abbildung 37: EDX-Analyse einer mit NanoFoil® gefügten Probe mit einem Anpressdruck von 11 MPa [P8]. (a) REM-Aufnahme im SE-Modus. (b) Elementverteilung von Sn. (c) Elementverteilung von Pd. (d) Elementverteilung von Ag. (e) Elementverteilung von Al. (f) Elementverteilung von Ni. Vergrößerung: 7500x.

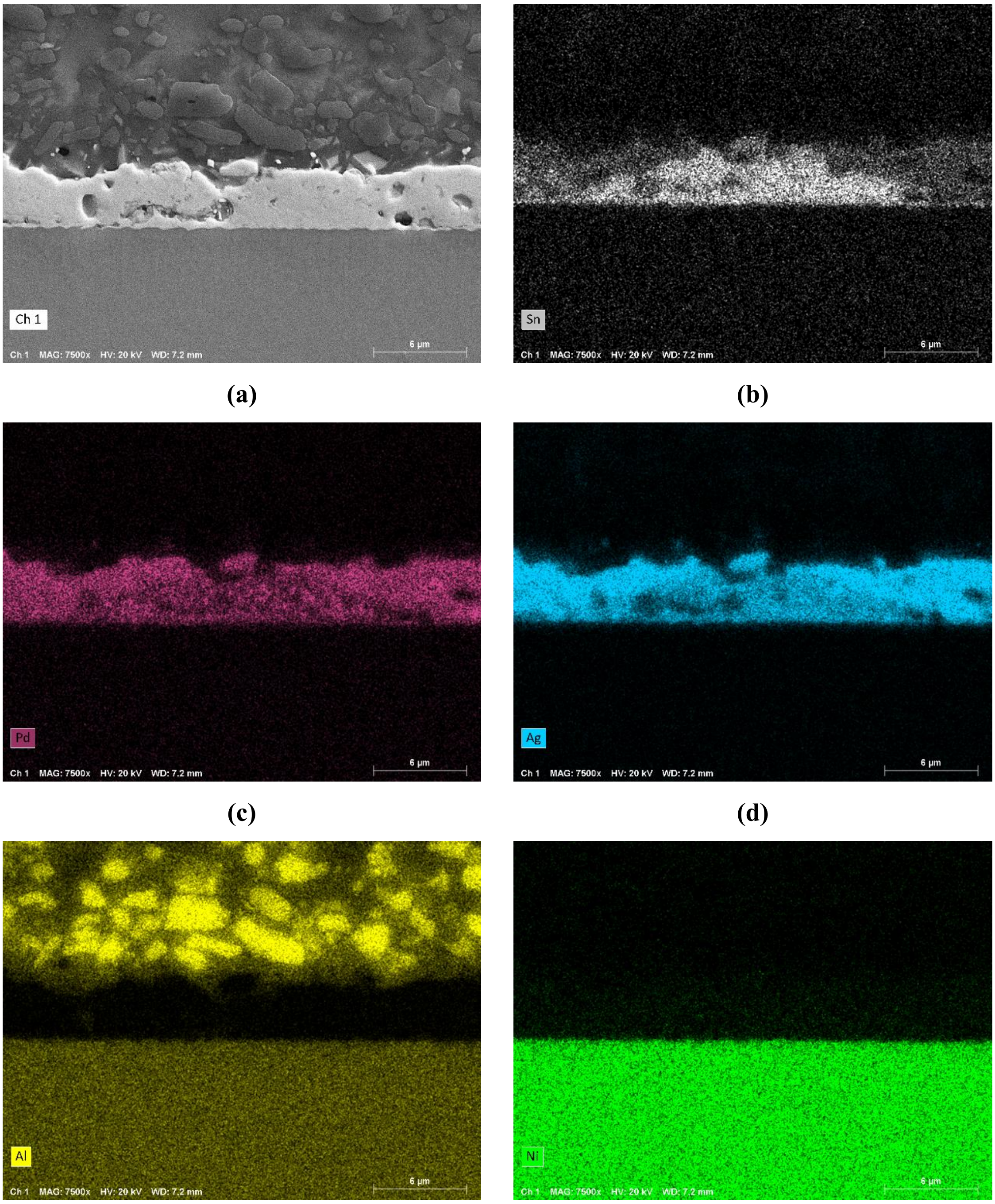

(a) (b) (c) (d) (e) (f)

Abbildung 38: EDX-Analyse einer mit NanoFoil® gefügten Probe mit einem Anpressdruck von 22 MPa [P8]. (a) REM-Aufnahme im SE-Modus. (b) Elementverteilung von Sn. (c) Elementverteilung von Pd. (d) Elementverteilung von Ag. (e) Elementverteilung von Al. (f) Elementverteilung von Ni. Vergrößerung: 7500x.

Bei den mit NanoFoil® gefügten Proben bildet sich bei einem niedrigen Fügedruck von 2 MPa (Abb. 36) eine breite Fügezone aus. Während das Sn dabei überwiegend in seinen ursprünglichen Bereichen konzentriert bleibt, sind Pd und Ag aus der Metallisierung nahezu gleichmäßig in die gesamte Fügezone diffundiert. Dort finden sich zusätzlich kleine

Anteile an Al und Ni aus dem RMS. Im Gegensatz zur Fügung mit dem abgeschiedenen RMS gibt es keine Unterschiede zwischen den beiden Grenzflächen LTCC/Lot und Lot/RMS.

Bei einem Fügedruck von 11 MPa (Abb. 37) schrumpft die Fügezone auf etwa die Hälfte ihrer ursprünglichen Größe zusammen. Obwohl sich die Elemente Sn, Pd und Ag wie zuvor vollständig durchmischen, ist an der Grenzfläche LTCC/Lot eine dünne Schicht mit geringer Konzentration von Sn sowie höheren Konzentrationen von Pd und Ag erkennbar. Bei einem Fügedruck von 22 MPa (Abb. 38) vermischen sich die Elemente Sn, Pd und Ag nach wie vor, jedoch bilden sich Stellen mit hoher Konzentration von Sn sowie niedrigen Konzentrationen Pd und Ag aus, und umgekehrt.

6.4.2 Schlussfolgerungen

1. Der Fügedruck muss in einem bestimmten Bereich liegen, um die Ausbildung adäquater IMP zu ermöglichen. Während bei niedrigen und hohen Fügedrücken keine Hinweise auf die Bildung einer IMP gefunden wurden, deutet die dünne Schicht an der Grenzfläche LTCC/Lot bei einem Fügedruck von 11 MPa auf eine solche hin.
2. Die exotherme Reaktion der reaktiven Folie erzeugt Temperaturen, die deutlich über den werkstofflichen Grenzen der eingesetzten Pd/Ag-Metallisierung liegen (siehe Kapitel 6.2). Die exotherme Reaktion läuft zwar innerhalb weniger Millisekunden ab, erreicht jedoch sehr hohe Spitzentemperaturen. Die dabei freigesetzte Wärme kann aufgrund der schlechten Wärmeleitfähigkeit des LTCC-Materials nicht schnell genug abgeleitet werden, sodass angenommen werden kann, dass die metallischen Schichten nahe des RMS ebenfalls entsprechend höhere Temperaturen erreichen, was zur Auflösung der verwendeten Pd/Ag-Metallisierung führen kann.
3. Das abgeschiedene RMS weist eine höhere Kompatibilität zur Pd/Ag-Metallisierung und dem LTCC-Material auf. Aufgrund der gestückelten Struktur des RMS wird die Reaktion an jedem Segmentwechsel kurz gebremst, was den Zeitraum der Wärmefreisetzung verlängert (vgl. Kapitel 6.1) und somit die entstehenden Spitzentemperaturen verringert. Zudem ist im abgeschiedenen RMS aufgrund seiner deutlich geringeren Dicke von nur 10 µm weniger chemische Energie gespeichert, sodass während der exothermen Reaktion weniger Wärme freigesetzt wird.

6.5 Funktionelle Charakterisierung

6.5.1 Charakterisierungsmethodik

Während der ersten Experimente traten Schwierigkeiten bei der elektrischen Zündung der abgeschiedenen RMS auf. Obwohl die exotherme Reaktion zwar initial ausgelöst werden konnte, kam sie in mehreren Fällen kurz nach der Zündung zum Erliegen. Nach eingehender Analyse wurde als wahrscheinlichste Ursache ein übermäßiger lokaler Energieeintrag durch die Zündschaltung identifiziert (siehe Kapitel 4.1.7). Dieser führte vermutlich zu einer lokalen Überhitzung und damit zu einem teilweisen Verlust der definierten Schichtstruktur, wahrscheinlich durch Verschmelzung einzelner Lagen des RMS. Dies verursachte Verzögerungen bei der Bearbeitung mehrerer WP, insbesondere der bruchmechanischen Charakterisierung und Umweltprüfungen. Daher waren die entsprechenden Untersuchungen zum Zeitpunkt der Niederschrift dieser Dissertation noch nicht abgeschlossen. Um dennoch eine methodische Grundlage für zukünftige Arbeiten zu schaffen, wurden drei Veröffentlichung in die vorliegende Dissertation eingebunden, die zwar keinen direkten Bezug zur reaktiven Fügetechnologie aufweisen, jedoch relevante methodische Entwicklungen beschreiben.

Paper 9 beschreibt die Konzeption und den Aufbau eines Prüfstands zur mechanischen Charakterisierung mikroelektronischer Verbindungen (Abb. 39). Die Auswertung der Probendeformationen erfolgt mittels DIC-Verfahren, das im Vergleich zu anderen Methoden wie der Nutzung von Laserextensometern [76, 77] geringere Vorbereitungszeiten erfordert. Durch Nutzung eines Stereo-Zoom-Mikroskops, SteREO Discovery.V20 (Carl Zeiss), können auch kleinste Kontakte beobachtet werden. Während des Versuchs werden die Kontakte kontinuierlich elektrisch überwacht, um Ausfälle so früh wie möglich zu detektieren. Für die Anwendung mit reaktiv gefügten Proben sind lediglich geringfügige Anpassungen, etwa speziell angepasste Probenhalterungen, erforderlich.

Eine systematische Methodik zur Analyse von Schad- und Bruchstellen wird in Paper 10 vorgestellt. Hierzu wurden keramische SMD-Widerstände mehreren Reflow-Zyklen unterzogen, und die maximale Scherfestigkeit mit dem Versuchsaufbau aus Paper 9 ermittelt. Die Ergebnisse belegen die prinzipielle Eignung der Methodik für die geplanten Untersuchungen, aber es ist zu berücksichtigen, dass der Ort des Versagens nicht zwangsläufig in der Lötstelle liegen muss. Abb. 40 zeigt exemplarisch eine solche Bruchstelle an einer Probe nach zwei Reflow-Zyklen, bei der die Ag/Ni-Metallisierung vom Bauteil abgelöst wurde. Ursache hierfür ist das Wachstum der IMP am Bauteil, wodurch die Adhäsion zwischen Lot und Metallisierung stärker als jene zwischen Metallisierung und Keramikkörper wird.

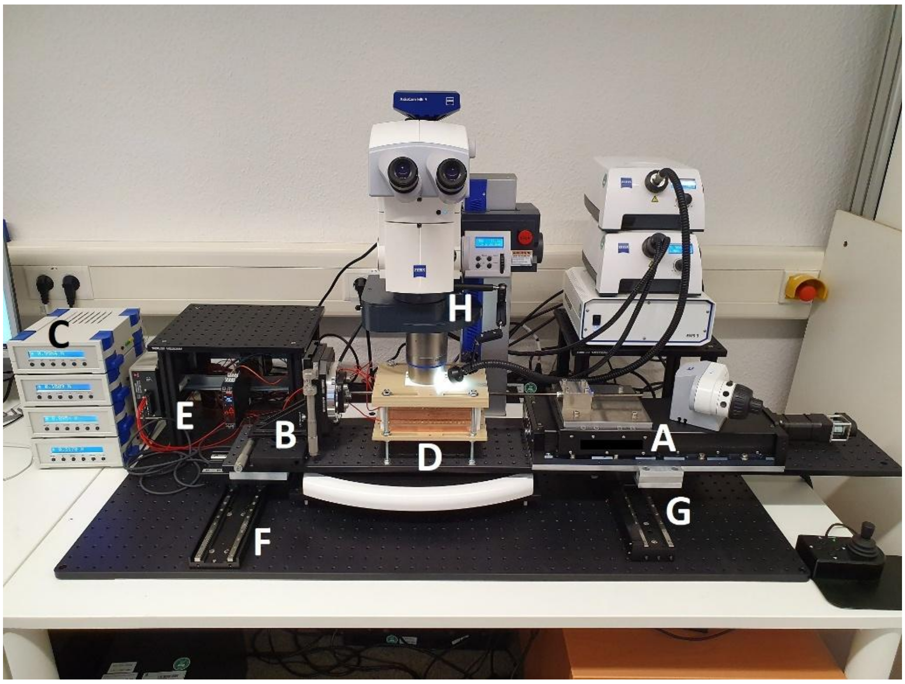

[redacted]

Abbildung 39: Versuchsaufbau zur mechanischen Charakterisierung elektrischer Kontakte [P9]. A: Aktor, der die Kraft auf die Proben ausübt. B: Dreidimensionaler Kraftsensor. C: Messverstärker zum Anschluss des Kraftsensors an den PC. D: Thermokammer zur Ermöglichung von Experimenten bei hohen Temperaturen. E: Temperatursteuerung der Thermokammer. F: Verschiebetische in x- und y-Richtung ohne Motoren. G: Motorisierte Verschiebetische, um das Setup unter dem Mikroskop positionieren zu können. H: Stereo-Zoom-Mikroskop mit integrierter Beleuchtung. © 2021 IEEE

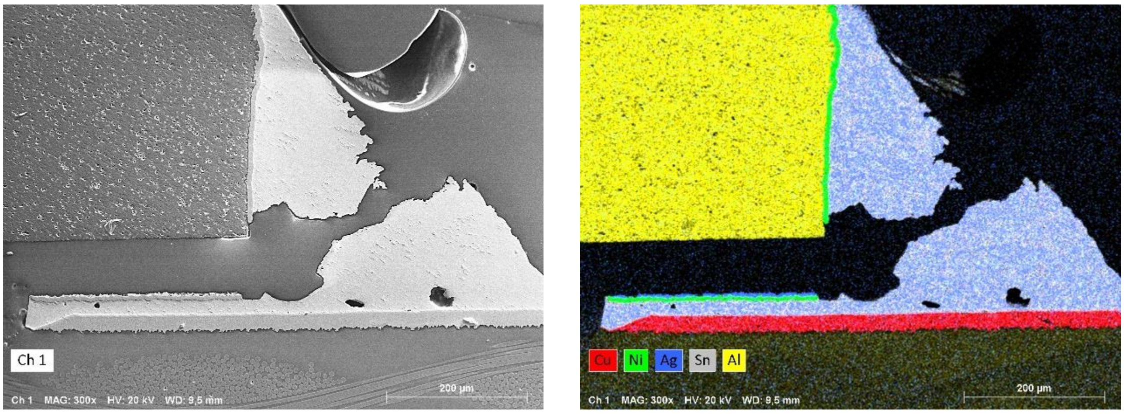

(a) **(b)**

Abbildung 40: EDX-Analyse der Bruchstelle eines SMD-Widerstands nach zwei Reflow-Zyklen und durchgeführtem Schertest [P10]. Aufgrund der höheren Adhäsion zwischen Lot (grau/blau) und Ag/Ni-Metallisierung (grün) als diejenige zwischen Metallisierung und keramischem Grundkörper (gelb) wurde die Metallisierung vom Bauteil abgelöst. (a) REM-Aufnahme im SE-Modus. (b) Elementverteilung von Cu, Ni, Ag, Sn und Al. Vergrößerung: 300x.

Paper 11 stellt einen elektrischen Prüfstand zur In-situ-Widerstandsmessung im Milli- bzw. Mikroohmbereich vor. Dieser eignet sich zur kontinuierlichen Überwachung der elektrischen Integrität von Lötverbindungen während Umweltprüfungen und erlaubt nicht nur die Detektion von Defekten unmittelbar nach ihrem Auftreten, sondern auch die Detektion von Widerstandsänderungen durch Änderungen in der Mikrostruktur der Lötstelle (etwa durch Mikrorisse oder das Wachstum der IMP). Abb. 41 zeigt ein mögliches Probenlayout, das für solche Versuche genutzt werden kann. Aufgrund der unterschiedlichen CTE von LTCC-Chip und PCB-Substrat entstehen in den Lötstellen thermomechanische Spannungen, die den Ausfall der Verbindung hervorrufen können.

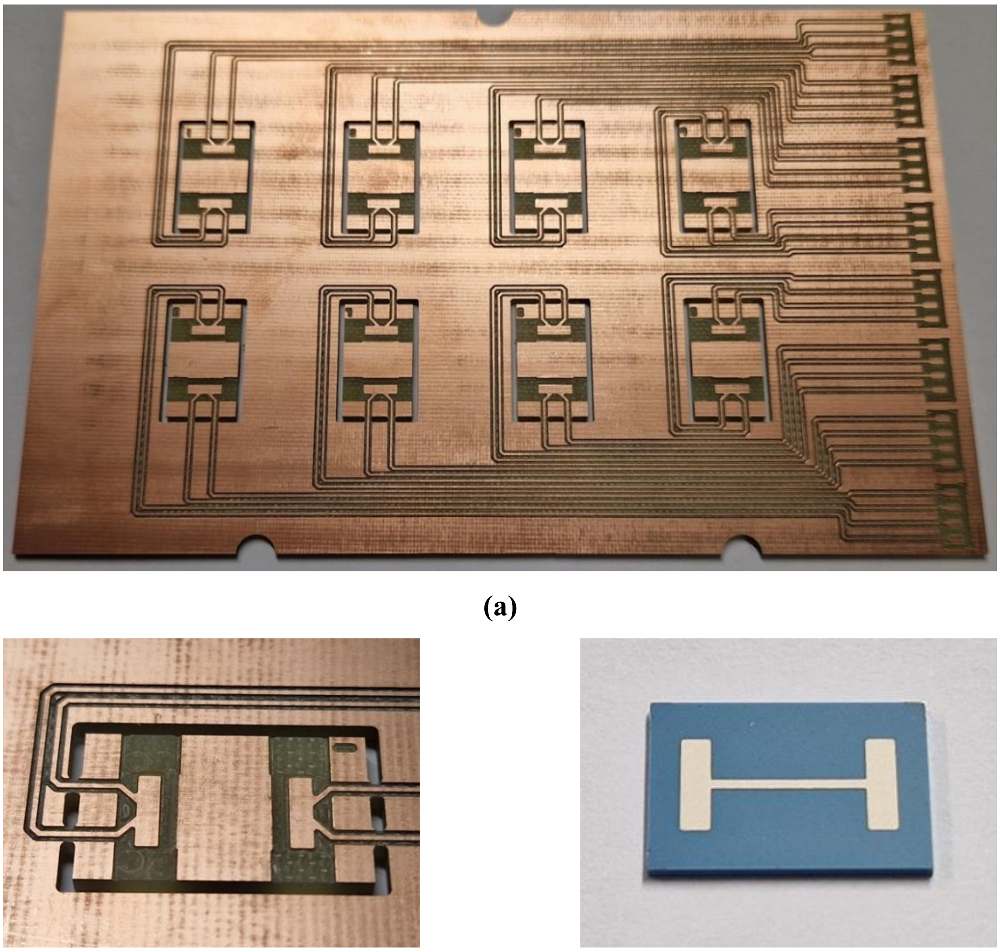
(a)

(b) **(c)**

Abbildung 41: (a) Testplatine für insgesamt acht Proben mit Anschluss-Pads zur Verbindung mit den elektrischen Messgeräten. (b) Detaillierte Ansicht der Pads, auf die die (c) LTCC-Chips reaktiv gefügt werden können. Aufgrund der unterschiedlichen CTE der Materialien entstehen während Umweltprüfversuchen thermomechanische Spannungen in den Lötstellen.

6.5.2 Schlussfolgerungen

1. Der vorgestellte Prüfstand eignet sich zur mechanischen Charakterisierung reaktiver Lötverbindungen. Die flexible Bauweise erfordert lediglich minimale Anpassungen an den Komponenten wie z. B. an Probenhalterungen, um solche Tests mit reaktiv gefügten Proben durchführen zu können. Durch Verwendung eines Stereo-Zoom-Mikroskops können auch kleinste Kontakte untersucht werden. Die Auswertung der Probendeformationen erfolgt mittels DIC-Verfahren, wodurch eine präzise Bestimmung der mechanischen Materialeigenschaften ermöglicht wird.
2. Die vorgestellten Messaufbauten eignen sich zur kontinuierlichen Überwachung der elektrischen Integrität reaktiver Lötverbindungen während Umweltprüfversuchen. Mit ihnen können sowohl Brüche als auch kleinste Widerstandsänderungen im Mikroohmbereich erfasst werden, die durch Änderungen in der Mikrostruktur hervorgerufen werden. Nach der Detektion eines Ausfalls kann die entsprechende Probe aus dem Prüfschrank entnommen und metallographisch untersucht werden.
3. Die vorgestellte Methodik zur Analyse von Schad- und Bruchstellen eignet sich zur Untersuchung mikrostruktureller Veränderungen an reaktiven Lötverbindungen sowie zur Schädigungsbewertung. Die metallographische Vorbereitung ermöglicht eine gezielte Untersuchung der Proben mit LM, REM und EDX-Analyse, wodurch sogar die einzelnen Schichten eines RMS sichtbar gemacht werden können.

7 Zusammenfassung

Das Ziel der Arbeit bestand in der Erforschung der Anwendungsbreite reaktiver Fügeprozesse auf keramischen LTCC-Substraten mit verschiedenen Oberflächenmorphologien. Zur Untersuchung der Fügeprozesse wurden experimentelle Methoden und Simulationen genutzt. Hierzu wurden Al/Ni-RMS auf LTCC-Oberflächen mit unterschiedlichen Rauheiten abgeschieden und hinsichtlich ihrer Morphologie mikroskopisch charakterisiert. Nach der Zündung wurden die erreichten Reaktionsgeschwindigkeiten und Spitzentemperaturen gemessen und zwischen den verschiedenen Konfigurationen verglichen. Bei realen Fügeprozessen lässt sich die Reaktion allerdings in der Regel nicht direkt beobachten, da sie verdeckt zwischen Bauteil und Substrat stattfindet. Ergänzend wurden daher verschiedene CFD-Modelle entwickelt, die die exotherme Reaktion eines RMS nachbilden, und deren Parameter an die experimentell gewonnenen Daten angeglichen wurden. Diese dienten der Bewertung der Eignung von in das LTCC-Material integrierten Pt-Sensoren und Thermopaaren zur Erfassung der Reaktionseigenschaften sowie dem Vergleich des Fügeverhaltens von LTCC- und Si-Substraten. In weiteren Versuchsreihen wurden experimentelle Fügeprozesse mit abgeschiedenen RMS und vorfabrizierten reaktiven Folien durchgeführt, wobei insbesondere der Einfluss des Fügedrucks auf die entstehenden Fügezonen untersucht wurde.

Die Ergebnisse zeigen, dass die Abscheidung und die Zündung eines RMS auf LTCC-Substraten trotz ihrer hohen Rauheit möglich sind. Während sich auf unbearbeiteten und polierten Oberflächen durchgängige Schichten bilden, entstehen auf laserbearbeiteten Proben segmentierte Schichten. Diese Segmente verursachen kurze Unterbrechungen in der Reaktionsausbreitung und reduzieren sowohl die Reaktionsgeschwindigkeit um bis zu 56 % als auch die Spitzentemperatur um bis zu 32 %. Die Simulationen bestätigen eine starke Korrelation zwischen beiden Größen und zeigen, dass die geringe Wärmeleitfähigkeit der LTCC, im Vergleich zu Si, zu bis zu 103 % höheren Spitzentemperaturen im Lot führt. Dies führt insbesondere bei der Verwendung vorfabrizierter Folien, deren Spezifikationen herstellerseitig festgelegt sind, zu einer Überschreitung der Temperaturgrenzen der Pd/Ag-Metallisierung. Bei abgeschiedenen RMS können die Reaktionsparameter bis zu einem gewissen Grad kontrolliert werden, beispielsweise durch die Menge des eingesetzten Lots.

In das LTCC-Material integrierte Pt-Sensoren erlauben eine Erfassung der Reaktionsgeschwindigkeit, sind jedoch für die Messung der Spitzentemperatur nur bedingt geeignet.

Gründe hierfür liegen in der Notwendigkeit einer elektrischen Isolierung der Sensoren vom RMS und ihrem großen Platzbedarf aufgrund ihres geringen spezifischen Widerstands. Die Nutzung integrierter Thermopaare stellt eine kompaktere Alternative dar, die bei einer Temperatur von ca. 800 °C eine messbare Spannungsdifferenz von 3,5 mV liefern.

Die Fügeversuche und deren Analyse zeigen eine starke Abhängigkeit des reaktiven Fügeprozesses vom angewandten Fügedruck. Ein zu geringer Druck führt zur Bildung großflächiger Lücken zwischen den Fügepartnern und somit zu noch schlechterer Wärmeableitung, während ein zu hoher Druck Delamination oder die Auflösung einzelner Schichten verursacht.

Der Vergleich der in dieser Untersuchung gewonnenen Erkenntnisse mit den zuvor publizierten Ergebnissen zum reaktiven Fügen metallischer, Si-basierter oder hybrider Verbindungen zeigt, dass sich diese Prozesse auf keramischen LTCC-Substraten aufgrund der deutlich geringeren Wärmeleitfähigkeit grundlegend unterscheiden. Die resultierenden hohen Temperaturen der exothermen Reaktion können zu lokalen Überhitzungen und somit zu einer Überschreitung der thermischen Grenzen des LTCC-Systems führen. Unter Berücksichtigung dieser Randbedingungen erscheint die Nutzung reaktiver Fügetechnologien im Bereich der keramischen LTCC-Substrate jedoch grundsätzlich realisierbar, sofern die Prozessparameter wie Schichtarchitektur, Fügedruck und Vorheiztemperaturen gezielt an die spezifischen Materialeigenschaften angepasst werden.

Literaturverzeichnis

[P1] E. Wiss, A. Schulz, A. Ruh, K. Jaekel, J. Müller und S. Wiese, „Morphologies of reactive nanolayer stacks sputtered on ceramic low-temperature cofired ceramic substrates having a micrometer-scale surface roughness“, *Adv. Eng. Mater.*, Bd. 27, Nr. 3, Art.-Nr. 2302284, DOI: 10.1002/adem.202302284.

[P2] A. Yuile, A. Schulz, E. Wiss, J. Müller und S. Wiese, „The simulated effect of adding solder layers on reactive multilayer films used for joining processes“, *Appl. Sci.*, Bd. 12, Nr. 5, Art.-Nr. 2397, DOI: 10.3390/app12052397.

[P3] E. Wiss, A. Schulz, A. Yuile, J. Müller und S. Wiese, „Application of reactive bonding methods on LTCC substrates“, in *2023 24th European Microelectronics and Packaging Conference & Exhibition (EMPC)*, Cambridge, Vereinigtes Königreich, September 2023, S. 1–6, DOI: 10.23919/EMPC55870.2023.10418406.

[P4] A. Yuile, N. Jaziri, E. Wiss, J. Müller und S. Wiese, „Simulations of thermocouple measurements during reactive bonding processes on LTCC substrates“, in *2024 IEEE 10th Electronics System-Integration Technology Conference (ESTC)*, Berlin, Deutschland, September 2024, S. 1–5, DOI: 10.1109/ESTC60143.2024.10712001.

[P5] E. Wiss, A. Yuile, A. Schulz, J. Müller und S. Wiese, „Reactive die bonding on LTCC substrates – analysis by CFD simulation“, in *2023 24th International Conference on Thermal, Mechanical and Multi-Physics Simulation and Experiments in Microelectronics and Microsystems (EuroSimE)*, Graz, Österreich, April 2023, S. 1–5, DOI: 10.1109/EuroSimE56861.2023.10100772.

[P6] A. Yuile, A. Schulz, E. Wiss, J. Müller und S. Wiese, „2D computational fluid dynamics simulation analysis of the assembly of low-temperature cofired ceramics/low-temperature cofired ceramics and Si/Si sandwiches“, *Adv. Eng. Mater.*, Bd. 27, Nr. 3, 2025, Art.-Nr. 2302283, DOI: 10.1002/adem.202302283.

[P7] E. Wiss, N. Jaziri, A. Yuile, J. Müller und S. Wiese, „Experimental study on reactive joining processes on LTCC substrates“, in *2024 IEEE 10th Electronics System-Integration Technology Conference (ESTC)*, Berlin, Deutschland, September 2024, S. 1–4, DOI: 10.1109/ESTC60143.2024.10712029.

[P8] E. Wiss, N. Jaziri, J. Müller und S. Wiese, „Impact of bonding pressure on the reactive bonding of LTCC substrates“, *Micromachines*, Bd. 16, Nr. 3, Art.-Nr. 321, DOI: 10.3390/mi16030321.

[P9] E. Wiss, D. Barth und S. Wiese, „Concept of a mechanical test setup for packaging materials using digital image correlation methods“, *2021 22nd International Conference on Thermal, Mechanical and Multi-Physics Simulation and Experiments in Microelectronics and Microsystems (EuroSimE)*, Online, April 2021, S. 1–6, DOI: 10.1109/EuroSimE52062.2021.9410859.

[P10] E. Wiss und S. Wiese, „The effect of multiple solder reflows on the formation of Cu_6Sn_5 intermetallics and the decomposition of SnAg3.0Cu0.5 solder joints in the framework of rework and reuse of MLCC components“, *Metals*, Bd. 14, Nr. 9, 2024, Art.-Nr. 986, DOI: 10.3390/met14090986.

[P11] E. Wiss, R. Metasch, D. Barth, V. Serea, M. Roellig und S. Wiese, „ Electrical diagnostics of passive components failure during reliability testing“, *2022 23th International Conference on Thermal, Mechanical and Multi-Physics Simulation and Experiments in Microelectronics and Microsystems (EuroSimE)*, St. Julian, Malta, April 2022, S. 1–8, DOI: 10.1109/EuroSimE54907.2022.9758860.

[1] M. Mueller und J. Franke, „Highly efficient packaging processes by reactive multilayer materials for die-attach in power electronic applications“, in *2014 IEEE 16th Electronics Packaging Technology Conference (EPTC)*, Singapur, Republik Singapur, November 2024, S. 477–481, DOI: 10.1109/EPTC.2014.7028295.

[2] J. Braeuer und T. Gessner, „A hermetic and room-temperature wafer bonding technique based on integrated reactive multilayer systems“, *J. Micromech. Microeng.*, Bd. 24, Nr. 11, 2014, Art.-Nr. 115002, DOI: 10.1088/0960-1317/24/11/115002.

[3] J. Braeuer, J. Besser, M. Wiemer und T. Gessner, „A novel technique for MEMS packaging: reactive bonding with integrated material systems“, *Sens. Actuators A: Phys.*, Bd. 188, 2012, S. 212–219, DOI: 10.1016/j.sna.2012.01.015.

[4] B. Boettge, J. Braeuer, M. Wiemer, M. Petzold, J. Bagdahn und T. Gessner, „Fabrication and characterization of reactive nanoscale multilayer systems for low-temperature bonding in microsystem technology“, *J. Micromech. Microeng.*, Bd. 20, Nr. 6, 2010, Art.-Nr. 064018, DOI: 10.1088/0960-1317/20/6/064018.

[5] S. Kanetsuki, S. Miyake, K. Kuwahara und T. Namazu, „Influence of bonding pressure on thermal resistance in reactively-bonded solder joints“, *Jpn. J. Appl. Phys.*, Bd. 55, 2016, Art.-Nr. 05GP17, DOI: 10.7567/JJAP.55.06GP17.

[6] S. Kanetsuki, K. Kuwahara, S. Egawa, S. Miyake und T. Namazu, „Effect of thickening outermost layers in Al/Ni multilayer film on thermal resistance of reactively bonded solder joints“, *Jpn. J. Appl. Phys.*, Bd. 56, 2017, Art.-Nr. 06GN16, DOI: 10.7567/JJAP.56.06GN16.

[7] S. Hertel, W. Schulte, M. Weiser, M. Becker, M. Wiemer und T. Otto, „Electrochemical deposition of reactive material systems for assembly and packaging applications“, *Micro-Nano-Integration; 7th GMM-Workshop*, Dortmund, Deutschland, 2018, S. 1–6.

[8] A. P. McClure, „Investigation of reactively structured Al/Ni multilayer foils and their applications in high temperature die attach“, Dissertation, Univ. of Maryland, College Park, Maryland, USA, 2008.

[9] J. Wang, E. Besnoin, A. Duckham, S. J. Spey, M. E. Reiss, O. M. Knio, M. Powers, M. Whitener und T. P. Weihs, „Room-temperature soldering with nanostructured foils“, *Appl. Phys. Lett.*, Bd. 83, Nr. 19, 2003, S. 3987–3989, DOI: 10.1063/1.1623943.

[10] J. Matteau, „NanoBond® assembly – a rapid, room temperature soldering process“, in *Proc. Int. Symp. Microelectron.*, Long Beach, California, USA, Oktober 2011, S. 000521–000526, DOI: 10.4071/isom-2011-WA2-Paper5.

[11] J. S. Subramanian, P. Rodgers, J. Newson, T. Rude, Z. He und E. Besnoin, „Room temperature soldering of microelectronic components for enhanced thermal performance“, in *Proceedings of the 6th International Conference on Thermal, Mechanical and Multi-Physics Simulation and Experiments in Micro-Electronics and Micro-Systems (EuroSimE)*, Berlin, Deutschland, 2005, S. 681–686, DOI: 10.1109/ESIME.2005.1502888.

[12] X. Qiu, „Reactive multilayer foils and their applications in joining“, Masterarbeit, Louisiana State Univ., Baton Rouge, Louisiana, USA, August 2007, DOI: 10.31390/gradschool_theses.2091.

[13] J. Zhang, F.-S. Wu, J. Zou, B. An und H. Liu, „Al/Ni multilayer used as a local heat source for mounting microelectronic components“, in *2009 International Conference on Electronic Packaging Technology & High Density Packaging (ICEPT-HDP)*, Beijing, China, August 2009, S. 838–841, DOI: 10.1109/ICEPT.2009.5270630.

[14] J. P. Levin, T. R. Rude, J. Subramanian, E. Besnoin, T. P. Weihs, O. M. Knio, D. Van Heerden, M. T. Powers und C. D. Enns „Room temperature lead-free soldering of microelectronic components using a local heat source“, in *ASM Materials Solutions Conference & Exposition*, Columbus, Ohio, USA, Oktober 2004, S. 75–79.

[15] K. Rzyman, Z. Moser, R. E. Watson und M. Weinert, „Enthalpies of formation of AlNi: experiment versus theory“, *J. Phase Equilibria*, Bd. 19, 1998, S. 106–111, DOI: 10.1361/105497198770342562.

[16] K. T. Raić, R. Rudolf, P. Ternik, Z. Zunić, V. Lazić, D. Stamenković, T. Tanasković und I. Anžel, „CFD analysis of exothermic reactions in al-au nano multi-layered foils“, *Mater. Tehnol.*, Bd. 45, Nr. 4, 2011, S. 335–338.

[17] A. Syed-Khaja, C. Kaestle, M. Mueller und J. Franke, „A comprehensive study on the automation potentials and complexities of advanced and alternative die-attach technologies for power electronic applications“, *Applied Mechanics and Materials*, Bd. 794, 2015, S. 320–327, DOI: 10.4028/www.scientific.net/AMM.794.320.

[18] J. Wang, E. Besnoin, A. Duckham, S. J. Spey, M. E. Reiss, O. M. Knio und T. P. Weihs, „Joining of stainless-steel specimens with nanostructured Al/Ni foils“, *J. Appl. Phys.*, Bd. 95, Nr. 1, 2004, S. 248–256, DOI: 10.1063/1.1629390.

[19] S. Simões, A. S. Ramos, F. Viana, M. T. Vieria und M. F. Vieira, „Joining of TiAl to steel by diffusion bonding with Ni/Ti reactive multilayers“, *Metals*, Bd. 6, Nr. 5, 2016, Art.-Nr. 96, DOI: 10.3390/met6050096.

[20] A. Duckham, S. J. Spey, J. Wang, M. E. Reiss, T. P. Weihs, E. Besnoin und O. M. Knio, „Reactive nanostructured foil used as a heat source for joining titanium“, *J. Appl. Phys.*, Bd. 96, Nr. 4, 2004, S. 2336–2342, DOI: 10.1063/1.1769097.

[21] K. Maekawa, S. Ito und T. Namazu, „Influence of bonded area size on cracking in reacted NiAl layer for crack-free reactive soldering“, *Jpn. J. Appl. Phys.*, Bd. 59, Nr. SI, 2020, Art.-Nr. SIIL01, DOI: 10.35848/1347-4065/ab769b.

[22] K. Maekawa, K. Kodama, S. Miyake und T. Namazu, „Laser-induced multiple points ignition test in Al/Ni exothermic reactive film for crack propagation control“, *Jpn. J. Appl. Phys.*, Bd. 60, Nr. SC, 2021, Art.-Nr. SCCL15, DOI: 10.35848/1347-4065/abf39c.

[23] X. Qiu und J. Wang, „Bonding silicon wafers with reactive multilayer foils“, *Sens. Actuators A: Phys.*, Bd. 141, Nr. 2, 2008, S. 476–481, DOI: 10.1016/j.sna.2007.10.039.

[24] X. Qiu und J. Wang, „Reactive multilayer foils for silicon wafer bonding“, *MRS Online Proceedings Library (OPL)*, Bd. 968, 2006, Art.-Nr. 0968-V02-06, DOI: 10.1557/PROC-0968-V02-06.

[25] T. Namazu, K. Ohtani, K. Yoshiki und S. Inoue, „Crack propagation direction control for crack-less solder bonding using Al/Ni flash heating technique”, in *2011 16th International Solid-State Sensors, Actuators and Microsystems Conference*, Beijing, China, Juni 2011, S. 1368–1371, DOI: 10.1109/TRANSDUCERS.2011.5969524.

[26] M. S. Tong, D. Sturgess, K. N. Tu und J. M. Yang, „Solder joints fabricated by explosively reacting nanolayers“, *Appl. Phys. Lett.*, Bd. 92, Nr. 14, 2008, Art.-Nr. 144101, DOI: 10.1063/1.2907850.

[27] H. Ji, Y. Qiao und M. Li, „Rapid formation of intermetallic joints through ultrasonic-assisted die bonding with Sn-0.7Cu solder for high temperature packaging application“, *Scr. Mater.*, Bd. 110, 2016, S. 19–23, DOI: 10.1016/j.scriptamat.2015.07.036.

[28] J. Wilde, „B4.1 – trends in assembly and packaging of sensors“, in *Proc. SENSOR 2009*, Bd. 1, 2009, S. 205–210, DOI: 10.5162/sensor09/v1/b4.1.

[29] C. K. Lee, J. K. Ahn, C. R. Lee, D. Kim und B. J. Baek, „Thermal analysis of LED lamp with LTCC-COB package“, *Microelectron. Int.*, Bd. 30, Nr. 1, 2013, S. 3–9, DOI: 10.1108/13565361311298169.

[30] T. Welker, „Methoden und Technologien zur Optimierung der Entwärmung aktiver und passiver Komponenten auf keramischen Mehrlagensubstraten“, Dissertation, Technische Universität Ilmenau, Ilmenau, Deutschland, 2018.

[31] H. Bartsch de Torres, C. Rensch, M. Fischer, A. Schober, M. Hoffmann und J. Müller, „Thick film flow sensor for biological microsystems“, *Sens. Actuators A: Phys.*, Bd. 160, Nr. 1–2, 2010, S. 109–115, DOI: 10.1016/j.sna.2010.04.010.

[32] Y. Fournier, „3D structuration techniques of LTCC for microsystems applications“, Dissertation, École Polytechnique Fédérale de Lausanne, Ecublens, Schweiz, 2010, DOI: 10.5075/epfl-thesis-4772.

[33] L. Golonka, P. Bembnowicz, D. Jurków, K. Malecha, H. Roguszczak und R. Tadaszak, „Low temperature co-fired ceramics (LTCC) microsystems“, *Opt. Appl.*, Bd. 41, Nr. 2, 2011, S. 383–388.

[34] A. Bittner und U. Schmid, „The porosification of fired LTCC substrates by applying a wet chemical etching procedure“, *J. Eur. Ceram. Soc.*, Bd. 29, Nr. 1, 2009, S. 99–104, DOI: 10.1016/j.jeurceramsoc.2008.05.030.

[35] T. Thelemann, M. Fischer, A. Groß und J. Müller, „LTCC-based fluidic components for chemical applications“, *J. Microelectron. Electron. Packag.*, Bd. 4, Nr. 4, 2007, S. 167–172, DOI: 10.4071/1551-4897-4.4.167.

[36] C. Jacq, T. Maeder und P. Ryser, „Sensors and packages based on LTCC and thick-film technology for severe conditions“, *Sadhana*, Bd. 34, 2009, S. 677–687, DOI: 10.1007/s12046-009-0031-z.

[37] D. Nowak und A. Dziedzic, „LTCC package for high temperature applications“, *Microelectron. Reliab.*, Bd. 51, Nr. 7, 2011, S. 1241–1244, DOI: 10.1016/j.microrel.2011.02.018.

[38] M. Santo Zarnik und D. Belavic, „Study of LTCC-based pressure sensors in water“, Bd. 220, 2014, S. 45–52, DOI: 10.1016/j.sna.2014.09.009.

[39] S. Seok, J. Kim und M. Lathi, „A study on the effect of wire bonding interconnects of BCB capped CPW to CPW on LTCC substrate“, *Microw. Opt. Technol. Lett.*, Bd. 56, Nr. 6, 2014, S. 1378–1381, DOI: 10.1002/mop.28355.

[40] P. Uhlig, „LTCC technology for planar microwave antenna systems“, Dissertation, Universität Duisburg-Essen, Duisburg, Essen, Deutschland, 2018, DOI: 10.17185/duepublico/47796.

[41] P. Uhlig, C. Günner, S. Holzwarth, J. Kassner, R. Kulke, A. Lauer und M. Rittweger, „LTCC short range radar sensor for automotive applications at 24 GHz“, in *Proc. IMAPS*, Long Beach, Kalifornien, USA, November 2004.

[42] K. Wörhoff, A. Prak, F. Postma, A. Leinse, K. Wu, T. J. Peters, M. Tichem, B. Amaning-Appiah, V. Renukappa, G. Vollrath, J. Balcells-Ventura, P. Uhlig, M. Seyfried, D. Rose, R. Santos, X. J. M. Leijtens, B. Flintham, M. Wale und D. Robbins, „Photonic hybrid assembly through flexible waveguides“, in *Silicon Photonics and Photonic Integrated Circuits V*, Brüssel, Belgien, April 2016, S. 298–305, DOI: 10.1117/12.2227814.

[43] Y. Fournier, T. Maeder, G. Boutinard-Rouelle, A. Barras, N. Craquelin und P. Ryser, „Integrated LTCC pressure/flow/temperature multisensor for compressed air diagnostics“, Bd. 10, Nr. 12, 2010, S. 11156–11173, DOI: 10.3390/s101211156.

[44] P. Ciosek, K. Zawadzki, J. Łopacińska, M. Skolimowski, P. Bembnowicz, L. J. Golonka, Z. Brzózka und W. Wróblewski, „Monitoring of cell cultures with LTCC microelectrode array“, Bd. 393, 2009, S. 2029–2038, DOI: 10.1007/s00216-009-2651-x.

[45] T. Welker und J. Müller, „Design, simulation and fabrication of liquid cooled LTCC devices utilizing integrated channels“, in *2016 15th IEEE Intersociety Conference on Thermal and Thermomechanical Phenomena in Electronic Systems (ITherm)*, Las Vegas, Nevada, USA, Mai 2016, S. 830–835, DOI: 10.1109/ITHERM.2016.7517632.

[46] A. L. Chlebowski, E. Y. Chow, C. Ellison und P. P. Irazoqui, „Integrated LTCC packaging for use in biomedical devices“, *Biomed. Mater. Eng.*, Bd. 22, Nr. 6, 2012, S. 361–372, DOI: 10.3233/BME-2012-0725.

[47] M. Matters-Kammerer, U. Mackens, K. Reimann, R. Pietig, D. Hennings, B. Schreinemacher, R. Mauczok, S. Gruhlke und C. Martiny, „Material properties and RF applications of high k and ferrite LTCC ceramics“, Bd. 46, Nr. 1, 2005, S. 134–143, DOI: 10.1016/j.microrel.2004.10.022.

[48] H. Jantunen, T. Kangasvieri, J. Vähäkangas und S. Leppävuori, „Design aspects of microwave components with LTCC technique“, Bd. 23, Nr. 14, 2003, S. 2541–2548, DOI: 10.1016/S0955-2219(03)00155-9.

[49] A. Bittner, A. Ababneh, H. Seidel und U. Schmid, „Influence of the crystal orientation on the electrical properties of AlN thin films on LTCC substrates“, Bd. 257, Nr. 3, 2010, S. 1088–1091, DOI: 10.1016/j.apsusc.2010.08.019.

[50] J. Müller und S. Wiese, *Reactive microjoining and packaging – mechanical, thermal and electrical functionalities*, Projektantrag für das spätere durch die Deutsche Forschungsgemeinschaft (DFG) geförderte Forschungsvorhaben, DFG-Projektnr. 426204742, 2018.

[51] D. P. Adams, „Reactive multilayers fabricated by vapor deposition: a critical review“, *Thin Solid Films*, Bd. 576, 2015, S. 98–128, DOI: 10.1016/j.tsf.2014.09.042.

[52] A. S. Rogachev und A. S. Mukasyan, „Combustion of heterogeneous nanostructural systems (Review)“, Bd. 46, 2010, S. 243–266, DOI: 10.1007/s10573-010-0036-2.

[53] T. W. Barbee Jr. und T. Weihs, „Ignitable heterogeneous stratified structure for the propagation of an internal exothermic chemical reaction along an expanding wavefront and method of making same“, U.S. Patent 5,538,795, 23.07.1996.

[54] T. P. Weihs und M. Reiss, „Method of making reactive multilayer foil and resulting product“, U.S. Patent 6,534,194, 18.03.2003.

[55] A. J. Gavens, D. Van Heerden, A. B. Mann, M. E. Reiss und T. P. Weihs, „Effect of intermixing on self-propagating exothermic reactions in Al/Ni nanolaminate foils“, *J. Appl. Phys.*, Bd. 87, Nr. 3, 2000, S. 1255–1263, DOI: 10.1063/1.372005.

[56] A. S. Rogachev, A. É. Grigoryan, E. V. Illarionova, I. G. Kanel, A. G. Merzhanov, A. N. Nosyrev, N. V. Sachkove, V. I. Khvesyuk und P. A. Tsygankov, „Gasless combustion of Ti-Al bimetallic multilayer nanofoils“, *Combust. Explos. Shock* Waves, Bd. 40, 2004, S. 166–171, DOI: 10.1023/B:CESW.0000020138.58228.65.

[57] A. E. Grigoryan, N. G. Elistratov, D. Yu. Kovalev, A. G. Merzhanov, A. N. Nosyrev, V. I. Ponomarev, A. S. Rogachev, V. I. Khvesyuk und P. A. Tsygankov, „Autowave propagation of exothermic reactions in Ti-Al thin multilayer films“, *Dokl. Phys. Chem.*, Bd. 381, Nr. 1–3, 2001, S. 283–287, DOI: 10.1023/A:1012952211911.

[58] C. Pauly, „Selbstfortschreitende Reaktionen in Ru/Al/X-Multilagen“, Dissertation, Universität des Saarlandes, Saarbrücken, Deutschland, 2017, DOI: 10.22028/D291-26931.

[59] A. S. Ramos und M. T. Vieira, „Intermetallic compound formation in Pd/Al multilayer thin films“, *Intermetallics*, Bd. 25, 2012, S. 70–74, DOI: 10.1016/j.intermet.2012.02.014.

[60] M. E. Reiss, C. M. Esber, D. Van Heerden, A. J. Gavens, M. E. Williams und T. P. Weihs, „Self-propagating formation reactions in Nb/Si multilayers“, *Mater. Sci. Eng. A*, Bd. 261, Nr. 1–2, 1999, S. 217–222, DOI: 10.1016/S0921-5093(98)01069-7.

[61] S. Tanaka, K. Kondo, H. Habu, A. Itoh, M. Watanabe und K. Hori, „B/TI multilayer reactive igniter for micro solid rocket array thruster“, in *2007 IEEE 20th International Conference on Micro Electro Mechanical Systems (MEMS)*, Hyogo, Japan, Januar 2007, S. 887–890, DOI: 10.1109/MEMSYS.2007.4433181.

[62] Indium Corporation, *NanoFoil® Product Data* Sheet, Form No. 98569 R4, März 2025. [Online]. Verfügbar unter: https://www.indium.com/wp-content/uploads/2025/03/NanoFoil-PDS-98569-R4-1.pdf [Zugriff am 11.06.2025]

[63] F. Z. Chrifi-Alaoui, M. Nassik, K. Mahdouk und J. C. Gachon, „Enthalpies of formation of the Al-Ni intermetallic compounds“, *J. Alloys Compd.*, Bd. 364, Nr. 1–2, 2004, S. 121–126, DOI: 10.1016/S0925-8388(03)00493-6.

[64] DIN 4760:2025-05, „Gestaltabweichungen – Begriffe, Ordnungssystem“, DIN Media GmbH, Berlin, Deutschland, 2025, DOI: 10.31030/3611597.

[65] E. Leidich und L. Deters, „Normen, Toleranzen, Passungen und Technische Oberflächen“, in *Konstruktionselemente des Maschinenbaus 1*, 9. Aufl., B. Sauer, Hrsg., Berlin, Heidelberg, Deutschland: Springer Vieweg, 2016, S. 46, DOI: 10.1007/978-3-642-39501-7_2.

[66] H. Wittel, C. Spura und D. Jannasch, „Toleranzen, Passungen, Oberflächenbeschaffenheit“, in *Roloff/Matek Maschinenelemente*, 25. Aufl., Wiesbaden, Deutschland: Springer Vieweg, 2021, S. 38, DOI: 10.1007/978-3-658-34160-2_2.

[67] A. Yuile und S. Wiese, „LTCC with temperature sensor array for monitoring of reactive die bond processes–design optimization using CFD“, *IEEE Trans. Compon. Packag. Manuf. Technol.*, Bd. 14, Nr. 1, 2024, S. 122–129, DOI: 10.1109/TCPMT.2024.3350161.

[68] A. Schulz, H. Bartsch, N. Gutzeit, S. Matthes, M. Glaser und A. Ruh, „Characterization of reactive multilayer systems deposited on LTCC featuring different surface morphologies“, in *MikroSystemTechnik Congress 2021*, Ludwigsburg, Deutschland, November 2021, S. 1–5.

[69] A. Schulz, A. Ruh, S. Wiese und J. Müller, „Characterization of reactive multilayer systems deposited on LTCC screen printing pastes featuring different surface morphologies suitable for reactive joining applications“, in *Ceramic Interconnect and Ceramic Microsystems Technologies (CICMT) 2022*, Wien, Österreich, Juli 2022, S. 1–5.

[70] F. Kraemer, C. Pauly, F. Muecklich und S. Wiese, „Simulation of a flip chip bonding technique using reactive foils“, in *2015 16th International Conference on Thermal, Mechanical and Multi-Physics Simulation and Experiments in Microelectronics and Microsystems (EuroSimE)*, Budapest, Ungarn, April 2015, S. 1–7, DOI: 10.1109/EuroSimE.2015.7103143.

[71] S. Liang, Y. Zhong, S. Robertson, A. Liu, Z. Zhou und C. Liu, „Investigation of thermo-mechanical and phase-change behavior in the Sn/Cu interconnects during self-propagating exothermic reaction bonding“, in *2020 IEEE 70th Electronic Components and Technology Conference (ECTC)*, Orlando, Florida, USA, Juni 2020, S. 269–275, DOI: 10.1109/ECTC32862.2020.00052.

[72] A. Zhang, Z. Zhou, L. Mo, F. Wu und H. Liu, „Solidification microstructure of tin-based solder in the rapid cooling condition“, in *2017 18th International Conference on Electronic Packaging Technology (ICEPT)*, Harbin, China, August 2017, S. 966–970, DOI: 10.1109/ICEPT.2017.8046604.

[73] Y. Wan, L. Zhou und F. Wu, „Effect of remelting heat treatment on the microstructure and mechanical properties of SnBi solder under high-speed self-propagation reaction“, *Sci. Rep.*, Bd. 12, Nr. 1, 2022, Art.-Nr. 9550, DOI: 10.1038/s41598-022-13776-z.

[74] N. Jaziri, J. Müller, B. Müller, A. Boughamoura, N. Gutzeit, B. Mezghani, A. B. Kouki und F. Tounsi, „Low-temperature co-fired ceramic-based thermoelectric generator with cylindrical grooves for harvesting waste heat from power circuits“, *Appl. Therm. Eng.*, Bd. 184, 2021, Art.-Nr. 116367, DOI: 10.1016/j.applthermaleng.2020.116367.

[75] N. Jaziri, N. Gutzeit, H. Bartsch, A. Boughamoura, J. Müller und F. Tounsi, „LTCC-based Y-type thermoelectric generator with an improved heat flow guide for automotive waste heat recovery“, *Sustain. Energy Fuels*, Bd. 6, Nr. 9, 2022, S. 2330–2342, DOI: 10.1039/D2SE00048B.

[76] W. H. Müller, H. Worrack, J. Sterthaus, J. Villain, J. Wilden und A. Juritza, „How to extract continuum materials properties for (lead-free) solders from tensile tests and nanoindentation experiments“, *Microsyst. Technol.*, Bd. 15, 2009, S. 45–55, DOI: 10.1007/s00542-008-0688-y.

[77] J. Villain, O. S. Brueller und T. Qasim, „Creep behaviour of lead free and lead containing solder materials at high homologous temperatures with regard to small solder volumes“, *Sens. Actuators A: Phys.*, Bd. 99, Nr. 1–2, 2002, S. 194–197, DOI: 10.1016/S0924-4247(01)00882-2.